UNIVERSITAT DE BARCELONA

Anisotropic interactions and self-bound solutions in Bose-Einstein condensates

Maria Arazo Sánchez

Doctoral thesis

Anisotropic interactions and self-bound solutions in Bose–Einstein condensates

Maria Arazo Sánchez

Dra. Montserrat Guilleumas Morell and Dr. Ricardo Mayol Sánchez

Universitat de Barcelona

Anisotropic interactions and self-bound solutions in Bose–Einstein condensates

Programa de doctorat en Física

Autora:
Maria Arazo Sánchez

Directors:
Dra. Montserrat Guilleumas Morell
Dr. Ricardo Mayol Sánchez

Tutor:
Dr. Joan Soto Riera

Universitat de Barcelona

A la Marisa y a Javier,
per totes les batalles que no m'heu deixat lluitar sola
y por no pedirme que fuera quien no soy.

Simplicity and order are, if not the principal, then certainly the most important guidelines for human beings in general

M. C. ESCHER

More empathy, less greed, more respect

PEOPLE'S FACES, KAE TEMPEST

Contents

List of figures

List of publications

The original work presented in this Thesis is based on the papers listed below.

- **Shell-shaped condensates with gravitational sag: contact and dipolar interactions.** Maria Arazo, Ricardo Mayol and Montserrat Guilleumas, New Journal of Physics 23, 113040 (2021). *Discussed in Chapter 5 (see Arazo et al., 2021b).*

- **Dynamical generation of dark–bright solitons through the domain wall of two immiscible Bose–Einstein condensates.** Maria Arazo, Montserrat Guilleumas, Ricardo Mayol and Michele Modugno, Physical Review A 104, 043312 (2021). *Discussed in Chapter 6 (see Arazo et al., 2021a).*

- **Self-bound crystals of antiparallel dipolar mixtures.** Maria Arazo, Albert Gallemí, Montserrat Guilleumas, Ricardo Mayol and Luis Santos, Physical Review Research 5, 043038 (2023). *Discussed in Chapter 7 (see Arazo et al., 2023a).*

- **Chiral currents in Bose–Einstein condensates subject to current-density interactions.** Maria Arazo, Montserrat Guilleumas, Ricardo Mayol, Vicente Delgado and Antonio Muñoz Mateo, Physical Review A 108, 053302 (2023). *Discussed in Chapter 8 (see Arazo et al., 2023b).*

- **Spinor Bose–Einstein condensates subject to current-density interactions.** Maria Arazo, Montserrat Guilleumas, Ricardo Mayol, Vicente Delgado and Antonio Muñoz Mateo, In preparation. *Discussed in Chapter 9.*

Abstract

Bose–Einstein condensation is a direct consequence of quantum statistical effects. It occurs in ultradilute gases at very low temperatures: most atoms condense into the lowest-energy state and behave as a single matter wave. In this thesis, we study Bose–Einstein condensates (BECs) of dilute and weakly interacting atoms within the mean-field framework and focus on two topics: anisotropic interactions and self-bound states.

In ultracold dilute gases, the most common atom–atom interactions are short-range and isotropic. However, the interactions can also be anisotropic, for instance, when the gas is either formed of atoms with a large magnetic moment or subject to an artificial gauge field, exhibiting dipolar and chiral interactions, respectively. The interacting nature of the system gives rise to two possible solutions that do not require external confinement: quantum droplets and solitons. Droplets emerge from the balance between quantum fluctuations and the mean-field interactions, while solitons are localized excitations sustained by the competition between the dispersion and nonlinearity of the medium.

We begin the thesis by developing the theoretical framework. First, we present single and multicomponent BECs, the mean-field regime and its constraints, and the conditions of existence for droplets and solitons. Then, we introduce dipolar interactions, their effect on the stability and geometry of the system, and how dipolar droplets, as well as crystals of droplets, may form due to the stabilizing effect of quantum fluctuations. Last, we present BECs coupled to artificial density-dependent gauge potentials, which have effective interactions that are chiral (i.e., depend on the direction of motion of the atoms).

The first system under consideration is a BEC confined in a shell-shaped potential in the presence of gravitational sag. We explore both the dipolar and nondipolar cases and study the interplay between the anisotropy of the dipolar interactions (or the lack thereof) and the privileged direction set by gravity. We study the ground-state configurations of the system and the dynamics when changing perturbatively the orientation or the strength of the gravitational force.

Afterward, we move to binary mixtures of nondipolar and dipolar BECs to investigate, respectively, the formation of solitons and droplets. In the first case, we consider a quasi-1D bosonic mixture within the immiscible regime. We examine the dynamics of a dark soliton moving through the domain wall between components, which may generate, in some cases, a dark–bright soliton. The resulting dark–bright soliton follows a harmonic-like trajectory. Concerning the dipolar case, we propose a two-component

BEC with antiparallel dipoles, which forms self-bound structures when unconfined. In the presence of confinement in the dipole direction, the mixture can form incoherent stripes if the interactions are symmetric and droplet crystals if they are asymmetric. These droplet crystals are composed of an array of incoherent droplets in one component surrounded by an interstitial superfluid in the other. In both cases, the resulting structures are self-bound in the transversal plane.

To study the effect of chiral interactions, we regard a quasi-1D BEC confined in a rotating ring geometry and coupled to a density-dependent gauge potential, which produces chiral currents. We give an analytical description of the general stationary states of the system (plane waves and solitons) and test their dynamical stability. Finally, we split the system into two components employing a double-well potential to obtain a 1/2-spinor condensate. Besides the linear coupling between the two spin states, the system also presents an effective spin–orbit coupling due to the chiral nature of the interactions. The solutions of the scalar case are also solutions of the spinor case, but now the system also supports states that may have nonzero polarization, leading, for instance, to Josephson vortices.

* * *

La condensació de Bose–Einstein és una conseqüència directa dels efectes de l'estadística quàntica. Té lloc en gasos ultradiluïts a temperatures molt baixes: els àtoms condensen a l'estat de mínima energia i es comporten com una única ona de matèria. En aquesta tesi estudiem condensats de Bose–Einstein diluïts d'àtoms amb interaccions febles dins del formalisme de camp mitjà, i ens centrem en dos temes: interaccions anisotròpiques i estats autolligats.

En gasos ultrafreds diluïts, les interaccions interatòmiques més comunes són de curt abast i isotròpiques. Tanmateix, les interaccions també poden ser anisotròpiques, per exemple, quan el gas està format per àtoms altament magnètics o bé quan està sotmès a un camp de gauge artificial, de manera que les interaccions són dipolars o quirals, respectivament. El caràcter interactuant del sistema dona lloc a dues possibles solucions que no requereixen un confinament extern: gotes quàntiques i solitons. Les gotes es formen gràcies al balanç entre les fluctuacions quàntiques i les interaccions de camp mitjà, mentre que els solitons són excitacions localitzades que mantenen la seva forma a causa de la competició entre la dispersió i la no-linealitat del medi.

Comencem la tesi desenvolupant el marc teòric. Primer de tot, presentem els condensats formats per una o més components, el règim de camp mitjà i les seves limitacions, i les condicions sota les quals les gotes i els solitons poden existir. Seguidament, introduïm les interaccions de tipus dipol–dipol, el seu efecte en l'estabilitat i la geometria del sistema, i com l'efecte estabilitzant de les fluctuacions quàntiques permet que es formin gotes dipolars així com cristalls de gotes. Per acabar, presentem condensats acoblats a potencials de gauge artificials que depenen de la densitat, els quals tenen unes interaccions efectives que són quirals (és a dir, interaccions que depenen de la direcció en què es mouen els àtoms).

El primer sistema que considerem és un condensat confinat en un potencial amb forma de closca sota l'efecte de la gravetat. Explorem tant el cas dipolar com el no-dipolar, i estudiem el joc entre l'anisotropia de les interaccions dipolars (o la seva absència) i la direcció privilegiada que dicta la gravetat. Estudiem les configuracions de l'estat fonamental del sistema i la dinàmica quan es pertorba l'orientació o la magnitud de la força de la gravetat.

A continuació, ens centrem en barreges binàries de condensats no-dipolars i dipolars per investigar, respectivament, la formació de solitons i gotes. En el primer cas, considerem una barreja bosònica quasi-1D dins del règim immiscible. Examinem la dinàmica d'un solitó fosc que es mou a través de la interfase entre les dues components, que pot donar lloc, en alguns casos, a un solitó fosc–brillant. El solitó que en resulta descriu una trajectòria harmònica. Respecte al cas dipolar, proposem un condensat de dues components amb dipols antiparal·lels, que pot donar lloc a estructures autolligades sense confinament extern. Quan el sistema està confinat al llarg de la direcció dels dipols, la barreja pot formar franges incoherents si les interaccions són simètriques i cristalls de gotes si són asimètriques. Aquests cristalls de gotes estan formats per una xarxa de gotes incoherents en una de les components envoltada per un superfluid intersticial a l'altre. En ambdós casos, les estructures que en resulten són autolligades en el pla transversal.

Per estudiar l'efecte de les interaccions quirals, considerem un condensat quasi 1D confinat en una geometria rotant tipus anell i acoblat a un potencial de gauge depenent de la densitat, de manera que els corrents persistents que es produeixen esdevenen quirals. Donem una descripció analítica dels estats estacionaris generals del sistema (ones planes i solitons), i comprovem la seva estabilitat dinàmica. Finalment, separem el sistema en dues components a través d'un potencial de doble pou per obtenir un condensat espinor 1/2. A part de l'acoblament lineal entre els dos estats d'espí, el sistema presenta a més un acoblament espí–òrbita efectiu per la naturalesa quiral de les interaccions. Les solucions del cas escalar són també solucions del cas espinor, però ara el sistema suporta a més estats que poden tenir una polarització no-nul·la, donant lloc, per exemple, a vòrtexs de Josephson.

Acknowledgements

The doctoral journey is one of those experiences that leaves a lasting mark. It is full of joy and wonder, but it is also a ride into uncertainty and obsession, and culminates in a brief yet intense period of isolation and reflection from which you are supposed to emerge with a dissertation and a matching self-confidence. If I have reached this stage where only the acknowledgments and the defense are left, it is thanks to all the people who have accompanied me along the way. Most of you have only received a very anxious *well thank you very much for everything* at best (sorry for that), so I will try to fix that here and give you all the proper gratitude you deserve.

Careful planning, unyielding enthusiasm, and too much coffee were essential ingredients for this project to reach its end successfully. However, this thesis wouldn't even exist without my supervisors. Thank you, Muntsa and Ricardo, for the careful readings and long meetings of these last months (you found *almost* all the little rabbits) and for all the physics discussions, laughs, and lunch conversations we had over the years. Thank you for bearing with all my complaints and worries. I will be forever grateful for the constant guidance and support you've given me during these four-ish years. I remember very well how low my communication level was when I started, but you didn't lose hope in me. Instead, you created a safe space for me in which to grow, and the way you trusted me and encouraged me despite the initial setbacks has taught me which sort of person I want to be if I ever have the opportunity to mentor someone. Also, the fact that you do not seem tired of either me or my thesis proves that it was not that bad in the end. It took me almost five years, Ricardo, but now I finally get your jokes, and I expect to return them in due time. And Muntsa, thank you for your closeness and for intervening in all those situations where the solution was talking to someone without offending them.

The several fruitful collaborations that led to the work presented in this thesis were also crucial for my growth as a scientist. In chronological order: Prof. Michele Modugno, Dr. Albert Gallemí, Prof. Luis Santos, Dr. Antonio Muñoz, and Prof. Vicente Delgado. Thank you all for enriching my academic life and sharing the joy of research, each in your own peculiar way. Michele, thank you for hosting me during my visit to Bilbao, back in the pre-pandemic times, and for having a lot of patience with my slow progress during the lockdown months. Luis, thank you for hosting me in Hannover for my stay. It was a very valuable experience for me both in the academic and personal sense, and I am grateful for the opportunity to learn from you. Albert, you made my Hannover months anything but boring; I enjoyed a lot discussing with you, and the laughs almost always compensated for your raw criticisms. That phase diagram we did during your

visit a Christmas ago was pure magic, though I'm glad it never saw the light of day. Vicente, thank you for your warm welcome during my short visit to La Laguna; you made me feel at home in less than a week. Antonio, I'm immensely grateful for all the lively discussions. Thank you for guiding me through the dark avenues of this new topic and for enduring my persistent emails. Thank you as well for reading part of this thesis so thoroughly. But now that the thesis is finished, please do *not* let me know if you find any more inconsistencies.

I joined the field of ultracold atoms thanks to Prof. Bruno Juliá and Prof. Artur Polls. Thank you two for introducing me to such a beautiful area and for supervising both my Bachelor's and Master's theses. Enduring *Computational Physics* as a student was honestly a nightmare, Bruno, but that weekly torture sparked my interest in numerical methods, so thank you for that as well.

I want to express my gratitude to all the people who have populated the 646V office during my PhD, even in the noninteracting months of the pandemic. I especially want to thank the remarkable triumvirate with whom I shared many hours and laughs (but not cookies) during these last months of writing frenzy and drama. Abel, Carlos, and Héctor: thank you for enduring my anxious presence and for the unasked distractions and collective procrastination. I wish you three a lot of luck for your own theses, and I hope you have some patience left after I defend mine. You will need it.

A big thank you must go to my high school physics teacher. With you, Dolors, I discovered the magic of science and you convinced me that doing physics and creative writing was not a matter of choosing one but of proper time management. And now I couldn't be happier with my decisions in that regard.

I'm also indebted to my therapist for their guidance and support in the intricacies of the PhD life as a neurodivergent person. Pandemic aside, 2020 was a complicated yet exceptional year, and our sessions during that summer changed my life.

To my writing friends, Marina, Esther, and Ricard: thank you for our yearly but fantastic meetings and for not complaining about my intermittent WhatsApp presence. It was fun to share this process of writing a thesis with you and hear your ideas and advice, though character issues are not something fixable here. Yet, writing a thesis is still writing, and I'm delighted to see that all we learned and suffered can also be useful elsewhere.

I owe a lot of teas and even hugs to my delocalized friends, thanks to whom I've learned to appreciate video and phone calls, although I will never like them nor sit still for that long. Sergi, it's been a pleasure to share so many breakfasts, bookstore visits, and well-formatted course notes with you. I remember escaping for coffee together after *General Relativity* to talk about stories and laugh at each other's bad jokes; here we are now, almost ten years later, with different circumstances but the same old habits. And, of course, journey before destination. Yolanda, the most chaotic and extroverted person I've ever met: I'm grateful for all our controversial discussions, and I hope we'll keep having them in the future. You've shown me that no matter how huge the opinion and age gaps are, it's always possible to find a common ground to build something together. Especially if food is involved. Helena, I would need a spreadsheet to thank you properly, and I know you would appreciate the format, but I'll keep it normal. Thanks

for listening to my endless doubts, for being there during the most difficult moments of these last years, and for understanding my long silences so well. Your friendship is a privilege and a gift, and I'm grateful for all the parts of your life in which you have included me.

Albert, Marta, and the martial family: I may no longer be an active member of the dojo, but the years I spent with you changed me radically. You taught me how to tolerate frustration and to speak up for myself, and I wouldn't be where I am now without your training, encouragement, and love.

Family-wise, I want to thank the Nicolaus for taking care of me from the other side of the mountains. Thank you, Maite, for your regular check-ups; Marcel, for being the mathematician of reference that any physicist needs; Adriana, for sharing your humanities' perspective of academia and for the best theater recommendations.

From the Sánchez branch of the family, I want to thank my aunt Neus, my uncle Antonio, and my cousins Sergi and Lorena for being a safe and solid presence in my life. Thanks for being my favorite travel pals and for all the good meals and laughs we have shared. I know this doesn't make much sense to you and that choosing this path may be puzzling from the outside, so double thanks for being there nonetheless.

I'm also grateful for the contribution to my education that my grandparents Ginés and Enriqueta had during my childhood and teenage years. Avi, you strongly encouraged me to follow whichever path my curiosity led me to and I will never forget that conversation we had when I was a sad sixteen-year-old who didn't fit anywhere. Iaia, you've shown me what sacrifice and strength are and, even though I cannot say we've always got along very well, I will forever love you.

Tons of thanks and love to the Irish sector for all the support and comic relief. Ailbhe, I don't have enough data yet to properly thank you, but keeping an eye on my obstinate brother is already enough reason for doing so. To Eric, I'm most grateful for the shared childhood and upbringing. And, now that we've somehow become functional adults, thank you for being a very persuasive sports enthusiast and sharing your life hacks with me. Your stubbornness is truly contagious, and if I went from scholarly couch potato to *let's try open-water swimming* it's mostly your fault. And, of course, thank you for all those long conversations we tend to have about life in general and navigating this crazy neurotypical world. I think we've almost got it.

Papa and Mama: I would need my whole lifetime to pay for all you did for me (though I know you did it all for free). You had to face things other parents never have to even think about, but your kindness, respect, and perseverance made the impossible just somewhat difficult. I especially want to thank my father, Javier, for teaching me to do things the right way even when no one else seems to care. Thanks, Papa, for sharing your passion for detail and perfectionism. I also want to thank my mother, Marisa, for addressing all my doubts and worries about managing and understanding people. Also, Mama, thank you for feeding me and listening to my strong opinions about bureaucracy during these last pre-submit weeks.

Last, but not least, thank you for everything else, Eulàlia: for your trust and love, for making me laugh when I most need it, and for accepting me both with and without masking. The last year has been one of those *fantastic* opportunities to grow, but I'm

sure we will make it all work. I've learned a lot with you, too, and these PhD years together have been, so far, the best ones of my life. Let's see now what surprises the postdoc era brings.

Barcelona,
March 9th, 2024

The work presented in this thesis has been supported by MINECO through FPI Grant PRE2018-084091.

1

Introduction

Bose–Einstein condensation occurs when cooling down a gas of identical bosons to fractions of microkelvins. At such low temperatures, quantum statistics govern the behavior of the system: the thermal de Broglie wavelength becomes of the order of the interparticle distance such that the individual wavepackets of the atoms overlap with each other, and a notable fraction of the gas condenses into the same lowest-energy state (Dalfovo et al., 1999; Leggett, 2001; Pethick and Smith, 2008; Pitaevskii and Stringari, 2016; Ueda, 2010). This transition was predicted a century ago by Bose (1924) and Einstein (1924, 1925) and was thus later named *Bose–Einstein condensation*. However, several decades had to pass for laser-based cooling and trapping methods to reach maturity. In general, the standard procedure to Bose-condense an atomic gas involves laser cooling, magnetic or optical trapping, and subsequent evaporative cooling (see for instance Ketterle and Van Druten, 1996; Metcalf and Van der Straten, 1999). The developments of these cooling and trapping techniques earned Chu (1998), Cohen-Tannoudji (1998), and Phillips (1998) the 1997 Nobel Prize.

It was not until the mid-1990s that the phenomenon of Bose–Einstein condensation was finally observed in alkali atoms, which have an internal structure suitable for the lasers that were available at the moment. The first Bose–Einstein condensates (BECs) were achieved with ultradilute gases of rubidium (Anderson et al., 1995), sodium (Davis et al., 1995), and lithium (Bradley et al., 1995, 1997a,b). Some years later, Ketterle (2002), Cornell and Wieman (2002) won the 2001 Nobel Prize for observing for the first time Bose–Einstein condensation in a weakly interacting and ultradilute gas of alkali atoms. Since then, research on BECs has expanded theoretically and experimentally, weaving into the fields of atomic physics, quantum optics, and condensed matter.

1.1 Bose–Einstein condensates

Although BECs of ultracold gases are very dilute, the extremely low temperatures enhance the effect of the interactions. In such dilute gases, the leading atom–atom interactions are two-body collisions. In alkali atoms, these interactions are short-range and isotropic, and may be repulsive or attractive. Three-body processes are infrequent but may still occur, and constitute the main loss mechanism of BECs and limit their

lifetimes in experiments. As three-body losses grow rapidly with the atomic density, the distance between atoms must be much larger than the typical range of the interactions to reduce their probability.

When the interactions are weak and the number of atoms is sufficiently large, one can tackle the many-body problem of very dilute ultracold gases with a mean-field approach in which each atom is surrounded by an effective potential that conveys the effect of all the other particles. Quantum fluctuations are negligible under these conditions and, as long as the temperature is well below the critical temperature for condensation, almost all the atoms condense into the lowest-energy state. The particles in the condensate then behave as a giant matter wave that is characterized by a macroscopic wavefunction, and the Gross–Pitaevskii equation (GPE) gives a good description of the static and dynamic properties of the system. The GPE is a Schrödinger-like equation with a nonlinearity term that incorporates the atom-atom interactions.

Superfluidity is a noteworthy feature of condensates that stems from the fact that N atoms populate all the same state with the same wavefunction (Dalfovo et al., 1999; Pitaevskii and Stringari, 2016) and it refers to the ability of the system to flow with no viscosity. Such a frictionless flow does not dissipate energy and is characterized by the so-called *speed of sound*, which is the velocity at which a sound wave may travel through the condensate. Quantized vortices (Gross, 1961; Pitaevskii, 1961) are a clear signature of the superfluid character of quantum systems and, in rotating multiply-connected geometries (such as a ring or a torus), these vortices (Schulte et al., 2002; Sinha and Castin, 2001) produce persistent currents (Abad, 2016; Abad et al., 2014; Andersen et al., 2006; Beattie et al., 2013; Cominotti et al., 2014, 2015; Gallemí et al., 2015; Kumar et al., 2018; Muñoz Mateo et al., 2015; Pecci et al., 2023; Polo et al., 2019; Ryu et al., 2007; Smyrnakis et al., 2014; Wu et al., 2015). Collective excitations of the system (Hutchinson and Zaremba, 1998; Jin et al., 1996; Mewes et al., 1996) and the presence of the scissors mode (Guéry-Odelin and Stringari, 1999; Maragò et al., 2000), for instance, are also a consequence of its superfluidity.

Since the particles in the BEC behave as a single matter wave, they can be described by a macroscopic wavefunction with a well-defined phase and exhibit coherent phenomena (Glauber, 1963). For two trapped BECs, when one removes the confinement, the condensates expand and overlap, forming interference patterns (Andrews et al., 1997). Phase coherence can also manifest as the Josephson effect (Anderson and Rowell, 1963; Josephson, 1962), which is the coherent transport of particles between two superfluid components. Josephson dynamics have been extensively studied in bosonic Josephson junctions (Albiez et al., 2005; Ferrini et al., 2008, 2010; Levy et al., 2007; Melé-Messeguer et al., 2011; Raghavan et al., 1999; Shin et al., 2005; Smerzi et al., 1997), which can be realized using a double-well potential. Bosonic Josephson junctions differ from superconducting Josephson junctions in that the nonlinearity of the contact interactions gives rise to a new dynamical regime, called *macroscopic quantum selftrapping*, where the population locks in one of the two sides of the junction.

Ultracold bosonic gases offer highly tunable experimental platforms: for example, one can externally control their geometry and atom–atom interactions, and induce light–matter interactions by coupling the atoms to external laser fields. For instance,

one can implement exotic potentials that result in curved geometries, such as rings and shells of atoms. In particular, ring potentials provide a simple yet versatile system for atomtronic devices (see Amico et al., 2021, 2022, and references therein). Shell-shaped BECs (Garraway and Perrin, 2016; Harte et al., 2018; Perrin and Garraway, 2017; White et al., 2006; Zobay and Garraway, 2001, 2004) can be obtained by employing radiofrequency-dressed adiabatic potentials to a conventional magnetic trap such that the atoms are confined to an ellipsoidal surface (see also Tononi and Salasnich, 2023, and references therein). Ring potentials, on the other hand, can be implemented using time-averaged adiabatic potentials (Arnold, 2012; Bell et al., 2016; Sherlock et al., 2011), painted potentials (Henderson et al., 2009; Schnelle et al., 2008), magnetic traps (Gupta et al., 2005; Morizot et al., 2006; Ryu et al., 2007), or Laguerre–Gauss beams (Wright et al., 2000), among other techniques.

Although this thesis focuses on the continuum description of ultracold bosonic gases, it is worth mentioning that ultracold atoms can also be confined in periodic potentials to form optical lattices (Bloch et al., 2008; Fisher et al., 1989; Greiner et al., 2002; Grimm et al., 2000; Jaksch et al., 1998; Lewenstein et al., 2012). In this case, the effective interactions can be much stronger than the contact interactions in regular ultracold gases such that the system reaches the strongly correlated regime. Thus, optical lattices present a promising platform for quantum simulation (Bañuls et al., 2020; Feynman, 1982; Georgescu et al., 2014; Gross and Bloch, 2017).

The interatomic interactions can be tuned by employing optical (Fedichev et al., 1996; Theis et al., 2004; Thomas et al., 2018) and magnetic (Cornish et al., 2000; Pollack et al., 2009) Feshbach resonances (Chin et al., 2010). Controlling the atom–atom interactions opens the possibility to either enhance the nonlinearity of the system or, in gases with a non-negligible dipolar moment, reduce the contact interactions such that dipole–dipole interactions dominate. Condensates with attractive contact interactions are also accessible by changing the sign of the s-wave scattering length through scattering resonances.

The landscape gets even richer when not all the atoms are identical. Bosonic mixtures can be *heteronuclear mixtures*, formed by atoms from various species (Grimm et al., 2000; Hall et al., 1998; Modugno et al., 2002; Mosk et al., 2001; Pires et al., 2014; Schäfer et al., 2022); *isotopic mixtures*, with different isotopes of the same atomic species (Ferrier-Barbut et al., 2014; Papp and Wieman, 2006; Schreck et al., 2001); or *spin mixtures*, which comprise atoms of the same species and isotope but in different spin states (Becker et al., 2008; Katsimiga et al., 2020; Kawaguchi and Ueda, 2012; Myatt et al., 1997; Stamper-Kurn and Ueda, 2013; Stamper-Kurn et al., 1998; Stenger et al., 1998). In all these mixtures, the interactions within each component and between them may be asymmetric, and depending on the interplay between interactions, bosonic mixtures may be miscible, immiscible, or unstable (Timmermans, 1998; Trippenbach et al., 2000). In spin mixtures, also known as *spinor condensates*, there can be a population transfer between components, which may be coupled either through light–matter interactions or by trapping the system in an external double-well potential. This coupling can be a coherent coupling between the wells or internal states (Matthews et al., 1999) or a spin–orbit coupling (Lin et al., 2011). In all cases, spinor condensates offer an excellent playground to explore

coherence effects such as Josephson dynamics (for more details, see Abad and Recati, 2013; Recati and Stringari, 2022, and references therein).

In addition, by tuning the light–matter interactions one can engineer artificial gauge potentials in ultracold gases where the internal states of the atoms are optically coupled (Chisholm et al., 2022; Edmonds et al., 2013a; Frölian et al., 2022), thus simulating electromagnetic effects with particles that are charge neutral (Dalibard, 2016; Dalibard et al., 2011; Goldman et al., 2014; Spielman, 2009). The system acquires a geometrical phase during the adiabatic path of the light-dressed states (Berry, 1984; Dum and Olshanii, 1996), which results in the emergence of these artificial gauge fields.

1.2 Anisotropic interactions

The most common atom–atom interactions in ultracold gases are short-range and isotropic. As a result, they can be characterized by a single parameter, the contact s-wave scattering length. The leading scattering processes only occur at small distances, and the mean interactions are equivalent in any direction. However, the behavior of the system can be markedly different with dipole–dipole interactions or when the effective contact interactions are chiral.

In gases of atoms with a high dipolar moment, the interactions acquire a long-range character and become anisotropic. The dipoles then behave analogously to magnets, and their orientation determines the strength of the interactions and whether the neat effect is attractive or repulsive. Due to this anisotropy and the long-range nature, dipolar gases present new phenomena as compared to nondipolar gases (Baranov, 2008; Baranov et al., 2002, 2012; Chomaz et al., 2022; Defenu et al., 2023; Góral et al., 2000; Lahaye et al., 2009).

The dipole moment can be either electric or magnetic. Electric dipole moments are not permanent and can be induced, for instance, using ultracold molecules (Bohn et al., 2017; Carr et al., 2009; Moses et al., 2017) and Rydberg atoms (Löw et al., 2012; Saffman et al., 2010). In this thesis, we will focus instead on atoms with non-negligible magnetic dipole moments, which are permanent. Alkali atoms have a small magnetic moment and thus are not very well suited to study dipolar physics, so one needs to consider atoms with a higher magnetic moment. The highly magnetic atoms most used in experiments are chromium (Beaufils et al., 2008; Griesmaier et al., 2005), erbium (Aikawa et al., 2012; McClelland and Hanssen, 2006), and dysprosium (Lu et al., 2010b, 2011), which have a dipole moment of 6 μ_B, 7 μ_B, and 10 μ_B, respectively (μ_B is the Bohr magneton). The first dipolar BEC was obtained with chromium atoms (Griesmaier et al., 2005). Some years later, erbium (Aikawa et al., 2012) and dysprosium (Lu et al., 2010b) BECs were experimentally realized, which spiked the interest in the field of ultracold dipolar gases. Other possible candidates among the lanthanide atoms are thulium (4 μ_B, Sukachev et al., 2010), holmium (9 μ_B, Miao et al., 2014), and europium (9 μ_B, Inoue et al., 2018). Mixtures of highly magnetic atoms (Bisset et al., 2021; Lee et al., 2021; Smith et al., 2021) have also been realized experimentally very recently (Durastante et al., 2020; Politi et al., 2022; Trautmann et al., 2018).

One can also obtain short-range anisotropic interactions from a contact interacting

system in the presence of artificial gauge fields, as could occur in optically coupled condensates, for instance. In this situation, a gauge potential that depends on the local atomic density can result in a system whose effective interactions become sensitive to the moving direction of the atoms. Such interactions are said to be chiral, as motion in different directions is not equivalent.

Aglietti et al. (1996) formulated a chiral theory for a 1D system in which the nonlinearity of the system comes from the current density instead of the number density due to the presence of a density-dependent gauge potential. Almost two decades later, Edmonds et al. (2013a) proposed optically coupled BECs as a good candidate for inducing density-dependent gauge potentials by tuning the light–matter interactions. Very recently, this proposal was further developed by Chisholm et al. (2022) and experimentally realized by Frölian et al. (2022) in a condensate with two Raman-coupled components and asymmetric scattering lengths. Artificial gauge potentials have also been realized for instance in trapped ions (Martinez et al., 2016) and in optical lattices (Clark et al., 2018; Görg et al., 2019; Yao et al., 2022).

Ultracold gases in the presence of these artificial vector potentials (Dalibard et al., 2011; Goldman et al., 2014) present different properties than their nonchiral counterparts (Edmonds et al., 2013a, 2015; Xu et al., 2023). Some of the new phenomena comprises spin–orbit coupling (Lin et al., 2009, 2011; Yang et al., 2021) and, in the case of density-dependent gauge potentials (Edmonds et al., 2013a; Greschner et al., 2014), vortices and collective modes with unusual properties (Butera et al., 2015, 2016; Chen and Zhai, 2012; Edmonds et al., 2015; Zhang et al., 2012; Zheng et al., 2015).

1.3 Self-bound states

Usually, BECs must be externally trapped because repulsive interactions lead the system to expand otherwise. However, under some circumstances, ultracold gases may support quantum droplets and solitons, which can exist in the absence of an external confinement. Both types of solutions can only arise in interacting systems, but the origin of their binding mechanism is fundamentally different.

In the regime where the mean-field description predicts a collapse of the condensate, the system may be stabilized by quantum fluctuations and give rise to self-bound quantum droplets (Böttcher et al., 2021; Chomaz et al., 2022). For this to occur, the small repulsion due to quantum fluctuations must counterbalance the contribution of the effective mean-field interactions, which must be attractive and small. This can happen in systems which have two independent interparticle interactions that result in a reduced mean-field contribution, such as dipolar condensates (Bisset et al., 2016; Böttcher et al., 2019b; Chomaz et al., 2016; Ferrier-Barbut et al., 2016a,b, 2018a; Kadau et al., 2016; Saito, 2016; Schmitt et al., 2016; Wächtler and Santos, 2016a,b), which have both contact and dipole–dipole interactions, and nondipolar mixtures (Cabrera et al., 2018; Cheiney et al., 2018; D'Errico et al., 2019; Ferioli et al., 2019, 2020; Guo et al., 2021; Naidon and Petrov, 2021; Petrov and Astrakharchik, 2016; Rakshit et al., 2019; Semeghini et al., 2018; Tengstrand and Reimann, 2022), where the interactions have a competition between

intracomponent and intercomponent forces. The theory that describes quantum droplets in the continuum includes a beyond mean-field (or Lee–Huang–Yang) correction to the mean-field formalism to account for the effect of quantum fluctuations, and was first developed for dipolar droplets by Lima and Pelster (2011, 2012) and soon after for nondipolar bosonic mixtures by Petrov (2015). Droplets were first experimentally realized with dipolar atoms (Ferrier-Barbut et al., 2016a; Kadau et al., 2016), and later with bosonic mixtures (Cabrera et al., 2018).

Here we focus on dipolar droplets, where the mean-field contribution is reduced by the balance between the contact and dipole–dipole interactions within the condensate. One feature of these droplets is that they can self-assemble into coherent arrays that are the ground state of the system (Baillie and Blakie, 2018; Cinti and Boninsegni, 2017; Macia et al., 2016; Wenzel et al., 2017). The interplay between the binding mechanism of droplets and the trapping geometry governs the formation of such crystals. The confinement along the dipole (axial) direction may be too strong for the system to sustain a single droplet, which instead breaks into several droplets that arrange in a crystalline structure. The resulting crystals hold together by the transversal confinement and may present supersolid features, i.e., a density-modulated profile (as in a solid) and phase coherence (as in a superfluid). Supersolid properties in dipolar gases were first observed experimentally in 2019 (Böttcher et al., 2019a; Chomaz et al., 2019; Tanzi et al., 2019a). The excitations and rotational properties of these highly dipolar systems have been extensively studied since then (Gallemí et al., 2020; Hertkorn et al., 2019; Šindik et al., 2022; Klaus et al., 2022; Norcia et al., 2022; Petter et al., 2019; Recati and Stringari, 2023; Roccuzzo et al., 2020, 2022; Sohmen et al., 2021; Tanzi et al., 2021; Tengstrand et al., 2021, 2023). Condensates with spin–orbit coupling may also present supersolid properties (Li et al., 2017; Martone et al., 2014; Putra et al., 2020; Recati and Stringari, 2022), although in that case, the density modulation does not originate from the intrinsic interactions of the system but from the light–matter coupling.

Solitons are localized perturbations that propagate without dispersion and which are stable solutions of 1D gases (Ablowitz et al., 2004; Barenghi and Parker, 2016; Carr et al., 2000c; Frantzeskakis, 2010; Kevrekidis et al., 2010, 2015; Scott et al., 1973; Shamailov and Brand, 2018; Weinstein, 1983). The binding mechanism of solitons comes from the balance between the dispersion of the medium and its nonlinear character. There are essentially two types of solitons, dark and bright, depending on the sign of the nonlinearity, which is determined by the contact interactions.

Bright solitons are the ground state of the system when the interactions are attractive (Carr and Castin, 2002; Cornish et al., 2006; Donley et al., 2001; Gammal et al., 2001; Gerton et al., 2000; Khaykovich et al., 2002; Ma and Huang, 2013; Marchant et al., 2013; Pérez-García et al., 1998; Roberts et al., 2001; Strecker et al., 2002). They present as self-bound wavepackets with a free-particle behavior. Dark solitons, on the other hand, are excited states of repulsive-interacting systems that show as a localized density dip with a phase jump across it, are not self-bound, and present a wave-like nature (Anderson et al., 2001; Brazhnyi and Konotop, 2003a,b; Burger et al., 1999; Denschlag et al., 2000; Dutton et al., 2001; Ginsberg et al., 2005; Gredeskul and Kivshar, 1989; Gredeskul et al., 1990; Konotop and Vekslerchik, 1994; Muryshev et al., 2002; Proukakis et al., 2004). In

general, solitons are unstable in higher dimensions (Dalfovo et al., 1999; Leggett, 2001; Sulem and Sulem, 2007), but stable dark and bright solitons can be achieved with tightly confined geometries in one and two dimensions (Brand and Reinhardt, 2001; Carr et al., 2000c; Feder et al., 2000; Muryshev et al., 1999). Modulational instability may also lead to the formation of soliton trains in a condensate (Everitt et al., 2017; Nguyen et al., 2017; Sanz et al., 2022).

Solitons have been extensively studied in multicomponent optical systems (Akhmediev et al., 1998; Desyatnikov et al., 2002; Hioe, 1999; Kivshar and Turitsyn, 1993; Manakov, 1973; Mitchell and Segev, 1997; Park and Shin, 2000; Pelinovsky and Kivshar, 2000; Skryabin, 2000; Zakharov and Manakov, 1975; Zakharov and Schulman, 1982), where soliton pairs, such as dark–dark, dark–bright and bright–bright solitons, can be realized (Afanasyev et al., 1989; Buryak et al., 1996; Chen et al., 1997; Radhakrishnan and Lakshmanan, 1995). In two-component BECs (Becker et al., 2008; Hall et al., 1998; Katsimiga et al., 2020; Kiehn et al., 2019; Morera et al., 2018; Morera-Navarro et al., 2018; Myatt et al., 1997; Pu and Bigelow, 1998; Timmermans, 1998), new solitonic states have been experimentally realized, for instance, dark–dark solitons (Hoefer et al., 2011), dark–bright solitons (Achilleos et al., 2011; Alotaibi and Carr, 2019; Becker et al., 2008; Busch and Anglin, 2001; Hamner et al., 2011; Middelkamp et al., 2011; Romero-Ros et al., 2022; Yan et al., 2015), and vortex–bright-soliton configurations (Anderson et al., 2000; Law et al., 2010; Richaud et al., 2020). The so-called *magnetic solitons*, which are localized perturbations of the spin density, appear in the particular case of mixtures with asymmetric interactions (Bresolin et al., 2023; Pitaevskii, 2016; Qu et al., 2016). Other peculiar solitonic solutions are *Josephson vortices*, which arise due to the presence of coherent coupling between components (Kaurov and Kuklov, 2005, 2006). Finally, *chiral solitons* can be observed in systems subject to current-density interactions (Aglietti et al., 1996; Bhat et al., 2021; Cheiney et al., 2018; Dingwall and Öhberg, 2019; Dingwall et al., 2018; Edmonds et al., 2013a; Gao et al., 2022; Griguolo and Seminara, 1998; Jia et al., 2022b; Öhberg and Wright, 2019).

1.4 Outline of the thesis

Bose–Einstein condensates (BECs) are the throughline of this thesis. We employ the theoretical three-dimensional description of weakly interacting and ultradilute gases in the continuum within the mean-field regime and explore two main themes.

First, we investigate how interactions that are not isotropic as the usual contact interactions affect the static and dynamic properties of BECs. In particular, we consider long-range dipolar interactions and short-range chiral interactions. Second, we study self-bound states such as droplets and solitons; for the first case, we add a beyond mean-field correction to the mean-field description, and for the second case, we reduce the system to 1D by tightly confining it along the other two directions.

In what follows, we give a brief summary of the remaining chapters of the thesis.

In *Chapter 2*, we present the phenomenon of Bose–Einstein condensation from a quantum statistics perspective, characterize the atom–atom interactions, and introduce in

detail the mean-field description. Within this formalism, the Gross–Pitaevskii equation is a standard treatment to study the static and dynamic properties of weakly interacting and ultradilute systems, and we employ it to analyze the ground state and excitations of BECs. Then, we discuss the stabilizing effect of quantum fluctuations against the mean-field collapse and how to include them as a beyond-mean-field correction. Afterward, we introduce two types of self-bound solutions that one can find in BECs: droplets and solitons. We first introduce bosonic binary mixtures, which can form self-bound droplets, and we then discuss their binding mechanism and main properties. Finally, we move to quasi-1D condensates and discuss the formation of solitonic solutions as a balance between the nonlinearity of the system and the dispersion.

Chapter 3 deals with the dipole–dipole interactions between highly magnetic atoms, though most of the discussion is general to dipolar systems, be it magnetic atoms, electric atoms, or polar molecules. We begin the chapter by reviewing the dipolar interactions and how to include them in the mean-field formalism, and we discuss their effect on the ground state and stability of the system. We also examine how the anisotropy of the interactions combines with the geometry of the confinement, and we explore the elementary excitations and instabilities of dipolar condensates, which present a more complicated picture than in nondipolar condensates. In particular, we introduce the roton instability, which appears in quasi-2D condensates and may be the onset of density modulations in the system. Later, we introduce quantum fluctuations and discuss the formation of self-bound dipolar droplets. In the presence of an external confinement, dipolar droplets can break into several droplets, forming crystals. These crystals may keep the superfluid character of a regular BEC while presenting a periodic structure, a phenomenon known as supersolidity.

Chapter 4 centers on the topic of chiral interactions. We first introduce artificial gauge fields and how one can design them in cold atoms by engineering geometric phases. In particular, we discuss gauge fields that depend on the local density of atoms (density-dependent potentials), which may result in chiral interactions. To explain the origin of these interactions, we focus on the simulation of artificial gauge fields in condensates with light–matter coupling. We first consider the simple case of a two-level atom to explore the main ideas. Then, we move to a two-component condensate where the asymmetry in the interparticle interactions and the coupling to an external space-dependent field results in a system with effective interactions that are chiral. At this point, we are ready to introduce the current-density interaction theory, which describes a quasi-1D system coupled to a density-dependent gauge potential such that the resulting interactions depend on the current density (i.e., they are chiral). We derive with some detail the equations of motion and conserved quantities of the system and finally particularize them to a ring potential described as a 1D system with periodic boundary conditions. We finish with a discussion about the constraints of the geometry and the stationary states supported by the system.

In *Chapter 5*, we investigate Bose–Einstein condensates in bubble trap potentials subject to a small gravity (Arazo et al., 2021b). In particular, we focus on thin shells and study dipolar and nondipolar condensates. We first explore the effects of the anisotropic nature of the dipolar interactions, which are already significant in the absence of gravity

and are enhanced when the polarization axis of the dipoles and the gravity are slightly misaligned. Then, in a setup with a small gravity, we investigate the dynamics of perturbative oscillations of these thin shell-shaped condensates triggered either by an instantaneous tilting of the gravity direction or a sudden change of the gravity strength.

Chapter 6 deals with immiscible binary mixtures of BECs with repulsive contact interactions (Arazo et al., 2021a). We study the dynamics of a dark soliton in 1D and analyze the reflection and transmission of such a soliton when it travels through the domain wall. We show that a dark–bright soliton can be generated dynamically by the interaction of the dark soliton with the domain wall and that this phenomenon occurs outside the regime of parameters of known stationary solutions. The dynamics of this dark–bright soliton are harmonic-like, with a numerical frequency that agrees well with the predictions of a semianalytical model.

In *Chapter 7*, we study the formation of self-bound droplet crystals in binary dipolar mixtures with antiparallel dipoles (Arazo et al., 2023a). In the absence of confinement, antiparallel dipolar mixtures form 3D self-bound droplet-ring structures. If one confines the system along the direction of the dipoles, it can form droplet crystals or stripe patterns depending on whether the intracomponent interactions are asymmetric or symmetric. These crystals are held together by the mutual attraction between the two components, unlike in crystals of scalar dipolar condensates. As in the case of ionic crystals in solid-state physics, the system has a genuine cohesive energy and remains self-bound with no need for an external trapping.

In *Chapter 8*, we study persistent currents in quasi-1D BECs, which become chiral in the presence of current-density interactions (Arazo et al., 2023b). We explore this phenomenon in ultracold atoms loaded in a rotating ring geometry and find analytical current-carrying stationary states that generalize the previously known solutions to the mean-field equations of motion. The dynamical stability of these states is tested through numerical simulations, which allows us to find stable currents for states with both constant and modulated density profiles. Decaying currents, on the other hand, appear only beyond a unidirectional velocity threshold.

In *Chapter 9*, we then generalize the previous study to spinor condensates, which present an effective spin–orbit coupling since the interactions come from the current density and are thus chiral (article in preparation). First, we analyze plane waves and their stability, which reveal a more nuanced picture due to the linear coupling between components. Then, we also consider nonlinear states such as solitons and Josephson vortices. The latter do not appear in scalar condensates and arise due to the current between spin components.

In *Chapter 10*, we present the global conclusions by summarizing the main results of this thesis, and we explore the future perspectives of these lines of research.

2

Self-bound states in Bose–Einstein condensates

A Bose–Einstein condensate (BEC) is a state of matter that can arise when cooling a confined, ultradilute and weakly interacting bosonic gas to very low temperatures, close to the absolute zero. In an ideal Bose gas, all particles collapse into the lowest-energy quantum state and thus Bose–Einstein condensation is a macroscopic quantum phenomenon. Bose–Einstein condensates were first experimentally realized in 1995 (Anderson et al.; Davis et al.) with alkali atoms.

In this chapter, we will introduce Bose–Einstein condensation and the mean-field formalism, and then we will describe the limits of this framework and extend it to include beyond mean-field effects (Section 2.1). The two last sections will focus on particular solutions of homogeneous systems that are self-bound: quantum droplets (Section 2.2), which arise in bosonic mixtures from the interplay between competing mean-field interactions and quantum fluctuations; and solitons (Section 2.3), that are stable solutions of one-dimensional (1D) condensates and originate from the balance between the nonlinearity and dispersion of the system.

2.1 Bose–Einstein condensates in the mean-field regime

The transition from a gas to a BEC, as well as the main features of condensation and the basic assumptions to describe such systems, are discussed in Subsection 2.1.1. Subsection 2.1.2 presents the mean-field framework, which is the theoretical foundation for the work developed in this thesis[1]. Subsection 2.1.3 closes this section by discussing the effect of quantum fluctuations and how one can extend the mean-field formalism to include them. This extension will be useful for the description of quantum droplets (see Section 2.2) and their dipolar counterparts (Chapters 3 and 7).

[1]For more details on the topics covered in Subsections 2.1.1 and 2.1.2, see the books by Foot (2004), Pethick and Smith (2008), Ueda (2010), and Pitaevskii and Stringari (2016); and the reviews by Dalfovo et al. (1999) and Leggett (2001).

2.1.1 Bose–Einstein condensation

The origin of Bose-Einstein condensation lies in the wave nature and the indistinguishability of identical bosons, as we will see first. Later, we will introduce the concepts of condensate fraction and depletion, and discuss the metastable nature of BECs and the effect of dimensionality on condensation. Finally, we will consider three- and two-body interactions, of which the later ones dominate, and introduce the contact pseudopotential that effectively describes the atom–atom interactions.

Spin–statistics connection for identical particles

Quantum particles that are identical (i.e., that have the same mass, charge and intrinsic spin) cannot be distinguished upon measurement of their properties if their wavepackets overlap. In classical mechanics, one can tell identical particles apart by the trajectories they describe through phase space. Yet in quantum mechanics such concept of *trajectory* does not exist, given the intrinsic uncertainty in position and momentum, so identical particles become indistinguishable under certain circumstances.

The relation between the spin of a particle and the statistics it obeys was first formulated by Fierz (1939) and Pauli (1940), and later Schwinger (1951) developed it further. This spin–statistics connection states the following: identical particles with integer (in multiples of $\hbar$) or zero spin are called *bosons* and abide by Bose–Einstein statistics; on the other hand, particles with a half-integer spin are known as *fermions* and follow Fermi–Dirac statistics. As a result of indistinguishability, the probability associated to a system of identical particles must remain the same under the interchange of any two particles, and the two different statistics restrict the corresponding wavefunction to be either symmetric for bosons or antisymmetric for fermions.

Consider for instance a system of two particles, which can be described by the wavefunction $\psi(\mathbf{r}_1, \mathbf{r}_2)$, where $\mathbf{r}_i$ is the position of each particle, and we are assuming there is no hyperfine degree of freedom for simplicity. The interchange of particles 1 and 2, in general, swaps the labels of the two particles and adds a global phase to the wavefunction, $e^{i\alpha}\psi(\mathbf{r}_2, \mathbf{r}_1)$. After a second exchange, since the particles are indistinguishable, one should recover the original wavefunction, $\psi(\mathbf{r}_1, \mathbf{r}_2) = e^{i2\alpha}\psi(\mathbf{r}_1, \mathbf{r}_2)$, from where α is either 0 or π, rendering the wavefunction symmetric in the first case (bosons) or antisymmetric in the second one (fermions)[2].To understand better the effect of these symmetry constraints, we define the wavefunction that describes two identical particles as

$$\psi(\mathbf{r}_1, \mathbf{r}_2) = \frac{1}{\sqrt{2}}\left[\phi(\mathbf{r}_1, \mathbf{r}_2) \pm \phi(\mathbf{r}_2, \mathbf{r}_1)\right], \tag{2.1}$$

where $\phi(\mathbf{r}_1, \mathbf{r}_2)$ solves the Schrödinger equation for two particles labeled 1 and 2, with $\mathbf{r}_i$ the spatial coordinates of particle i. We have frozen the spin degree of freedom, but the argument holds if also considering a spin coordinate σ_i. The wavefunction

[2]In two-dimensional systems, however, one can have quasi-particles for which α is neither 0 nor π and, consequently, behave very differently from bosons or fermions and follow intermediate fractional statistics. Such quasi-particles are known as *anyons* (Wilczek, 1982).

$\psi(\mathbf{r}_1, \mathbf{r}_2)$ is then symmetrized (+) for bosons and antisymmetrized (−) for fermions, and the probability of finding two identical particles at the same point $\mathbf{r}_1 = \mathbf{r}_2 = \mathbf{r}$ is $|\psi(\mathbf{r}, \mathbf{r})|^2 = 2|\phi(\mathbf{r}, \mathbf{r})|^2$ for bosons and $|\psi(\mathbf{r}, \mathbf{r})|^2 = 0$ for fermions. From these results one can extract two key concepts: that fermions cannot occupy the same quantum state, as the Pauli exclusion principle tells us; while bosons do not have such occupation restrictions and instead tend to cluster with a probability that is twice that of the distinguishable case. Bose–Einstein condensation therefore can only arise in gases of identical bosons.

The clustering of bosons magnifies as the number of bosons increases: the symmetrized wavefunction for N bosons can be written as

$$\psi(\mathbf{r}_1, \mathbf{r}_2, \ldots, \mathbf{r}_N) = \frac{1}{\sqrt{N!}} \sum_{(i_1, \ldots, i_N)} \phi(\mathbf{r}_{i_1}, \mathbf{r}_{i_2}, \ldots, \mathbf{r}_{i_N}) \,, \tag{2.2}$$

such that the probability of finding all N bosons at the same point is $|\psi(\mathbf{r}, \mathbf{r}, ..., \mathbf{r})|^2 = N!|\phi(\mathbf{r}, \mathbf{r}, ..., \mathbf{r})|^2$. This effect, however, only occurs when the particles are indistinguishable so their wavepackets overlap.

Quantum effects at low temperatures

The size of the wave packets that describe the particles is given by the thermal de Broglie wavelength associated to the gas at a given finite temperature T,

$$\lambda_{\mathrm{dB}} = \frac{h}{p} = \frac{h}{\sqrt{2\pi\, m\, k_B T}} \,, \tag{2.3}$$

where h and k_B are Planck and Boltzmann constants, m is the mass of a boson and p its momentum; λ_{dB} grows with decreasing temperature and gives an idea of how delocalized the particles of a gas are.

At high, ordinary temperatures, the average interatomic distance $d = n^{-1/3}$, where n is the average density of the gas, is much larger than the de Broglie wavelength, $\lambda_{\mathrm{dB}} \ll d$. Thus, the particles of the gas scatter throughout the container that holds them and behave as billiard balls, following Boltzmann statistics. In this regime, quantum effects are negligible, and the gas can be described classically.

As the temperature lowers, the de Broglie wavelength increases and one has to describe particles using quantum mechanics. At a critical temperature T_c, the de Broglie wavelength becomes of the order of the distance between particles, $\lambda_{\mathrm{dB}} \sim d$, such that the wave packets start to overlap and quantum effects become noticeable. This point is the onset of Bose–Einstein condensation: the particles coalesce into a single wave packet and become indistinguishable. Since the probability $|\psi|^2$ grows with an $N!$ factor due to the bosons' tendency to cluster, below T_c a large number of particles start to condense into a single-particle state such that condensation becomes macroscopic when N is very large. Eventually, in a noninteracting system at $T = 0$, all the bosons constitute a coherent cloud of atoms that occupy all the same lowest-energy state, forming a pure BEC (ideal gas) that behaves as a giant matter wave.

The critical temperature T_c for Bose–Einstein condensation does not depend on the atomic interactions, which illustrates that condensation stems purely from quantum statistics[3]. It does depend though on the confining geometry and the dimensionality.

Condensate fraction, quantum depletion and dimensionality

The *condensate fraction* characterizes the fraction of atoms that occupy the lowest energy state, and decreases with increasing temperature. For a noninteracting gas of N atoms, the condensate fraction is

$$\frac{N_0}{N} = 1 - \left(\frac{T}{T_c}\right)^{\alpha}, \tag{2.4}$$

where $N_0 = N - N_T$ is the number of atoms in the condensate and N_T is the number of atoms in excited states. In three dimensions, the parameter α is $3/2$ for a box potential and 3 for a harmonic oscillator, so the dependence on the critical temperature is stronger in a harmonically confined gas.

The atomic interactions can promote particles from the condensate to excited states, an effect known as *quantum depletion*. This depletion of the condensate[4] due to interactions is typically 1% or less for most experiments in weakly interacting gases. Therefore, quantum depletion is usually neglected and, close to zero temperature, one can consider all the atoms to have the same single-particle wavefunction.

Condensation is always possible at $T = 0$ and in three-dimensions (3D), but a reduced dimensionality and the geometry of the confinement will determine whether condensation at a given temperature $T < T_c$ is possible or not, as thermal fluctuations may destabilize the condensed phase (Giorgini et al., 1997). In the thermodynamic limit, Bose–Einstein condensation only occurs at a finite temperature T for a uniform gas in 3D, while trapped gases can have condensation in either 2D or 3D (Lewenstein et al., 2012). However, in those cases where condensation does not occur at $T \neq 0$, for a finite N one can still have a large condensate fraction for low enough temperatures that are available experimentally. In these reduced dimensionalities, further increasing the temperature can give rise to quasi-condensate phases, which do not possess off-diagonal long-range order[5], one of the main characteristics of BECs.

To reduce the dimensionality of the system, one should remove the condition that the temperature of the gas is much larger than the zero-point energy[6] in one or two

[3]The origin of Bose–Einstein condensation is statistical, but repulsive interactions can further enhance condensation in weakly interacting gases.

[4]The quantum depletion is defined as $\sim (n a_s^3)^{1/2}$, where n is the average density of the gas and a_s is the scattering length that characterizes the two-body interactions (which will be discussed further later on).

[5]An important feature of BECs is that they exhibit *off-diagonal long-range order* (Yang, 1962), which can be understood from the indistinguishability of the particles. The one-body density matrix is defined as $\rho_1(\mathbf{r}, \mathbf{r}') = \langle \hat{\psi}^\dagger(\mathbf{r})\hat{\psi}(\mathbf{r}')\rangle$, with $\hat{\psi}^\dagger(\mathbf{r})$ and $\hat{\psi}(\mathbf{r})$ the particle creation and annihilation operators. Usually, ρ_1 decreases with the distance and eventually vanishes. In the presence of Bose–Einstein condensation, however, ρ_1 approaches a finite value instead, since particles at positions $\mathbf{r}$ and $\mathbf{r}'$ are no longer distinguishable due to their wave packets overlapping. When this happens, one says that the system keeps spatial coherence over long distances.

[6]The zero-point energy is the energy of the lowest mode in the system (i.e., the ground state energy), a residual energy that arises from the Heisenberg uncertainty principle. In a harmonic-oscillator potential

dimensions (see Section 2.3 for the 1D case).

Metastability and three-body losses

The Bose–Einstein condensed phase is actually metastable: at the usual pressure conditions and low temperatures of BECs, the equilibrium configuration corresponds to a solid phase, in which case the effects of the interactions increase significantly. For a gas to crystallize, two atoms need to form a molecule, and the most probable way for this to happen is by a third atom participating in the process to eliminate the binding energy of the molecule. Therefore, the dominant recombination processes that may bring the system to the crystal phase at very low temperatures are three-body events, which are crucial to the destabilization of BECs and are also their main loss mechanism of atoms (Burt et al., 1997; Kagan et al., 1985).

The rate loss for three-body processes is given by $dn/dt = -Ln^3$, where L is the rate coefficient and n is the average density (Pethick and Smith, 2008). The dependence with n^3 indicates that it is a three-body event, since the probability of three atoms being close goes with the third power of n. For this reason, BECs have to be very dilute to suppress three-body recombination and ensure a lifetime large enough for experiments. However, BECs can still be in kinetic equilibrium with respect to two-body processes.

Atom–atom interactions

At the usual temperatures and densities of dilute BECs, three-body interactions are rare processes, so the dominant atom–atom interactions are two-body collisions. In such events, the most important parameters are the relative position of the atoms involved and the initial relative kinetic energy. In addition, the separation between particles is larger than the length scale associated with the atomic interactions by around an order of magnitude.

The interatomic potential for alkali-like atoms has two clear regimes: a strong electrostatic repulsion between the atoms at short distances due to the overlapping of the two electronic clouds, and an attraction caused by the van der Waals interaction at large distances. The van der Waals interaction originates from the electric dipole–dipole interaction between atoms, and goes with the interatomic distance r as $-1/r^6$ with a coefficient that is very large for alkali atoms. The key parameter for characterizing the interactions then will be the distance between the atoms.

Therefore, we can model the potential as a hard-sphere potential for small distances with a van der Waals tail for long distances, where r_c is the radius of the hard core and determines the range of the potential:

$$U(r) = \begin{cases} \infty & r \leq r_c \\ -\frac{\alpha}{r^6} & r > r_c \end{cases} . \tag{2.5}$$

For a weakly interacting and dilute system, the low-energy scattering processes will be the most relevant ones. Therefore, interactions between atoms will only occur when

of frequency ω_{ho}, the zero-point energy is $\hbar\omega_{\text{ho}}/2$.

the two atoms are close together and the energy of the scattering event is very low. Due to this, the interatomic potential is effectively short-range, which justifies that one can approximate the atom–atom interaction between two atoms at positions $\mathbf{r}$ and $\mathbf{r}'$ by a contact pseudopotential with the following form:

$$V(\mathbf{r}-\mathbf{r}') = \frac{4\pi\hbar^2}{m}\, a_s\, \delta(\mathbf{r}-\mathbf{r}')\,, \tag{2.6}$$

with δ the Dirac delta function and a_s the s-wave scattering length[7], which is the leading contribution to the low-energy scattering between two atoms. It is useful to introduce here the *coupling constant*

$$g = \frac{4\pi\hbar^2 a_s}{m}, \tag{2.7}$$

which characterizes the strength of the interactions and their character: repulsive for $g > 0$ and attractive for $g < 0$. The condensate will then present a different behavior depending on the sign of the scattering length.

This pseudopotential (2.6) described solely by the s-wave scattering length will be enough to describe the mean-field interactions of BECs. From now on we will refer to these interactions as simply *contact interactions* (see Subsection 2.1.2 for the full formalism).

Feshbach resonances

The sign and magnitude of the effective contact interactions can be controlled in experimental settings by means of optically or magnetically tuned Feshbach resonances (Chin et al., 2010). These resonances occur when the energy of a scattering process between two atoms comes close to the energy of a bound state of the interatomic potential; this resonant coupling may be adjusted through an external magnetic field that modifies the energy of the bound state.

The following expression describes the behavior of the scattering length with the magnetic field B (Moerdijk et al., 1995):

$$a_s(B) = a_{\mathrm{bg}}\left(1 - \frac{\Delta}{B - B_0}\right), \tag{2.8}$$

with a_{bg} the background scattering length (i.e., the value far from resonance), Δ the width of the resonance and B_0 the resonance position where a_s diverges (Chin et al., 2010).

Figure 2.1 shows the behavior of the scattering length with the magnetic field. At some values of the external magnetic field B, the scattering length diverges, which is where the Feshbach resonances occur; on either side of the divergence the scattering length changes sign and, at some point, crosses zero. Through Feshbach resonances it is then possible to tune the scattering length to very small values or even zero, which will be particularly useful for condensates of magnetic atoms to enhance the effect of the dipole–dipole interactions (see Chapter 3).

[7] In the typical BECs, the scattering lengths are usually two orders of magnitude larger than a_0, the Bohr radius, which sets the scale of the atomic size.

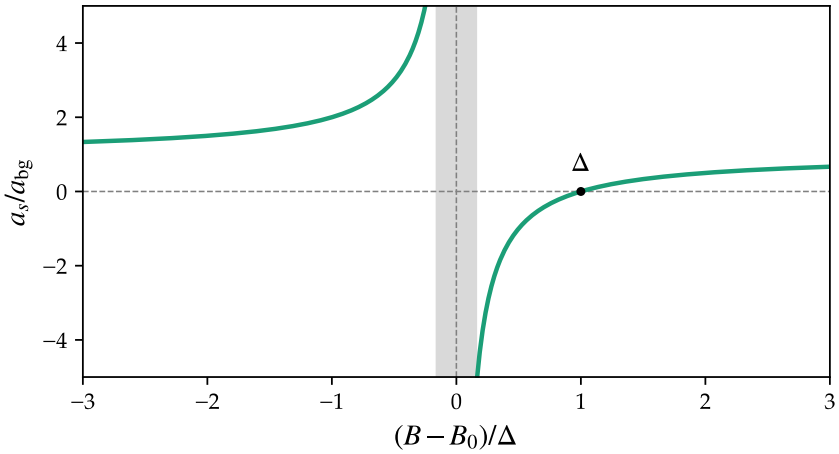

Figure 2.1: Scattering length a_s in a magnetically tuned Feshbach resonance (2.8) as a function of the magnetic field B. The scattering length a_s diverges in the vicinity of the resonance, B_0 (shaded area) and changes sign at either side of the resonance. The parameter Δ is the width of the resonance, and corresponds to the value of $B - B_0$ for which the scattering length becomes zero. The value of the scattering length far from resonance is a_{bg}.

2.1.2 Mean-field formalism

In this subsection we present a mean-field description of BECs and overview their main static and dynamic features. We will first derive the Gross–Pitaevskii equation (GPE), treating the interactions within a mean-field framework in a way that is analogous to the Hartree–Fock method employed in fermionic systems. After that, we will discuss the relevant length scales of trapped and untrapped systems and present a dimensionless version of the GPE in terms of such length scales. Finally, we will sketch the main static properties of weakly interacting and very dilute BECs and comment on elementary excitations to set the foundations for more complicated systems.

This mean-field treatment of BECs captures very well their main static and dynamic properties, but it fails to describe, for instance, the correlations between particles. However, this approach will be enough for the topics covered in this thesis, with some corrections that will be discussed in Subsection 2.1.3, Section 2.2 and, later on, in Chapters 3 and 4.

Gross–Pitaevskii equation

The N-body Hamiltonian for a gas of N identical trapped bosons at $T = 0$ is[8]

$$H = \sum_{i=1}^{N} \left[-\frac{\hbar^2 \nabla_i^2}{2m} + V_{\mathrm{ext}}(\mathbf{r}_i) \right] + \frac{1}{2} \sum_{i=1}^{N} \sum_{j \neq i} V(\mathbf{r}_i - \mathbf{r}_j) \,, \tag{2.9}$$

[8]This is the general Hamiltonian for identical particles, and thus it is valid both for fermions and bosons. Here we will focus on bosons from now on.

where $\hbar$ is the reduced Planck constant and m is the mass of an atom. The bosons are trapped in a generic external potential $V_{\text{ext}}(\mathbf{r})$, and $V(\mathbf{r}_i - \mathbf{r}_j)$ is the interatomic potential[9], which accounts for the two-body interactions. Since the particles are indistinguishable, the Hamiltonian that describes the system is invariant under the interchange of spatial coordinates between two particles.

Finding the exact ground state of this Hamiltonian (2.9) is, in general, a complex problem; instead, we will find an approximate solution by considering a trial wavefunction $\Psi(\mathbf{r}_1, \mathbf{r}_2, \ldots, \mathbf{r}_N)$ for the ground state and minimizing the energy

$$E[\Psi] = \frac{\langle \Psi | H | \Psi \rangle}{\langle \Psi | \Psi \rangle} \,. \tag{2.10}$$

In a noninteracting gas, all the bosons occupy the ground state of the external potential; thus, including interactions will modify the ground state of the system. Although the atom–atom interactions are usually difficult to characterize, we are dealing with dilute gases where the interactions are weak, so we can apply a Hartree approach[10] and assume that all the bosons are in the same single-particle state: the condensate. Therefore, we write the total wavefunction as a symmetrized product of single-particle wavefunctions,

$$\Psi(\mathbf{r}_1, \mathbf{r}_2, \ldots, \mathbf{r}_N) = \prod_{i=1}^{N} \phi(\mathbf{r}_i) \,, \tag{2.11}$$

with $\langle \phi | \phi \rangle = \int |\phi(\mathbf{r})|^2 \, d\mathbf{r} = 1$ such that $\Psi(\mathbf{r}_1, \ldots, \mathbf{r}_N)$ is also normalized to 1.

Using this state Ψ (2.11) and the many-body Hamiltonian H (2.9), the energy functional defined in Eq. (2.10) then reads

$$\begin{aligned} E[\phi, \phi^*] \;=\; & N \int d\mathbf{r}\, \phi^*(\mathbf{r}) \left(-\frac{\hbar^2 \nabla^2}{2m} + V_{\text{ext}}(\mathbf{r}) \right) \phi(\mathbf{r}) \\ & + \frac{N(N-1)}{2} \int \int d\mathbf{r}\, d\mathbf{r}'\, \phi^*(\mathbf{r}) \phi^*(\mathbf{r}') V(\mathbf{r} - \mathbf{r}')\, \phi(\mathbf{r}) \phi(\mathbf{r}') \,, \end{aligned} \tag{2.12}$$

where the first two terms are the kinetic and external potential contributions to the energy, and the last one corresponds to the atom–atom interactions.

Now, to minimize the energy (2.12) with the constraint of normalization $\langle \Psi | \Psi \rangle = 1$, we introduce a Lagrange multiplier λ and set the variations with respect to ϕ and ϕ^* to zero,

$$\frac{\delta}{\delta \phi^*} \left[E[\phi, \phi^*] - \lambda \langle \Psi | \Psi \rangle \right] = 0 \,. \tag{2.13}$$

Introducing Eq. (2.12) into Eq. (2.13) gives

$$N \int d\mathbf{r}\, \delta\phi^*(\mathbf{r}) \left\{ \left[-\frac{\hbar^2 \nabla^2}{2m} + V_{\text{ext}}(\mathbf{r}) + (N-1) \int d\mathbf{r}'\, V(\mathbf{r} - \mathbf{r}') \, |\phi(\mathbf{r}')|^2 \right] \phi(\mathbf{r}) - \lambda \phi(\mathbf{r}) \right\} = 0 \,, \tag{2.14}$$

[9] The 1/2 factor that goes with the potential is included to avoid double counting.

[10] In such a mean-field approximation one assumes that each particle moves independently in an effective potential that encompasses the average effect of the interactions between this particle and the other $N - 1$ particles.

and, since $\delta\phi^*$ is arbitrary, yields

$$\left[-\frac{\hbar^2\nabla^2}{2m} + V_{\text{ext}}(\mathbf{r}) + (N-1)\int d\mathbf{r}'\, V(\mathbf{r}-\mathbf{r}')\,|\phi(\mathbf{r}')|^2\right]\phi(\mathbf{r}) = \lambda\phi(\mathbf{r})\,, \tag{2.15}$$

which is a nonlinear Schrödinger-like equation. The Lagrange multiplier λ corresponds to the *chemical potential*[11], i.e., the energy necessary for adding a particle to the system, and is usually denoted by μ.

Assuming that $N \gg 1$ such that $N - 1 \simeq N$, and introducing the condensate wavefunction $\psi(\mathbf{r}) = \sqrt{N}\phi(\mathbf{r})$, which is normalized to N, then Eq. (2.15) becomes the well-known time-independent version of the Gross–Pitaevskii equation (GPE),

$$\left[-\frac{\hbar^2\nabla^2}{2m} + V_{\text{ext}}(\mathbf{r}) + \int d\mathbf{r}'\, V(\mathbf{r}-\mathbf{r}')\,|\psi(\mathbf{r}')|^2\right]\psi(\mathbf{r}) = \mu\psi(\mathbf{r})\,. \tag{2.16}$$

Finally, replacing the interatomic potential $V(\mathbf{r}-\mathbf{r}')$ with an effective contact pseudopotential (2.6), one gets

$$\left[-\frac{\hbar^2\nabla^2}{2m} + V_{\text{ext}}(\mathbf{r}) + g|\psi(\mathbf{r})|^2\right]\psi(\mathbf{r}) = \mu\psi(\mathbf{r})\,, \tag{2.17}$$

where g is the coupling constant that characterizes contact interactions (2.7) and the number density of the gas is given by the density of the condensate[12],

$$n(\mathbf{r}) = |\psi(\mathbf{r})|^2\,. \tag{2.18}$$

Equation (2.17) is the time-independent GPE. The energy of the system, assuming $N \gg 1$ and introducing the contact pseudopotential (2.6) into the energy functional (2.12), is then given by

$$E[\psi] = \int d\mathbf{r}\left[\frac{\hbar^2}{2m}|\nabla\psi(\mathbf{r})|^2 + V_{\text{ext}}(\mathbf{r})|\psi(\mathbf{r})|^2 + \frac{1}{2}g|\psi(\mathbf{r})|^4\right]\,. \tag{2.19}$$

The evolution of the condensate is governed by the time-dependent GPE,

$$i\hbar\frac{\partial\psi(\mathbf{r},t)}{\partial t} = \left[-\frac{\hbar^2\nabla^2}{2m} + V_{\text{ext}}(\mathbf{r}) + g|\psi(\mathbf{r},t)|^2\right]\psi(\mathbf{r},t)\,, \tag{2.20}$$

which is the Gross–Pitaevskii equation in its most ubiquitous form. The time-independent version of the GPE (2.17) can be obtained by introducing the ansatz

$$\psi(\mathbf{r},t) = \psi(\mathbf{r})\,e^{-i\,\mu t/\hbar} \tag{2.21}$$

[11] Assuming that $\phi(\mathbf{r})$ does not vary when removing an atom and that $N \gg 1$, then one can calculate the energy (2.12) of the system with $N-1$ atoms, E_{N-1}, and compare it to the energy of the full system E_N, which gives $E_N - E_{N-1} = \lambda$. This is actually the chemical potential $\mu = \partial E/\partial N$, which corresponds to the energy required to add a particle to the system while keeping the total number constant.

[12] This is valid because we are neglecting the condensate depletion due to quantum and thermal fluctuations, an assumption that we will discuss later (see Subsection 2.1.3).

into Eq. (2.20).

Here we have derived the GPE (2.17) following a Hartree–Fock-like approach. However, one can address the many-body problem using the second quantization formalism as well (see, for instance, Pitaevskii and Stringari, 2016), and Chapter 4 presents an alternative derivation of the GPE from the quantum action using variational equations.

Relevant length scales

So far, we have seen that, at zero temperature, the s-wave scattering length and the interparticle distance provide suitable scales to characterize the interactions and the density of the gas[13] (Leggett, 2001). The interactions and the confinement (for harmonically trapped gases) also bring in two other length scales relevant to the description of the system: the healing length and the oscillator length.

For a system trapped in an anisotropic three-dimensional harmonic-oscillator potential (Pethick and Smith, 2008),

$$V_{\mathrm{ho}}(\mathbf{r}) = \frac{1}{2}m\left(\omega_x^2 x^2 + \omega_y^2 y^2 + \omega_z^2 z^2\right) , \tag{2.22}$$

the lengths associated to each frequency ω_i are $a_{\mathrm{ho},i} = \sqrt{\hbar/(m\omega_i)}$. One can then define the characteristic *oscillator length* for the geometric mean of the frequencies, $\omega_{\mathrm{ho}} = (\omega_x\omega_y\omega_z)^{1/3}$, as

$$a_{\mathrm{ho}} = \sqrt{\frac{\hbar}{m\omega_{\mathrm{ho}}}} . \tag{2.23}$$

The oscillator length can be understood as a measure of the width that the ground state of a single particle would have in this trap, as given by the Schrödinger equation. Therefore, it gives an idea of the length scale of the system due to the harmonic confinement.

The interacting nature of the system, on the other hand, can be characterized by the so-called *healing length*. In a homogeneous system of constant density n, the healing length ξ can be calculated as the distance for which the two energy contributions in Eq. (2.19) balance: the kinetic energy, defined as $\hbar^2/(2m\xi^2)$, and the interaction energy, which is gn. Thus, the healing length,

$$\xi = \frac{\hbar}{\sqrt{2m|g|n}} , \tag{2.24}$$

is the minimum distance over which the density can change from 0 to n (its bulk value) without the kinetic energy term (i.e., the quantum pressure) diverging (Bongs and Sengstock, 2004). It describes then the distance over which the condensate adjusts or heals to restore equilibrium when subjected to perturbations or due to local collisions. Since ξ grows with $|g|^{-1/2}$, systems with stronger interactions will have a shorter healing length. If the healing length is of the order of the size of the system, though, the boundary conditions affect the whole system (Pitaevskii and Stringari, 2016). For

[13] The thermal de Broglie wavelength (2.3) at the critical temperature is also a relevant length scale.

trapped systems, the healing length is evaluated at either the central density of the condensate n_0 or at the average density instead (Dalfovo et al., 1999). The healing length is useful when studying soliton solutions (see Section 2.3) and superfluidity; in this last case, for example, it provides the typical size of the core of quantized vortices that form in the condensate under rotation (Gross, 1961; Pitaevskii, 1961).

One can use any of these length scales to rewrite the time-dependent Gross–Pitaevskii equation (2.20) in dimensionless units. Introducing the unit length l (either a_{ho}, a_s or ξ), the unit energy is defined as $\epsilon = \hbar^2/(ml^2)$, and the unit time as $\tau = \hbar/\epsilon = ml^2/\hbar$. Denoting the dimensionless variables by a tilde (e.g., $x = \tilde{x}\, l$), the time-dependent GPE can be written as

$$i\partial_{\tilde{t}}\tilde{\psi} = \left(-\frac{1}{2}\nabla_{\tilde{r}}^2 + \tilde{V}_{\text{ext}} + 4\pi\tilde{a}_s|\tilde{\psi}|^2\right)\tilde{\psi}\,. \tag{2.25}$$

For example, in the case of an isotropic harmonic oscillator, $\omega_x = \omega_y = \omega_z = \omega_{\text{ho}}$, the unit length is $l = a_{\text{ho}}$ and the dimensionless potential is $\tilde{V}_{\text{ext}} = \tilde{r}^2/2$:

$$i\partial_{\tilde{t}}\tilde{\phi} = \left(-\frac{1}{2}\nabla_{\tilde{r}}^2 + \frac{1}{2}\tilde{r}^2 + 4\pi N\frac{a_s}{a_{\text{ho}}}|\tilde{\phi}|^2\right)\tilde{\phi}\,, \tag{2.26}$$

where we have redefined the wavefunction as $\tilde{\psi} = \sqrt{N}\tilde{\phi}$ such that $\tilde{\phi}$ is normalized to 1.

Ground state

The shape of a condensate of noninteracting bosons trapped in a harmonic-oscillator potential (2.22) is a Gaussian function of width a_{ho} (2.23), and its peak density (i.e., the density at the center of the trap) will be proportional to the total number of atoms N, as described by the appropriately normalized Schrödinger equation.

The atom–atom interactions will modify the ground state of the noninteracting case according to the sign of the effective interactions and their strength, which can be characterized by the dimensionless parameter from Eq. (2.26), $N|a_s|/a_{\text{ho}}$ (Pethick and Smith, 2008; Pitaevskii and Stringari, 2016). The effect of the interactions on the ground state of the system can be seen very clearly if one considers the ground state energy of a uniform (untrapped) gas of constant density n, which from Eq. (2.19) reads

$$\frac{E_0}{N} = \frac{gn}{2}\,. \tag{2.27}$$

For repulsive interactions, the energy (2.27) is minimized by decreasing the density, so the gas expands, while for attractive interactions the system collapses. In the general (trapped) case, this translates into the two following behaviors.

1. Repulsion between the atoms ($g > 0$) causes the gas to expand[14] and reduce its peak density. If the interaction is very large, $N|a_s|/a_{\text{ho}} \gg 1$, one can neglect the kinetic term in the GPE (2.20). In this situation, know as the *Thomas–Fermi limit*, the size of the cloud increases enough that the density profile becomes very smooth.

[14] Without harmonic confinement, the gas expands uniformly, so in general we will need an external trapping to avoid the free expansion.

2. On the other hand, if the interaction is attractive ($g < 0$), the condensate has to increase its central density to reduce the interaction energy. For small interactions, the zero-point kinetic energy compensates this effect and stabilizes the system in a confined system. However, if the interaction is too strong then the kinetic energy is not enough to overcome the attraction between atoms and the gas collapses. The critical number of atoms above which the condensate is unstable is of the order of $a_{\text{ho}}/|a_s|$.

It is worth noting here that the collapse described in the attractive case occurs for 3D and 2D systems. In 1D, however, the condensate does not collapse but instead decays into a bright soliton, which is the ground state of the system in this case (see Section 2.3).

Elementary excitations

Up to now we have discussed the ground state of the system within the mean-field regime. To study its dynamical behavior under linear excitations, we introduce the ansatz (Dalfovo et al., 1999; Pethick and Smith, 2008; Pitaevskii and Stringari, 2016)

$$\psi(\mathbf{r},t) = e^{-i\mu t/\hbar}\left\{\phi_0(\mathbf{r}) + \sum_j \left[u_j(\mathbf{r})e^{-i\omega_j t} + v_j^*(\mathbf{r})e^{+i\omega_j t}\right]\right\}, \tag{2.28}$$

which defines the perturbed state as the ground state $\phi_0(\mathbf{r})$ plus a collection of excitation modes (i.e., the perturbation). These modes, labeled j, are plane waves with frequency ω_j and complex amplitudes u_j and v_j. We then introduce $\psi(\mathbf{r},t)$ into the time-dependent GPE (2.20) and linearize, since we want to study small oscillations[15]. Equating terms with the same exponent and identifying the time-independent GPE (2.17) for $\phi_0(\mathbf{r})$, we obtain the Bogoliubov equations (Bogoliubov, 1947). These equations can be written in matrix form as

$$\begin{pmatrix} (\hat{H}_0 - \mu) + 2g\,|\phi_0|^2 & g\,\phi_0^2 \\ g\,(\phi_0^*)^2 & -\left[(\hat{H}_0 - \mu) + 2g\,|\phi_0|^2\right] \end{pmatrix} \begin{pmatrix} u(\mathbf{r}) \\ v(\mathbf{r}) \end{pmatrix} = \hbar\omega \begin{pmatrix} u(\mathbf{r}) \\ v(\mathbf{r}) \end{pmatrix}, \tag{2.29}$$

where we have defined the single-particle energy operator $\hat{H}_0 = -\hbar^2\nabla^2/(2m) + V_{\text{ext}}(\mathbf{r})$ and dropped the index j for simplicity.

For a uniform gas ($V_{\text{ext}} = 0$), the density of the condensate (2.18) is constant, $n(\mathbf{r}) = n_0$, and the chemical potential is simply $\mu = gn_0$. In this case, the translational symmetry of the system allows us to choose plane-wave solutions for the excitation modes with wavevector $\mathbf{k}$,

$$u(\mathbf{r}) = u\,e^{i\,\mathbf{k}\cdot\mathbf{r}} \quad \text{and} \quad v(\mathbf{r}) = v\,e^{i\,\mathbf{k}\cdot\mathbf{r}}. \tag{2.30}$$

The Bogoliubov equations (2.29) then lead to the dispersion relation

$$(\hbar\omega)^2 = \frac{\hbar^2k^2}{2m}\left(\frac{\hbar^2k^2}{2m} + 2gn_0\right), \tag{2.31}$$

[15] Only the terms up to first order in the perturbation amplitudes u_j and v_j will be relevant, so higher orders can be neglected.

that gives the spectrum of the excitations. These frequencies have to be real to be solutions of the Bogoliubov equations; complex frequencies will indicate a dynamical instability. For real frequencies, the perturbation to the ground state for a given mode is $ue^{-i\omega t} + ve^{+i\omega t}$, which are sinusoidal oscillations with small amplitudes u and v. If the frequency ω is complex, however, the $e^{-i\omega t}$ term will decay with time, but $e^{+i\omega t}$ will instead give oscillations that grow exponentially and eventually destabilize the system.

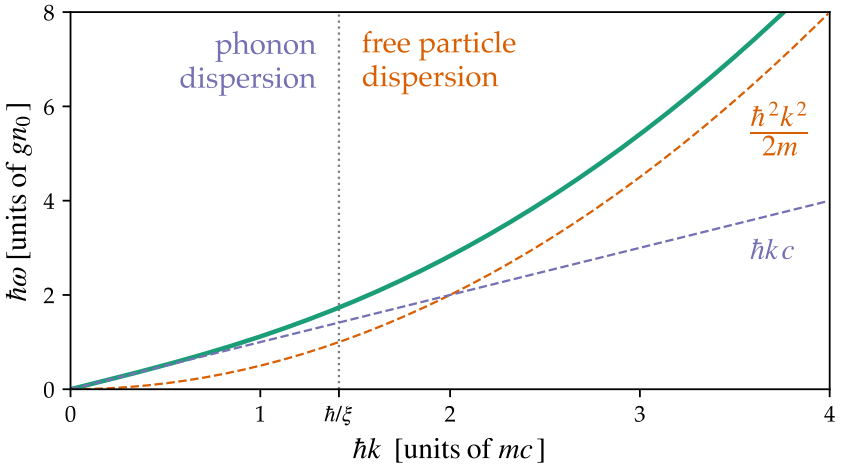

Figure 2.2: Excitation spectrum of a uniform gas (2.31). The energy of the excitations $\hbar\omega$ is given in units of the interaction energy gn_0, and the momentum $\hbar k$ in units of mc, where c is the speed of sound. Excitations behave as free particles for large momenta, with energy $\hbar^2k^2/(2m)$, and as phonons at low momenta, with energy $\hbar kc$. The transition between these two regimes is determined by $k = 1/\xi$ (dotted line), where ξ is the healing length (2.24). The solid line corresponds to the excitation energy given by Eq. (2.31) and the dashed lines are the phonon and free-particle limits.

The excitation spectrum (see Fig. 2.2) shows two clear behaviors: for large momenta, it shows the dispersion of a free particle, with energy $\hbar^2k^2/(2m)$, while for low momenta ($k \to 0$), it tends to the phonon dispersion with frequency $\omega = ck$ and $c = \sqrt{gn_0/m}$ the speed of sound. Note that c acquires an imaginary part if $g < 0$, when the system is predicted to collapse.

The transition between the linear (phonon) and quadratic (free particle) behaviors occurs when the kinetic energy $\hbar^2k^2/(2m)$ and the interaction energy gn_0 become similar. This corresponds to a wavenumber that is the inverse of the healing length (2.24), which in terms of the speed of sound can be written as $\xi = \hbar/(\sqrt{2}mc)$. This indicates that for length scales above the healing length ξ the particles show a collective behavior, while at length scales below ξ they behave as free particles (Pitaevskii and Stringari, 2016).

2.1.3 The role of quantum fluctuations

The Gross–Pitaevskii equation (2.20) is only valid within the mean-field regime and under the assumption that $N \gg 1$ such that a small variation in the number of atoms is irrelevant and $N - 1 \simeq N$. Furthermore, the mean-field regime requires two main

conditions that are also implicit in the derivation of the equation. First, the gas must be dilute and weakly interacting, i.e., $n|a_s|^3 \ll 1$ with n the average density, such that quantum fluctuations are negligible. This is known as the *diluteness condition*. Secondly, it has to be cooled to very low temperatures, $T \ll T_c$ (i.e., few tens of nK), so thermal fluctuations become negligible too. Both conditions are essential for the mean-field approximation and the Hartree approach employed to remain applicable.

When these two conditions hold, the quantum depletion of the condensate is negligible and the condensate fraction is $N_0/N \approx 1$. In this case, we can assume that mostly all atoms occupy the lowest-energy state (i.e., the condensate) and describe them with a single macroscopic wavefunction.

In what follows we will still assume that the gas is very close to $T = 0$, but we will consider stronger interactions (or higher densities) so that quantum fluctuations become relevant.

Beyond mean-field correction

When the diluteness and weakly interacting condition ($n|a_s|^3 \ll 1$) does not hold any more, quantum fluctuations contribute to the system significantly. Mostly all the atoms of the system are still on the condensate, but a small fraction will populate the excited states due to quantum fluctuations, which increases the energy of the system. In this situation, one can consider the first correction to the mean-field approximation, which leads to a shift to the ground state energy of the system that accounts for the quantum fluctuations of the collective modes in the BEC (i.e., the zero-point energy of the Bogoliubov excitations). This correction term was first calculated in 1957 by Lee, Huang, and Yang (Lee and Yang, 1957; Lee et al., 1957), and it is hence known as the Lee–Huang–Yang (LHY) correction.

For the uniform gas, the corrected energy per particle of the ground state reads

$$\frac{E_0}{N} = \frac{gn}{2}\left[1 + \frac{128}{15\sqrt{\pi}}\left(na_s^3\right)^{1/2}\right]. \tag{2.32}$$

The first term in the energy per particle (2.32) corresponds to the mean-field energy (2.27) and the second term is the LHY correction[16]. The LHY correction increases with the density n and the interaction strength g, and has a stronger dependence[17] on the density than the mean-field energy.

From this corrected ground-state energy (2.32), the chemical potential $\mu = \partial E_0/\partial N$ is then modified as

$$\mu = gn\left[1 + \frac{32}{3\sqrt{\pi}}\left(na^3\right)^{1/2}\right]. \tag{2.33}$$

Introducing the beyond mean-field correction to μ [second term in Eq. (2.33)] into the time-dependent GPE (2.20), one obtains the extended Gross–Pitaevskii equation that takes into account quantum fluctuations.

[16]This correction has been calculated for a homogeneous system, so to include it in a trapped system one has to consider the *local density approximation*, which assumes that the density of the system does not vary much in terms of the length scales of the system.

[17]The mean field term goes with $|\psi|^2$ and the LHY term with $|\psi|^3$.

Equation (2.32) also reveals that, in conditions that lie well within the mean-field regime, the LHY correction is indeed very small, so one can neglect the effect of quantum fluctuations and make use of the standard Gross–Pitaevskii and mean-field formalism to obtain a good description of the system.

Effect of quantum fluctuations

The mean-field approximation predicts a collapse of the system when the interactions are attractive; however, a repulsive LHY correction can compensate this effect. Therefore, quantum fluctuations can stabilize the system against collapse, which will be crucial for the formation of quantum droplets (see Section 2.2 and Petrov, 2015).

BECs can form droplets when the mean-field contribution to the energy alone would lead to the collapse of the system, and droplets emerge when the mean-field interactions and the LHY correction are balanced. Since the density of the system is limited by three-body losses, the LHY correction is usually very small. Then, for droplets to form there must be competing interactions within the condensate so the mean-field contribution is strongly reduced. Systems with such competing interactions are, for instance, mixtures of two condensates, where the inter- and intracomponent interactions can be attractive and repulsive, respectively (see Section 2.2). Dipolar condensates of highly magnetic atoms can also form droplets, since they exhibit both dipolar and contact interactions (see Chapter 3). Finally, one can also have droplet formation in dipolar mixtures, where all the interactions mentioned above participate in the balance (see Chapters 3 and 7).

2.2 Self-bound droplets in binary mixtures

Confinement is crucial to the existence of BECs: if $g > 0$ the gas expands without an external trap, while for $g < 0$ the gas collapses except for very weak interactions, where the presence of a confining potential can counterbalance the attraction. Quantum droplets, on the other hand, are self-bound, as they exist without external confinement.

Tuning the mean-field interactions such that their contribution is small and attractive can lead to the formation of droplets instead of collapse due to the effect of quantum fluctuations. This stabilizing mechanism occurs when the mean-field attraction is counterbalanced by the repulsive beyond mean-field effects, which are small. For the mean-field contribution to be small as well, there have to be competing interactions within the system. In mixtures of condensates, self-bound droplets can form due to the balance between inter- and intracomponent interactions, which results in an attractive mean-field contribution that the quantum fluctuations can stabilize.

We will start with the basic mean-field theory for bosonic mixtures on Subsection 2.2.1 and discuss their stability and excitations. Later, in Subsection 2.2.2, we will introduce the common beyond mean-field treatment for self-bound droplets in binary mixtures, which constitutes a simplified yet powerful single-component model, and the regimes and conditions in which droplets can be studied. Finally, Subsection 2.2.3 points out the main properties of self-bound droplets. These will serve as a reference for dipolar

droplets (see Chapter 3), where the anisotropy of the interaction leads to a more nuanced behavior. We will end this section with a brief comment about the connection between droplets and another type of self-bound solution, bright solitons, that will be explored in detail in Section 2.3.

2.2.1 Bosonic binary mixtures

A bosonic mixture of two condensates (either two completely different atomic species, two different isotopes, or the same species in different hyperfine states) can be described within the mean-field regime by two coupled time-dependent Gross–Pitaevskii equations (Pitaevskii and Stringari, 2016):

$$i\hbar\frac{\partial\psi_\sigma(\mathbf{r},t)}{\partial t} = \left[-\frac{\hbar^2\nabla^2}{2m_\sigma} + V_{\text{ext}}(\mathbf{r}) + g_{\sigma\sigma}\,|\psi_\sigma(\mathbf{r},t)|^2 + g_{\sigma\sigma'}\,|\psi_{\sigma'}(\mathbf{r},t)|^2\right]\psi_\sigma(\mathbf{r},t)\,. \tag{2.34}$$

Each component, labeled $\sigma = 1, 2$ (with $\sigma' \neq \sigma$), can be described by its own wavefunction $\psi_\sigma(\mathbf{r})$ and the corresponding density $n_\sigma(\mathbf{r}) = |\psi_\sigma(\mathbf{r})|^2$. The total density of the system is defined as $n(\mathbf{r}) = n_1(\mathbf{r}) + n_2(\mathbf{r})$, and the local difference between densities, sometimes called *spin density* or *magnetization*, is $n_s(\mathbf{r}) = n_1(\mathbf{r}) - n_2(\mathbf{r})$. The mass m_σ may be different for each component, and the total number of atoms in the mixture then is $N = N_1 + N_2$. The intra- ($\sigma\sigma$) and intercomponent ($\sigma\sigma'$) contact interactions are defined by the coupling constants (2.7)

$$g_{\sigma\sigma} = \frac{4\pi\hbar^2 a_{\sigma\sigma}}{m_\sigma} \quad \text{and} \quad g_{12} = \frac{2\pi\hbar^2 a_{12}}{m_{12}}\,, \tag{2.35}$$

where a_{11} and a_{22} are the scattering lengths that characterize the atom–atom interactions within each component, a_{12} the interactions between them (with $a_{12} = a_{21}$), and $m_{12} = m_1 m_2/(m_1 + m_2)$ is the reduced mass.

The energy functional of the system can be obtained in a way analogous to the scalar case (i.e., the single-component case, see Subsection 2.1.2), and reads

$$E[\psi_1,\psi_2] = \int d\mathbf{r}\left[\sum_{\sigma=1,2}\left(\frac{\hbar^2}{2m_\sigma}\,|\nabla\psi_\sigma|^2 + V_{\text{ext}}\,|\psi_\sigma|^2 + \frac{1}{2}\,g_{\sigma\sigma}\,|\psi_\sigma|^4\right) + g_{12}\,|\psi_1|^2|\psi_2|^2\right], \tag{2.36}$$

with $\mathcal{E}$ the energy density such that $E[\psi_1,\psi_2] = \int d\mathbf{r}\,\mathcal{E}$. The total energy of the system contains now the energy of each component, as given by Eq. (2.19), plus twice the interaction energy between them.

Miscibility condition

The sign and magnitude of the parameters g_{11}, g_{22} and g_{12} will determine the type of ground state and the behavior of the system:

- If all the interactions are attractive, i.e., $g_{11,22,12} < 0$, the system collapses, as in the scalar case[18].

[18] At least in 2D and 3D systems. In 1D systems, as with one component, the system may support bright solitons instead of collapsing (see Section 2.3).

- If the interactions are repulsive instead, with $g_{11,22,12} > 0$, then the mixture is stable and can either be miscible (the two wavefunctions overlap) or immiscible (the two components show a phase-separated configuration).
- If the intercomponent interactions are attractive, $g_{12} < 0$, but the intracomponent ones are repulsive, $g_{11,22} > 0$, the system can form quantum droplets (see 2.2.3).

The miscible–immiscible phase transition is given by the interplay between the intra- and intercomponent interactions. To understand this transition, we consider a uniform gas confined in a box potential in the miscible phase, such that the two components occupy the same volume and the energy density of the system (2.36) is

$$\mathcal{E}[n_1, n_2] = \frac{1}{2} g_{11}\, n_1^2 + \frac{1}{2} g_{22}\, n_2^2 + g_{12}\, n_1 n_2 \,. \tag{2.37}$$

For the system to be miscible and stable (a local minimum in the energy), the Hessian matrix of $\mathcal{E}[n_1, n_2]$ and its determinant need to be positive (Ao and Chui, 1998; Pethick and Smith, 2008; Pu and Bigelow, 1998; Timmermans, 1998),

$$\begin{bmatrix} \frac{\partial^2 \mathcal{E}}{\partial n_1^2} & \frac{\partial^2 \mathcal{E}}{\partial n_1 \partial n_2} \\ \frac{\partial^2 \mathcal{E}}{\partial n_1 \partial n_2} & \frac{\partial^2 \mathcal{E}}{\partial n_2^2} \end{bmatrix} = \begin{bmatrix} g_{11} & g_{12} \\ g_{12} & g_{22} \end{bmatrix} , \tag{2.38}$$

from where one can find that the intracomponent interactions have to be repulsive, $g_{11,22} > 0$, and the following condition:

$$g_{11} g_{22} > g_{12}^2 \,. \tag{2.39}$$

This condition (2.39), often called the *miscibility condition*, allows us to characterize three possible regimes in terms of the intercomponent interactions (Riboli and Modugno, 2002):

1. For $|g_{12}| < \sqrt{g_{11} g_{22}}$, the system is *miscible* and stable within this region. For values of g_{12} outside this region, however, the miscible mixture is no longer stable and the sign of the intercomponent interactions g_{12} will determine the behavior of the system.
2. For $g_{12} > 0$ and $g_{12} > \sqrt{g_{11} g_{22}}$, the mixture is *immiscible*. The system spontaneously breaks the translational symmetry and presents a phase-separated configuration.
3. For $g_{12} < 0$ and $g_{12} < -\sqrt{g_{11} g_{22}}$, the attractive interactions drive the system to *collapse*.

It is in this last scenario, where the mean-field framework predicts the system to collapse, that droplets will emerge due to the stabilizing mechanism of quantum fluctuations (see Section 2.2). These droplets are self-bound because they originate from the competition between the mean-field energy and the quantum fluctuations, so there is no need of an external confinement to sustain them.

Excitation spectrum

The spectrum of excitations for a binary mixture can be calculated following a procedure analogous to the scalar case (see *elementary excitations* in Subsection 2.1.2) by considering the ansatz in Eq. (2.28) for the wavefunction of each component, such that the complex amplitudes are u_σ and v_σ (with $\sigma = 1, 2$).

Assuming for simplicity that the two components are miscible, untrapped and have the same mass m, average density $n_0/2$ and intracomponent coupling constant $g_{11} = g_{22} = g$, one obtains two dispersion relations by considering excitations that can be either in phase or out of phase:

$$u_1(\mathbf{r}) = u\, e^{i\,\mathbf{k}\cdot\mathbf{r}}\,,\ v_1(\mathbf{r}) = v\, e^{i\,\mathbf{k}\cdot\mathbf{r}} \quad \text{and} \quad u_2(\mathbf{r}) = \pm\, u\, e^{i\,\mathbf{k}\cdot\mathbf{r}}\,,\ v_2(\mathbf{r}) = \pm\, v\, e^{i\,\mathbf{k}\cdot\mathbf{r}}. \tag{2.40}$$

In-phase excitations, also known as *density modes* or density excitations, give

$$(\hbar\omega_d)^2 = \frac{\hbar^2 k^2}{2m}\left(\frac{\hbar^2 k^2}{2m} + (g + g_{12})\, n_0\right), \tag{2.41}$$

which correspond to the bulk perturbations (i.e., changes in the total density) one finds in the scalar case (2.31). On the other hand, out-of-phase excitations, called *spin modes* or spin excitations, yield

$$(\hbar\omega_s)^2 = \frac{\hbar^2 k^2}{2m}\left(\frac{\hbar^2 k^2}{2m} + (g - g_{12})\, n_0\right), \tag{2.42}$$

which are local variations between the densities of each component (i.e., perturbations to the spin density). The two branches are gapless, i.e., their energies are zero at $k = 0$.

Figure 2.3 shows the excitation spectrum for a miscible and uniform mixture in the different stability regimes discussed before. For $|g_{12}| < g$ (Fig. 2.3, left panel), the two branches have real frequencies, so both density and spin excitations are stable. In the immiscibility regime, where $g_{12} > 0$ and $g_{12} > g$ (Fig. 2.3, central panel), the density branch $\hbar\omega_d$ is stable but the spin branch $\hbar\omega_s$ becomes unstable (i.e., has a complex frequency) for low momenta. This instability eventually drives the system to phase separate, and the two components become immiscible. Finally, in the regime where $g_{12} < 0$ and $g_{12} < -g$ (Fig. 2.3, right panel), while spin excitations are stable, the density excitations are not, and destabilize the system to collapse.

As in the scalar case (2.31), the two branches present a free-particle behavior at large k and a phonon dispersion at low k, which defines the two corresponding sound velocities, $c_d = \sqrt{(g + g_{12})\, n_0/(2m)}$ and $c_s = \sqrt{(g - g_{12})\, n_0/(2m)}$. These two different sound velocities determine the healing length associated to each branch, $\xi_{d,s} = \hbar/(\sqrt{2} m c_{d,s})$, which give an idea of the minimum length scales for which density or spin excitations, respectively, can occur.

Spin mixtures

We have considered so far a general mixture where the two components can either be different atomic species or the same species (be it different isotopes or the same isotope in different hyperfine states).

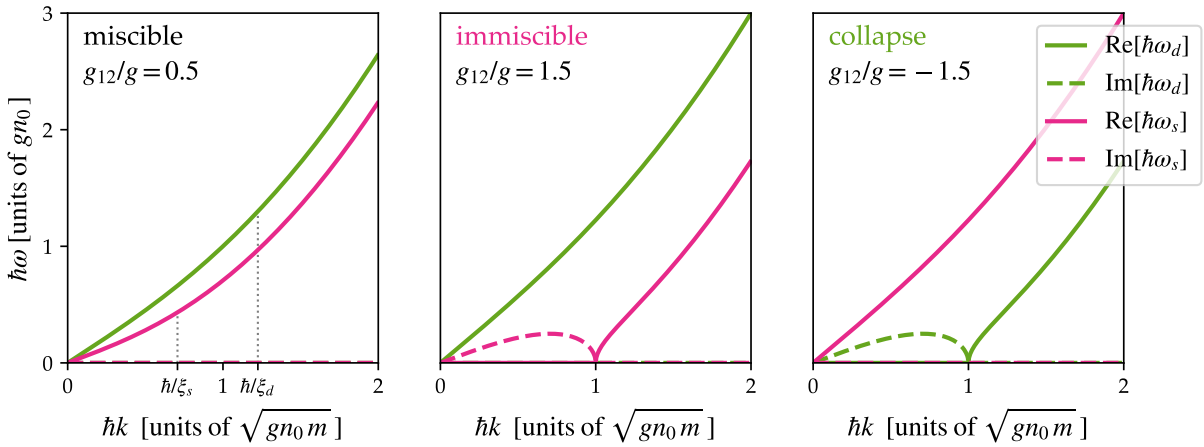

Figure 2.3: Excitation spectrum of a binary mixture in the miscible and uniform case with density $n_0/2$ and intracomponent coupling constant $g > 0$ equal for each component. [As reference, see Eq. (2.31) and Fig. 2.2 for the scalar case.] Solid lines correspond to the real part of the density (2.41) and spin (2.42) branches, and the dashed lines show their imaginary parts. (We recall that imaginary frequencies are the onset of instabilities.) Each panel corresponds to the three regimes described in the text: (left) the miscible regime, for $|g_{12}| < g$, where all excitations are stable; (center) the immiscible regime, for $g_{12} > g$, where the spin excitations are unstable; and (right) collapse, for $g_{12} < -g$, where the density excitations are unstable. The healing lengths $\xi_{d,s}$ associated to each branch characterize the length scales of density and spin excitations, respectively.

A particular case is that of *spin mixtures*, also referred to as *spinor condensates*, in which the gas is composed of atoms of the same species that occupy two different hyperfine states so the hyperfine degree of freedom (the spin) becomes relevant as well. This setup is particularly interesting since, besides the contact intercomponent interactions of a usual mixture, now the two components can also exchange particles by the *coherent coupling*[19] of these two states (Abad and Recati, 2013; Matthews et al., 1999).

Coherently coupled condensates will be introduced in Chapter 9, where we will study mixtures for which the effective interactions come from a density-dependent gauge potential.

2.2.2 Effective single-component model

In the present subsection we will see how the LHY correction (introduced in Subsection 2.1.3) can stabilize the system and allow for the formation of droplets in binary mixtures (introduced in Subsection 2.2.1), as predicted by Petrov (2015).

The energy functional for a binary mixture that takes into account quantum fluctuations is

$$E[\psi_1, \psi_2] = E_{\mathrm{MF}} + \int d\mathbf{r}\, \mathcal{E}_{\mathrm{LHY}}(n_1, n_2)\,, \tag{2.43}$$

[19] Rabi or Raman coupling are common terms in the literature as well.

where E_{MF} is the mean-field energy functional (2.36) and $\mathcal{E}_{\mathrm{LHY}}$ is the LHY correction to the energy density (Fort and Modugno, 2021; Petrov, 2015),

$$\mathcal{E}_{\mathrm{LHY}} = \frac{8}{15\pi^2}\left(\frac{m_1}{\hbar^2}\right)^{3/2}(g_{11}n_1)^{5/2} f\left(\frac{m_2}{m_1}, \frac{g_{12}^2}{g_{11}g_{22}}, \frac{g_{22}\,n_2}{g_{11}\,n_1}\right), \tag{2.44}$$

which comes from the zero-point energy of the Bogoliubov modes (as discussed in Subsection 2.1.3). The function f is dimensionless and positive, and we introduce the variables $x = g_{12}^2/(g_{11}g_{22})$ and $y = g_{22}n_2/(g_{11}n_1)$ to simplify notation. For equal masses, $m_1 = m_2 = m$, the function f reduces to

$$f(1, x, y) = \sum_{\pm}\left[1 + y \pm \sqrt{(1-y)^2 + 4xy}\right]^{5/2}\frac{1}{4\sqrt{2}}. \tag{2.45}$$

It is useful to define the parameter $\delta g = g_{12} + \sqrt{g_{11}g_{22}}$, since $\delta g < 0$ in the region where the miscible mixture is no longer stable and the mean-field collapse is predicted to occur (see discussion about miscibility in Subsection 2.2.1). We will focus on the unstable region but close to the boundary $\delta g \approx 0$, i.e., when δg is small compared to g_{11} and g_{22} (and both are positive).

From the analysis of this mechanical instability and the competition between the mean-field and LHY contributions (Petrov, 2015), one can obtain the two following conditions:

1. It is energetically favorable to minimize $[(n_1\sqrt{g_{11}} - n_2\sqrt{g_{22}})/\sqrt{g_{11}+g_{22}}]^2$, which becomes the spin density (i.e., the local difference between densities) when $g_{11} = g_{22}$. Therefore, spin excitations are negligible.

2. The quantity $[(n_1\sqrt{g_{22}} + n_2\sqrt{g_{11}})/\sqrt{g_{11}+g_{22}}]^2$, which is the total density if $g_{11} = g_{22}$, should be maximized. This results in both components increasing their densities and the density ratio n_2/n_1 being locked to

$$\frac{n_2}{n_1} = \sqrt{\frac{g_{11}}{g_{22}}}. \tag{2.46}$$

These conditions allow one to describe the miscible mixture with an effective single-component model that is valid for low energies, such that both components can be described by the same spatial mode $\phi(\mathbf{r}, t)$,

$$\psi_i(\mathbf{r}, t) = \sqrt{n_i}\,\phi(\mathbf{r}, t). \tag{2.47}$$

This approximation provides a good description of the ground state as well as the low-energy excitations of the droplet. For simplicity, one can assume that the masses of the two components are equal to m. Then, the mixture can be described by a single equation of motion for the wavefunction ϕ (Böttcher et al., 2021; Cabrera et al., 2018),

$$i\hbar\frac{\partial\phi}{\partial t} = \left(-\frac{\hbar^2\nabla^2}{2m} + V_{\mathrm{ext}} + \alpha n_0|\phi|^2 + \gamma n_0^{3/2}|\phi|^3\right)\phi, \tag{2.48}$$

where $n_0 = n_1 + n_2$ is the peak density of the mixture. The mean-fied coefficient α is

$$\alpha = \frac{2\sqrt{g_{22}/g_{11}}}{\left(1+\sqrt{g_{22}/g_{11}}\right)^2}\,\delta g\,, \tag{2.49}$$

and the LHY term coefficient γ is defined as

$$\gamma = \frac{32}{3\sqrt{\pi}}\left(\frac{m}{4\pi\hbar^2}\right)^{3/2}\left(\frac{\sqrt{g_{22}g_{11}}}{1+\sqrt{g_{22}/g_{11}}}\right)^{5/2} f\left(1, \frac{g_{12}^2}{g_{11}g_{22}}, \sqrt{\frac{g_{22}}{g_{11}}}\right). \tag{2.50}$$

The parameter $\delta g = g_{12} + \sqrt{g_{11}g_{22}}$ appears in the mean-field coefficient α (2.49). Therefore, defining the coupling constants such that $\delta g \approx 0$, one can obtain a small and attractive mean-field contribution. Regarding the LHY coefficient γ (2.50), if $\gamma = 0$ the system collapses; but if $\gamma \neq 0$, then the two terms can balance out each other and droplets can form. Therefore, droplets will emerge in the region where the miscible mixture collapses. Since this balance occurs for particular values of g_{11} and g_{22}, and their ratio fixes the density ratio (2.46), droplets will need an intrinsic imbalance in the number of atoms to form.

2.2.3 Quantum droplets

Quantum droplets in binary mixtures were first predicted by Petrov (2015) and observed both in confined geometries (Cabrera et al., 2018; Cheiney et al., 2018) and in an unconfined setting (Semeghini et al., 2018). Their dipolar counterparts will be explored in detail in Chapter 3. Here we will summarize some main properties of droplets in binary mixtures, which will serve as a basis to understand droplets in dipolar condensates.

Binding mechanism and equilibrium density

When the intercomponent interactions are attractive and the intracomponent interactions are repulsive such that the total mean-field contribution is weakly attractive, a repulsive beyond mean field contribution can stabilize the system (see schematic representation of this binding mechanism in Fig. 2.4). This leads to a minimum in the total energy (2.43) that corresponds to a bound state for a particular value of the density n_0, called the *equilibrium density*, since it is the density at which droplets will be stable. The equilibrium density only depends on the interactions in the gas, which are characterized by the s-wave scattering lengths. Therefore, due to the isotropy of the interactions, these droplets will be spherically symmetric.

As a result of the balance between energy contributions, quantum droplets are self-bound, which means that they can be sustained even in the absence of an external trapping, in contrast to BECs.

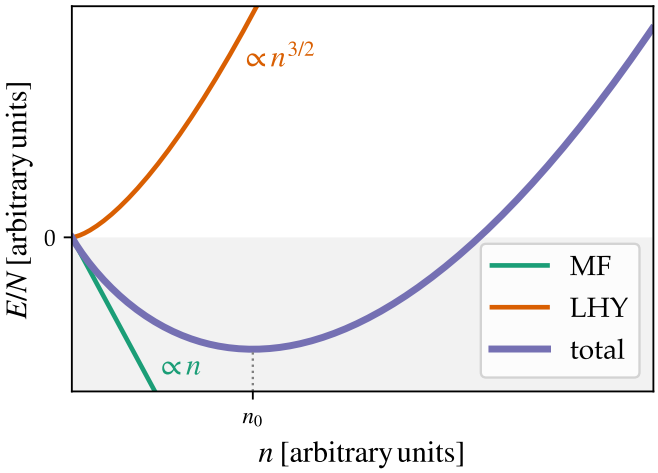

Figure 2.4: Binding mechanism of droplets in a binary mixture. The mean-field (MF) energy per particle is attractive and proportional to n, while the beyond mean-field (LHY) energy per particle is repulsive and grows with $n^{3/2}$, where n is the total density of the mixture. The energy per particle of the system shows a minimum when the two contributions balance each other at a density n_0 (dotted line), the equilibrium density, at which the droplet will stabilize.

Three-body losses

Increasing the density of a condensate in the appropiate conditions (see Subsection 2.2.2) will eventually lead to the formation of a droplet. Therefore, due to the higher densities of droplets[20], their main decay mechanism are three-body losses, which grow with n^3. The density of the droplet will have to be larger than that of the original condensate so the LHY correction is large enough to overcome the mean-field attraction. This in turn will increase the rate of three-body losses, which will limit greatly the lifetimes of these states in experimental settings.

Critical atom number

Quantum droplets can only be sustained when their number of atoms exceeds a particular critical number. This critical number of atoms arises from the competition between the binding mechanism of the droplet and the kinetic energy[21]. The kinetic energy increases the energy per particle due to dispersion, and it can dominate over the other energy contributions if the number of atoms (and thus the density) is too small. In this case, the dispersion makes the droplet unstable and drives the system to a gas phase. The critical atom number depends on the strengths of the interactions involved.

[20]Compared to liquid helium droplets, however, these droplets are much less dense, actually by several orders of magnitude.

[21]This situation resembles that of attractive condensates, where the collapse can be stabilized by the external confinement if the interactions are not too strong.

Liquid-like saturation

Just as liquid droplets, quantum droplets also exhibit a saturation value of their density. In general, the shape of a droplet is characterized by two parts: the *bulk* is the central region of the droplet, where the density is highest (i.e., the peak density), and the *surface* corresponds to the region where the density of the droplet goes from its maximum to its minimum. For a small number of atoms, the droplet is mostly surface. Increasing the number of atoms increases the bulk of the droplet. However, at the critical number of atoms, saturation occurs, and the droplet acquires a flat-top shape. Adding more atoms, then, only increases the size of the droplet, not its peak density.

Self-evaporation

Self-bound droplets also exhibit self-evaporation[22]. For a certain regime of atom numbers, there are no excitation modes below the particle-emission threshold (i.e., the chemical potential), such that the only way for the system to get rid of the extra energy is by expelling particles. This means that, in those conditions, excitations will cause the droplet to lose particles and stabilize into a droplet with a smaller number of atoms (Ferioli et al., 2020; Hu and Liu, 2020; Petrov, 2015). For atom numbers outside this region, the system can sustain excitations.

The self-evaporation effect is usually hard to observe in mixtures of the same atomic species, where three-body recombination is an important loss mechanism and strongly limits the lifetime of the droplet (Cabrera et al., 2018; Semeghini et al., 2018). As an alternative, one can consider a K–Rb mixture, for instance, where the contact interactions are stronger and allow for smaller densities (Fort and Modugno, 2021), which decreases the three-body losses.

Bright soliton to droplet transition

Quantum droplets resemble bright solitons in that neither of them are sustained by an external confinement. Reducing the system to one-dimension, it is possible to form a self-bound droplet from a bright soliton, as was shown by Cheiney et al. (2018) with a bosonic mixture confined in an optical waveguide. Bright solitons are localized perturbations that propagate without deformation and can be the ground state of a quasi-1D BEC with attractive interactions (more details in Section 2.3).

Both droplets and solitons are self-bound solutions that arise from the interplay of two competing interactions. However, this balance is fundamentally different: mean-field interactions and quantum fluctuations give rise to droplets, while attractive interactions and dispersion to bright solitons. Quantum droplets require a minimum number of atoms to become self-bound, but bright solitons have instead a maximum number of atoms above which these solutions are no longer stable. Therefore, the regimes in which each of them can exist is different, and the strength of the interactions and the number

[22]This phenomenon does not happen in droplets of single-component dipolar condensates (see Chapter 3).

of atoms play a crucial role in determining whether those two states can be smoothly connected.

2.3 Solitons in quasi-1D condensates

Solitons are exact solutions of the 1D Gross–Pitaevskii equation in the absence of an external confinement[23]. We will begin with Subsection 2.3.1 by introducing a reduction of the GPE (2.20) to 1D that will allow us to describe quasi-1D systems within the mean-field regime. Then, we will present the basics of solitons and their properties in Subsection 2.3.2.

The treatment presented here will be extended to binary mixtures (Chapter 6) and to ring geometries where the interactions originate from a density-dependent gauge potential (Chapters 4, 8 and 9).

2.3.1 One-dimensional Gross–Pitaevskii equation

To realize a quasi-1D condensate, we consider a strong transversal confinement, $\omega_x \ll \omega_y, \omega_z$, such that the excited states in the y and z directions are not energetically accessible, i.e., $\mu \ll \hbar\omega_y, \hbar\omega_z$. Then, the condensate wavefunction $\Psi(\mathbf{r}, t)$ that describes the 3D condensate can be factorized as

$$\Psi(\mathbf{r}, t) = \psi(x, t)\, \varphi(y, z)\,. \tag{2.51}$$

For weak interactions, the transversal modes can be approximated by the ground state of the harmonic oscillator (i.e., a Gaussian function), since the excited states in such modes will have a much larger energy. Then, we define

$$\varphi(y, z) = \frac{1}{\sqrt{\pi\, a_y a_z}} \exp\left[-\frac{1}{2}\left(\frac{y^2}{a_y^2} + \frac{z^2}{a_z^2}\right)\right], \tag{2.52}$$

where a_y and a_z are the harmonic lengths (2.23) in each direction, and $\varphi(y, z)$ is normalized to $\int dy \int dz\ \varphi(y, z) = 1$.

The relevant physics will occur in the x direction since the degrees of freedom of the y and z directions are frozen, so one can integrate out the transversal modes. Therefore, to obtain an effective 1D equation of motion, we introduce the factorized wavefunction (2.51) into the 3D time-dependent GPE (2.20), project over $\varphi^*(y, z)$ and integrate for all y and z to get rid of the transversal degrees of freedom. The resulting 1D Gross–Pitaevskii equation reads

$$i\hbar \frac{\partial \psi(x, t)}{\partial t} = \left[-\frac{\hbar^2 \nabla^2}{2m} + V_{\text{ext}}(x) + g_{1\text{D}}\, |\psi(x, t)|^2\right] \psi(x, t)\,, \tag{2.53}$$

[23] Or when the trapping potential is uniform.

where g_{1D} is the 1D coupling constant. It relates to the 3D coupling constant (2.7) and to the scattering length a_s as

$$g_{1D} = \frac{g}{2\pi\, a_y a_z} = \frac{2\hbar^2}{m}\frac{a_s}{a_y a_z}\,. \tag{2.54}$$

For a binary mixture, one can obtain the two coupled GPEs in 1D following the same procedure. Assuming equal masses, the normalized 1D coupling constants are

$$g^{(1D)}_{\sigma\sigma'} = \frac{g_{\sigma\sigma'}}{2\pi\, a_y a_z}\,, \tag{2.55}$$

where $g_{\sigma\sigma'}$ denotes (for $\sigma = 1, 2$), the 3D inter- and intracomponent coupling constants (2.35).

2.3.2 Solitons

Solitons or solitary waves are localized perturbations of the density that propagate without changing their shape (Barenghi and Parker, 2016; Pethick and Smith, 2008; Pitaevskii and Stringari, 2016). These density-modulated solutions arise from the interplay between the nonlinearity of the system (the interactions) and the dispersion (the quantum pressure). In general, solitons are only stable in 1D geometries, and are exact analytical solutions of the 1D homogeneous GPE (2.53), which is an integrable model[24]. The nature of the interactions lead to two types of solitons, known as *dark solitons* for repulsive interactions and as *bright solitons* for attractive interactions.

Dark solitons

Dark solitons present as a localized depletion in the density, and the phase shows a jump across its density profile with a large phase variation at the density dip. In general, they can move at a given velocity that must be below the speed of sound c (Frantzeskakis, 2010). The ground state of a homogeneous system has an unmodulated (i.e., constant) density, while a dark soliton is an excited state. The general solution for a dark soliton moving at a velocity v is (Pethick and Smith, 2008; Tsuzuki, 1971)

$$\psi_D(x,t) = \sqrt{n_0}\left\{ i\frac{v}{c} + \sqrt{1-\frac{v^2}{c^2}}\tanh\left[\sqrt{1-\frac{v^2}{c^2}}\frac{x-vt}{\sqrt{2}\xi}\right]\right\} e^{-i\mu t/\hbar}\,, \tag{2.56}$$

where n_0 is the density of the homogeneous background. For $v = 0$, the density goes to zero at the center of the soliton and the phase has a sharp π-jump, as shown in Fig. 2.5. Moving dark solitons are often referred to as *gray solitons*, while the term *dark* is reserved for static solitons, but here we will call them *dark* regardless of their velocity. For larger

[24] A system is integrable when it has, at least, as many conserved quantities as degrees of freedom. For the 1D GPE (2.53), conserved quantities of physical relevance would be the norm, the momentum, and the energy.

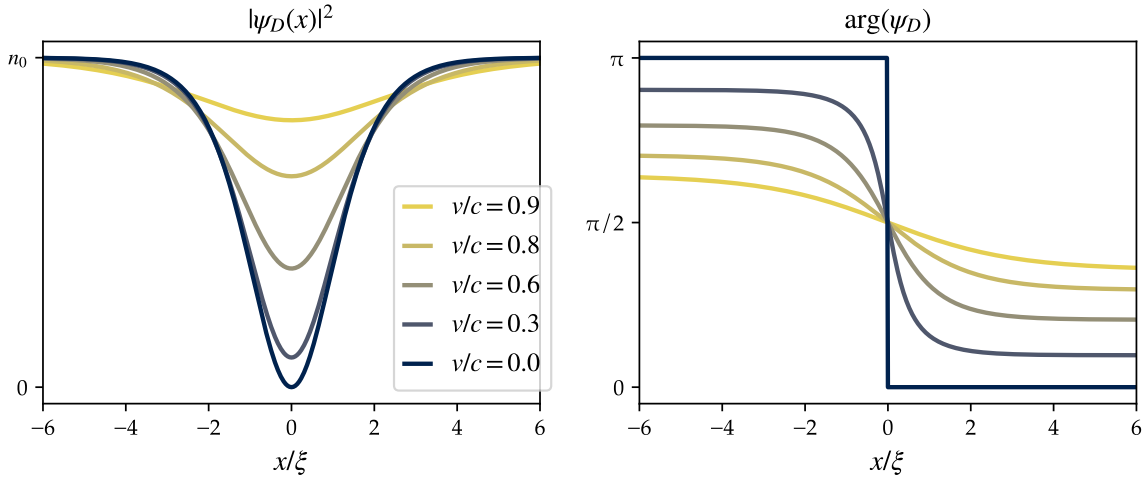

Figure 2.5: Dark solitons moving at different velocities v. The density profile (left panel) shows a minimum at the center of the soliton, which is zero for a stationary soliton and increases with the velocity; at $v = c$, the soliton merges with the homogeneous background, with density n_0. The phase (right panel) presents a jump with a large gradient at the center of the soliton; the jump is sharp for $v = 0$, and smoothens for increasing velocity. The healing length ξ characterizes the size of the soliton.

velocities (see Fig. 2.5), the density at the center departs from zero as nv^2/c^2, the width of the soliton (which goes with the healing length ξ) increases with the velocity, and the phase jump smoothens as $2\arccos(v/c)$.

For small velocities, the soliton can behave as a particle with negative effective mass m_s, which allows one to calculate the soliton energy as that of a free particle, with kinetic energy $m_s v^2/2$. Note that since the mass is negative, solitons with a higher energy will move more slowly.

Bright solitons

Bright solitons are solutions of the GPE for attractive interactions, where the uniform system would be expected to collapse. In this situation, the ground state of the homogeneous system is instead a bright soliton, where the dispersion of the medium counterbalances the attractive interactions, so the resulting soliton becomes self-bound. The general solution is (Pethick and Smith, 2008)

$$\psi_{\mathrm{B}}(x) = \sqrt{n_0}\,\mathrm{sech}\left(\frac{x}{\sqrt{2}\xi}\right), \tag{2.57}$$

where n_0 is the central density. The soliton gets narrower as the strength of the interactions increases, since its size is characterized by the healing length ξ (2.24), which goes with $|g|^{-1/2}$. As opposed to dark solitons, the height and width of bright solitons do not depend on the velocity of the soliton, and bright solitons do not have any restriction in terms of velocity as dark solitons do. Like dark solitons, bright solitons also behave as particles but with a positive mass.

3

Dipolar condensates, self-bound droplets and supersolids

Dipolar Bose–Einstein condensates are governed by long-range and anisotropic interactions. As a result, the behavior and the properties of these systems are much richer and nuanced than in nondipolar condensates (see Chapter 2). These new phenomena arise mainly from the interplay between the anisotropy of the dipolar interactions, the isotropic contact interactions, and the confining potential. Dipolar condensates have been studied extensively within the mean-field approximation, which provides a good description of the statics and dynamics of dipolar condensates. However, the mean-field approach fails at portraying the emergence of two new exotic phases that stem from quantum fluctuations: droplets and supersolids. Droplets are self-bound states, which do not require an external confinement to sustain them; supersolids, on the other hand, are density modulated solutions that show both superfluid and crystalline properties.

Quantum fluctuations come from the probabilistic nature intrinsic to quantum mechanics. In systems where the mean-field energy is small enough, they enable the stabilization of self-bound droplets and the emergence of supersolid phases in situations where the mean field describes a collapse. As we saw on Chapter 2, in the mean-field formalism one usually neglects quantum fluctuations and assumes that all the atoms of the gas condense. It is possible however to extend the mean-field framework to account for quantum fluctuations.

The chapter is organized as follows[1]. Section 3.1 presents the dipole–dipole interactions and gives an overview of the basic properties of dipolar condensates. In Section 3.2, we introduce a beyond mean-field correction to describe the effect of quantum fluctuations and study the formation of self-bound droplets. In the presence of an external confinement, these droplets can arrange in droplet arrays and eventually lead to supersolids. The formalism studied in this chapter will be extended to dipolar binary mixtures in Chapter 7.

[1]The overview presented in this chapter is by no means extensive and focuses mainly on the concepts that are most relevant to this thesis (for more comprehensive reviews on these topics, see for instance Böttcher et al., 2021; Chomaz et al., 2022; Lahaye et al., 2009).

3.1 Dipolar condensates

Dipolar condensates have been a highly active field of research, both from theoretical and experimental perspectives, in the last two decades. Here we will lay out the main properties of weakly interacting BECs in the presence of dipolar interactions.

We will first discuss in Subsection 3.1.1 the anisotropy and long-range character of the dipole–dipole interaction and present its standard treatment within the mean-field regime. Then, in Subsection 3.1.2 we will focus on the static properties of the system and discuss the conditions under which the system collapses. We will also see that the presence of an external confinement allows for two new phenomena that one cannot find in nondipolar BECs: magnetostriction, which is the elongation of the condensate with respect to the shape of the trap, and the stabilizing effect of the confinement against collapse in some circumstances. Finally, in Subsection 3.1.3 we will study the elementary excitations of the system and discuss the origin of the two main instabilities one can have in a dipolar condensate: the phonon instability, that leads to a global collapse of the system, and the roton instability, which causes instead a series of local collapses in the condensate.

3.1.1 Dipole–dipole interactions

Particles that interact via dipole–dipole interactions have either a magnetic dipole moment μ or an electric dipole moment d (Chomaz et al., 2022; Lahaye et al., 2009), which are fundamentally different.

There are no permanent electric dipole moments. Instead, electric dipoles come from charge displacement in space, so one can tune them by applying an external electric field. Systems that present such electric dipoles are, for instance, polar molecules, Rydberg atoms or light-induced dipoles.

On the other hand, permanent magnetic dipoles do exist, since the magnetic dipole moment comes from the internal structure of the atoms (the total angular momentum, which comprises the orbital angular momentum and the electronic and nuclear spins). Therefore, the atomic species determines the magnetic dipole moment. One can understand the interaction between two particles with a permanent magnetic moment as the interaction of the spin of one of the particles with the magnetic field that the spin of the other particle creates. We will focus on magnetic dipoles from now on, although most results are general for both kinds of dipoles.

Interaction potential between two dipoles

The interaction between two magnetic dipoles $\boldsymbol{\mu}_1$ and $\boldsymbol{\mu}_2$ at positions $\mathbf{r}_1$ and $\mathbf{r}_2$ is given by

$$U_{\mathrm{dd}}(\mathbf{r}) = \frac{\mu_0}{4\pi} \frac{(\boldsymbol{\mu}_1 \cdot \boldsymbol{\mu}_2)\, r^2 - 3\,(\boldsymbol{\mu}_1 \cdot \mathbf{r})(\boldsymbol{\mu}_2 \cdot \mathbf{r})}{r^5}\,, \tag{3.1}$$

where $\mathbf{r} = \mathbf{r}_1 - \mathbf{r}_2$ is the relative position of the dipoles, r their relative distance and μ_0 is the permeability of vacuum.

We consider two polarized identical bosons, such that the dipoles have the same strength μ and are oriented along the same direction. We choose the z axis as polarization direction, i.e., $\boldsymbol{\mu}_1 = \boldsymbol{\mu}_2 = \mu\,\hat{\mathbf{e}}_z$, where $\hat{\mathbf{e}}_z$ is the unitary vector in the z direction and the strength of the dipoles μ is determined by the atomic species. Then, the dipole–dipole potential (3.1) simplifies to

$$U_{\mathrm{dd}}(\mathbf{r}) = \frac{C_{\mathrm{dd}}}{4\pi}\frac{1-3\cos^2\theta}{r^3}\,. \tag{3.2}$$

The angle between the polarization direction $\hat{\mathbf{e}}_z$ and the relative position of the particles $\mathbf{r}$ is θ, and we have introduced the coupling constant $C_{\mathrm{dd}} = \mu_0\mu^2$ to characterize the strength of the interaction. For electric dipoles, one obtains a coupling constant $C_{dd} = d^2/\epsilon_0$, where d is the electric dipole moment and ϵ_0 is the permittivity of vacuum. The coupling constant of the dipolar interaction C_{dd} is usually higher for electric dipoles than magnetic dipoles[2].

The dipole–dipole interaction presents two main characteristics that contact interactions do not have. First, it is *long range*, since the potential (3.2) decays with r^{-3}, in contrast to the short-range character of the van der Waals (i.e., contact) interactions (2.5), that we characterized in terms of the s-wave scattering length a_s and decreases with r^{-6}. Secondly, the potential (3.2) has an angular dependence, which means that the interactions are *anisotropic*, unlike contact interactions, that are isotropic. As one can see from Eq. (3.2), this dependence on the angle implies that the interactions will be attractive along z (the direction of the dipoles) and repulsive in the xy plane.

The behavior of the interaction potential can be understood by three particular scenarios that depend on the angle between the polarization direction and the relative position of the dipoles:

- For $\theta = \pi/2$, the dipoles locate side by side and $(1-3\cos^2\theta) = 1$, which yields a repulsive interaction.
- For $\theta = 0$, the dipoles are placed in a head-to-tail configuration and $(1-3\cos^2\theta) = -2$, such that the interaction is attractive and twice as strong as in the side-by-side configuration.
- For $\theta_m = \arccos(1/\sqrt{3})$, which is usually called the *magic angle*, the interactions vanish.

For intermediate angles, the interaction is effectively attractive for $\theta < \theta_m$ and repulsive for $\theta > \theta_m$. The anisotropy of the interactions is a crucial factor in the stability of confined systems. Since the interactions are no longer spherically symmetric, the

[2]The electric dipole moment d of an atom or a molecule is usually of the order of ea_0, with e the electron charge and a_0 the Bohr radius (for a Rydberg atom, the charge separation is much larger, and so is the dipole moment). The magnetic dipole moment μ, on the other hand, is of the order of the Bohr magneton μ_{B}. Then, comparing the two coupling constants, $\mu_0\mu^2/(d^2/\epsilon_0) \sim \mu_0\mu_{\mathrm{B}}\epsilon_0/(e^2a_0) = \alpha^2/4$, where $\alpha \approx 10^{-2}$ is the fine structure constant, one can see that the electric moment is much larger than the magnetic moment (Chomaz et al., 2022; Lahaye et al., 2009).

interplay between the geometry of the confinement and the effective dipolar interaction plays a determining role, as we will discuss later.

It is worth noting that, due to their anisotropic character, dipolar interactions do not conserve the orbital angular momentum, which means that there can be inelastic scattering processes where the angular momentum changes (i.e., spin flips). These processes are often referred to as *dipolar relaxation*, which leads to heating and large atom losses in systems of highly magnetic dipoles (Burdick et al., 2015). Even though the elastic interactions are the most common, these relaxation processes are thus an important loss mechanism for strongly dipolar gases.

Effect on the contact interactions and interatomic pseudopotential

The scattering processes change in the presence of dipole–dipole interactions, which not only add a long-range behavior but also affect the short-range effective interactions. Therefore, the scattering length a_s that characterizes the short-range interactions will depend on the dipolar moment μ.

To describe the interactions, one can assume that the van der Waals interactions dominate at short distances and the dipole–dipole interactions do so at long distances, such that the interatomic potential can be written as a pseudopotential of the form

$$\begin{aligned} V(\mathbf{r}-\mathbf{r}') &= \frac{4\pi\hbar^2}{m}\, a_s\, \delta(\mathbf{r}-\mathbf{r}') + \frac{C_{\mathrm{dd}}}{4\pi}\frac{1-3\cos^2\theta}{|\mathbf{r}-\mathbf{r}'|^3} \\ &= g\,\delta(\mathbf{r}-\mathbf{r}') + U_{\mathrm{dd}}(\mathbf{r}-\mathbf{r}')\,, \end{aligned} \tag{3.3}$$

The first term in Eq. (3.3) corresponds to the usual short-range contact interactions but the scattering length a_s is modified by the strength of the dipolar interactions, and g is the coupling constant defined in Eq. (2.7). The second term represents the long-range interactions, which are characterized by the dipole–dipole potential $U_{\mathrm{dd}}(\mathbf{r}-\mathbf{r}')$ we introduced before (3.2). Since we will consider a given atomic species the dipole moment is fixed; thus, the dependence of the scattering length on the dipole moment will not play an important role. Moreover, one can tune the scattering length by means of Feshbach resonances (see Chapter 2), and decreasing the scattering length will be of particular interest to enhance the effect of the long-range interactions.

The pseudopotential (3.3) is valid away from scattering resonances (see the original proposal by Yi and You, 2000, 2001). It works well at the mean-field level, where one can effectively treat the contact-interacting part (short-range) and the dipolar part (long range) separately[3].

Tuning the dipolar interactions

Consider a gas of bosons fully polarized along the z direction. It is possible to tune the dipolar interactions by rotating the polarizing magnetic field $\mathbf{B}$ around the z

[3]The fact that the two interactions can eventually be treated separately is not obvious and has been subject to long debate in the literature (for extensive discussions on the issue, see Chomaz et al., 2022; Lahaye et al., 2009), though it is now a well established procedure in the mean-field formalism.

axis[4] (Giovanazzi et al., 2002; Tang et al., 2018),

$$\mathbf{B}(t) = B\left\{\cos\varphi\,\hat{\mathbf{e}}_z + i\sin\varphi\left[\cos(\Omega t)\,\hat{\mathbf{e}}_x + \sin(\Omega t)\,\hat{\mathbf{e}}_y\right]\right\}\,, \tag{3.4}$$

where Ω is the rotation angular frequency and φ is the angle with respect to the z axis. If the frequency Ω is smaller than the Larmor frequency[5] but is much larger than the time scales of the system (given by the trapping frequencies), the dipoles will follow the external field $\mathbf{B}(t)$ adiabatically and precess around the z axis. As a result, the time-averaged potential provides the relevant physical description:

$$\langle U_{\rm dd}(t)\rangle = \frac{C_{\rm dd}}{4\pi}\frac{1-3\cos^2\theta}{r^3}\left(\frac{3\cos^2\varphi-1}{2}\right)\,, \tag{3.5}$$

where the time average is taken over a period $2\pi/\Omega$. The last factor is 1 when $\varphi = 0$, takes the value 0 at the magic angle $\varphi = \theta_m$, and is $-1/2$ when $\varphi = \pi/2$ so that the sign of the dipole–dipole interactions is inverted and the interactions are then referred to as *antidipolar* (Kirkby et al., 2023; Mukherjee et al., 2023). As a result, one can vary the effective interactions by changing the angle φ.

Interaction potential in momentum space

The dipolar potential in Fourier space is useful for studying elementary excitations, provides further insight into the anisotropy of the interactions and is convenient for numerical calculations.

The dipole–dipole potential (3.2) can be rewritten in terms of the spherical harmonic $Y_{\ell m}(\theta,\varphi)$ with $\ell = 2$ and $m = 0$ in spherical coordinates as

$$U_{\rm dd}(\mathbf{r}) = -\frac{C_{\rm dd}}{4\pi}\sqrt{\frac{16\pi}{5}}\frac{Y_{20}(\theta,\varphi)}{r^3}\,, \tag{3.6}$$

where θ is, as before, the angle between the relative position of the particles and the polarization direction, and φ is the azimuthal angle (contained in the xy plane), which plays no role here.

One can define the Fourier transform of $U_{\rm dd}(\mathbf{r})$ as

$$\tilde{U}_{\rm dd}(\mathbf{k}) = \mathcal{F}[U_{\rm dd}(\mathbf{r})] = \int U_{\rm dd}(\mathbf{r})\,e^{-2\pi i\,\mathbf{k}\cdot\mathbf{r}}\,d\mathbf{r}\,, \tag{3.7}$$

with $\mathbf{k}$ the wavevector[6]. One way of calculating the Fourier transform, where we replace $U_{\rm dd}(\mathbf{r})$ by the potential defined in Eq. (3.6), is by expanding the exponential in Eq. (3.7) in terms of Bessel functions and spherical harmonics. Then, the angular integrals can be

[4] In 2D systems, one can also tune the interactions by changing the trap angle with respect to the polarization angle.

[5] The Larmor frequency, defined as $\mu B/\hbar$, is the frequency at which a magnetic moment μ precesses when subjected to a magnetic field of strength B.

[6] Note we have introduced the phase 2π for numerical convenience following the FFTW3 algorithm (Frigo and Johnson, 2005).

calculated using the orthonormal properties of spherical harmonics. To evaluate the radial integral, one can introduce in the limits of the integral (0 and ∞) a cutoff b at small distances, and a cutoff R at large distances[7] (Lu et al., 2010a; Ronen et al., 2006). Since the size of the atoms is much smaller than the distance at which interactions occur, one can set $b \to 0$. Then, the Fourier transform of the potential is

$$\tilde{U}_{\mathrm{dd}}(\mathbf{k}) = \frac{C_{\mathrm{dd}}}{3}\left(3\cos^2\theta_k - 1\right)\left[1 + \frac{3\cos(2\pi kR)}{(2\pi kR)^2} - \frac{3\sin(2\pi kR)}{(2\pi kR)^3}\right], \tag{3.8}$$

where θ_k is the angle between the polarization direction and $\mathbf{k}$. For large distances ($R \to \infty$), one gets the most common expression,

$$\tilde{U}_{\mathrm{dd}}(\mathbf{k}) = \frac{C_{\mathrm{dd}}}{3}\left(3\cos^2\theta_k - 1\right). \tag{3.9}$$

Finally, the full interaction pseudopotential (3.3) in momentum space is

$$\tilde{V}(\mathbf{k}) = \mathcal{F}\left[V(\mathbf{r})\right] = g + \tilde{U}_{\mathrm{dd}}(\mathbf{k}). \tag{3.10}$$

For contact-interacting gases, the interaction potential in momentum space (3.10) depends only on g, i.e., the strength of the interaction[8]. For dipolar gases, however, the potential presents an angular dependence (i.e., with θ_k) due to the anisotropic character of the interactions. As a consequence, the anisotropy in momentum space will show in the dispersion relation of the excitations, which will be then anisotropic. It is worth noting that neither the contact term nor the dipolar term depend on k in 3D gases, but that this may not be the case in quasi-2D systems (see Subsection 3.1.3). The fact that the Fourier transform of the potential may depend on k in lower dimensions could lead those systems to a new type of instability and exhibit structured excitations.

Mean-field formalism and dipolar Gross–Pitaevskii equation

Here we will discuss the mean-field formalism for a fully polarized dipolar gas of N bosons at $T = 0$. The Gross–Pitaevskii equation can be written in terms of a generic interatomic potential (2.16) such that in time-dependent form reads

$$i\hbar\frac{\partial\psi(\mathbf{r},t)}{\partial t} = \left[-\frac{\hbar^2\nabla^2}{2m} + V_{\mathrm{ext}}(\mathbf{r}) + \int d\mathbf{r}'\, V(\mathbf{r}-\mathbf{r}')\,|\psi(\mathbf{r}',t)|^2\right]\psi(\mathbf{r},t). \tag{3.11}$$

Replacing $V(\mathbf{r}-\mathbf{r}')$ with the pseudopotential (3.3), one gets

$$i\hbar\frac{\partial\psi(\mathbf{r},t)}{\partial t} = \left[-\frac{\hbar^2\nabla^2}{2m} + V_{\mathrm{ext}}(\mathbf{r}) + g|\psi(\mathbf{r},t)|^2 + \int d\mathbf{r}'\, U_{\mathrm{dd}}(\mathbf{r}-\mathbf{r}')\,|\psi(\mathbf{r}',t)|^2\right]\psi(\mathbf{r},t), \tag{3.12}$$

[7] The cutoff at large distances is introduced to avoid the different replicas (which arise naturally when calculating in momentum space) from interacting with each other, since the interaction is long range. This effect can otherwise be avoided by considering a numerical grid much larger than the condensate.

[8] Note that the Fourier transform of the contact part is just g, since $\tilde{U}_s(\mathbf{k}) = g\int \delta(\mathbf{r})e^{-2\pi i\,\mathbf{k}\cdot\mathbf{r}}\,d\mathbf{r} = g$.

where $U_{\rm dd}$ is the dipole-dipole potential (3.2). We recover the GPE from the contact-interacting gas (2.20) with an additional term that accounts for the dipolar interactions and that is nonlocal. Introducing a time-dependent ansatz (2.21), $\psi(\mathbf{r},t) = \psi(\mathbf{r})\, e^{-i\mu t/\hbar}$, one finds the equation for the stationary state $\psi(\mathbf{r})$,

$$\left[-\frac{\hbar^2\nabla^2}{2m} + V_{\rm ext}(\mathbf{r}) + g|\psi(\mathbf{r})|^2 + \int d\mathbf{r}'\, U_{\rm dd}(\mathbf{r}-\mathbf{r}')\,|\psi(\mathbf{r}')|^2\right]\psi(\mathbf{r}) = \mu\psi(\mathbf{r})\,, \tag{3.13}$$

which is the time-independent Gross–Pitaevskii equation for a dipolar gas.

The GPE, Eqs. (3.12) and (3.13), is now an integro-differential equation due to the nonlocal term and thus it is, in general, difficult to solve numerically. To facilitate the calculation, the standard procedure is to compute the dipolar term in momentum space, where it only has an angular dependence as opposed to its nonlocal character in real space. Then, one can recover the dipolar term in real space by inverse Fourier transforming the product of the density and the potential in Fourier space,

$$\int d\mathbf{r}'\, U_{\rm dd}(\mathbf{r}-\mathbf{r}')\,|\psi(\mathbf{r}')|^2 = \mathcal{F}^{-1}\left[\tilde{n}\,\tilde{U}_{\rm dd}(\mathbf{k})\right]\,. \tag{3.14}$$

The inverse Fourier transform is denoted by $\mathcal{F}^{-1}$, and $\tilde{U}_{\rm dd}$ and $\tilde{n}$ are the Fourier transforms of the dipolar potential and the density, respectively[9]. The dipolar potential $\tilde{U}_{\rm dd}$ is given by the analytical expression we introduced earlier (3.9), and the density $\tilde{n}$ can be calculated numerically[10].

Finally, the energy functional of the system can be calculated analogously to the case with only contact interactions (see Section 2.1), and reads

$$E[\psi] = \int d\mathbf{r}\left[\frac{\hbar^2}{2m}|\nabla\psi(\mathbf{r})|^2 + V_{\rm ext}(\mathbf{r})|\psi(\mathbf{r})|^2 + \frac{1}{2}g|\psi(\mathbf{r})|^4\right. \tag{3.15}$$

$$\left. + \frac{1}{2}\int d\mathbf{r}\,|\psi(\mathbf{r})|^2 \int d\mathbf{r}'\, U_{\rm dd}(\mathbf{r}-\mathbf{r}')|\psi(\mathbf{r}')|^2\right]\,. \tag{3.16}$$

Comparing with the nondipolar case (2.19), the energy is the same but with an additional contribution due to the dipolar interactions.

Length scales of the system

The behavior of a dipolar BEC will largely depend on the relative strength between the dipole–dipole and contact interactions, which affect the stability of the system (see Subsection 3.1.2). While the contact interactions are governed by the scattering length a_s, the strength of the dipolar interactions can be characterized by the dipolar length,

$$a_{\rm dd} = \frac{C_{\rm dd}m}{12\pi\hbar^2}\,. \tag{3.17}$$

[9] We have used the convolution theorem, $\int \mathrm{d}\mathbf{r}'\, g(\mathbf{r}')f(\mathbf{r}-\mathbf{r}') = f * g = \mathcal{F}^{-1}\left[\tilde{f}(\mathbf{k})\,\tilde{g}(\mathbf{k})\right]$, where $\tilde{f}(\mathbf{k})$ and $\tilde{g}(\mathbf{k})$ are the Fourier transforms of the functions $f(\mathbf{r})$ and $g(\mathbf{r})$, and $f * g$ is their convolution product.

[10] This is why we defined the Fourier transform with the same phase as in the FFTW3 algorithm.

Then one can define the dimensionless parameter

$$\varepsilon_{\mathrm{dd}} = \frac{a_{\mathrm{dd}}}{a_s} = \frac{C_{\mathrm{dd}}}{3g} = \frac{g_{\mathrm{dd}}}{g}\,, \tag{3.18}$$

which gives the relative strength of the interactions, and where we have defined $g_{\mathrm{dd}} = C_{\mathrm{dd}}/3$.

In addition, the oscillator length (2.23) will also be a relevant length scale when confining the system along the polarization direction of the dipoles (see Subsection 3.1.3). For instance, in quasi-2D systems the oscillator length associated to the tight confinement will be particularly relevant for the stability and formation of periodic structures in these systems (see also Section 3.2 and Chapter 7).

3.1.2 Ground-state properties

The interplay between the interactions and the geometry of the trapping potential plays a crucial role in the stabilization of the system. We will begin by discussing the untrapped system and its collapse, and then introduce a confinement with cylindrical symmetry that allows us to calculate the ground state of the system in the Thomas–Fermi limit. Later we will explore two novel properties of dipolar condensates: magnetostriction (i.e., the elongation of the gas due to interactions when confined), and the stabilization effect of the confinement. Comparisons with the nondipolar case (i.e., with only contact interactions) will be discussed during the whole subsection (see Chapter 2 for reference).

Collapse of a uniform dipolar gas

The anisotropy of the dipole–dipole interactions means that the interactions are attractive along the z direction (the polarization of the dipoles) and repulsive along the x and y directions. As a result, a purely dipolar (with no contact interactions) unconfined gas is unstable, since the attractive part of the interactions drives the system to collapse. This effect is usually called a *global collapse*, and originates from the phonon instability (see discussion on the spectrum of excitations in Subsection 3.1.3). However, the presence of repulsive contact interactions may stabilize the system if confined, and a trapping potential in itself may also prevent collapse, as in the nondipolar case. In the last case, the situation is more nuanced due to the dipole–dipole interactions.

The onset of this mechanical instability, in a uniform gas, is determined by the parameter $\varepsilon_{\mathrm{dd}}$, which characterizes the relative strength of the dipolar interactions compared to the contact interactions. The value $\varepsilon_{\mathrm{dd}} = 1$ will set the upper limit for stability. For a larger $\varepsilon_{\mathrm{dd}}$ (i.e., for stronger dipolar interactions), the contact interactions are not enough to counterbalance the attractive effect of the dipolar interactions and the system becomes unstable. While here we will assume that quantum fluctuations are negligible and that the system can be described within the mean-field regime, in Section 3.2 we will see that in the unstable regime quantum fluctuations can stabilize the system and lead to the formation of droplets, as occurs with binary mixtures (see Chapter 2).

In the following we will focus on dipolar condensates with both contact and dipolar interactions (unless said otherwise), and we will also confine the system to discuss the effect of geometry in its ground state and stability.

Anisotropic trapping

Let us consider a general anisotropic confinement to address trapped systems. Given the symmetry of the dipole–dipole interactions, one can choose cylindrical symmetry with respect to the z axis (i.e., the direction of the dipoles). We will refer to the xy confinement as *transversal* or *radial* confinement, with frequency $\omega_x = \omega_y = \omega_\rho$ and radial coordinate $\rho^2 = x^2 + y^2$, and to the z confinement, with frequency ω_z, as *axial* confinement. The trapping potential reads,

$$V_{\text{ext}}(\mathbf{r}) = \frac{1}{2} m \left(\omega_\rho^2 \rho^2 + \omega_z^2 z^2 \right) . \tag{3.19}$$

The trap anisotropy (or aspect ratio) is usually defined as $\lambda = \omega_z/\omega_\rho$, and describes three possible geometries that determine the shape of a nondipolar BEC:

- For a *spherical* geometry ($\lambda = 1$), the condensate is spherically symmetric.
- For an *oblate* geometry ($\lambda > 1$), the condensate is pancake-shaped: a disk in the xy plane, with a tighter confinement along the z direction.
- For a *prolate* geometry ($\lambda < 1$), the condensate is cigar-shaped, with z the trap's long axis.

Unlike nondipolar gases, dipolar gases will not follow exactly the shape of the trap, and the geometry of the confinement will play a crucial role in the stability of the system.

Before discussing those properties, it is useful to introduce here the Thomas–Fermi approximation to characterize the effect of magnetostriction, which is the elongation of the cloud in the presence of anisotropic interactions.

Thomas–Fermi limit

If the number of atoms is very large and the interactions are sufficiently strong, the quantum pressure term (i.e., the kinetic energy) becomes negligible compared to the interactions (Pitaevskii and Stringari, 2016). This is known as the *Thomas–Fermi limit* or *approximation* (see Subsection 2.1.2 in Chapter 2). The time-independent GPE (3.13) in this limit reads

$$V_{\text{ext}}(\mathbf{r}) + g n(\mathbf{r}) + \int d\mathbf{r}' \, U_{\text{dd}}(\mathbf{r} - \mathbf{r}') \, n(\mathbf{r}') = \mu \, . \tag{3.20}$$

While solving this equation for the nondipolar case is straightforward, the GPE is now nonlocal due to the dipolar interactions. As a consequence, this leads to a transcendental equation in the Thomas–Fermi limit, with no analytical solution, for the aspect ratio of the condensate κ (Eberlein et al., 2005; O'Dell et al., 2004; Parker and O'Dell, 2008):

$$\frac{\kappa^2}{\lambda^2} \left[\frac{3\varepsilon_{\text{dd}} f(\kappa)}{1 - \kappa^2} \left(\frac{\lambda^2}{2} + 1 \right) - 2\varepsilon_{\text{dd}} - 1 \right] = \varepsilon_{\text{dd}} - 1 \, . \tag{3.21}$$

The aspect ratio of the condensate (or condensate anisotropy) is defined as $\kappa = R_\rho/R_z$, where R_ρ and R_z are the Thomas–Fermi radii in the radial and axial directions and characterize the widths of the condensate. The function $f(\kappa)$ comes from integrating

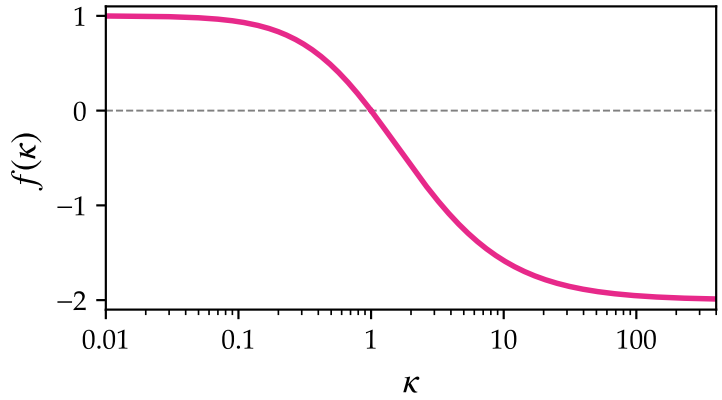

Figure 3.1: Behavior of $f(\kappa)$, defined in Eq. (3.22), as a function of the aspect ratio of the condensate κ. The function is approximately 1 (positive) for $\kappa < 1$ and tends to -2 (negative) for $\kappa \gg 1$. The horizontal axis is in logarithmic scale for clarity.

the angular part of the dipolar potential,

$$f(\kappa) = \frac{1+2\kappa^2}{1-\kappa^2} - \frac{3\kappa^2 \operatorname{arctanh}\sqrt{1-\kappa^2}}{(1-\kappa^2)^{3/2}}\,, \tag{3.22}$$

and, as Fig. 3.1 shows, it decreases monotonically from $f(\kappa \to 0) = 1$ for prolate traps to $f(\kappa \to \infty) = -2$ for oblate traps, with a zero crossing at $\kappa = 1$.

Note that in the absence of dipole–dipole interactions, Eq. (3.21) reduces to a very simple form, $\kappa^2/\lambda^2 = 1$ (we recall that $\lambda = \omega_z/\omega_\rho$), which corresponds to a BEC with only contact interactions: the distortion of the condensate follows that of the trap. In dipolar condensates, however, the aspect ratio κ depends on the strength of the dipolar interactions, so the shape of the condensate inherits the anisotropy of the dipolar interactions. And, unlike in the nondipolar case, the condensate anisotropy is not only determined by the confinement, but also by the strength of the interactions.

Similar to the nondipolar case, the ground state in the Thomas–Fermi limit takes the form of an inverted parabola, but it is distorted by the anisotropy of the interactions. The solution is characterized by the density

$$n(\rho, z) = n_0 \left[1 - \frac{\rho^2}{R_\rho^2} - \frac{z^2}{R_z^2}\right]\,, \tag{3.23}$$

where the central density, $n_0 = 15N/(8\pi R_\rho^2 R_z)$, is a constant given by normalization.

While the density $n(\rho, z)$ (3.23) is the same for both nondipolar and dipolar BECs, the Thomas–Fermi radii R_z and R_ρ (i.e., the widths of the condensate) are different for

the dipolar case,

$$R_\rho = \left[\frac{15gN\kappa}{4\pi m\omega_\rho^2}\left\{1+\varepsilon_{\rm dd}\left(\frac{3}{2}\frac{\kappa^2 f(\kappa)}{1-\kappa^2}-1\right)\right\}\right]^{1/5}, \tag{3.24}$$

and $R_z = R_\rho/\kappa$.

One can obtain equivalent results (Giovanazzi et al., 2003) for κ (3.21) by using a Gaussian ansatz (see for instance Góral and Santos, 2002; Yi and You, 2000, 2001). However, both approaches are only useful when describing a ground state with a maximum density at the center of the trap, which will not always be the case in dipolar gases (e.g., the red blood cell structure).

Geometric stabilization and magnetostriction

Trapped dipolar gases present two properties that are not shared by nondipolar systems (i.e., with only contact interacitons), as we will discuss now.

First, the dipolar interactions tend to elongate the condensate along the direction of the dipoles due to the attractive part of the interactions (see for instance Góral et al., 2000; Santos et al., 2000; Stuhler et al., 2005). This effect is known as *magnetostriction* (or *electrostriction* for electric dipoles), and is given by a difference between the aspect ratios of the condensate κ and the trap λ (i.e., the condensate is more elongated than the trap), as one can see from Eq. (3.21), since $\kappa \neq \lambda$. This elongation effect can be understood, for example, by considering the dipolar contribution to the energy in the Thomas–Fermi limit. Replacing the Thomas–Fermi density (3.23) into the energy functional (3.15), one finds

$$E_{\rm dd} = -\frac{15}{7}\frac{N^2\hbar^2 a}{m}\frac{\varepsilon_{\rm dd}}{R_\rho^2 R_z} f(\kappa) = -\frac{4}{7}\frac{n_0 N}{2}\,\varepsilon_{\rm dd}\, g\, f(\kappa)\,, \tag{3.25}$$

where the function $f(\kappa)$, Eq. (3.22), captures the anisotropic nature of the interactions (see Fig. 3.1). One can see from Eq. (3.25) and Fig. 3.1 that the dipolar energy is reduced by decreasing κ, which means elongating the trap along z.

Similarly to nondipolar condensates, the presence of a trapping potential may stabilize the system against collapse, but for dipolar condensates the geometry of the confinement is crucial when determining the stability of the system (see for instance Bohn et al., 2009; Koch et al., 2008). Considering dipoles polarized along the z axis, we can discuss the stability of the system for the three geometries introduced before:

- *Spherical trap* ($\lambda = 1$). The cloud elongates along the direction of the dipoles due to magnetostriction. The system is stable unless the dipole–dipole interactions are so strong that the attractive part of the interaction dominates and drives the system to collapse. In this case, a repulsive contact interaction can compensate the attractive part and stabilize the system.

- *Prolate trap* ($\lambda < 1$). If the trap is cigar-shaped and longer along the polarization direction, it forces the dipoles to align in a head-to-tail configuration. As a result,

the dipolar interactions are mainly attractive, and the system collapses towards the center of the trap unless a strong repulsive contact interaction prevents it.

- *Oblate trap* ($\lambda > 1$). The confinement along the direction of the dipoles is tighter than in the other directions and the trap has the shape of a disk. Confining more strongly along the polarization direction will cause the dipoles to be mostly side by side. Then, the effective dipolar interactions are mainly repulsive, and the system is thus stable in most cases. It can still collapse, however, but it will be a *local* collapse instead of a global one caused by the presence of a roton minimum in the excitation spectrum (see Subsection 3.1.3).

Due to the interplay between the anisotropy of the interactions and the trap, ground states that exhibit spontaneous symmetry breaking[11] emerge for certain aspect ratios of the trap. An example of such ground states is the biconcave (i.e., red blood cell) structure one can find in pancake traps (Martin and Blakie, 2012). These exotic ground states cannot be described within the Thomas–Fermi approximation, and require instead a numerical approach.

Henceforward, we will consider either spherical or oblate traps ($\lambda \geq 1$) such that the condensate is stable against the global collapse caused by the attractive part of the interactions.

3.1.3 Elementary excitations and instabilities

In the last subsection we saw that the system can exhibit a global (mechanical) collapse when the attractive part of the interaction dominates. We also mentioned a second possible instability due to a tight confinement along the polarization of the dipoles that may lead to local collapses in the condensate. These two instabilities are often called phonon and roton instabilities due to their different origin, and we will discuss them here by analyzing the excitation spectra in different settings.

Phonon instability in a three-dimensional uniform gas

Let us consider first a uniform gas (i.e., with no external confinement) with density n_0. The spectrum of excitations can be calculated by performing the standard Bogoliubov analysis, as we did in Subsections 2.1.1 and 2.2.1 for the nondipolar scalar case and for the binary mixture, respectively (Bogoliubov, 1947),

$$(\hbar\omega)^2 = \frac{\hbar^2 k^2}{2m}\left[\frac{\hbar^2 k^2}{2m} + 2n_0\tilde{V}(\mathbf{k})\right] . \tag{3.26}$$

Equation (3.26) is analogous to the nondipolar case (2.31) with the $2n_0 g$ term replaced by $2n_0\tilde{V}(\mathbf{k})$, where $\tilde{V}(\mathbf{k})$ is the Fourier transform of the whole interaction potential (3.10).

[11] In other words, with structures that differ from those with a central maximum density, as the Thomas–Fermi solution or a Gaussian ansatz.

Then, introducing the Fourier transform of the dipolar interactions $\tilde{U}(\mathbf{k})$ as defined by Eq. (3.9), the spectrum of excitations is (Santos et al., 2000)

$$(\hbar\omega)^2 = \frac{\hbar^2 k^2}{2m}\left[\frac{\hbar^2 k^2}{2m} + 2gn_0\left\{1 + \varepsilon_{\rm dd}(3\cos^2\theta_k - 1)\right\}\right] . \tag{3.27}$$

We recall here that θ_k is the angle between $\mathbf{k}$ (i.e., the direction of the excitations) and

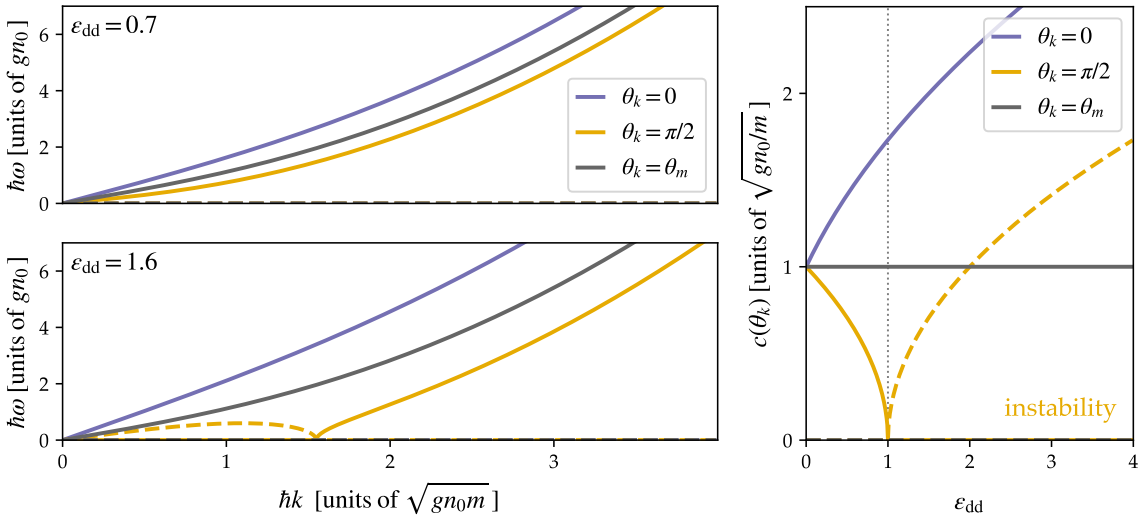

Figure 3.2: Left: excitation spectrum of a 3D uniform gas with dipole–dipole interactions and interaction strength $\varepsilon_{\rm dd} = 0.7$ (top panel) and $\varepsilon_{\rm dd} = 1.6$ (bottom panel). Solid lines correspond to the excitation energies (3.27) for $\theta_k = 0, \pi/2$ and θ_m as labeled by the legend, and the dashed line indicates their imaginary part. We recall that the magic angle θ_m is the angle at which the dipolar interactions vanish such that the system is effectively nondipolar (i.e., contact-interacting only). Right: speed of sound as a function of the parameter $\varepsilon_{\rm dd}$ for the two limit angles ($\theta_k = 0$ and $\pi/2$) and for the magic angle θ_m in solid lines. The dashed line corresponds to the imaginary part of the speed of sound, which becomes nonzero if $\varepsilon_{\rm dd} > 1$ for $\theta_k = \pi/2$. The system is stable for $\varepsilon_{\rm dd} < 1$, which shows in the spectrum as the energies of the excitations are real. However, for $\varepsilon_{\rm dd} > 1$, the slowest mode ($\theta_k = \pi/2$) acquires an imaginary part at low momenta, which corresponds to an imaginary speed of sound, and the system becomes unstable (see further discussion in the main text).

the polarization direction of the dipoles. Thus, even though the system is uniform (isotropic), the spectrum of excitations is anisotropic due to the interactions, as Fig. 3.2 (left) shows.

We recover the same two regimes in terms of the momenta as in the nondipolar case (see discussions in Chapter 2). Excitations show a free-particle behavior in the limit of large momenta and a phononic behavior in the limit of low momenta (see Fig. 3.2, left). Now, however, the frequency of the phonons is $\omega = c(\theta_k)\, k$. Therefore, the angular dependency of the potential in momentum space implies that the speed of sound has an

angular dependence too,

$$c(\theta_k) = \sqrt{\frac{gn_0}{m}}\sqrt{1 + \varepsilon_{\mathrm{dd}}(3\cos^2\theta_k - 1)}\,, \tag{3.28}$$

where $\sqrt{gn_0/m}$ is the speed of sound for the nondipolar case. As a result, the speed of sound is different for excitations propagating at different angles (see Fig. 3.2, right). Considering for instance the two limit cases, one can see the following scenarios (illustrated in Fig. 3.2):

- Excitations that propagate along the direction of the dipoles ($\theta_k = 0$) have the highest speed of sound, and their frequency and speed of sound are always real. They are the most energetic modes and are often called *hard modes*.
- Excitations that instead propagate perpendicular to the direction of the dipoles ($\theta_k = \pi/2$) have the lowest possible speed of sound. They are the least energetic ones and are usually referred to as *soft modes*. These modes can have imaginary frequencies for some parameters, which destabilize the system.

For the magic angle $\theta_m = \arccos(1/\sqrt{3})$, the dipole–dipole interactions vanish and the system only presents contact interactions.

The speed of sound (3.28) for the slowest excitations (the most unstable, i.e., with $\theta_k = \pi/2$) is zero when $\varepsilon_{\mathrm{dd}} = 1$ and becomes imaginary for $\varepsilon_{\mathrm{dd}} > 1$, as shows Fig. 3.2 (right). When the frequencies of these excitations become imaginary, the system is unstable and a global collapse occurs. Since this instability happens at low momenta (large wavelengths), it is often called the *phonon instablity*, as in the case of nondipolar condensates (see Subsection 2.1.2 in Chapter 2).

The phonon instability then is a mechanical instability that comes from the attractive part of the interactions, and leads to a global collapse of the system towards the center of the trap. Here we have studied this instability on an isotropic gas, but the stability will change significantly when adding in the anisotropy of the confinement. Moreover, as we will see next, this global collapse will also occur in cigar-shaped condensates with the dipoles oriented along the large axis.

Collapse in a confined gas

The conditions for the interaction strengths under which mechanical collapse occurs can also be studied in terms of the ground state energies[12]. For a condensate confined in an external potential and in the Thomas–Fermi limit, the kinetic and potential energies can be neglected, such that the total energy will only have two contributions[13]: the

[12] See Koch et al. (2008); they use a Gaussian ansatz instead of a Thomas–Fermi profile as we do here, but the discussion is the same.

[13] The mean-field energies scale with N^2 (note that $n_0 \propto N$) while the kinetic and potential energies are linear with N, and therefore the last two are negligible for large enough N.

contact and dipolar interactions. Using a Thomas–Fermi profile (3.23), Eq. (3.25) gives the dipolar energy, which we rewrite here,

$$E_{\mathrm{dd}} = -\frac{2}{7} n_0 N g \, \varepsilon_{\mathrm{dd}} \, f(\kappa) \,, \tag{3.29}$$

and the energy contribution of the contact interactions is

$$E_c = \frac{2}{7} n_0 N g. \tag{3.30}$$

Then, the total energy is

$$E = \frac{2}{7} n_0 N g \left[1 - \varepsilon_{\mathrm{dd}} \, f(\kappa)\right] \,, \tag{3.31}$$

where $\varepsilon_{\mathrm{dd}} = a_{\mathrm{dd}}/a_s$ (3.18). We consider the case of $g < 0$, which is the situation that leads to collapse. The total energy E must be negative to minimize the energy, and this gives the condition for instability:

$$a_s < a_{\mathrm{dd}} \, f(\kappa) \,. \tag{3.32}$$

Depending on the trap anisotropy we can have two different scenarios:

1. For cigar-shaped traps ($\lambda < 1$), as discussed earlier, the dipoles tend to be head to tail, which means that $\kappa \ll 1$ and thus the dipolar interactions are mostly attractive. In this case (see Fig. 3.1), $f(\kappa) \approx 1$, and from the above condition (3.32) we find that the condensate is stable if $a_s > a_{\mathrm{dd}}$. Notice that this condition corresponds to the $\varepsilon_{\mathrm{dd}} < 1$ condition for stability that we discussed in the unconfined case.

2. In the opposite situation of pancake-shaped traps with $\lambda \gg 1$, the attractive part of the interaction is mostly suppressed by the confinement and the repulsion between dipoles is twice as strong as is the attractive interaction, $f(\kappa) \approx -2$ (see Fig. 3.1). In this case, a_s must fulfill that $a_s < -2a_{\mathrm{dd}}$ for the condensate to be stable.

We will focus on this last scenario next.

Roton instability in a quasi–two-dimensional condensate

In the 3D homogeneous case, we saw that the dipolar interactions introduce an angular dependence into the excitation spectrum (3.27). However, in a quasi-2D condensate, the excitation spectrum may not only depend on the angle θ_k but also on the modulus of $\mathbf{k}$. This can happen when the interactions are strong enough that, despite being quasi-2D, the system starts to feel the 3D nature of the dipolar interactions. The resulting spectrum is known as *roton–maxon spectrum* (O'Dell et al., 2003; Santos et al., 2003), and leads to a new type of instability, the *roton instability*.

Let us consider a uniform system confined only along the polarization direction of the dipoles (there is no transversal confinement). The confinement along z is tight enough such that the system is quasi-2D but the atoms are still allowed to move in the z direction (the trap's length scale is much larger than the length scales that characterize

the interactions). The trap along z introduces a new length scale that becomes relevant in the physics of the system, which will translate into a favored momentum in the dispersion relation.

One can reduce the dimensionality of the system to 2D when $\mu \ll \hbar\omega_z$ (see Chapter 2) such that the degrees of freedom that correspond to the z coordinate are frozen. However, the roton instability occurs for $\mu \gg \hbar\omega_z$ (i.e., the Thomas–Fermi regime), where we have considered a system confined in z, so that the standard approach is no longer valid[14]. However, we can still use an effective quasi-2D approach to understand the appearance of a roton minimum and its associated instability (Lahaye et al., 2009).

To reduce the problem to a quasi-2D regime (see a detailed discussion in Ticknor et al., 2011), we consider a Gaussian ansatz[15] for the z direction,

$$\chi(z) = \frac{1}{a_z\sqrt{\pi}} \exp\left(-\frac{z^2}{a_z^2}\right), \tag{3.33}$$

with a_z the oscillator length (2.23), so that the condensate wavefunction can be then approximately factorized as $\Psi(\mathbf{r}, t) = \chi(z)\,\psi(\rho, t)$. Calculating the 2D Fourier transform of the dipolar potential with the factorized wavefunction yields

$$\tilde{U}_{\rm dd}(k_\rho) = \frac{g_{\rm dd}}{a_z\sqrt{2\pi}} F_{\rm 2D}\left(k_\rho \frac{a_z}{\sqrt{2}}\right), \tag{3.34}$$

where $\mathbf{k}_\rho$ is the wavevector in the transversal plane (with modulues k_ρ) and $g_{\rm dd}$ is the usual 3D dipolar coupling constant, $g_{\rm dd} = C_{\rm dd}/3$. The function $F_{\rm 2D}$ is given by

$$F_{\rm 2D}(q) = 2 - 3q\sqrt{\pi}\exp(q^2)\,\mathrm{erfc}(q), \tag{3.35}$$

with $\mathrm{erfc}(q)$ the complementary error function and $\mathbf{q} = \mathbf{k}_\rho\, a_z/\sqrt{2}$ (see Fig. 3.3, top panel, for more details). Unlike in the 3D homogeneous case (3.9), the 2D Fourier transform (3.34) depends on the modulus of $\mathbf{k}_\rho$.

With this, the dispersion relation (3.26) reads

$$(\hbar\omega)^2 = \frac{\hbar^2 k_\rho^2}{2m}\left[\frac{\hbar^2 k_\rho^2}{2m} + 2g_{\rm 2D}\, n_{\rm 2D}\left\{1 + \varepsilon_{\rm dd} F\left(k_\rho \frac{a_z}{\sqrt{2}}\right)\right\}\right], \tag{3.36}$$

[14] The roton instability appears in different regimes for attractive or repulsive contact interactions in pancake-shaped condensates. If $g > 0$, it occurs when $\mu \gg \hbar\omega_z$ (as stated in the main text) and the quasi-2D approach is not valid. In this case, the condensate has a Thomas–Fermi density profile along z, and the instability comes from attractive part of the dipolar interactions at large momenta (i.e., the system feels the 3D nature of the interaction). If $g < 0$, on the other hand, the roton instability can appear for $\mu \ll \hbar\omega_z$ (so that the usual 2D approach is valid), and the condensate has a Gaussian profile in z. In this case, this 2D-roton originates from the attractive nature of the contact-interactions, i.e., $g < 0$, and a stronger dipolar interaction can stabilize the system (for more details, see Lahaye et al., 2009, and references therein).

[15] Alternatively, one can also consider a Thomas–Fermi profile instead (see for instance Santos et al., 2003). The quantitative results depend on the density profile that one chooses for the axial direction, but the qualitative argument is the same.

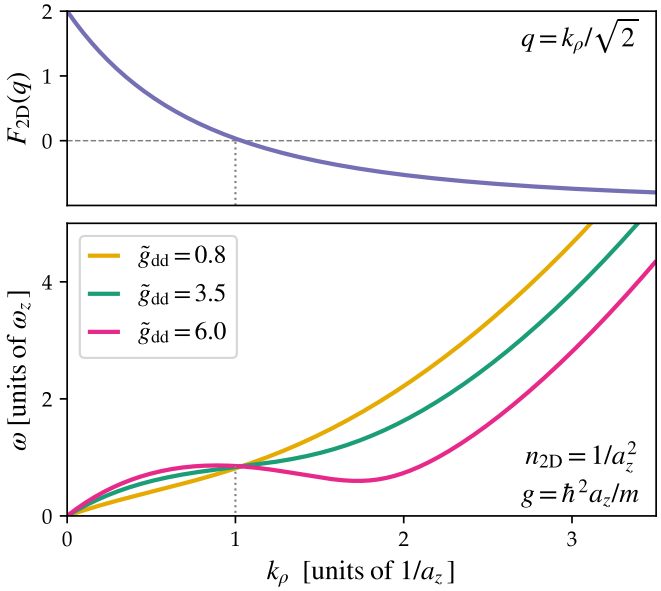

Figure 3.3: Roton–maxon spectrum (bottom panel) and 2D Fourier transform of the dipole–dipole potential (top panel) for a quasi-2D dipolar gas confined along the polarization direction z. All quantities are given in units of a_z, the oscillator length associated to the axial confinement. The Fourier transform F_{2D} (top panel) portrays the behavior of the interactions, which change sign at $k_\rho \approx 1/a_z$. The excitation spectrum (bottom) shows the energy for different strengths of the dipolar interactions, characterized here by the dipolar coupling constant $g_{dd} = \tilde{g}_{dd}\hbar^2 a_z/m$. For illustrative convenience, we have defined the 2D density as $n_{2D} = 1/a_z^2$ and the contact coupling constant as $g = \hbar^2 a_z/m$. For small values of the dipolar coupling constant (cases with $\tilde{g}_{dd} = 0.8$ and 3.5), the dispersion relation has the usual monotonic shape, with the phonon and free-particle regimes for low and high momenta, respectively. However, if the dipolar interactions are strong enough ($\tilde{g}_{dd} = 6$ case), the excitation spectrum shows a local maximum followed by a local minimum at a finite k_ρ, and is thus often referred to as *roton–maxon spectrum* as in liquid helium. Note that in this last case the two limits (phonon and free-particle dispersion) are still present.

where n_{2D} is the average 2D density (in the plane) and n_0 is the total average density such that $n_0 = n_{2D}/(a_z\sqrt{2\pi})$. The 2D coupling constant is $g_{2D} = g/(a_z\sqrt{2\pi})$, with g the 3D coupling constant.

As in both the dipolar uniform case and the nondipolar case, the excitations behave as phonons at small momenta and as free particles at large momenta (see Fig. 3.3, bottom). However, in some cases a minimum appears in the excitation spectrum due to the Fourier transform (see Fig. 3.3, top) changing its sign: the interaction is repulsive for $k_\rho \ll 1/a_z$ (low momenta), and it is attractive for $k_\rho \gg 1/a_z$ (large momenta). As a result, the dipolar interactions increase the energy in the phononic regime, where the kinetic energy is very small, and reduce it at larger momenta, when the Fourier transform of the dipolar potential becomes attractive. This causes the *roton minimum*. At even larger k_ρ, however, the kinetic energy dominates over the dipolar energy and it increases the energy again towards the free-particle regime.

Since the sign of the Fourier transform changes at $k_\rho = 1/a_z$ (see Fig. 3.3), the wavelength of the roton is set by the confinement along the direction of the attractive part of the dipolar interactions. One can reduce the energy of the roton by increasing either the density or the strength of the dipolar interactions. Then, the *roton instability* appears when the energy becomes zero. The presence of the roton instability will be the onset of density modulations in the condensate, as we will discuss in the next section.

3.2 Dipolar droplets and supersolids

In the last section we introduced dipolar condensates, where the atoms interact via both contact and dipole–dipole interactions, and studied their static properties and stability through a mean-field description. However, similarly to nondipolar gases (Chapter 2), the mean-field approach may no longer be valid at larger densities or stronger interactions, when the quantum fluctuations start to be relevant and deplete the condensate.

Dipolar condensates where beyond mean-field effects are not negligible can be described by a Gross–Pitaevskii equation extended to include the effect of quantum fluctuations (Subsection 3.1.1), as in nondipolar condensates (Chapter 2). Quantum fluctuations can stabilize the system against collapse and give rise to droplets, where the competing interactions are the repulsive contact interactions and the dipole–dipole interactions. This results in a small mean-field contribution that counterbalances the beyond mean-field energy. However, while the stabilizing mechanism of dipolar droplets is the same as in droplets of nondipolar binary mixtures (see Section 2.2.3), the resulting states will have different properties due to the distinct nature of the interactions involved (Subsection 3.1.2).

The presence of an anisotropic external confinement, which has already a crucial effect in the stability of the system (see Subsections 3.1.2 and 3.1.3), can force the droplets to assemble into an array and form a droplet crystal, a behavior that droplets of nondipolar mixtures cannot exhibit. These droplet crystals have no global coherence, since the individual droplets are isolated (i.e., do not overlap) due to the strong repulsion with the other droplets. Between the regular BEC regime and the array of isolated droplets regime, however, there is a region for certain parameters in which the whole crystal may retain the superfluid character of the condensate while showing at the same time crystalline properties. This phenomenon is known as *supersolidity* (Subsection 3.2.3).

3.2.1 LHY correction

The LHY correction comes from the zero-point energy of the excitations (see Chapter 2). Since the presence of dipole-dipole interactions modifies the spectrum of excitations (3.27), the LHY correction is modified as well. For a dipolar condensate, the energy functional with a beyond mean-field correction is

$$E[\psi] = E_{\mathrm{MF}} + \int d\mathbf{r}\, \mathcal{E}_{\mathrm{LHY}}\,, \tag{3.37}$$

where E_{MF} is the mean-field energy functional (3.15). The LHY correction to the energy density (Lima and Pelster, 2011, 2012), calculated for a homogeneous system, is

$$\mathcal{E}_{\mathrm{LHY}} = \frac{2}{5}\, g_{\mathrm{LHY}}\, n^{5/2}\,, \tag{3.38}$$

with n the density of the gas. The strength of the correction g_{LHY} is given by

$$g_{\mathrm{LHY}} = \frac{32}{3\sqrt{\pi}}\, g\, a_s^{3/2}\, Q_5(\varepsilon_{\mathrm{dd}})\,, \tag{3.39}$$

where $Q_5(x)$ is defined as

$$Q_5(\varepsilon_{\mathrm{dd}}) = \frac{1}{2}\int_0^{\pi} d\theta_k \sin\theta_k \left[1 + \varepsilon_{\mathrm{dd}}(3\cos^2\theta_k - 1)\right]^{5/2} \approx 1 + \frac{3}{2}\varepsilon_{\mathrm{dd}}^2\,. \tag{3.40}$$

The approximation in Eq. (3.40) is valid for small values of $\varepsilon_{\mathrm{dd}}$, as shown in Fig. 3.4 (dotted line). The function $Q_5(\varepsilon_{\mathrm{dd}})$ is a monotonic function (see Fig 3.4) that comes from the averaged contribution of the dipole–dipole interactions. As opposed to the mean-

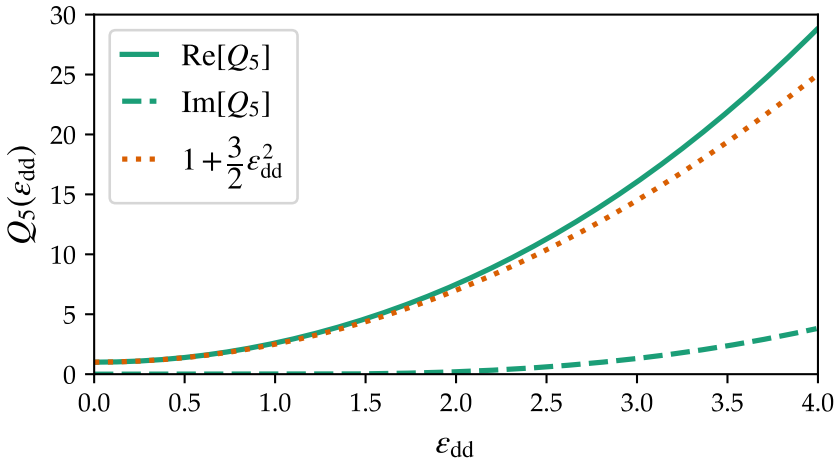

Figure 3.4: Averaged contribution of the dipole–dipole interactions, given by $Q_5(\varepsilon_{\mathrm{dd}})$ (3.40). The solid line is the real part of the function while the dashed line corresponds to its imaginary part, which increases with $\varepsilon_{\mathrm{dd}}$. Note, however, that it is very small, and can be neglected if $\varepsilon_{\mathrm{dd}} \lesssim 3$. The dotted line indicates the function $1 + 3\varepsilon_{\mathrm{dd}}^2/2$, which approximates $Q_5(\varepsilon_{\mathrm{dd}})$ for small values of $\varepsilon_{\mathrm{dd}}$.

field energy terms, Q_5 depends on the relative strength of the two competing interactions (contact and dipolar), $\varepsilon_{\mathrm{dd}} = a_{\mathrm{dd}}/a_s$, and not on their individual contributions. Therefore, the LHY correction is always repulsive, and note that it grows with a power 5/2 of the density n, as opposed to the n^2 dependence of the mean-field contributions.

The LHY correction to the energy (3.38) is strictly valid only for $\varepsilon_{\mathrm{dd}} < 1$, since for larger values the homogeneous system is unstable due to the phonon instability. In this unstable regime, Q_5 acquires an imaginary part (see Fig. 3.4). However, for the range of interactions usually considered ($\varepsilon_{\mathrm{dd}} \lesssim 3$), this imaginary part is very small, and one can neglect it in the theoretical description and use Eq. (3.38) nonetheless.

Extended Gross–Pitaevskii equation

Similarly to the nondipolar case (see Chapter 2), the LHY correction (3.38) is calculated for a homogeneous system and one considers two assumptions to extend the mean-field description using the corrected energy (3.37). First, that all the atoms are in the condensate. The correction accounts for the energy shift due to excitations, but the quantum depletion is still very small and one can neglect it. Second, that the density varies slowly enough so that one can calculate the energy shift locally, for a given $n(\mathbf{r})$, which is known as *local density approximation* (LDA). The LDA is valid even beyond the instability, and it is a good approximation as long as the droplet remains elongated (Wächtler and Santos, 2016b). Given these two conditions, the local correction to the chemical potential reads

$$\mu_{\rm LHY} = \frac{\partial \mathcal{E}_{\rm LHY}}{\partial n} = g_{\rm LHY}\, n^{3/2}(\mathbf{r}) = g_{\rm LHY}|\psi(\mathbf{r})|^3 \,. \tag{3.41}$$

Then, the time-dependent GPE for dipolar gases (3.12) can be extended by including the $\mu_{\rm LHY}\,\psi(\mathbf{r},t)$ term,

$$\begin{aligned} i\hbar\frac{\partial\psi(\mathbf{r},t)}{\partial t} \;=\; & \left[-\frac{\hbar^2\nabla^2}{2m} + V_{\rm ext}(\mathbf{r}) + g|\psi(\mathbf{r},t)|^2 \right. \\ & \left. + \int d\mathbf{r}'\, U_{\rm dd}(\mathbf{r}-\mathbf{r}')\,|\psi(\mathbf{r}',t)|^2 + g_{\rm LHY}|\psi(\mathbf{r},t)|^3\right]\psi(\mathbf{r},t)\,. \end{aligned} \tag{3.42}$$

This formalism allows us to study the main static and dynamic properties of dipolar self-bound droplets, as we will see next.

3.2.2 Self-bound dipolar droplets

Quantum fluctuations can prevent the collapse predicted by the mean-field formalism. This stabilizing mechanism is intrinsic to the system and leads to a quantum droplet, which is much more dilute than an ordinary liquid but denser than a condensate that is stable in the mean-field regime. Due to the higher density of droplets as compared with the mean-field condensate, three-body losses are the main decay mechanism and hugely limit the lifetimes of droplets.

In the last chapter, we reviewed the main properties of quantum droplets in nondipolar binary mixtures (see Section 2.2). Here we will focus on droplets of dipolar condensates (Böttcher et al., 2021; Chomaz et al., 2022) and remark the main differences with their nondipolar counterparts.

Dipolar droplets were first observed experimentally with ^{164}Dy atoms (Ferrier-Barbut et al., 2016a,b; Kadau et al., 2016) and later described theoretically (Bisset et al., 2016; Wächtler and Santos, 2016a), and are also self-bound solutions, i.e., they exist without need of confinement (Baillie et al., 2016). One fundamental difference with nondipolar droplets is that, due to the anisotropy of the dipole–dipole interactions, the binding mechanism of dipolar droplets is also anisotropic. This results in two important consequences, as illustrated in Fig. 3.5:

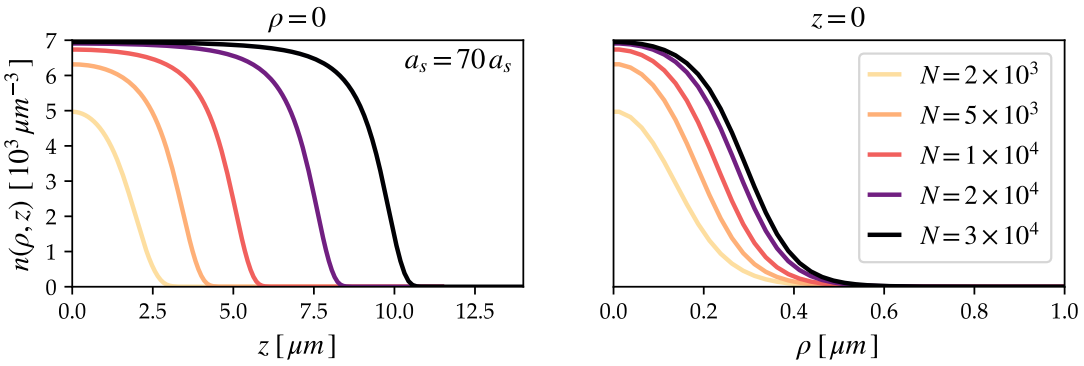

Figure 3.5: Density of a self-bound dipolar droplet along the radial (ρ) and axial (z) coordinates for different atom numbers, calculated by numerically solving the extended GPE. We considered a gas of N dysprosium atoms with scattering length $a_s = 70\,a_0$, and atom numbers ranging from 2000 to 30000. The density along the z direction (left panel) saturates after a certain number of atoms is reached, but such saturation does not occur along the ρ direction (right panel).

1. The droplets are elongated along the axial direction (i.e., the polarization direction), since the interactions are effectively attractive in that direction, so it is more favorable for the system to add more particles along the axial direction than in the transversal directions, where the dipolar interactions are instead repulsive.

2. The liquid-like saturation of the peak density only occurs along the axial direction, as shown in Fig. 3.5. In the transversal directions, on the other hand, the interactions are mostly repulsive, and the density does not saturate.

Once saturation occurs in the axial direction, as with nondipolar droplets, increasing further the number of atoms does not change the peak density but leads to an increase in the size of the droplet. The saturation value is independent of the number of atoms, as in nondipolar droplets.

Droplets form at the density for which the mean-field and beyond mean-field contributions balance. This density is the equilibrium density, and one can define it by neglecting the kinetic energy and using a Gaussian ansatz (Chomaz et al., 2022; Ferrier-Barbut et al., 2016a),

$$n_0 = \frac{\pi}{a_s^3}\left(\frac{\varepsilon_{\rm dd}\, f(\kappa) - 1}{16 Q_5(\varepsilon_{dd})}\right)^2 , \tag{3.43}$$

where $f(\kappa)$ is defined by Eq. (3.22). From Eq. (3.43) one can deduce that the droplet is ultradilute, i.e., $n_0\, a_s^3 \ll 1$. This occurs because the effective mean-field interactions $\varepsilon_{\rm dd}\, f(\kappa) - 1$ are very small, and because the beyond mean-field contribution, $Q_5(\varepsilon_{dd})$, is much larger.

The critical (i.e., minimum) atom number that dipolar droplets require to be self-bound is also determined by the balance between the binding mechanism and the kinetic energy, such that it depends on the strength of the interactions. The kinetic energy

prevents the formation of self-bound droplets if the number of atoms is too small, but for a large number of atoms the interactions dominate and the effect of the kinetic energy is negligible.

Finally, in dipolar droplets, there is at least one collective mode below the particle emission threshold (Baillie et al., 2017; Böttcher et al., 2021) and, as a result, dipolar droplets do not exhibit self-evaporation[16].

3.2.3 Anisotropically confined droplets

The external confinement plays a critical role in the stability and properties of the system even when quantum fluctuations are negligible (see discussion in Section 3.1). Here we will discuss the effect of an anisotropic trapping on dipolar droplets when quantum fluctuations become relevant. Even though dipolar droplets are self-bound objects and thus do not need an external confinement to exist, the presence of such a trapping may lead to the emergence of density-modulated states (i.e., crystals of droplets) that, in some cases, can exhibit supersolid properties. This occurs specially if the confinement along the polarization direction is tight.

The density of a dipolar droplet shows a weak dependence on the trapping potential: while a BEC that is stable in the mean-field regime adapts to the trap (see Subsection 3.1.2), dipolar droplets are always markedly elongated. However, the confinement does play a role in the nature of the transition from a mean-field BEC (a low-density state) to a self-bound droplet (a high-density state) when changing the scattering length a_s. For a fixed small atom number N, of the order of 10^4, and a shallow confinement (Bisset et al., 2016; Chomaz et al., 2022; Wächtler and Santos, 2016a), the phase diagram in terms of the scattering length a_s and the aspect ratio of the trap $\lambda = \omega_z/\omega_\rho$ defines two regions:

- In cigar-shaped traps elongated along the polarization direction ($\lambda < 1$) and in slightly oblate traps ($\lambda \gtrsim 1$), the BEC and droplet regimes are connected through a crossover. The transition is smooth because the trap and the elongation (which is caused by the anisotropy of the dipole–dipole interactions) both favor similar geometries.

- In pancake-shaped traps ($\lambda > 1$), this transition is discontinuous and presents an intermediate bistable region in which both solutions (the BEC and the droplet) are local minima in the energy.

Therefore, one can explore this transition (and the two regions) by changing the geometry of the trap (varying thus the aspect ratio λ).

Droplet crystals

For systems with more atoms or with a tighter axial confinement, the phase diagram is different. The bistability region is instead populated by a continuum of density-modulated states with different number of droplets, i.e., droplet crystals (Kadau et al.,

[16] As we discussed on Chapter 2, for a particular regime of atom numbers, a droplet of a nondipolar binary mixture cannot sustain excitations and instead evaporates partially to form a smaller droplet.

2016), and with a large shot-to-shot variability. This occurs because starting from a mean-field BEC in the bistable region (above a given critical λ) and lowering the scattering length leads to a modulational instability (Ferrier-Barbut et al., 2018b). Since the BEC–droplet transition in this region is discontinuous, these states are metastable: the system cannot follow the ground state and instead breaks into smaller droplets.

However, droplet crystals (i.e., density-modulated states) can in fact be the ground state of a dipolar gas (Baillie and Blakie, 2018) for a large enough number of atoms. Compressing an isotropic droplet (either classical or quantum) deforms it to keep the density constant. In dipolar droplets, however, the binding mechanism is anisotropic, and compressing the droplet along the polarization direction has a large energy cost due to the dipolar interactions. This leads to the frustration of the droplet, since it becomes favorable for the system to break into smaller droplets. Then, the smaller droplets arrange into crystals[17] due to the repulsion between their dipoles, and thus the ground state of the system can form spontaneous density modulations.

These arrays break the continuous translational symmetry of the system and, although each individual droplet is superfluid, the crystals as a whole are incoherent, since the droplets are isolated (i.e., the density drops to zero between them).

Supersolids

In some cases, the droplets are not fully isolated but have spatial overlap, such that the system does not lose its global phase coherence. This coherent array of droplets is known as a *supersolid*, since it exhibits at the same time the frictionless flow of a superfluid and the crystal-like periodic density modulation of a solid. In a supersolid, two continuous symmetries of the system are broken (Boninsegni and Prokof'ev, 2012): the translational symmetry (by showing a periodic modulation of the density), and the phase invariance of the condensate (since the system is no longer symmetric under a phase change, i.e., loses its phase coherence). Supersolidity emerges when the breaking of these two symmetries comes from the intrinsic interactions of the system. For a tight axial confinement and a large atom number, supersolid properties exist for a narrow range of scattering lengths close to the transition between the mean-field BEC and the incoherent array of droplets (Chomaz et al., 2019; Roccuzzo and Ancilotto, 2019; Tanzi et al., 2019a). Figure 3.6 shows for comparison the density profiles of a mean-field BEC, a supersolid and a crystal of droplets.

The system will then be supersolid if it exhibits both spatial order and superfluidity, but for superfluidity to be present the system needs to have phase coherence. A strong indication of superfluidity can be obtained by repeated time-of-flight measurements: if the interference patterns show the interference of multiple droplets, then the system presents global phase coherence (Böttcher et al., 2019a). This does not happen in an incoherent array of droplets. However, spatial order and global phase coherence are not enough to prove superfluidity, and one has to study also the elementary excitations of the system.

[17] These crystals are held together by the external confinement. This will not be the case in crystals of antiparallel dipolar mixtures (see Chapter 7).

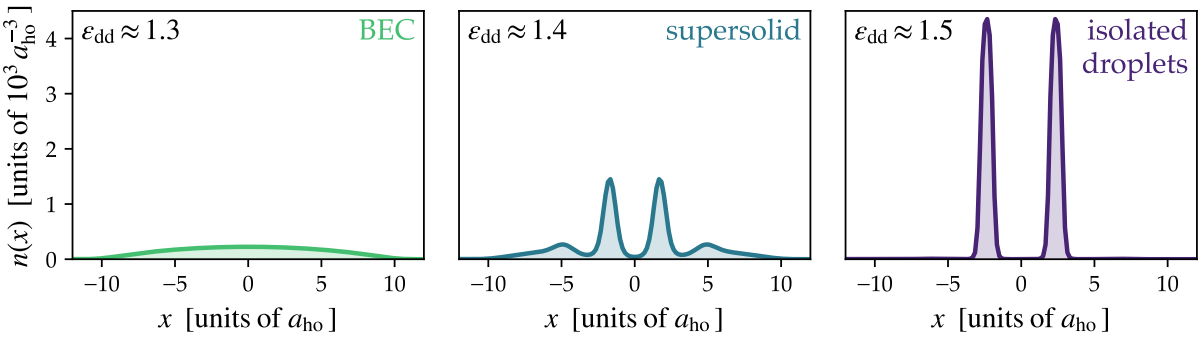

Figure 3.6: Density profiles along the x axis for a mean-field stable BEC (left), a coherent crystal (center), with supersolid properties, and an incoherent crystal (right), where the droplets are isolated. Calculated for a gas of $N \sim 30000$ dysprosium atoms in an anisotropic trap such that $\omega_x < \omega_y \ll \omega_z$ and varying the scattering length $a_s \sim 90\, a_0$ to obtain the three cases. All quantities are in units of a_{ho}, the oscillator length associated to the mean frequency of the trap. Note that the isolated droplets (right) have a much larger density than the mean-field stable BEC (left).

In an axially-confined dipolar system, if the scattering length is small (and thus ε_{dd} is large) the interactions present a momentum dependence that shows in the spectrum of excitations as a minimum at a finite k, called the roton minimum (see Subsection 3.1.3). This minimum corresponds to a perturbative density modulation on top of the condensate. When the roton mode softens (i.e., the roton minimum reaches zero), the system may transition to an array of droplets, since the roton corresponds to a privileged length scale determined by the tight confinement along the polarization direction. In a cigar-shaped condensate, a single roton mode softens, which determines the wavelength of the modulation; in contrast, the situation is more nuanced in pancake-shaped condensates, since there are several angular and radial rotons softening at the same time (Hertkorn et al., 2021a,b; Norcia et al., 2021; Zhang et al., 2021).

Periodic modulations of the density, also referred to as the *stripe phase*, appear also in a miscible two-component mixture with spin–orbit coupling (Li et al., 2017). In that case, however, the modulations are not determined by a favored wavevector as a result of anisotropic interactions within the system, but by an external field.

4

Chiral condensates in rotating rings

The electric and magnetic properties of strongly correlated matter make these materials valuable for many technological applications. However, the experimental realization of these systems is very challenging, and one cannot fully control the gauge fields that emerge naturally in charged systems (e.g., the electron charge is a universal constant). Ultracold gases, on the other hand, present a great degree of experimental and theoretical controllability, and so gases of neutral atoms offer an excellent platform for simulating gauge theories.

In the last decades, there has been a great interest in artificial gauge potentials, which allow charge-neutral ultracold atoms to behave like charged particles in magnetic fields. In such settings, one can fully control the gauge fields imposed on the atoms by external means. Therefore, one can simulate typical effects of electronically charged systems in weakly interacting neutral atoms. In addition, these low-energy platforms could also allow one to explore phenomena so far restricted to high-energy systems.

Artificial gauge potentials can arise in neutral particles either by rotating the system or by engineering geometric phases; the latter one will be the focus of this chapter. In particular, we are interested in density-dependent gauge potentials, which can emerge in a weakly interacting condensate due to the optical coupling of the internal states of the atoms. These gauge fields appear due to the geometrical phases that the system acquires during the adiabatic path of the resulting dressed states. As a result of the light–matter interaction, these condensates can present chiral properties, as we will first introduce in this chapter and then explore in more detail in Chapters 8 and 9. We will consider the cases of a scalar and a linearly coupled condensate in a rotating ring, respectively.

In Section 4.1, we will introduce artificial gauge fields and see how one can induce a density-dependent gauge potential in an ultracold Bose gas by means of light–matter interactions. The effective interactions of the resulting system come from the current density and thus present chiral properties. In Section 4.2, we will focus on the 1D scenario and introduce the 1D chiral theory with a density-dependent gauge potential. This theory will allow us to study condensates with current-density interactions. We will finish this section by considering the particular case of a quasi-1D condensate confined on a ring potential, which presents chiral currents and chiral solitons under rotation.

4.1 Density-dependent gauge potentials in cold atoms

Ultracold atoms are charge neutral and so remain unaffected by electromagnetic fields. However, one can emulate the dynamics of charged particles by engineering artificial gauge fields in ultracold atomic systems.

We will start in Subsection 4.1.1 by presenting the concept of gauge fields through the classical example of electromagnetism. We will then introduce artificial gauge fields in quantum systems, where artificial potentials can emerge from geometric phases when the system follows an adiabatic evolution. In the most common examples of gauge fields, the fields are independent of the properties of matter and are instead imposed externally on the system. Here, we will consider the case of density-dependent potentials, in which the emergent gauge fields depend on the local density of particles. One can engineer these types of gauge potentials in optically coupled ultracold atoms by tuning the light–matter interactions, as we will discuss in Subsection 4.1.2.

4.1.1 Artificial gauge fields

Gauge theories are essential in the understanding of the interactions between elementary particles (Goldman et al., 2014; Lancaster and Blundell, 2014; Zee, 2010). In a gauge theory, the Lagrangian that describes the system is invariant under certain local transformations, known as *gauge transformations*. As a result, the states and observables of the system are also invariant under such transformations (i.e., gauge invariant), which connects with the concept of *gauge symmetries*. Unlike global symmetries, gauge symmetries lead to local conservation laws: they vary from point to point in space and time, and the conservation ensures gauge invariance locally. Thus, the role of a *gauge field* is to preserve the gauge symmetry when particles interact. In electromagnetism, for example, the gauge field is the electromagnetic potential (the vector and scalar potentials), as we will discuss next. In a quantized theory, the *gauge boson* is the quantum of the gauge field, which mediates the interaction and corresponds to the photon in the case of electromagnetism. As a result, matter and the gauge field are coupled through these conservation laws, such as the conservation of the electric charge in electromagnetism.

Electromagnetism

Let us consider the case of electromagnetism as an example (Dalibard, 2016). Electromagnetism describes the interactions between light (an electromagnetic field) and matter[1].

For a static magnetic field $\mathbf{B}(\mathbf{r})$, Gauss's law for magnetism is $\nabla \cdot \mathbf{B} = 0$, which directly implies that magnetic monopoles do not exist. From Gauss's law, one can define the *vector potential* $\mathbf{A}$, the curl of which is the magnetic field $\mathbf{B}$,

$$\nabla \times \mathbf{A} = \mathbf{B}\,. \tag{4.1}$$

[1]The quantum counterpart of electromagnetism is quantum electrodynamics (QED), in which the gauge boson is the photon.

This vector potential is not uniquely defined. Two vector potentials $\mathbf{A}$ and $\mathbf{A}'$ defined such that $\nabla \times (\mathbf{A} - \mathbf{A}') = 0$ correspond to the same magnetic field $\mathbf{B}$ and result in the same physical behavior. Therefore, the vector potential $\mathbf{A}$ associated to a given system is not unique. Using that the curl of a gradient is zero, one can add to the vector potential the gradient of an arbitrary scalar function $\chi(\mathbf{r})$, also called the *scalar potential*, which is not uniquely defined either. Therefore, two vector potentials associated to the same magnetic field are related by the gauge transformation

$$\mathbf{A}'(\mathbf{r}) = \mathbf{A}(\mathbf{r}) + \nabla\chi(\mathbf{r})\,. \tag{4.2}$$

The scalar and vector potentials, χ and $\mathbf{A}$, enter the coupling term between electromagnetic fields and charged matter through the action of the fields[2]. The choice of $\mathbf{A}$ is called a *gauge*, and the *gauge freedom* refers to the redundancy in the gauge choice. The Lagrangian that describes the system depends on the gauge, since the vector potential $\mathbf{A}$ enters into its definition. However, Lagrangian functions that correspond to different gauge choices for the same magnetic field $\mathbf{B}$ only differ by a total time derivative, and thus correspond to the same physical system. For a particle with charge q, velocity $\mathbf{v}$ and mass m, the Hamiltonian corresponding to the Lagrangian function that describes the system is

$$H = \frac{\big(\mathbf{p} - q\mathbf{A}(\mathbf{r})\big)^2}{2m}\,, \tag{4.3}$$

where $\mathbf{p} = m\mathbf{v} + q\mathbf{A}$ is the canonical (conjugate) momentum.

In quantum mechanics, the canonical momentum is $\hat{\mathbf{p}} = -i\hbar\nabla$ and the kinetic (mechanical) momentum[3] is $\hat{\mathbf{\Pi}} = \hat{\mathbf{p}} - q\mathbf{A}(\mathbf{r})$. The particle is now characterized by its wavefunction $\psi(\mathbf{r}, t)$, and the Schrödinger equation,

$$i\hbar\frac{\partial\psi(\mathbf{r},t)}{\partial t} = \frac{\big(-i\hbar\nabla - q\mathbf{A}(\mathbf{r})\big)^2}{2m}\psi(\mathbf{r},t)\,, \tag{4.4}$$

describes its evolution.

A wavefunction ψ that is solution of the Schrödinger equation for a given choice of the vector potential $\mathbf{A}$ will not be a solution of the equation for another gauge choice $\mathbf{A}'$, given by (4.2). Therefore, one has to modify the phase of the wavefunction as well[4], such that a gauge transformation consists in two changes (Dalibard, 2016): Eq. (4.2) for the vector potential, and

$$\psi'(\mathbf{r},t) = \psi(\mathbf{r},t)\exp\left(\frac{iq\chi(\mathbf{r})}{\hbar}\right) \tag{4.5}$$

for the wavefunction. With these two substitutions, the wavefunctions ψ and ψ' are each solution of the Schrödinger equation (4.4) with vector potential $\mathbf{A}$ and $\mathbf{A}'$, respectively.

[2]The coupling itself is the electric charge.

[3]Note that the canonical momentum $\hat{\mathbf{p}}$ is not gauge invariant, but the kinetic momentum $\hat{\mathbf{\Pi}}$ is.

[4]Since $\mathbf{A}$ and $\mathbf{A}'$ describe the same system, the probability densities $|\psi|^2$ and $|\psi'|^2$ should also give the same physics and thus any gauge transformation can only involve changes to the phase.

In electromagnetism, the gauge field is the vector potential and the local gauge symmetry is a U(1) Abelian symmetry[5]. This symmetry reflects that one can change arbitrarily the phase of the wavefunction of a charged particle without affecting the physics of the system. As a consequence, the electric charge is conserved locally, which ensures the U(1) gauge invariance.

Artificial gauge fields

Gauge potentials emerge naturally from electromagnetic fields, which interact with charged matter, but one can also engineer gauge fields in physical systems that are charge neutral using ultracold atoms. In that case, then, one usually considers the behavior of a system coupled to an artificial (or synthetic) gauge field with a vector potential $\mathcal{A}$ that can be described by a Hamiltonian $\mathcal{H}(\hat{\mathbf{p}} - \mathcal{A})$ (Aidelsburger et al., 2018). Artificial gauge fields have many applications. For example, in the particular case of artificial magnetism, the artificial gauge field is designed to emulate magnetic-like effects. These fields can be Abelian or non-Abelian; in the last case, the potentials can be tailored to reproduce spin–orbit effects (Goldman et al., 2014).

The simplest way to create an artificial gauge field is through the rotation of the system (Cooper, 2008; Fetter, 2009). The Lorentz force that acts on a charged particle is $q\mathbf{v}\times\mathbf{B}$, with $\mathbf{B}$ a uniform magnetic field. This resembles the Coriolis force that appears in a gas under rotation, $2m\mathbf{v}\times\mathbf{\Omega}$, where $\mathbf{\Omega}$ is the angular velocity. Therefore, in analogy to the electromagnetic case, one can define an effective vector potential and magnetic field that appear in the rotating frame, which is a noninertial system of reference (Dalibard, 2016; Goldman et al., 2014).

Artificial gauge potentials can also be engineered using laser beams that modify the light–matter interactions. In this sense, cold atoms are a very good platform for such gauge potentials, since one can tune experimentally the parameters that determine the dynamics.

The vector potential associated to either a natural or an artificial gauge field is not a directly observable quantity. However, a particle moving through such a field can acquire a geometrical phase that is measurable. We will explore this concept next.

Geometric phases

Let us consider the time evolution of a general quantum system described by the time-dependent Hamiltonian $\mathcal{H} = \mathcal{H}(\lambda)$, where $\lambda = \lambda(t)$ is a set of external parameters that depend on time (Berry, 1984). We will show now that if the state of the system performs an adiabatic evolution, it can acquire a geometric phase when the external

[5]The U(1) group is topologically a circle and corresponds to the group of rotations around a fixed axis. Therefore, the U(1) symmetry means that the wavefunction which describes the system is invariant under phase rotations such that any measured quantity should not change when the phase of the wavefunction is arbitrarily varied. The term *Abelian* refers to symmetry groups where the order in which one applies the operators and transformations does not matter, and an example of an Abelian group is the U(1) group (i.e., rotations). In non-Abelian groups, on the other hand, the transformations do not commute.

parameters $\boldsymbol{\lambda}$ travel along a closed trajectory[6] in parameter space, $\boldsymbol{\lambda}(0) = \boldsymbol{\lambda}(\tau)$, with τ the final time (for reference, see for instance Aidelsburger et al., 2018; Dalibard, 2016; Goldman et al., 2014).

The instantaneous eigenstates and eigenenergies of the system are $\mathcal{H}(\boldsymbol{\lambda})|\varphi_n(\boldsymbol{\lambda})\rangle = \mathcal{E}_n(\boldsymbol{\lambda})|\varphi_n(\boldsymbol{\lambda})\rangle$. We assume that the system $|\psi(t)\rangle$ is initially prepared in the m-th state, $|\psi(0)\rangle = |\varphi_m(\boldsymbol{\lambda})\rangle$, and that the energy $\mathcal{E}_m(\boldsymbol{\lambda})$ is well separated from the energies of other states by a gap along the entire trajectory of the parameters $\boldsymbol{\lambda}(t)$. If the parameters evolve slowly enough compared to the frequencies associated to the energy gaps, the adiabatic theorem predicts that the system remains in the instantaneous ground state during the whole evolution, $|\varphi_m(\boldsymbol{\lambda})\rangle$.

Since the eigenstates can be defined with an arbitrary complex phase factor, we define the state as

$$|\psi(t)\rangle = e^{i\phi(t)}|\varphi_m(\boldsymbol{\lambda})\rangle\,, \tag{4.6}$$

where $\phi(t)$ is a phase that the state may acquire during the evolution. Introducing the evolved state (4.6) into the Schrödinger equation, $i\hbar\partial_t|\psi(t)\rangle = \mathcal{H}(\boldsymbol{\lambda})|\psi(t)\rangle$, yields

$$-\left(\frac{\partial\phi(t)}{\partial t}\right)|\varphi_m(\boldsymbol{\lambda})\rangle + i\frac{\partial}{\partial t}|\varphi_m(\boldsymbol{\lambda})\rangle = \frac{1}{\hbar}\mathcal{E}_m(\boldsymbol{\lambda})\,|\varphi_m(\boldsymbol{\lambda})\rangle\,. \tag{4.7}$$

Projecting over $\langle\varphi_m(\boldsymbol{\lambda})|$, the time derivative of the phase becomes

$$\frac{\partial\phi(t)}{\partial t} = i\langle\varphi_m(\boldsymbol{\lambda})|\frac{\partial}{\partial t}|\varphi_m(\boldsymbol{\lambda})\rangle - \frac{1}{\hbar}\mathcal{E}_m(\boldsymbol{\lambda})\,. \tag{4.8}$$

We then integrate over time to find the phase at a time τ:

$$\phi(\tau) = i\int_0^\tau \langle\varphi_m(\boldsymbol{\lambda})|\frac{\partial}{\partial t}|\varphi_m(\boldsymbol{\lambda})\rangle\,dt - \frac{1}{\hbar}\int_0^\tau \mathcal{E}_m(\boldsymbol{\lambda})\,dt = \vartheta(\tau) + \theta(\tau)\,. \tag{4.9}$$

The phase (4.9) has two contributions that are both gauge invariant (i.e., that remain unchanged if one modifies the eigenstates by adding a phase factor) when following a closed path. The dynamic phase[7]

$$\theta(\tau) = -\frac{1}{\hbar}\int_0^\tau \mathcal{E}_m(\boldsymbol{\lambda})\,dt \tag{4.10}$$

is the phase that the state of the system acquires due to its dynamical evolution and depends on the duration of the trajectory, τ. On the other hand, the geometric phase

$$\vartheta(\tau) = i\int_0^\tau \langle\varphi_m(\boldsymbol{\lambda})|\frac{\partial}{\partial t}|\varphi_m(\boldsymbol{\lambda})\rangle\,dt\,, \tag{4.11}$$

[6]The state also acquires a geometric phase when following an open path, but it vanishes with the appropiate choice of phase for the eigenstates of the instantaneous Hamiltonian.

[7]This contribution is only gauge invariant if the path followed is a closed trajectory in parameter space. Otherwise, different phase paths can have different time derivatives.

also called the *Berry phase* after Berry (1984), is the phase that the state acquires due to the evolution of $\boldsymbol{\lambda}$ in parameter space. Using that

$$\frac{\partial}{\partial t}|\varphi_m(\boldsymbol{\lambda})\rangle = \boldsymbol{\nabla}_{\boldsymbol{\lambda}}|\varphi_m(\boldsymbol{\lambda})\rangle \frac{d\boldsymbol{\lambda}}{dt}\,, \tag{4.12}$$

one can rewrite the Berry phase (4.11) as the integration over a closed contour $\mathcal{C}$ in parameter space such that $\boldsymbol{\lambda}(0) = \boldsymbol{\lambda}(\tau)$,

$$\vartheta(\tau) = i \oint \langle \varphi_m(\boldsymbol{\lambda})|\boldsymbol{\nabla}_{\boldsymbol{\lambda}}\varphi_m(\boldsymbol{\lambda})\rangle \, d\boldsymbol{\lambda} = \frac{1}{\hbar}\oint \boldsymbol{\mathcal{A}}(\boldsymbol{\lambda}) \cdot d\boldsymbol{\lambda}\,, \tag{4.13}$$

where we have introduced the *Berry connection*,

$$\boldsymbol{\mathcal{A}}(\boldsymbol{\lambda}) = i\hbar \, \langle \varphi_m(\boldsymbol{\lambda})|\boldsymbol{\nabla}_{\boldsymbol{\lambda}}\varphi_m(\boldsymbol{\lambda})\rangle\,. \tag{4.14}$$

In contrast to the dynamic phase, the Berry phase (4.13) does not depend on the duration τ, only in the path followed by the external parameters $\boldsymbol{\lambda}$. Under a local gauge transformation, the wavefunction $|\varphi_m(\boldsymbol{\lambda})\rangle$ is replaced by

$$|\varphi'_m(\boldsymbol{\lambda})\rangle = e^{i\zeta(\boldsymbol{\lambda})}|\varphi_m(\boldsymbol{\lambda})\rangle\,, \tag{4.15}$$

and, as a result, the Berry connection $\boldsymbol{\mathcal{A}}$ (4.14) transforms as

$$\boldsymbol{\mathcal{A}}' = \boldsymbol{\mathcal{A}} - \boldsymbol{\nabla}_{\boldsymbol{\lambda}}\zeta(\boldsymbol{\lambda})\,, \tag{4.16}$$

where $\zeta(\boldsymbol{\lambda})$ is a scalar function. Thus, when the parameters $\boldsymbol{\lambda}$ follow a closed path in parameter space, the Berry phase $\vartheta(\tau)$ (4.13) is a gauge-invariant quantity, and the Berry connection $\boldsymbol{\mathcal{A}}$ (4.14) transforms like the vector potential of electromagnetism, $q\mathbf{A}$, under a gauge transformation. Introducing the *Berry curvature*,

$$\boldsymbol{\mathcal{B}}(\boldsymbol{\lambda}) = \boldsymbol{\nabla}_{\boldsymbol{\lambda}} \times \boldsymbol{\mathcal{A}}(\boldsymbol{\lambda})\,, \tag{4.17}$$

and making use of Stokes' theorem, one can rewrite the Berry phase (4.13) as

$$\vartheta(\tau) = \frac{1}{\hbar}\oint \boldsymbol{\mathcal{A}}(\boldsymbol{\lambda}) \cdot d\boldsymbol{\lambda} = \frac{1}{\hbar}\iint_{\mathcal{S}} d\mathbf{S} \cdot \boldsymbol{\mathcal{B}}(\boldsymbol{\lambda})\,. \tag{4.18}$$

The Berry curvature $\boldsymbol{\mathcal{B}}$ (4.17) is gauge invariant and resembles a magnetic field in parameter space, where $\mathcal{S}$ is the surface delimited by the closed path $\mathcal{C}$ in parameter space.

To sum up, one can engineer artificial gauge fields in quantum systems by designing vector potentials that provide nonzero Berry curvatures in parameter space. Then, the system can be described by an effective Hamiltonian, for the case of an atom with some internal states, of the form

$$\mathcal{H}_{\text{eff}} = \frac{(\hat{\mathbf{p}} - \boldsymbol{\mathcal{A}})^2}{2m} + V_{\text{eff}}\,, \tag{4.19}$$

where V_{eff} comprises any other terms, such as the internal motion of the atoms or the external confinement. In cold atoms, geometric phases can emerge in particles with some internal structure due to light–matter coupling, as we will see in Subsection 4.1.2.

These geometric phases can lead to remarkable physical phenomena, such as the Aharonov–Bohm effect in the case of electromagnetism. In quantum mechanics, a particle with charge q acquires a geometric phase, called the *Aharonov–Bohm phase* (Aharonov and Bohm, 1959), when travelling along a closed path C. This phase is defined as $\gamma = 2\pi\,\Phi/\Phi_0$, where Φ is the magnetic flux through C and $\Phi_0 = h/q$ is the flux quantum, and does not depend on the duration of the trajectory. One could say that the Aharonov–Bohm phase is related to the vector potential, not to the magnetic field itself, as illustrated by the Aharonov–Bohm effect.

Consider charged particles that move around an infinite solenoid, such that there is no magnetic field in the area accessible to the particles. Although the magnetic field vanishes outside the solenoid, the vector potential does not and, as a result, the particles moving in that region accumulate a geometric phase when traveling around a closed contour. This phase is proportional to the magnetic flux inside the solenoid Φ, and thus can be related to the vector potential that characterizes the magnetic field by

$$\gamma = \frac{2\pi}{\Phi_0} \iint_S \mathbf{B}(\mathbf{r}) \cdot d\mathbf{S} = \frac{1}{\hbar} \oint q\mathbf{A}(\mathbf{r}) \cdot d\mathbf{r}\,. \tag{4.20}$$

Therefore, the presence of a vector potential shows in the acquisition of a geometric phase, and this will be central to the engineering of artificial gauge fields.

The fact that the Aharonov–Bohm phase is related to the potential rather than to the fields is a common statement in the literature. However, it is important to note that the vector potential is not an observable and that gauge invariance is actually a manifestation of this nonobservable character (Jackson and Okun, 2001). Yet, in the case of the Aharonov–Bohm effect, the geometric phase (4.20) is an observable when the particle travels around a closed contour. As we have seen, one can write the closed integral on the vector potential in terms of the magnetic flux by using Stokes's theorem. Then, the Aharonov–Bohm phase depends either on the vector potential or (nonlocally) on the magnetic field but, in any case, the local vector potential is not an observable.

Density-dependent gauge potentials

The artificial gauge potentials studied in cold atoms systems are usually static, so the time dependence of the gauge field is experimentally controlled. Thus, they depend only on the external driving parameters (e.g., the light–matter coupling or rotation frequencies). The gauge fields that emerge from these potentials neither propagate in vacuum nor are influenced by matter (Goldman et al., 2014).

One can introduce an interaction between matter and the gauge field by designing a vector potential that depends on the density of the atoms, as $\mathcal{A}(\mathbf{r}, t) \propto n(\mathbf{r}, t)$, such that matter affects the vector potential locally and dynamically. The fields that arise from these density-dependent gauge potentials do not propagate in the absence of matter[8].

[8] As opposed to electromagnetic fields, which can propagate in vacuum.

The back action between matter and the artificial gauge field may give rise to unusual properties such as 1D anyons (Keilmann et al., 2011) and chiral solitons (Edmonds et al., 2013a; Frölian et al., 2022).

The fact that these artificial gauge fields cannot propagate in the absence of matter allows one to remove the gauge fields from the formalism and reduce it to only the matter degrees of freedom. Then, the gauge field and matter are coupled through the local conservation law that ensures the gauge invariance of the model. As a result, designing a density-dependent gauge potential is equivalent to engineering the matter–matter interactions (Chisholm et al., 2022), as we will discuss next.

4.1.2 Simulation with optically coupled condensates

Consider the center-of-mass motion of an atom with internal degrees of freedom. One can generate artificial vector potentials when the internal dynamics of the system depends parametrically on the atom's position (Goldman et al., 2014). Light–matter interactions, for instance, can couple the internal states of the atoms such that the transitions depend on the center-of-mass position.

We will first discuss the simplest case of a two-level atom with light–matter coupling, where the system's state can acquire a geometric phase by adiabatically following one of the light-dressed states. Then, we will finish this section by outlining how one can induce density-dependent gauge potentials in ultracold gases by considering a Raman-coupled two-component condensate with asymmetric scattering lengths.

Two-level atom

Let us consider a two-level atom moving in a monochromatic laser field of frequency ω (Dalibard, 2016; Dalibard et al., 2011). The system has two degrees of freedom: the center-of-mass motion, and the internal electronic states coupled by the laser field. The total Hamiltonian of the atom is

$$\mathcal{H} = \left(\frac{\hat{\mathbf{p}}^2}{2m} + V \right) \mathbb{I}_2 + U \,, \tag{4.21}$$

with $V = V(\mathbf{r})$ an external trapping potential, $\mathbb{I}_2$ the 2×2 identity matrix acting on the internal degrees of freedom, and $U = U(\mathbf{r})$ the Hamiltonian for the internal motion and the atom–light coupling, which depends on the position of the atom $\mathbf{r}$. The eigenstates of the bare atom are $|1\rangle$ and $|2\rangle$, i.e., the two levels of the atom. In the presence of atom–light coupling, the eigenstates of the internal Hamiltonian are usually referred to as *dressed states* (i.e., the states dressed by the atom–light coupling).

The detuning[9] between the atomic transition and the laser beam is Δ, and ω_R is the Rabi frequency[10]. To take into account that the detuning is in general nonzero, one

[9] The detuning is the energy difference between the coupling laser and the atomic transition.

[10] The Rabi frequency is the oscillation frequency of the population in the two levels.

defines the generalized Rabi frequency, $\Omega = \sqrt{\Delta^2 + |\omega_R|^2}$. Then, the atom–light coupling U can be written as a 2×2 matrix in the basis $\{|1\rangle, |2\rangle\}$:

$$U = \frac{\hbar}{2}\begin{pmatrix} \Delta & \omega_R^* \\ \omega_R & -\Delta \end{pmatrix} = \frac{\hbar\Omega}{2}\begin{pmatrix} \cos\alpha & e^{-i\beta}\sin\alpha \\ e^{i\beta}\sin\alpha & -\cos\alpha \end{pmatrix}, \tag{4.22}$$

where we have introduced the so-called mixing angle α and phase angle β, such that $\omega_R = |\omega_R|\, e^{i\beta}$, $\cos\alpha = \Delta/\Omega$ and $\sin\alpha = |\omega_R|/\Omega$.

Diagonalizing U (4.22) gives the eigenvalues $E_\pm = \pm\hbar\Omega/2$ and the dressed states (eigenstates of the light-coupled internal Hamiltonian)

$$|\varphi_+\rangle = \cos(\alpha/2)|1\rangle + e^{i\beta}\sin(\alpha/2)|2\rangle\,, \quad |\varphi_-\rangle = -e^{i\beta}\sin(\alpha/2)|1\rangle + \cos(\alpha/2)|2\rangle\,. \tag{4.23}$$

If the state of the system follows adiabatically[11] one of the dressed states[12], for instance $|\varphi_+\rangle$ (Dalibard, 2016), the associated vector potential[13] or Berry connection, introducing the dressed state (4.23) into Eq. (4.14), is

$$\mathcal{A}(\mathbf{r}) = i\hbar\,\langle\varphi_+|\nabla\varphi_+\rangle = \frac{\hbar}{2}\,(\cos\alpha - 1)\,\nabla\beta\,, \tag{4.24}$$

the effective magnetic field or Berry curvature (4.17) is

$$\mathcal{B}(\mathbf{r}) = \nabla\times\mathcal{A} = \frac{\hbar}{2}\,\nabla\,(\cos\alpha)\times\nabla\beta\,, \tag{4.25}$$

and the associated scalar potential is (Dalibard et al., 2011)

$$\zeta(\mathbf{r}) = \frac{\hbar^2}{2m}\left|\langle\varphi_-|\nabla\varphi_+\rangle\right|^2 = \frac{\hbar^2}{8m}\left[(\nabla\alpha)^2 + \sin^2\alpha\,\left(\nabla\beta\right)^2\right]. \tag{4.26}$$

This scalar potential relates to the kinetic energy associated to the internal motion of the atom. Note that if the dressed states do not have spatial dependence, i.e., $|\nabla\varphi_\pm\rangle = 0$, then $\mathcal{A}$ (4.24) and ζ (4.26) are zero. The spatial dependence of the dressed states can be achieved by adjusting the coupling parameters such that the coupling laser's detuning and phase have a nonzero gradient.

The state of the system is $|\Psi\rangle = \psi_+(\mathbf{r},t)|\varphi_+\rangle + \psi_-(\mathbf{r},t)|\varphi_-\rangle$. However, we will consider that the system follows adiabatically the $|\varphi_+\rangle$ state such that $\psi_- \approx 0$. Then, projecting the Schrödinger equation $i\hbar\partial_t|\Psi\rangle = \mathcal{H}|\Psi\rangle$ into the $|\varphi_+\rangle$ state, with $\mathcal{H}$ the

[11] The *adiabatic approximation* assumes, generally, that a subset $m \le n$ of the n dressed states of the system is energetically well separated from all the other states. Therefore, one can project the dynamics into the truncated space of the internal states m (Goldman et al., 2014). Here we consider $m = 1$ and $n = 2$.

[12] The adiabatic approximation is not always valid due to temperature-induced transitions. An alternative setup is to consider a Raman transition instead of a two-level system.

[13] The vector potential $\mathcal{A}$ is Abelian when all its cartesian components commute with each other. If the system instead evolves following m instantaneous eigenstates (instead of only one), the accumulated geometric phase is replaced by a $m \times m$ matrix that acts on the reduced space of m states. Then, the corresponding vector potential is also a $m \times m$ matrix which is non-Abelian and represents an effective spin–orbit coupling in parameter space (Aidelsburger et al., 2018).

full Hamiltonian (4.21), the effective Hamiltonian that describes the system is (Dalibard et al., 2011)

$$\mathcal{H}_{\text{eff}} = \frac{(\hat{\mathbf{p}} - \boldsymbol{\mathcal{A}})^2}{2m} + V + E_+ + \zeta\,, \tag{4.27}$$

whith V the external potential, E_+ the energy of the $|\varphi_+\rangle$ state and ζ the scalar potential (4.26). Then, the evolution of the system is given by the Schrödinger-like equation

$$i\hbar\frac{\partial\psi}{\partial t} = \left[\frac{(\hat{\mathbf{p}} - \boldsymbol{\mathcal{A}})^2}{2m} + V + E_+ + \zeta\right]\psi\,, \tag{4.28}$$

where $\psi = \psi_+$ is the amplitude of the dressed state $|\varphi_+\rangle$. The Berry curvature (4.25) is nonzero in this reduced atomic dynamics. The two geometric potentials, $\boldsymbol{\mathcal{A}}$ and ζ, originate from the spatial dependence of the dressed states and appear when the state $|\varphi_-\rangle$ is adiabatically eliminated.

Two-component BEC with asymmetric interactions

Here we consider the case of a weakly interacting Bose gas of two components coupled by an external space-dependent electromagnetic field, where each component corresponds to the population in the two available hyperfine states of the atoms. The single-particle Hamiltonian for the noninteracting system is Eq. (4.21). The light–matter coupling term U between the two components is given by

$$U = \frac{\hbar\Omega}{2}\begin{pmatrix} 0 & e^{-i\beta} \\ e^{i\beta} & 0 \end{pmatrix}\,, \tag{4.29}$$

where now Ω is the two-photon Rabi frequency that characterizes the light–matter coupling, $\beta = \beta(\mathbf{r})$ is the phase of the coupling laser, and we have set the detuning Δ from the two-photon Raman resonance to zero for simplicity[14].

Similarly to the case of a two-level atom, an artificial gauge potential can emerge due to the atom–light coupling when the gradient of the detuning is nonzero. We will see now how the mean-field interactions between atoms can induce an effective density-dependent detuning (Goldman et al., 2014).

A binary mixture of N interacting two-level atoms can be described by two coupled Gross–Pitaevskii equations [Eqs. (2.34), see Chapter 3 for more details]. Then, the mean-field Hamiltonian (Edmonds et al., 2013a) is

$$\mathcal{H} = \left(\frac{\hat{\mathbf{p}}^2}{2m} + V\right)\mathbb{I}_2 + U + \mathcal{V}_{\text{int}}\,, \tag{4.30}$$

[14]Raman transitions can be used to couple two sublevels of the atomic ground state by using two counterpropagating laser beams. These transitions involve two photons: one beam induces transitions from one of the hyperfine states to an excited state (that plays no role in the dynamics), and the second beam de-excites the atoms to the other hyperfine state.

with $\mathcal{V}_{\text{int}}$ the atom–atom mean-field interactions,

$$\mathcal{V}_{\text{int}} = \begin{pmatrix} g_{11}|\psi_1|^2 + g_{12}|\psi_2|^2 & 0 \\ 0 & g_{22}|\psi_2|^2 + g_{12}|\psi_1|^2 \end{pmatrix}, \tag{4.31}$$

where $n_\sigma = |\psi_\sigma|^2$ is the density of each component ($\sigma = 1, 2$) such that the total density $n_1 + n_2$ is normalized to N and $g_{\sigma\sigma'}$ characterizes the inter- and intracomponent contact interactions. We will assume there is no external confinement ($V = 0$) for simplicity.

If the energy of the mean-field interactions $g_{\sigma\sigma'}n_\sigma$ is much smaller than the light–matter coupling $\hbar\Omega$ (i.e., the system is weakly interacting), one can calculate the dressed states perturbatively[15] (Edmonds et al., 2013a):

$$|\varphi_\pm\rangle = |\varphi_\pm^{(0)}\rangle \pm \frac{g_{11} - g_{22}}{8\hbar\Omega} n_\pm |\varphi_\mp^{(0)}\rangle, \tag{4.32}$$

where $|\varphi_\pm^{(0)}\rangle = \left(|1\rangle \pm e^{i\beta}|2\rangle\right)/\sqrt{2}$ are the dressed states for the noninteracting case (4.23) and $n_\pm = |\psi_\pm|^2$ are the densities of the dressed states. Then, the corresponding vector potentials (4.14) are

$$\mathcal{A}_\pm = \mathcal{A}^{(0)} \pm \mathbf{a}_1 n_\pm(\mathbf{r}), \tag{4.33}$$

where $\mathcal{A}^{(0)} = -(\hbar/2)\nabla\beta$ is the vector potential (4.24) for the unperturbed case. The strength of the density dependence $\mathbf{a}_1$ is defined as

$$\mathbf{a}_1 = \frac{g_{11} - g_{22}}{8\Omega} (\nabla\beta). \tag{4.34}$$

For asymmetric interactions ($g_{11} \neq g_{22}$), the vector potential depends linearly on the density, which introduces a back action between matter and the (artificial) gauge field. The mean-field atom–atom interactions induce an effective detuning (i.e., shift the electronic levels of the atoms), as one can see from Eq. (4.32), which results in an artificial vector potential.

All the parameters involved in the strength of the density-dependent vector potential (i.e., the Rabi frequency, the gradient of the phase $\nabla\beta$ and the difference in scattering lengths $a_{11} - a_{22} \propto g_{11} - g_{22}$) can be tuned experimentally by adjusting the light–matter coupling through the laser parameters and the scattering lengths via Feshbach resonances (Chin et al., 2010).

As in the single-particle case, one can eliminate one of the dressed states such that the system follows the other dressed state adiabatically[16]. The geometric vector and scalar potentials are revealed when one projects the full system into one of the dressed states. We choose $|\varphi_+\rangle$, redefine the corresponding vector potential $\mathcal{A} = \mathcal{A}_+$ (4.33) and denote with ψ the wavefunction of the dressed state, with density $n = n_+$. The evolution of the system then can be described by an effective Gross–Pitaevskii equation analogous

[15] Since $g_{\sigma\sigma'}n_\sigma \ll \hbar\Omega$, one can treat the atom–atom interactions $\mathcal{V}_{\text{int}}$ as a small perturbation to the light–matter interaction U.

[16] The adiabatic approximation requires that any induced detuning (i.e., the energy associated to the eigenstate $|\varphi_+\rangle$) must be small compared to the Rabi frequency Ω such that the recoil energy of the atoms is much smaller than the energy associated to the Rabi frequency.

to Eq. (4.28) that includes the density-dependent gauge potential (see Edmonds et al., 2013a, for a detailed derivation):

$$i\hbar\frac{\partial\psi}{\partial t} = \left[\frac{(\hat{\mathbf{p}} - \boldsymbol{\mathcal{A}})^2}{2m} + \mathbf{a}_1 \cdot \mathbf{J}(\psi, \psi^*) + gn + \zeta\right]\psi\,, \tag{4.35}$$

where $\mathbf{J}$ is the current density,

$$\mathbf{J}(\psi, \psi^*) = \frac{\hbar}{2mi}\left[\psi\left(\boldsymbol{\nabla} + \frac{i}{\hbar}\boldsymbol{\mathcal{A}}\right)\psi^* - \psi^*\left(\boldsymbol{\nabla} - \frac{i}{\hbar}\boldsymbol{\mathcal{A}}\right)\psi\right]\,, \tag{4.36}$$

which arises due to the presence of a nonzero vector potential. The effective contact coupling constant g is $g = (g_{11} + g_{22} + 2g_{12})/4$, and the scalar potential ζ, defined by Eq. (4.26), is given by

$$\zeta = \frac{1}{2m}|\boldsymbol{\mathcal{A}}^{(0)}|^2\,. \tag{4.37}$$

Here, two terms contribute to the nonlinearity of the GPE (4.35): the usual term gn and also the term with the current $\mathbf{J}$. In 1D, as we will see with more detail in Section 4.2, this term describes effective interactions that, due to the current-density dependence, are chiral (i.e., moving in one direction or the other is not equivalent).

We are interested in particular in the 1D case. The GPE (4.35) can be reduced to 1D by setting the phase of the incident laser to $\beta = kx$ and using the ansatz[17] $\psi(\mathbf{r}, t) = \phi(x, t)e^{-ikx/2}$ (Edmonds et al., 2013a) such that the GPE becomes

$$i\hbar\frac{\partial\phi}{\partial t} = \left[\frac{(\hat{p} - a_1 n)^2}{2m} + a_1 J + g\,n + \zeta_1\right]\phi\,, \tag{4.38}$$

with $a_1 = k(g_{11} - g_{22})/(8\Omega S_t)$ the strength of the current nonlinearity (with S_t the effective transversal area) and $\zeta_1 = (\hbar k)^2/(8m)$ the 1D scalar potential. Note however that this equation (4.38) is not gauge invariant. To obtain a gauge-invariant equation, one can eliminate the vector potential from the kinetic term by transforming the wavefunction by (4.5), which in turn modifies the current (as we will see in Subsection 4.2.1).

This 1D equation is equivalent to the chiral theory proposed by Aglietti et al. (1996) and supports chiral solitons (which propagate only in one direction), as we will discuss in the following section and Chapters 8 and 9. Besides chiral solitons, the 1D system with periodic boundary conditions presents persistent currents in which the ground state changes from one rotational state to another at a given critical density[18].

In this system, coupling matter to a gauge potential that depends linearly on the density is equivalent to engineering chiral interactions. As we have discussed in this section, such chiral interactions can be realized in a two-component BEC with asymmetric interactions controlled with coherent coupling (Edmonds et al., 2013a) and coupling the momentum and internal state of the atoms via two-photon processes (Chisholm et al., 2022; Frölian et al., 2022).

[17] We are assuming that the laser is a plane wave propagating along x, such that its phase is $\beta = kx$, with k the wavevector in the x direction. Thus, the motion of the atoms is restricted to the x direction.

[18] In a usual (i.e., nonchiral) ring BEC under rotation, the onset of current is given by the rotation frequency, not the number of particles.

4.2 Current-density interaction theory

In the late 1990s, the quest for the description of 1D anyons in the continuum (Rabello, 1995, 1996) led to the development of a gauge theory, which we will refer to as *chiral theory*, with a nonlinearity that emerges from the current density and that supports chiral solitons (Aglietti et al., 1996). The theory is chiral in nature because it breaks Galilean invariance, i.e., motion in one direction or the other is not equivalent. This theory is a reduction to 1D of the Chern–Simons theory, which describes anyons in 2D (Zhang et al., 1989).

Chiral interactions naturally emerge when describing a light-coupled two-component BEC with asymmetric contact interactions (see Section 4.1). The chiral theory can be reduced to a model where the atoms have interactions that, to leading order, depend linearly on the current density and thus are chiral. As we discussed in Subsection 4.1.2, this reduction was experimentally and theoretically proposed for a weakly interacting BEC with two internal states (and asymmetric interactions) that are optically coupled (Chisholm et al., 2022; Frölian et al., 2022). The coupling can be implemented, for instance, using two counterpropagating lasers in a Raman configuration such that the atoms acquire momentum along the propagation direction of the lasers. As a result, the scattering properties of the dressed states depend on the momentum of the atoms, i.e., they are chiral. In such a system, designing a density-dependent gauge potential is, as we saw in Section 4.1, equivalent to engineering chiral interactions between the atoms.

In this section, we will explore the theoretical tools to introduce a density-dependent gauge potential in a quasi-1D weakly interacting BEC. In Subsection 4.2.1, we will introduce a vector potential that depends linearly on the density and explicitly derive the Gross–Pitaevskii-like equation with chiral interactions following Aglietti et al. (1996) and Jackiw (1997) from an action principle. This approach is complementary to the Hartree-like method employed in Chapter 2, and allows one to identify the energy as a conserved quantity. Later, in Subsection 4.2.2, we will reformulate the model in the rotating frame, which will be the theoretical foundations for Chapters 8 and 9.

4.2.1 Equation of motion with a current-density nonlinearity

Let us consider a quasi-1D weakly interacting Bose gas within the mean-field regime, characterized by a wavefunction $\phi(x,t)$ that is normalized to the number of atoms N, and with number density $n(x,t) = |\phi(x,t)|^2$. The Lagrangian density $\mathcal{L}(x,\phi,\partial_x\phi)$ that describes the system is

$$\mathcal{L} = i\hbar\,\phi^*\frac{\partial\phi}{\partial t} - \mathcal{E}\,, \tag{4.39}$$

where $\mathcal{E}$ is the energy density (Jackiw, 1997),

$$\mathcal{E} = \frac{1}{2m}\left|\left(\hat{p} - \mathcal{A}\right)\phi\right|^2 + \frac{g}{2}|\phi|^4\,, \tag{4.40}$$

with $\hat{p} = -i\hbar\partial_x$ the momentum operator, g the 1D coupling constant of the atom–atom interactions and $\mathcal{A}(x,t)$ a gauge potential. In particular, we consider a density-dependent

vector potential of the form

$$\mathcal{A}(x,t) = -\frac{\hbar\kappa}{2}|\phi(x,t)|^2\,, \tag{4.41}$$

where κ is a dimensionless constant that we define positive for simplicity and which characterizes the strength of the density dependence. Then, the Lagrangian density (4.39) reads:

$$\mathcal{L} = i\hbar\,\phi^*\frac{\partial\phi}{\partial t} - \frac{1}{2m}\left|\left(-i\hbar\frac{\partial}{\partial x} + \frac{\hbar\kappa}{2}|\phi|^2\right)\phi\right|^2 - \frac{g}{2}|\phi|^4\,. \tag{4.42}$$

To obtain the equations of motion from the Lagrangian density (4.42), we employ the variational equation

$$\frac{\partial\mathcal{L}}{\partial\phi^*} - \frac{\partial}{\partial x}\left[\frac{\partial\mathcal{L}}{\partial(\partial_x\phi^*)}\right] = 0\,. \tag{4.43}$$

Replacing $\mathcal{L}$ (4.42) into Eq. (4.43) yields

$$i\hbar\frac{\partial\phi}{\partial t} = \frac{1}{2m}\left(-i\hbar\frac{\partial}{\partial x} + \frac{\hbar\kappa}{2}|\phi|^2\right)^2\phi + g|\phi|^2\phi + \frac{\hbar\kappa}{2}J\phi\,, \tag{4.44}$$

where $J = J(x,t)$ is the current density,

$$J = -\frac{1}{2m}\left[\phi\left(\hat{p}+\mathcal{A}\right)\phi^* - \phi^*\left(\hat{p}-\mathcal{A}\right)\phi\right] = \frac{\hbar}{m}\,\mathrm{Im}\left[\phi^*\left(\frac{\partial}{\partial x} + i\frac{\kappa}{2}|\phi|^2\right)\phi\right]\,. \tag{4.45}$$

Equation (4.44) is equivalent to the 1D GPE for an optically coupled BEC with asymmetric interactions [Eq. (4.38) in Subsection 4.1.2] and differs only in the ζ_1 term of Eq. (4.38), which corresponds to an energy shift. To avoid confusion, here we will refer to $J(x,t)$ as *current density* and to $n(x,t) = |\phi(x,t)|^2$ as *number density*.

Chiral Gross–Pitaevskii equation

A gauge-invariant description can be obtained by eliminating the density dependence from the kinetic term in Eq. (4.45) such that one obtains the equation of motion with only current-density interactions. We perform the Jordan–Wigner transformation to the wavefunction (Aglietti et al., 1996; Edmonds et al., 2013a; Frölian et al., 2022),

$$\psi(x,t) = \phi(x,t)\exp\left[i\frac{\kappa}{2}\int^x |\phi(y,t)|^2\,dy\right] = \phi(x,t)\exp\left[-\frac{i}{\hbar}\int^x \mathcal{A}(y,t)\,dy\right]\,, \tag{4.46}$$

where the lower limit of the integral can be an arbitrary value $a < x$, since it only affects the phase of ψ. The number density is unchanged, $n(x,t) = |\phi(x,t)|^2 = |\psi(x,t)|^2$, and so is the vector potential $\mathcal{A}(x,t)$ (4.41). Using Eq. (4.46), the current density $J = J(x,t)$ (4.45) transforms as

$$J = \frac{\hbar}{2mi}\left(\psi^*\frac{\partial\psi}{\partial x} - \psi\frac{\partial\psi^*}{\partial x}\right) = \frac{\hbar}{m}\,\mathrm{Im}\left[\psi^*\frac{\partial\psi}{\partial x}\right]\,. \tag{4.47}$$

The continuity equation in 1D,

$$\frac{\partial n}{\partial t} + \frac{\partial J}{\partial x} = 0\,, \tag{4.48}$$

ensures the conservation of the particle number and links the number and current densities. Then, using the transformed wavefunction (4.46) and the continuity equation (4.48), the time derivative of ϕ can be written as

$$\frac{\partial \phi}{\partial t} = \left(\frac{\partial \psi}{\partial t} - i\frac{\kappa}{2}\psi J\right) \exp\left[-i\frac{\kappa}{2}\int^{x} |\psi(y)|^2\, dy\right]\,. \tag{4.49}$$

Introducing Eqs. (4.46) and (4.49) into the equation of motion (4.44) gives

$$i\hbar\frac{\partial \psi}{\partial t} = -\frac{\hbar^2}{2m}\frac{\partial^2 \psi}{\partial x^2} + \left(gn + \hbar\kappa J\right)\psi\,, \tag{4.50}$$

which yields a gauge-invariant description of the system. Equation (4.50) is a Gross–Pitaevskii-like equation where the nonlinearity comes from two sources: the usual contact interactions and the chiral (i.e., current-density) interactions characterized by the strength parameter κ. Therefore, the system can be described by the mean-field Hamiltonian

$$\mathcal{H} = \frac{\hat{p}^2}{2m} + gn + \hbar\kappa J\,. \tag{4.51}$$

Current-density interactions

Although the usual GPE (2.53) in 1D is integrable, the chiral GPE (4.50) is nonintegrable in general due to the presence of the nonlinear current term. In addition, unlike the usual GPE, Eq. (4.50) supports chiral solitons (Aglietti et al., 1996; Griguolo and Seminara, 1998; Jackiw, 1997) as a result of breaking the Galilean invariance.

The physical consequences of the current-density interactions can be examined by writing the wavefunction in terms of the density and its phase, $\psi(x,t) = \sqrt{n(x,t)}e^{i\theta(x,t)}$, such that the current density (4.47) simplifies to

$$J = n\,\frac{\hbar}{m}\,\frac{\partial \theta}{\partial x}\,. \tag{4.52}$$

Then, one can write the chiral GPE (4.50) as

$$i\hbar\frac{\partial \psi}{\partial t} = -\frac{\hbar^2}{2m}\frac{\partial^2 \psi}{\partial x^2} + g_{\text{eff}}\, n\,\psi\,, \tag{4.53}$$

where the effective coupling constant is

$$g_{\text{eff}} = g + \kappa\,\frac{\hbar^2}{m}\frac{\partial \theta}{\partial x}\,, \tag{4.54}$$

and is modulated by the phase variations. Therefore, the interplay between the contact-interacting term gn and the current-density term $\hbar\kappa J$ will lead to bright solitons when the effective interactions (4.54) are attractive and to dark solitons when they are repulsive.

Conserved energy

Here we will derive the expression for the energy of the system, which is conserved due to the time-translation invariance of the system (Jackiw, 1997). We start from the energy density $\mathcal{E}$ (4.40) for the density-dependent vector potential $\mathcal{A}$ (4.41), which reads

$$\mathcal{E} = \frac{1}{2m}\left|\left(\hat{p} + \frac{\hbar\kappa}{2}|\phi|^2\right)\phi\right|^2 + \frac{g}{2}|\phi|^4 . \tag{4.55}$$

Rewriting the wavefunction by means of the Jordan–Wigner transformation (4.46) and introducing the momentum operator $\hat{p}$ one gets

$$\left(\hat{p} + \frac{\hbar\kappa}{2}|\phi|^2\right)\phi = (\hat{p}\psi)\exp\left[-i\frac{\kappa}{2}\int^x |\psi(y)|^2\, dy\right] , \tag{4.56}$$

such that the energy density becomes

$$\mathcal{E} = \frac{1}{2m}\left|\hat{p}\psi\right|^2 + \frac{g}{2}|\psi|^4 . \tag{4.57}$$

One obtains the energy by spatial integration of $\mathcal{E}$ (4.57),

$$E = \int \mathcal{E}\, dx = \frac{1}{2m}\int |\hat{p}\psi|^2\, dx + \frac{g}{2}\int |\psi|^4\, dx . \tag{4.58}$$

Using that $\int |\hat{p}\psi|^2\, dx = \int \psi^*\hat{p}^2\psi\, dx$, we rewrite the conserved energy as

$$E = \frac{1}{2m}\int \psi^*\hat{p}^2\psi\, dx + \frac{g}{2}\int |\psi|^4\, dx . \tag{4.59}$$

Notice that the conserved (total) energy does not include any explicit contribution from the current-density interactions, it only includes the kinetic energy and the contact interaction energy. We will use the conserved energy (4.59) to identify the ground states of the system in Chapters 8 and 9.

4.2.2 Chiral currents in ring potentials

In this subsection we will focus on a ring geometry under rotation, where a superfluid system can support persistent currents (states with vorticity). In the presence of current-density interactions, these currents become chiral. This system will be further studied with a single BEC with chiral interactions (Chapter 8) and a two-component BEC with coherent coupling (Chapter 9).

Equation of motion in the rotating frame

Here we will generalize the chiral equation of motion (4.50) to include rotation. For a system that rotates around the z axis with angular velocity $\mathbf{\Omega} = \Omega\,\hat{\mathbf{e}}_z$, a general

static Hamiltonian $\mathcal{H}$ transforms to the rotating frame (Cooper, 2008; Fetter, 2009) as $\mathcal{H}_\Omega = \mathcal{H} - \boldsymbol{\Omega}\cdot\hat{\mathbf{L}}$, with $\hat{\mathbf{L}} = \mathbf{r}\times\hat{\mathbf{p}}$ the angular momentum operator. In 1D, $\boldsymbol{\Omega}\cdot\hat{\mathbf{L}} = \Omega\hat{L}_z$, where $\hat{L}_z = -i\hbar\partial_\varphi$ is the z-component of the angular momentum operator and φ is the rotation angle. Then, a 1D Hamiltonian $\mathcal{H}$ in the rotating frame is

$$\mathcal{H}_\Omega = \mathcal{H} - \Omega\hat{L}_z\,, \tag{4.60}$$

where the term $-\Omega\hat{L}_z$ favors states with positive angular momentum. For the particular case of the chiral GPE (4.53) derived in Subsection 4.2.1, we rewrite the angular momentum operator as $\hat{L}_z = (\partial_\varphi x)\,\hat{p}$, add an energy shift $mv^2/2$ to account for the rotation energy[19] and replace $\mathcal{H}$ by the Hamiltonian of the chiral GPE (4.51). Then, the Hamiltonian in the rotating frame reads

$$\mathcal{H}_\Omega = \frac{\hat{p}^2}{2m} + gn + \hbar\kappa J - \Omega\,\frac{\partial x}{\partial\varphi}\,\hat{p} + \frac{1}{2}mv^2\,. \tag{4.61}$$

Considering a ring of radius R (i.e., imposing periodic boundary conditions) and using polar coordinates such that $x = \varphi R$ and $v = \Omega R$, we rewrite the Hamiltonian in the rotating frame (4.61) as

$$\mathcal{H}_\Omega = \frac{\left(\hat{p} - m\Omega R\right)^2}{2m} + gn + \hbar\kappa J\,. \tag{4.62}$$

One can obtain the equation of motion by replacing Eq. (4.62) into the Schrödinger equation, $i\hbar\partial_t\psi = \mathcal{H}_\Omega\,\psi$, and introducing the mechanical (kinetic) momentum operator[20],

$$\hat{\Pi} = \hat{p} - m\Omega R\,. \tag{4.63}$$

Then, the equation of motion in the rotating frame is

$$i\hbar\frac{\partial\psi}{\partial t} = \left(\frac{\hat{\Pi}^2}{2m} + gn + \hbar\kappa J\right)\psi\,. \tag{4.64}$$

This equation corresponds to the nonrotating version (4.50) with the momentum operator $\hat{p}$ replaced by the kinetic momentum operator $\hat{\Pi}$, and will be the basis of the theoretical model we will use in Chapter 8 to study stationary states in rotating rings with current-density interactions. Therefore, the conserved energy is analogous to the one of the nonrotating case (4.59),

$$E_\Omega = \frac{1}{2m}\int\psi^*\hat{\Pi}^2\psi\,dx + \frac{g}{2}\int|\psi|^4\,dx\,, \tag{4.65}$$

as it includes $\hat{\Pi}$ instead of $\hat{p}$.

[19] We shift the energy by this constant value for convenience such that the equation of motion can be written in a more simplified form [see Eq. (4.62)].

[20] Using classical mechanics, one can see that the (canonical) momentum operator $\hat{p}$ is the same in both the laboratory and rotating frames.

Note that imposing periodic boundary conditions on the system affects the Jordan–Wigner transformation (4.46) we performed to remove the vector potential $\mathcal{A}$ from the equation of motion, since both the phase and the density of the wavefunction on such a ring geometry are quantized. As a result, mapping the density-dependent gauge potential into a Gross–Pitaevskii equation with chiral interactions (4.64) will only be possible for certain densities. This issue will be discussed with detail in Chapter 8.

Stationary states and chiral solitons

The chiral GPE (4.64) supports states that are stationary in the rotating frame, such as plane waves and solitons, which exhibit chiral properties. We cover this topic in more detail in Chapter 8, while Chapter 9 generalizes the study to a two-component BEC with coherent coupling between the components.

For open boundary conditions (i.e., the infinite case), one can describe solitons analytically by means of hyperbolic functions [see Eqs. (2.56) and (2.57) in Chapter 2]. However, these functions are not valid for periodic boundary conditions (i.e., the ring geometry), as we will discuss in Chapter 8, and one needs to use Jacobi elliptic functions instead. See Appendix A for an introduction to these functions and their main properties, which we will use in Chapter 8.

5

Dipolar and nondipolar shell-shaped condensates under gravity

Shell-shaped BECs, which are thin shells of atoms (i.e., BECs that are empty on the inside), can be realized using radiofrequency-dressed potentials. In these systems, the atoms are confined in a quasi-2D curved geometry. Thus, although the system is still 3D, the confinement restricts the motion of the atoms to a 2D closed surface. Such curved geometries present new features that flat geometries lack: for instance, the system has periodic boundary conditions and a local curvature (for more details on the topic, see review by Tononi and Salasnich, 2023, and references therein).

In BECs, the geometry of the confinement plays a vital role in the static and dynamic properties of the system, as we already discussed for nondipolar and dipolar systems in Chapters 2 and 3, respectively. Therefore, shell-shaped condensates provide a way to investigate condensation, superfluidity, and other phenomena of BECs in topologies with a connected and closed surface (Bereta et al., 2019; Móller et al., 2020; Tononi and Salasnich, 2019; Tononi et al., 2022) instead of the usual open surface of a flat condensate. The effect of the shell-shaped geometry has been studied, for instance, in the transition from a full, spherical BEC to a thin shell of atoms (Rhyno et al., 2021), where the new boundary modifies the collective modes of the system[1] (Lannert et al., 2007; Merloti et al., 2013; Padavić et al., 2018; Sun et al., 2018). The critical temperature changes with the geometry as well, being lower in shells than in full condensates (Tononi et al., 2020). Vortex formation (Bereta et al., 2021), in turn, is affected too by the curvature since the simplest vortex configuration allowed on a 2D shell is the vortex–antivortex pair (Padavić et al., 2020) instead of the single vortex. Finally, ellipsoidal shells have a nonuniform density due to the anisotropy of the confinement, and this results in a complex dynamical behavior (Bereta et al., 2021; Caracanhas et al., 2022).

Radiofrequency-dressed potentials (Garraway and Perrin, 2016; Harte et al., 2018; Perrin and Garraway, 2017; White et al., 2006; Zobay and Garraway, 2001, 2004) arise by applying a radiofrequency magnetic field to a gas of cold atoms with different spin states confined in a conventional harmonic magnetic trap. The resulting dressed states are position-dependent, i.e., the dressed potential forms a double well along any axis.

[1] The collective modes in particular and the overall behavior of shells are also affected by the presence of gravity, which we will introduce later.

Consequently, the atoms are trapped in an ellipsoidal 3D surface. The first hollow condensate was realized in 2004 (Colombe et al.). However, this condensate was not a closed shell due to the gravitational sag, which depletes the shell; due to Earth's gravity, the atoms sag to the bottom of the trap, and shell-shaped BECs are destroyed. For this reason, to experimentally obtain shell-shaped condensates, one needs microgravity conditions, meaning that the effect of gravity is small enough to neglect it. The first fully shell-shaped BEC was realized very recently (Carollo et al., 2022) using a microgravity environment.

Besides radiofrequency-induced adiabatic potentials, one can also achieve shell-shaped BECs by means of an optically trapped binary heteronuclar mixture in the immiscible regime (Wolf et al., 2022), which was experimentally done also in 2022 (Jia et al.). This setup allows one to study shells on Earth[2], but it has the limitation that one needs two immiscible components and thus the core of the shell is filled by the other component. This experimental proposal may provide a good alternative for dipolar systems, where the dipolar relaxation could limit the lifetime of shell-shaped BECs. However, here we will focus on adiabatic potentials, which will be introduced with more detail later. Then, to realize these shells, one needs to reduce the effect of gravity.

Microgravity experiments with cold atoms have been carried out, for instance, in drop towers (Müntinga et al., 2013; van Zoest et al., 2010), suborbital launch vehicles (Becker et al., 2018), Einstein elevators (Condon et al., 2019) and, more recently, in the NASA Cold Atom Laboratory (CAL) on the International Space Station (Aveline et al., 2020; Elliott et al., 2018; Frye et al., 2021; Lundblad et al., 2019). The proposal for an experimental framework to realize shell-shaped BECs at CAL (Lundblad et al., 2019) lead to further interest in these hollow condensates under microgravity conditions (Meister et al., 2019; Tononi and Salasnich, 2019; Tononi et al., 2020).

Yet, in this chapter, we are interested in the effect of a small gravity in shell-shaped BECs. Then, to guarantee that shells are not destroyed by the gravitational sag, we consider values of gravity larger than microgravity to study its effect but still smaller than the terrestrial gravity by some orders of magnitude. This restricted range of gravities holds for the particular parameters we used in the numerical calculations (see Sections 5.2 and 5.3). However, one can extend this range to other values (see Section 5.4) by considering a different set of parameters as long as both the mean-field regime and the thin-shell limit hold (we will discuss those conditions in Section 5.1).

Theoretical work on shell-shaped BECs has focused mostly on contact-interacting atoms (i.e., nondipolar condensates). For atoms with a non-negligible magnetic moment, dipole–dipole interparticle interactions are also relevant (see Chapter 3). Dipolar shell-shaped BECs have been studied in the limit of a thin shell (Diniz et al., 2020) and under rotation (Adhikari, 2012). Whereas contact interactions are short-range and isotropic, the interaction between atoms with a dipolar moment is long-range and anisotropic (Lahaye et al., 2009). Due to these features of dipole–dipole interactions, dipolar BECs are specially sensitive to the geometry of the trapping potential. Moreover, the fact that the dipole polarization introduces a privileged direction in the system may endow

[2]In this case, one still needs to counterbalance the gravitational sag to avoid the displacement of the center of mass of each component, which is not the same due to the different masses.

dipolar BECs with additional sensitivity to tiny changes in orientation, such as gravity perturbations.

Our motivation in this chapter is to explore the effects of the dipole–dipole interaction in thin shell-shaped condensates. Additionally, since experiments in microgravity conditions may suffer gravity perturbations, we analyze the dynamics of small oscillations in small-gravity conditions, both for dipolar and nondipolar condensates, which could yield to identify small changes in the direction or magnitude of the gravity.

The chapter is organized as follows. In Section 5.1, we introduce the theoretical framework and shell-shaped potentials. Section 5.2 explores the ground-state configurations in the presence of gravitational sag both for dipolar and nondipolar BECs. Two cases for the gravity are then considered: when it is parallel to the z-axis (which is the polarization direction of the dipoles in dipolar BECs), and when it is slightly misaligned. In Section 5.3, we analyze the dynamics of small oscillations due to a tiny variation in either the direction or strength of gravity. Section 5.4 extends our study to other sets of parameters and ranges of gravity. Finally, in Section 5.5 we summarize our results.

5.1 Shell-shaped BECs

We consider a dilute and weakly interacting gas of N dipolar bosons at zero temperature. As we discussed in Chapter 3, the Gross–Pitaevskii equation (3.12) accurately describes such a dipolar BEC within the mean-field framework[3] in the absence of gravity:

$$i\hbar\frac{\partial\psi(\mathbf{r},t)}{\partial t} = \left[-\frac{\hbar^2\nabla^2}{2m} + V_{\text{ext}}(\mathbf{r}) + g|\psi(\mathbf{r},t)|^2 + V_{\text{dd}}(\mathbf{r})\right]\psi(\mathbf{r},t)\,, \tag{5.1}$$

with the condensate wavefunction $\psi(\mathbf{r},t)$ normalized to the total number of atoms N and where m is the mass of the atoms. The atom–atom mean-field interaction is characterized by the contact interaction through the coupling constant (2.7)

$$g = \frac{4\pi\hbar^2 a_s}{m}\,, \tag{5.2}$$

where a_s is the s-wave scattering length, and by the dipole–dipole interaction

$$V_{\text{dd}}(\mathbf{r}) = \int d\mathbf{r}'\, U_{\text{dd}}(\mathbf{r}-\mathbf{r}')\,|\psi(\mathbf{r}',t)|^2\,. \tag{5.3}$$

[3]For the mean-field approximation to hold, one assumes that both quantum and thermal fluctuations are negligible (see Chapter 2 for more details). In the present chapter, we do not include any beyond mean-field correction, as the mean-field approximation is enough to describe the interplay between the dipolar interactions and the gravitational sag. Outside this regime, however, shell-shaped dipolar BECs may eventually form supersolid structures in highly dipolar systems due to the stabilizing effect of quantum fluctuations (Sánchez-Baena et al., 2023a). The emergence of supersolidity in such systems depends both on the interactions and on the parameters of the trapping potential and, unlike dipolar shells in the mean-field regime, the resulting supersolids remain almost unaffected by the gravitational sag (Ciardi et al., 2024). Thermal fluctuations may also facilitate the formation of supersolids in such systems, as was observed very recently for dipolar BECs (Sánchez-Baena et al., 2023b).

For a sample of dipolar atoms fully polarized along the z-axis with dipolar moment $\boldsymbol{\mu} = \mu\,\hat{\mathbf{e}}_z$, the dipolar potential (3.2) is

$$U_{\mathrm{dd}}(\mathbf{r}-\mathbf{r}') = \frac{C_{\mathrm{dd}}}{4\pi}\frac{1-3\cos^2\theta}{|\mathbf{r}-\mathbf{r}'|^3}\,. \tag{5.4}$$

We recall that $|\mathbf{r}-\mathbf{r}'|$ is the relative distance between particles, θ is the angle between $\mathbf{r}-\mathbf{r}'$ and the direction of polarization, and C_{dd} is $\mu_0\mu^2$ (d^2/ϵ_0) for a magnetic (electric) dipole moment.

Contact interactions are characterized by the s-wave scattering length a_s. Similarly, one can introduce an effective length for the dipole–dipole interactions (3.17),

$$a_{\mathrm{dd}} = \frac{C_{\mathrm{dd}}m}{12\pi\hbar^2}\,. \tag{5.5}$$

Then, the relative strength of the interactions is given by the ratio of these two characteristic lengths $\varepsilon_{\mathrm{dd}} = a_{\mathrm{dd}}/a_s$ (3.18).

5.1.1 Shell-shaped potentials

Shell-shaped BECs can be realized experimentally by using time-dependent, radiofrequency induced adiabatic potentials within a conventional magnetic trap (as was originally proposed by Zobay and Garraway, 2001, 2004).

In atoms with some internal states, the potentials that determine the center-of-mass motion of the atoms depend on these internal states. When two or more of the internal states are coupled by a radiofrequency external field, the motion of the atoms is no longer determined by the bare potentials but by the so-called *dressed* (or adiabatic) potentials. The resulting adiabatic potentials[4] are widely tunable.

These bubble (or shell-shaped) potentials can be written as (Rhyno et al., 2021; Zobay and Garraway, 2001, 2004)

$$V_{\mathrm{bubble}}(\mathbf{r}) = \frac{1}{2}m\omega_0^2 a_{\mathrm{ho}}^2\sqrt{\frac{1}{4}\left(r^2-\Delta\right)^2+\Omega^2}\,, \tag{5.6}$$

where $a_{\mathrm{ho}} = \sqrt{\hbar/(m\omega_{\mathrm{ho}})}$ is the harmonic oscillator length, with ω_{ho} the frequency of the bare harmonic confinement, and ω_0 is the single-particle frequency of small oscillations. The dimensionless parameters Δ and Ω control the radius and width of the shell, and physically correspond to the effective detuning between the applied radiofrequency field and the energy of the internal states (Δ) and to the Rabi coupling between those energy states (Ω). One can study the transition from a filled spherical BEC to a hollowed BEC, which implies a change in topology, by tuning these parameters.

[4] The term *adiabatic* then comes from the fact that these potentials emerge from an adiabatic deformation of a conventional magnetic trap. See review by Perrin and Garraway (2017) for more details on radiofrequency-dressed adiabatic potentials.

If the thickness of the shell is small compared to its radius, the bubble trap potential (5.6) can be approximated by a radially-shifted harmonic trap (Padavić et al., 2018; Sun et al., 2018):

$$V_{\text{ext}}(\mathbf{r}) = \frac{1}{2} m\omega^2 (r - r_0)^2 \ ; \tag{5.7}$$

this situation is the so-called *thin-shell limit*[5]. This potential (5.7) defines a spherically symmetric shell[6] of radius r_0, with effective frequency $\omega = \omega_x = \omega_y = \omega_z$ and radial coordinate $r^2 = x^2 + y^2 + z^2$.

5.2 Ground states: interactions and gravity

Let us consider from now on a typical dipolar BEC within the mean-field regime, e.g., $N = 10000$ ^{164}Dy atoms polarized along the z-axis with magnetic dipolar moment $\mu = 10\,\mu_{\text{B}}$, scattering length $a_{\text{s}} = 120\,a_0$, and mass $m = 164$ amu. The relative strength of the interactions is $\varepsilon_{\text{dd}} = 1.11$ in this case.

In this section, we will characterize the ground state of the system in the absence of gravity with and without dipolar interactions (Subsection 5.2.1) and then analyze the effect of the gravitational sag for both cases (Subsection 5.2.2). We obtain the ground state wavefunction for the 3D spherical-shell geometry described above by numerically solving the time-independent GPE[7] (5.1) with the imaginary-time propagation method.

Both for the results presented in this section and those in Section 5.3, we have verified that the numeric results do not change when changing the number of points or the size of the numerical grid. Regarding the density profiles plotted along the chapter, the size of the 3D box we show in the figures is 16 μm $\times$ 16 μm $\times$ 16 μm. As in the other chapters, we will refer to condensates with only contact interactions as *nondipolar* and to those with both contact and dipolar interactions as *dipolar*.

5.2.1 Dipole–dipole interactions

Due to the anisotropic character of the dipole–dipole interactions, the density of the ground state elongates along the polarization direction to minimize the energy of the system. This effect, known as magnetostriction, combines with the geometry of the trapping potential to bring in new configurations that are not present in nondipolar

[5]The thin-shell limit occurs for large values of the detuning Δ. Since the bubble trap potential (5.6) has a minimum at $r = r_0 = \sqrt{\Delta}$, the thin-shell limit is applicable for shells with a large radius.

[6]One should consider ellipsoidal traps, as in the experiments, for a more realistic description of the system. However, we will consider spherical shells for simplicity since the ellipsoidal geometry results in shells with a nonuniform density, which adds more complexity to the system.

[7]As discussed in Chapter 3 when introducing the mean-field formalism for dipolar condensates, we recall here that the dipolar term turns the GPE into a nonlocal and integro-differential equation that is, in general, more complicated to solve. To facilitate calculations, one can evaluate the dipolar interaction integral using Fourier transform techniques (see Abad et al., 2009, and references therein); in particular, we use the FFTW package by Frigo and Johnson (2005).

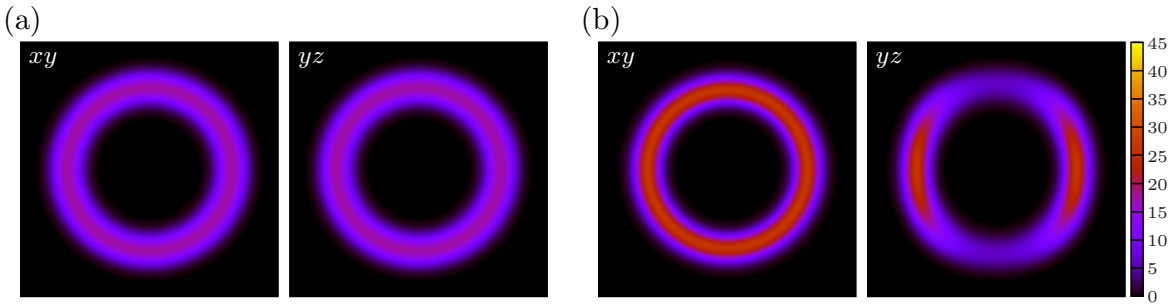

Figure 5.1: Bose–Einstein condensate confined in a spherical shell-shaped potential with frequency $\omega = 2\pi \times 100$ Hz and radial shift $r_0 = 3\sqrt{3}\ \mu$m. (a) Nondipolar and (b) dipolar BEC with $\epsilon_{dd} = 1.11$. The dipoles have a magnetic moment $\mu = 10\,\mu_B$ and are oriented parallel to the z-axis. The left (right) panel of each case represents the 2D density profile in the xy (yz) plane for a spherical shell-shaped BEC. Each plane shows a view of 16 μm $\times$ 16 μm. The color scale corresponds to the density and ranges from 0 (black) to 45 μm^{-3} (yellow). All the following figures of this chapter use the same color scale and numerical grid. For reference, the peak density is (a) 17.48 μm^{-3} and (b) 26.97 μm^{-3}.

systems[8].

Figure 5.1 shows the 2D contour plots of the density in the xy plane (left panels) and yz plane (right panels) for a BEC confined in a shell-shaped potential (5.7). The plots correspond to a nondipolar condensate (a), and a dipolar condensate with the dipoles aligned with the z-axis (b). The BEC is shell-shaped and has a hollow core due to the confinement. Note that the density distribution for the nondipolar case is isotropic [see Fig. 5.1(a): both left and right panels are equivalent]. In the presence of dipole–dipole interactions, on the other hand, the density accumulates around the equatorial region of the shell [see right panel of Fig. 5.1(b)]. In the equator of the shell, the dipoles sit mostly head to tail such that the effective interaction is attractive, while in the polar region, the dipoles lie in a side-by-side configuration instead, which results in a repulsive interaction.

This anisotropy in the ground state of the system, which comes from the anisotropic character of the dipolar interactions, has already been observed in spherical shell-shaped potentials (Adhikari, 2012; Diniz et al., 2020) and appears as well in toroidal condensates (Abad et al., 2010). Although the density profiles in the xy plane are almost the same for the dipolar and nondipolar cases [compare left panels on Fig. 5.1(a) and (b)], the peak density (i.e., its maximum value) is higher when dipole-dipole interactions are present than when the system presents only contact interactions. This asymmetry in the density profile increases with the relative strength between the interactions ε_{dd} (Abad et al., 2010; Adhikari, 2012), as one may expect.

[8]In the first dipolar condensates, for instance, this effect was already observed as the appearance of novel structured ground states for some values of the strength of the dipolar interactions and the trap anisotropy (Lahaye et al., 2009). Later on, this feature led to the proposal of a self-induced bosonic Josephson junction in a dipolar condensate confined in a toroidal trap (Abad et al., 2011, 2015).

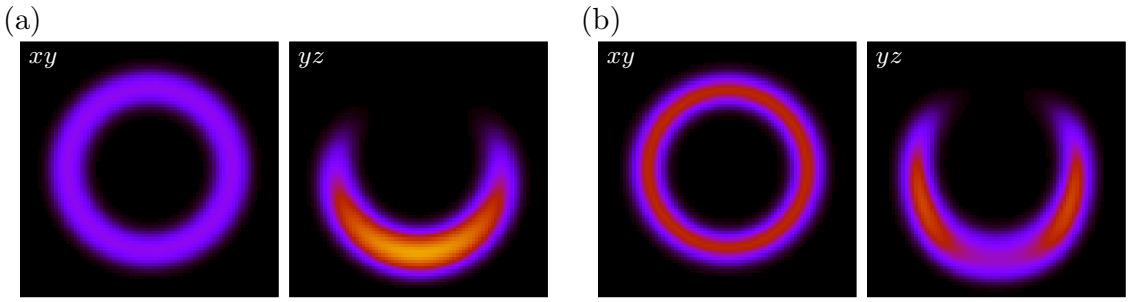

Figure 5.2: Same case as plotted in Fig. 5.1 but in the presence of a small gravity of strength $0.005\, g_{\mathrm{E}}$ and aligned with the z-axis, with $g_{\mathrm{E}} = 9.8\ \mathrm{m\,s^{-2}}$ the terrestrial gravity. (a) Nondipolar BEC. (b) Dipolar BEC, where dipoles have magnetic moment $\mu = 10.0\, \mu_{\mathrm{B}}$ and are aligned with the z-axis. The color scale and box size are the same as in Fig. 5.1. For reference, the peak density is (a) 38.91 $\mu\mathrm{m}^{-3}$ and (b) 29.26 $\mu\mathrm{m}^{-3}$.

5.2.2 Gravitational sag

One can account for the effect of gravity by including an additional potential term to the GPE (5.1), which we will refer to the *gravitational sag potential* V_g (Sun et al., 2018). To study the effects of the anisotropy of the dipole–dipole interactions, we consider that the direction of gravity is in general not aligned with any of the axes of the trap but lies instead in the xz plane. Then, the gravitational sag potential reads

$$V_g(\mathbf{r}) = mg\,(x\sin\vartheta + z\cos\vartheta)\ , \tag{5.8}$$

where ϑ is the angle between the direction of gravity and the z-axis (i.e., the polarization direction). If the gravity is aligned with the z-axis ($\vartheta = 0$), the gravitational sag simplifies to $V_g(z) = mgz$, which is equivalent to displacing the center of the trap vertically (Jezek et al., 2004; Sun et al., 2018).

In this Subsection, we investigate the effect of gravity in the spherical shell-shaped dipolar and nondipolar condensates that we considered previously (see Subsection 5.2.1). We will limit our study to small strengths of gravity, i.e., values larger than microgravity but still smaller than Earth's gravity by some orders of magnitude, since the terrestrial gravity destroys shell-shaped condensates (Lundblad et al., 2019).

Gravity aligned with the z-axis

Let us first consider a gravity aligned with the z-axis which, for dipolar BECs, is parallel to the polarization direction. Figure 5.2 shows the numerical results [see Fig. 5.1 for comparison without gravity]. As one can see in the yz plane (right panel) of the nondipolar case [Fig. 5.2(a)], the atoms fall to the bottom of the shell-shaped potential. Due to the axial symmetry of the system (confinement, gravity, and polarization), the density distribution in the xz plane is the same as in the yz plane. The deformation of the trap results in a partially filled shell and is a clear signature of the gravitational sag (Frye et al., 2021; Sun et al., 2018).

In the presence of dipole–dipole interactions [Fig. 5.2(b)], the interplay between their anisotropic character, the confining potential, and the gravitational sag leads to

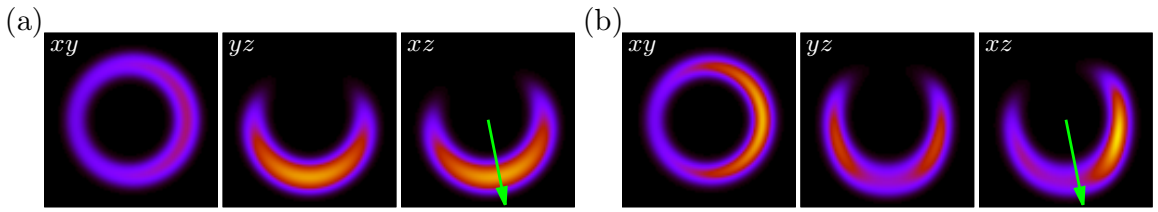

Figure 5.3: Same as Fig. 5.2 but with an angle $\vartheta = -0.2$ rad between the gravity and the z-axis such that gravity lies in the xz plane. (a) Nondipolar BEC. (b) Dipolar BEC with dipoles polarized along the z-axis. The green arrow in the xz plane indicates the direction of gravity.

a partially filled shell as in the nondipolar case, but now with a density depletion in the bottom region. As we discussed in the situation with no gravity, the repulsive interaction between two parallel dipoles significantly reduces the density at the bottom of the condensate [see the right panel of Fig. 5.2(b)]. Then, the maximum-density band lies slightly below the equatorial region, depending on the balance between the gravity and the dipolar moment of the atoms.

Misaligned gravity

We now explore a more general situation where the gravity and polarization direction are not aligned. Instead, gravity forms an angle ϑ with the z-axis and lies in the xz plane. We show in Fig. 5.3 the 2D contour density plots in the three planes: xy (left), yz (middle), and xz (right). Figure 5.3(a) corresponds to a nondipolar BEC, and Fig. 5.3(b) to a dipolar one. For a nondipolar BEC, the density profile in the yz plane remains almost unaltered as compared to Fig. 5.2(a), but the maximum of the density in the xz plane tilts in the direction of gravity, which is marked with a green arrow in the right panels of Figs. 5.3(a) and (b). As one can see in the xy plane, this tilting also produces an accumulation of particles on the right side of the bottom region of the shell.

The situation becomes more complex for dipolar BECs, when the gravity and the dipoles are not aligned, since the polarization axis fixes a privileged direction that breaks the symmetry. As a result, the density profiles in the xz and yz planes are now different from the nondipolar case [see Fig. 5.3(b)]. The density configuration in the yz plane is similar as well to the density profile when the gravity is parallel to the z-axis [see the right panel of Fig. 5.2(b)]. However, changes in the density in the xz plane are more significant now: the maximum of the density lies in the right lobe of the shell and, compared to the direction of gravity, has a larger tilting angle. Within this region, the dipoles mostly lie head to tail, which results in an effective attractive interaction, whereas in the bottom of the shell the atoms sit side by side and thus the net interaction is repulsive.

Note that this symmetry-breaking phenomenon that shows in the xz plane is an effect of the anisotropic character of the dipole–dipole interactions and depends both on the tilting angle ϑ and on the strength of gravity. In Fig. 5.4, we plot the density profiles in the three planes (xy, yz and xz) for a condensate confined in the same shell-shaped

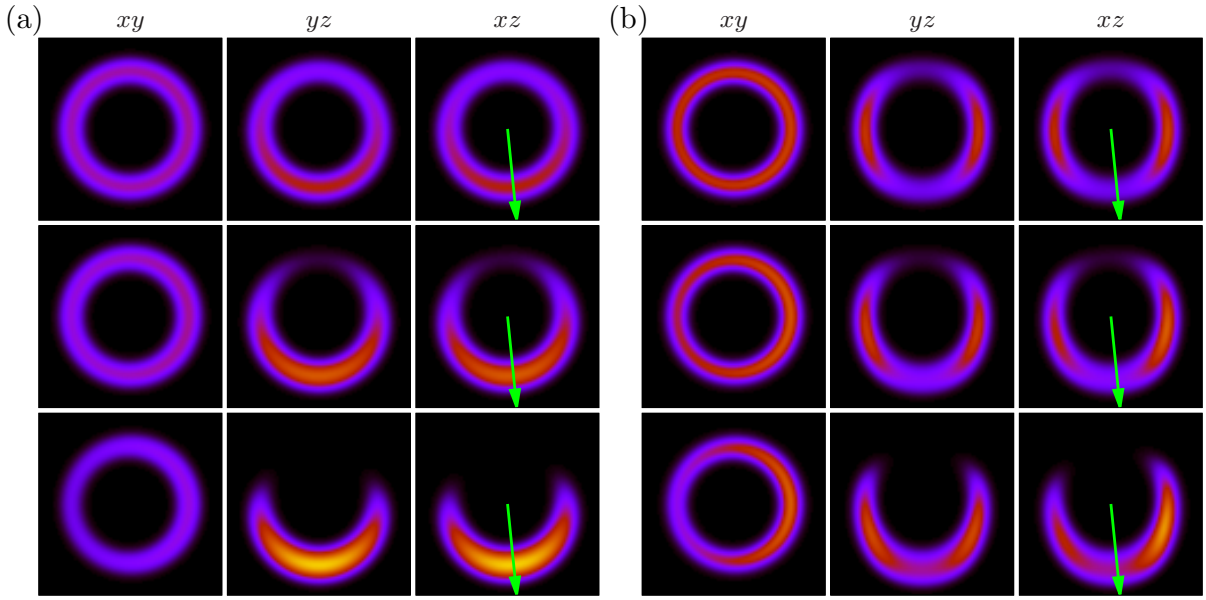

Figure 5.4: Same as Fig. 5.3 with an angle $\vartheta = -0.1$ rad between the gravity and the z-axis. (a) Nondipolar BEC. (b) Dipolar BEC, with dipoles polarized along the z-axis. The strength of gravity for each case, from top to bottom, is 0.001 g_{E}, 0.003 g_{E}, and 0.006 g_{E}.

potential and for different (small) values of the gravity ($0.001 \leq g/g_{\mathrm{E}} \leq 0.007$), which is tilted an angle $\vartheta = -0.1$ rad from the z-axis. Figure 5.4(a) shows the numerical results for a nondipolar BEC, and Fig. 5.4(b) for a dipolar BEC. For small values of the strength of gravity (below 0.003 g_{E}), the condensate forms a full shell that has a higher density on the bottom. Increasing the strength (above 0.004 g_{E}), the system is no longer a full shell due to the sag effect of the gravity, which depletes the top of the trap such that the shape of the condensate is a hollow half shell. In the presence of dipolar interactions, their anisotropic character counterbalances the effect of gravity. Then, as a result, the hole that appears at the top of the shell is small compared with the nondipolar case.

5.3 Dynamics of small oscillations

This section explores the dynamical response of the system when subjected to gravity perturbations. In particular, we trigger the dynamics by instantaneous changing either gravity's strength or its tilting angle. To obtain the real-time evolution of the system, we solve the GPE (5.1) numerically[9].

First, in Subsection 5.3.1, we consider gravity can be tilted forming a small angle ϑ

[9]We have calculated some cases with longer evolution times to check the numerical value of the frequencies and determine the precision with which we obtain them. For example, for a nondipolar BEC with gravity strength $g = 0.005\, g_{\mathrm{E}}$ and angle variation of 0.1 rad [see Figs. 5.5(a) and 5.6(a)] we obtain the frequency 15.80 Hz for an evolution time $t_{\mathrm{f}} = 0.3$ s, and 15.82 Hz for $t_{\mathrm{f}} = 1.0$ s. We have also checked for other cases that the results start to vary at the second decimal digit. Therefore, the estimated error of the frequencies given in Subsections 5.3.1 and 5.3.2 is ±0.05 Hz.

		Gravity		Frequency (Hz)	
		Angle (rad)	Strength (g_{E})	Nondipolar	Dipolar
Variations in the angle	Half shell	$-0.1 \rightarrow 0.0$	0.005	15.80	10.71
	Full shell	$-0.1 \rightarrow 0.0$	0.002	15.87	10.62
Variations in the strength	Half shell	0.0	$0.005 \rightarrow 0.006$	24.69	25.12
	Full shell	0.0	$0.003 \rightarrow 0.002$	16.10	22.20

Table 5.1: Summary of numerical frequencies obtained from the oscillation of the center of mass for the particular cases studied in Subsections 5.3.1 and 5.3.2. We indicate the angle with the z-axis and the strength of gravity, and which of them is changed to trigger the dynamics. For each situation, we give the frequency for both nondipolar and dipolar BECs, and we indicate if the shape of the ground state is a half shell or a full shell. The frequency associated to variations in the angle (see Subsection 5.3.1) is calculated from the oscillation of $\langle x(t)\rangle$. For variations in the strength (see Subsection 5.3.2), we calculate the frequency from the oscillation of $\langle z(t)\rangle$.

with the z-axis but is still contained in the xz plane. Then, we suddenly align it with the z-axis at $t = 0$. Later, in Subsection 5.3.2, the gravity is parallel to the z-axis ($\vartheta = 0$), and we investigate the dynamics by slightly changing its strength from g_0 to g. To avoid large oscillations and more complex dynamics, we constrain our study to small variations. Table 5.1 provides a summary of all the particular cases discussed in this section.

5.3.1 Variations in the orientation of gravity

We consider $\vartheta = -0.1$ rad for all the results presented here. For a given strength of gravity, we have checked that the dynamics are the same regardless of the sign and magnitude of the initial tilting angle as long as the angle is small. We begin this subsection by studying two particular cases (with $g > 0.004\, g_{\mathrm{E}}$ and $g < 0.004\, g_{\mathrm{E}}$, respectively) to discuss the effect that the shape of the ground state has on the dynamics. The results we present for discussion are the oscillations of the center of mass (Fig. 5.5, see numerical frequencies in Tab. 5.1) and snapshots of the density for selected times within the first period of the evolution (Fig. 5.6). Finally, we analyze how the oscillation frequency depends on the strength of gravity (see Fig. 5.7).

Particular cases

We start with a gravity of strength $g = 0.005\, g_{\mathrm{E}}$ such that the system resembles a half shell, as we discussed in Section 5.2. First, we consider a nondipolar shell-shaped BEC. In Fig. 5.5(a), we present the time evolution of the coordinates of the center of mass: $\langle x(t)\rangle$, $\langle y(t)\rangle$, and $\langle z(t)\rangle$. Since we prepare the condensate with a slight misalignment of the gravity, the sudden alignment with the z-axis forces the system to bounce back and forth in the xz plane around the new equilibrium position, the z-axis. This behavior shows as a sinusoidal-like oscillation of $\langle x(t)\rangle$ as a function of time, while the other coordinates remain almost unaltered. The sinusoidal fit of the numerical evolution of

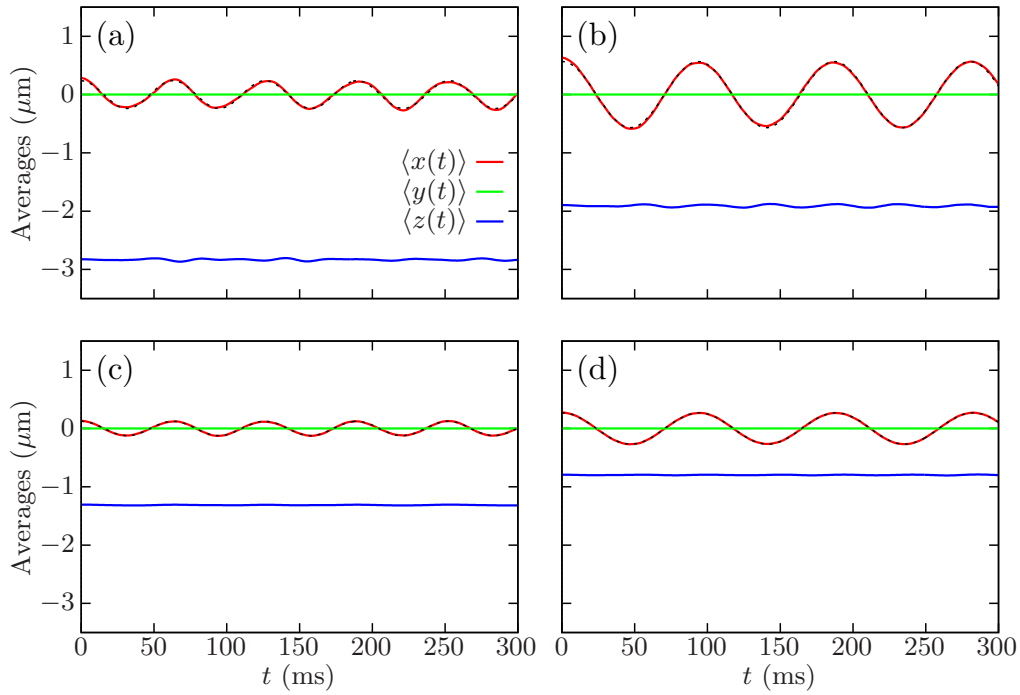

Figure 5.5: Numerical evolution of the center-of-mass coordinates. Gravity is initially tilted an angle $\vartheta = -0.1$ rad with the z-axis. We consider the two possible static regimes described in the text: a half shell for $g = 0.005\, g_{\mathrm{E}}$ in a (a) nondipolar and (b) dipolar condensate, and a full shell for $g = 0.002\, g_{\mathrm{E}}$ in a (c) nondipolar and (d) dipolar condensate. The black dashed lines indicate the sinusoidal fits of the numerical results for $\langle x(t)\rangle$, from where we obtain the oscillation frequencies: (a) 15.80 Hz, (b) 10.71 Hz, (c) 15.87 Hz, and (d) 10.62 Hz. See summary of numerical frequencies in Tab. 5.1.

$\langle x(t)\rangle$ gives a frequency of 15.80 Hz[10]. Figure 5.6(a) displays a few snapshots of the 2D density profiles in the two planes where the oscillations are observable, xy and xz. The times shown in the plot cover a whole period of the oscillation. Since the shell-shaped BEC is 3D, the oscillatory behavior of $\langle x(t)\rangle$ [see Fig. 5.5(a)] produces symmetric rearrangements of the density in the other directions, as one can see in the xy plane of Fig. 5.6(a).

Figure 5.5(b) shows the numerical evolution of the center of mass for a dipolar condensate with an initial tilting angle of gravity $\vartheta = -0.1$ rad. As we discussed before [see Section 5.2 and Fig. 5.4(b)], the filled region of the shell-shaped potential appears at a larger tilting angle in a dipolar condensate than in a nondipolar one. This feature of the anisotropy of the dipole–dipole interactions results in a larger oscillation amplitude of $\langle x(t)\rangle$ in dipolar BECs. The sinusoidal fit of the numerical evolution of $\langle x(t)\rangle$ gives a frequency of 10.71 Hz; as in the nondipolar case, the other components of the center of mass of the system, $\langle y(t)\rangle$ and $\langle z(t)\rangle$, show practically no variations. When the gravity is suddenly aligned, the system oscillates around the z-axis as expected. However, unlike

[10]We checked that the frequency of oscillation is close to this value when the initial angle $|\vartheta|$ is approximately below 0.15 rad.

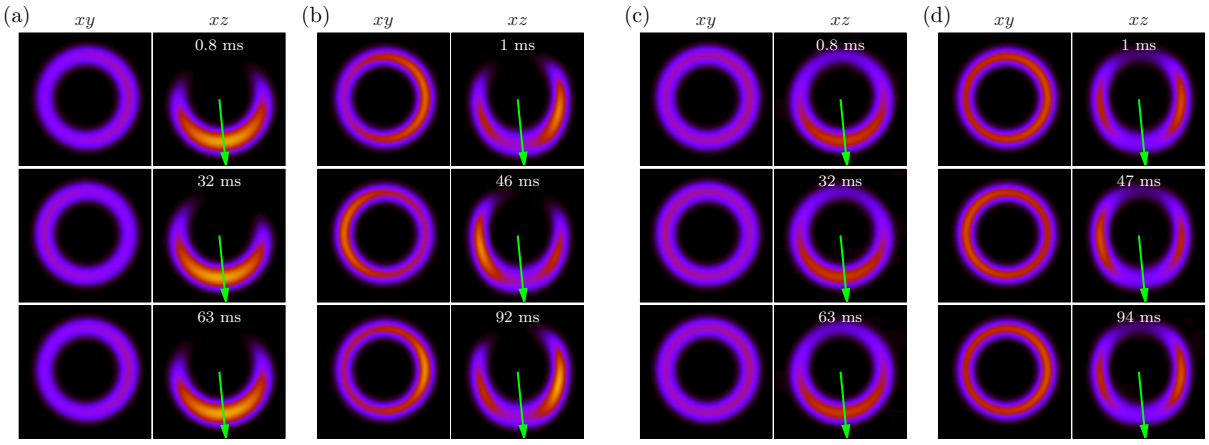

Figure 5.6: Snapshots of the 2D density profiles in the xy (left panels) and xz (right panels) planes at different times of the evolution. We do not show the yz planes because the densities remain unchanged there, as the variation in gravity is constrained to the xz plane. The initial tilt of the gravity is $\vartheta = -0.1$ rad, and we study the same two situations as in Fig. 5.5: a half shell for $g = 0.005\, g_{\mathrm{E}}$ in either (a) a nondipolar BEC or (b) a dipolar BEC, and a full shell for $g = 0.002\, g_{\mathrm{E}}$ in (c) a nondipolar BEC and (d) a dipolar BEC. In both dipolar cases, the dipoles have magnetic moment $\mu = 10\, \mu_{\mathrm{B}}$. The green arrow shows the initial direction of gravity, which is later aligned with the z-axis to start the dynamics. See summary of cases in table 5.1.

in the nondipolar case, the atoms do not cross over the bottom region of the half shell, where the net dipolar interaction is repulsive: their movement is instead constrained to the high-density band that appears below the equatorial region. One can see this behavior in Fig. 5.6(b), which shows a few snapshots covering one period in the xy and xz planes.

Finally, we study the situation where the gravity is small enough that the BEC still retains its full shell shape. In particular, we consider $g = 0.002\, g_{\mathrm{E}}$. From Fig. 5.5(c) and (d), one can see that the oscillations of $\langle x(t) \rangle$ are broader and slower in the dipolar BEC than in the nondipolar one, as in the previous case. The oscillation frequencies we obtain from the fit are 15.87 Hz (nondipolar BEC) and 10.62 Hz (dipolar BEC), which resemble those from the previous case. If we compare these oscillations [Fig. 5.5(c) and (d)] with those obtained for a heavier gravity [Fig. 5.5(a) and (b)], we observe that the frequencies are similar in both the nondipolar and the dipolar BECs, but the amplitudes of the oscillations are much lower now. From the snapshots of the density we show in Fig. 5.6(c) and (d), one can see that in the case of a smaller gravity, as expected, the atoms can move around the whole shell (not just the lower part), which could explain why the oscillations of the center of mass are more restricted in the x direction. We will explore in more detail the effect of gravity in the dynamics in the following subsection.

The role of gravity

Here, we study the dynamics of small oscillations due to variations in the tilting angle (initially $\vartheta = -0.1$ rad in all the cases) for different strengths of gravity. In Fig. 5.7, we

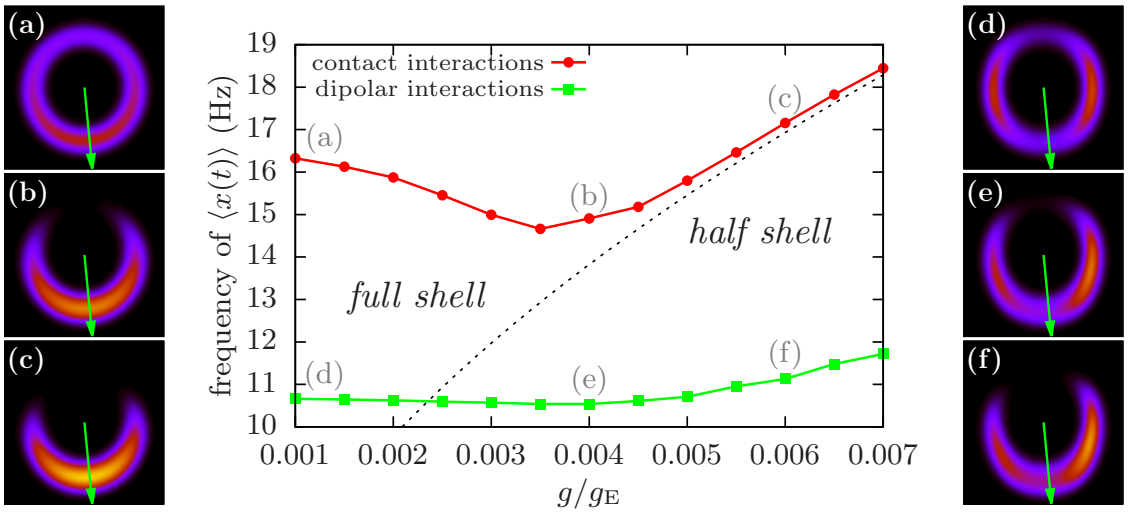

Figure 5.7: Oscillation frequency of $\langle x(t)\rangle$ as a function of the gravity for a nondipolar (red) and dipolar (green) BEC, where the gravity has an initial tilting angle $\vartheta = -0.1$ rad. We obtain the oscillation frequency by fitting a sinusoidal function to the numerical data. The panels on both sides show the 2D density profiles of the initial state in the xz plane (which contains gravity) for the different values of the gravity labeled from (a) to (f), both for the nondipolar BEC (left panels) and the dipolar one (right panels). The green arrow, as in the previous figures, marks the direction of gravity. Lines between data points are added to guide the eye. The dashed line indicates the frequency of a mathematical pendulum, $\sqrt{g/r_0}$, with fixed length r_0.

show the oscillation frequency of the x coordinate of the center of mass, $\langle x(t)\rangle$, as a function of the strength of gravity. We consider both nondipolar and dipolar BECs. As Fig 5.7 shows, the oscillation frequency depends on the strength of gravity, and two different behaviors arise: first, starting from the lowest gravity studied here, the frequency decreases as g increases until it reaches a particular value (between $0.003\, g_{\mathrm{E}}$ and $0.004\, g_{\mathrm{E}}$); then it increases again. These two behaviors are related to the two distinct shapes that can be observed in the ground states of the system for different values of gravity, as we show in Fig. 5.4 and discussed in Section 5.2: when the strength of gravity is small, the ground state of the system is a full shell, while for heavier values of gravity it resembles a half shell.

At small strengths of gravity, the condensate is a full shell with a higher density at the bottom of the trap. Then, an increase in gravity drags more atoms to the bottom of the trap, which leads to a decrease in the oscillation frequency. When considering dipolar interactions, though, their anisotropic nature compensates for the effect of gravity; as a result, the oscillation frequency becomes almost invariant to small changes in the strength of gravity.

On the other hand, at larger values of g, the system is no longer a full shell but a half shell, and the oscillation frequency increases as the strength of gravity does. The angular frequency of a mathematical pendulum is related to gravity g and its length l by $\sqrt{g/l}$. For the nondipolar case, in particular, we can see that for $g > 0.004\, g_{\mathrm{E}}$, the frequency approaches this behavior as g grows. For comparison, we show in Fig. 5.7 the

frequency for a pendulum (see dashed line) assuming a fixed length $l \sim r_0 = 3\sqrt{3}\,\mu$m. In the dipolar case, the frequency also grows with gravity for $g > 0.005\,g_{\rm E}$. However, now the system does not behave like a mathematical pendulum. The atoms bounce from the right to the left lobe, but they never cross the bottom region of the shell since they can only move around the high-density band, as we show in Fig. 5.6 and discuss in the accompanying text. Therefore, the classical pendulum analogy fails in this case.

5.3.2 Variations in the strength of gravity

In the previous subsection, we discussed the dynamics due to variations in the angle of gravity. Here we fix the angle of gravity with the z-axis to zero ($\vartheta = 0$) and study the system's response to variations in the strength of gravity. As before, we constrain our study to small oscillations, which now translates to small variations in the strength of gravity. We start by preparing the system under a gravity g_0 aligned with the z-axis, and then, at $t = 0$, we change g_0 to g.

In the first part of this subsection, we study in detail two cases: first, when $g, g_0 > 0.004\,g_{\rm E}$, so the corresponding ground states resemble a half shell, as discussed in Section 5.2; then, we set $g, g_0 < 0.004\,g_{\rm E}$, with both values of gravity laying in the regime where the system is still a full shell. See Tab. 5.1 for a summary of the numerical frequencies obtained and Fig. 5.8 for some snapshots of the evolution. For these cases, we choose a large change in gravity ($|g - g_0| = 0.001\,g_{\rm E}$) to see the system's dynamics well. In the second part, we fix a smaller value of the variation ($|g - g_0| = 0.0001\,g_{\rm E}$) to study small oscillations and compare the frequencies of oscillation obtained for different values of the final gravity g (see Fig. 5.9).

Particular cases

In the first case of our study, the initial strength of gravity is $g_0 = 0.005\,g_{\rm E}$, and the evolution starts when we abruptly increase it to $g = 0.006\,g_{\rm E}$. Within these values of the gravity, the ground state of the system resembles a half shell, as we already mentioned (see the last row in Fig. 5.4). In Fig. 5.8(a) and (b), we plot the densities at different times to show the dynamics of both the nondipolar and dipolar cases (the snapshots cover a whole period of the oscillation). In the nondipolar case [Fig. 5.8(a)], the atoms are mainly located at the bottom of the shell, occupying a region that shrinks and grows periodically due to the increase in gravity. This behavior resembles a spring that oscillates vertically. Here, though, the movement of the atoms is confined to the surface of the shell. In the dipolar case [Fig. 5.8(b)], instead, the band of maximum density appears below the equatorial region. Then, the sudden change in gravity causes this band to oscillate along the z direction. Since the gravity is parallel to the z-axis, we study the oscillation frequency of the z coordinate of the center of mass through a sinusoidal fit to the numerical results for $\langle z(t)\rangle$. We obtain a frequency of 24.69 Hz for the nondipolar BEC and 25.12 Hz for the dipolar one. Unlike in Subsection 5.3.1, here we find that both frequencies are similar.

For the second case, where the gravity is small enough that the system has the shape of a full shell, we decrease the initial gravity $g_0 = 0.003\,g_{\rm E}$ to $g = 0.002\,g_{\rm E}$. The dynamics

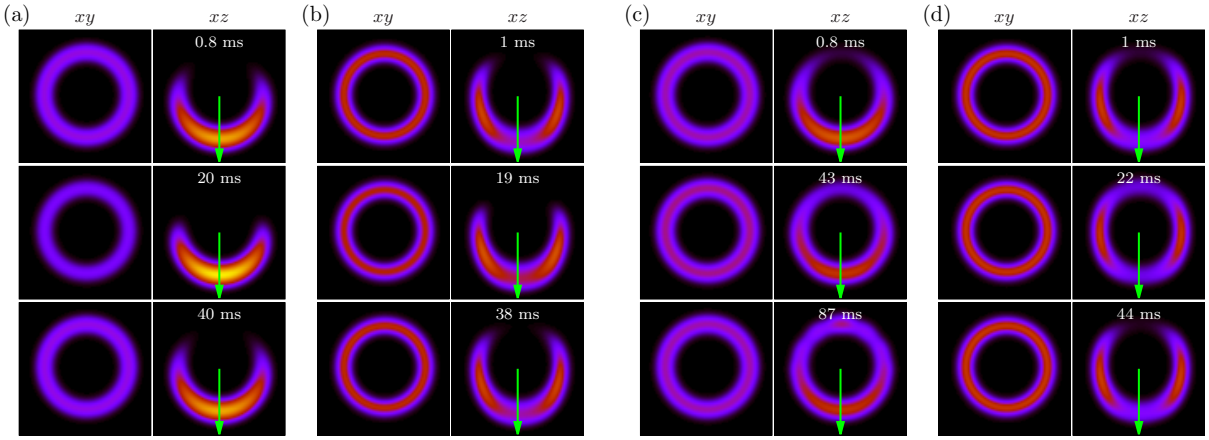

Figure 5.8: Snapshots of the 2D density profiles in the xy (left) and xz (right) planes at different times of the evolution. Gravity is parallel to the z-axis, and we vary its strength from g_0 to g at $t = 0$. Since the densities in the xz and yz planes are equivalent, we do not show the yz planes. First case, half shell: $g_0 = 0.005\, g_E$ and $g = 0.006\, g_E$, for (a) a nondipolar and (b) a dipolar condensate. Second case, full shell: $g_0 = 0.003\, g_E$ and $g = 0.002\, g_E$, also for (c) a nondipolar and (d) a dipolar BEC. The dipole moment, $\mu = 10\, \mu_B$, is the same for all the cases with dipolar interactions. See summary of cases in Tab. 5.1. Note that the density accumulation that appears in case (c) at the top of the shell, the right panel, of the last row: it comes from considering such a large change in gravity, $|g - g_0| = 0.001\, g_E$. To avoid this, we study the effect of gravity on the oscillation frequency (Figs. 5.7 and 5.9) with smaller variations.

are very similar to the previous case, as one can see in Fig. 5.8(c) and (d). In this case, however, the oscillation frequencies of $\langle z(t) \rangle$ for the nondipolar and dipolar BECs are more different; in particular, we find 16.10 Hz for the nondipolar BEC and 22.20 Hz for the dipolar one.

The oscillations of the center of mass in both frequency and amplitude depend on the strength of gravity. These results match those found in Subsection 5.3.1. In nondipolar BECs, when the gravity is light and the system is a full shell, we find that the oscillations are slow and broad since the atoms can move around the whole shell. For a heavier gravity, the atoms drop to the bottom of the trap. Then, the amplitude of the oscillation decreases while its frequency increases. The differences found in dipolar BECs come from the anisotropic nature of the dipolar interactions, which counterbalances gravity. The band of maximum density is no longer at the bottom region but below the equator. Therefore, compared to the nondipolar case, the oscillations change much less when one considers different strengths.

The role of gravity

Finally, we study the dynamics of small oscillations induced by a variation in the strength of gravity and how these results differ depending on whether the value of gravity is relatively small (and the ground state resembles a full shell) or large (when the system becomes a half shell). We choose $|g - g_0| = 0.0001\, g_E$ to ensure small oscillations. For

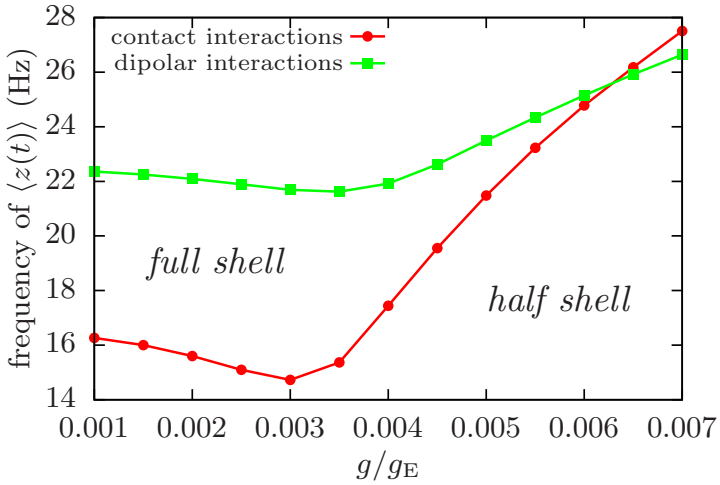

Figure 5.9: Oscillation frequency of $\langle z(t)\rangle$ as a function of the final gravity g, with initial gravity $g_0 = g + 0.0001\, g_E$. The red line corresponds to the nondipolar case, and the green line to the dipolar interacting BEC. As before, we obtain the oscillation frequency by fitting a sinusoidal function to the numerical data. Lines are added to guide the eye.

these values of $g - g_0$, the results we obtain for a given g are equivalent in frequency and amplitude either if $g > g_0$ or $g < g_0$. Therefore, we define from now on g_0 such that $g_0 = g + 0.0001\, g_E$.

In Fig. 5.9, we plot the frequency of oscillation of $\langle z(t)\rangle$ as a function of the final gravity g. The results resemble those from Fig. 5.7. The frequency increases with the final gravity for large values of the gravity (when the system is a half shell), while it decreases with the final gravity for smaller values (when the system resembles a full shell). Since the dipolar interaction compensates for the gravity, the effect of the variation in strength is more noticeable in the nondipolar BEC than in the dipolar BEC (as in Subsection 5.3.1) for small final gravities.

Comparing the results obtained for the nondipolar BEC either with changes in strength (see Fig. 5.9, red line) and orientation (see Fig. 5.7, red line), we can see that the frequencies lie within a similar range of values in both cases. The frequencies we obtain now for the dipolar BEC, however, are faster. This increase in frequency is an effect of the anisotropy of the dipolar interactions. In the first scenario (see Fig. 5.7, green line) the center of mass moves mainly along the x-axis, and all the dipoles point towards the z-axis. Then, an atom that moves in that direction feels a net repulsive interaction from its neighbors, which reduces the frequency of oscillation. In the second scenario (see Fig. 5.9, green line) the center of mass moves instead around the z-axis. Since the resulting interaction between dipoles along the direction of motion is attractive and twice as large as in the previous case, the frequency of the oscillation is much larger.

5.4 Extension to other systems

We write the time-dependent Gross-Pitaevskii equation (5.1) in dimensionless units in the usual way[11]: using the oscillator length $a_{\mathrm{ho}} = \sqrt{\hbar/(m\omega)}$ as the unit length, ω^{-1} as the unit time, and $\hbar\omega$ as the unit energy. Then, one can define three dimensionless constants, which are the coefficients of the gravitational, contact-interacting and dipolar terms of the dimensionless equation: $G = g/(a_{\mathrm{ho}}\omega^2)$, $C = 4\pi N a_{\mathrm{s}}/(a_{\mathrm{ho}})$, and $D = N m \mu_0 \mu^2/(4\pi\hbar^2 a_{\mathrm{ho}})$. We also define the dimensionless radius $\xi_0 = r_0/a_{\mathrm{ho}}$.

Thus, the system can be scaled in terms of these dimensionless constants. In our configuration, the numerical values are: $G = 31.62\,\tilde{g}$, $C = 1016.46$, $D = 268.27$ and $\xi_0 = 6.62$, where we introduce the gravity in units of the terrestrial gravity $\tilde{g} = g/g_{\mathrm{E}}$ for convenience, and we also fix $\varepsilon_{\mathrm{dd}} = 1.11$. With these values, one can translate the same physics to another set of parameters that are experimentally accessible in ^{52}Cr (Koch et al., 2008; Lahaye et al., 2007), ^{164}Dy (Lu et al., 2011), or ^{168}Er (Aikawa et al., 2012).

For example, we consider a condensate of ^{168}Er with $N = 10^4$ atoms, which has a dipolar moment of $7\,\mu_{\mathrm{B}}$. One can obtain the configuration proposed with our dimensionless constants by choosing a scattering length $a_{\mathrm{s}} \sim 60\,a_0$ and a trap frequency $\omega \sim 2\pi \times 390$ Hz. Then, the radius of the resulting shell is $r_0 \sim 2.6\,\mu$m, and the range of valid gravities (large enough that its effect is noticeable but does not destroy the system) is, in this case, between $0.008\,g_{\mathrm{E}}$ and $0.050\,g_{\mathrm{E}}$.

More generally, we can use these dimensionless constants and state that our study can be extended to values of gravity between $0.003\,g_{\mathrm{E}}$ and $0.023\,g_{\mathrm{E}}$ in units of $a_{\mathrm{ho}}\,\omega^2$. Consequently, it is possible to explore a different range of gravities by considering another set of parameters for the system.

For instance, going back to the system we consider in this chapter (^{164}Dy), one could study a range of gravities closer to microgravity by increasing the number of atoms and the radius of the shell, and reducing the frequency of the trap. Particularly, with $N \sim 3 \times 10^4$, $\omega \sim 2\pi \times 11$ Hz and $r_0 \sim 15.6\,\mu$m, the range of valid gravities lies between $4 \times 10^{-5}\,g_{\mathrm{E}}$ and $26 \times 10^{-5}\,g_{\mathrm{E}}$.

5.5 Summary of results

In the present chapter, we have studied the statics and dynamics of nondipolar and dipolar shell-shaped condensates in the presence of a small gravity. We have constrained our study to gravity values above microgravity (and thus non-negligible) and below terrestrial gravity, which destroys shells.

First of all, we have analyzed the ground states of the system in three cases: without gravitational sag, with gravity parallel to the z-axis (which is the polarization direction we considered for dipolar BECs), and with a small gravity misaligned with the z-axis and contained in the xz plane. We have discussed the effect of the dipolar interactions in either of the three cases. Next, we have done a more general analysis of the ground states to examine the effect of gravity's strength. Observing the shape that the system

[11] See derivation of Eq. (2.26) in Chapter 2 for more details

displays, we have defined two regimes: a full shell for small gravities and a half shell for larger gravities. These two regimes play a relevant role in the dynamical behavior of the system.

Later, we have studied the dynamics of small oscillations due to changes in the orientation and strength of gravity. For each of those two scenarios, and comparing the full shell and half shell regimes, we have studied two particular cases and we have analyzed, more generally, the effect that gravity has in the behavior of the oscillations when the variation (in angle or strength) is fixed and very small. With this, we have seen how the two static regimes translate into two distinct dynamical behaviors: the oscillation frequency increases with gravity for large values of gravity (half shell) while it decreases for smaller values (full shell). Additionally, we have compared the results obtained for nondipolar BECs with those obtained for their dipolar counterparts. We have discussed that dynamics due to changes in angle or strength are equivalent in the nondipolar BECs, but the dynamical behavior differs in dipolar BECs due to the anisotropic nature of their interactions, which counterbalances the effect of gravity. We have shown that even though the dipolar interaction adds a privileged direction to the one already defined by gravity, the resulting shells with gravitational sag and dipolar interactions present a configuration that, compared to the nondipolar one, is less sensitive to misalignments and perturbations in the gravitational sag.

Finally, we have extended our study to other systems, and we have seen that the range of valid gravities depends on the particular system in consideration. Therefore, one could choose a set of parameters (namely the mass, the frequency, and the number of atoms) such that the gravitational effects are neither negligible nor destructive at much smaller gravities than the ones we have studied here. We want to stress that the physics of shell-shaped condensates under gravitational sag is not limited to dysprosium BECs, as we have considered here. It can also be exported to other condensates with controllable contact interactions, either with and without dipolar interactions.

The atomic cloud in this system is not only sensitive to changes in its orientation, but it is also sensitive to small gravitational variations, either in its direction or strength. However, one cannot discern directly from our results (especially in the nondipolar case) if the cause of the oscillations is a change in gravity's orientation or its strength. Studying instead a more simplistic configuration, such as a ring-shaped BEC, may shed some light on how to discriminate between these two situations. In any case, these findings could pave the way to the experimental realization of a gravity or accelerometer sensor intended for small gravity conditions. Monitoring gravity and its changes from space in satellite missions (see Migliaccio et al., 2019, and references therein) is another possible application of this system. To conclude, we want to point out the experimental feasibility of the proposed system. We have used values for the experimental parameters that are currently available in laboratories.

6

Dynamical generation of dark–bright solitons in immiscible mixtures

A homogeneous quasi-1D Bose gas can be described within the mean-field framework by the 1D Gross–Pitaevskii equation (GPE), as in Eq. (2.53),

$$i\hbar\frac{\partial\psi(x,t)}{\partial t} = \left[-\frac{\hbar^2\nabla^2}{2m} + V_{\text{ext}}(x) + g_{1\text{D}}\,|\psi(x,t)|^2\right]\psi(x,t)\,. \tag{6.1}$$

This equation sustains soliton solutions (also called *matter waves*) if the external potential $V_{\text{ext}}(x)$ is either zero or uniform, as we discussed in Chapter 2 (see Section 2.3). For a harmonically confined system with a tight confinement along the y and z directions, the 1D coupling constant $g_{1\text{D}}$ relates to the 3D coupling constant $g_{3\text{D}}$ as (2.54),

$$g_{1\text{D}} = \frac{g_{3\text{D}}}{2\pi\,a_y a_z} = \frac{2\hbar^2}{m}\frac{a_s}{a_y a_z}\,, \tag{6.2}$$

where $a_{y,z}$ are the oscillator lengths in the y and z directions (the frozen directions) and a_s is the s-wave scattering length. The coupling constant characterizes the strength of the atom–atom interactions, which add a nonlinear term to the equation, $g_{1\text{D}}\,|\psi|^2\,\psi$. In Chapter 8, we will study an analogous system where the nonlinearity comes instead from the current density. We already introduced solitons in Chapter 2, but we will recall here their main properties.

Solitons are localized excitations that result from the competition between the nonlinearity and the dispersion of the system (Pitaevskii and Stringari, 2016). A key feature of solitons is that they propagate without changing their shape; such solutions that are robust against perturbations are often referred to as *topological states*. The sign of the coupling constant yields two different types of solitons in BECs (Frantzeskakis, 2010; Kevrekidis et al., 2010; Shamailov and Brand, 2018): dark (for $g > 0$) and bright (for $g < 0$) solitons.

Dark solitons exist when the interactions are repulsive, and are density dips characterized by a phase jump across the density profile. These solitons can be analytically

described[1] by

$$\psi_{\mathrm{D}}(x) = \sqrt{n_0}\tanh\left(\frac{x}{\sqrt{2}\xi}\right), \tag{6.3}$$

where n_0 is the density of the homogeneous background and $\xi = \hbar/\sqrt{2m|g|n_0}$ is the healing length (2.24). Bright solitons, which appear for attractive interactions, are self-bound wavepackets of the form (2.57)

$$\psi_{\mathrm{B}}(x) = \sqrt{n_0}\,\mathrm{sech}\left(\frac{x}{\sqrt{2}\xi}\right). \tag{6.4}$$

Bright solitons are the ground state of the system in 1D when the interactions are attractive; in higher dimensions, however, the condensate collapses due to attraction. In general, both dark and bright solitons are unstable in two- and three-dimensional systems.

Binary mixtures of condensates (Pu and Bigelow, 1998; Timmermans, 1998) provide a more complex scenario to study solitonic states (see Subsection 2.2.1 in Chapter 2). These mixtures can be composed of two hyperfine states, two isotopes of the same atomic species, or two completely different species. For generality, therefore, we will use the term *component* instead of *species*. The interplay between the inter- and intracomponent interactions, each characterized by the corresponding coupling constant, leads to different regimes: within the mean-field approximation, a miscible mixture can be stable, phase separate, or collapse. In addition, the competition between the two types of atom–atom interactions leads to novel solitonic states, such as dark–dark solitons (Hoefer et al., 2011) or dark–bright solitons (Becker et al., 2008; Hamner et al., 2011; Middelkamp et al., 2011). This last case will be the main focus of the present chapter.

Dark–bright (DB) solitons occur in a binary mixture with only repulsive interactions. Yet the bright component can exist now due to the density dip of the dark soliton in the other component, which plays the role of a confining potential. As a result, the dark soliton in one of the components traps atoms of the other, which forms a bright soliton. For simplicity, we will usually refer to the component with the bright soliton as the *bright component* and to the other, with a dark soliton, as the *dark component*. These DB solitons are solutions of the two-component 1D system in the so-called *Manakov limit*, i.e., when all the interactions are of the same strength (see Kevrekidis and Frantzeskakis, 2016, and references therein). In the general case, analytic solutions only exist for a restricted range of the interaction strengths (Yan et al., 2015). However, one can still find numerical solitonic solutions, such as DB soliton trains, outside those limits.

Solitons are solutions of the homogeneous system, either untrapped or confined in a uniform potential. Nevertheless, they can also exist in the presence of harmonic confinement. In this case, the soliton is stable but its profile is deformed due to the changing background density (Barenghi and Parker, 2016). A dark soliton in a single-component condensate oscillates with a frequency that is $1/\sqrt{2}$ times the frequency of the trap (Busch and Anglin, 2000). In a two-component system, a DB soliton in

[1] See Eq. (2.56) for a more general situation in which the soliton can move.

a harmonic trap oscillates with a different frequency (Becker et al., 2008; Busch and Anglin, 2001; Middelkamp et al., 2011). The bright component that fills the core of the dark component slows down the soliton due to the increased mass, which results in an oscillation frequency that is smaller than the oscillation of a single dark soliton.

In the present chapter, we will consider a harmonically trapped bosonic binary mixture in the immiscible regime. In equilibrium, the mixture phase separates, and each component occupies a different domain. The interface or *domain wall* is the region where the two components overlap. The propagation of a dark soliton in such an immiscible mixture has been investigated by Öhberg and Santos (2001a,b) and, for a particular set of parameters, by Zheng et al. (2019).

Our motivation in this chapter is to investigate the reflection and transmission of solitonic states in an immiscible and weakly interacting binary mixture. In particular, we focus on the effect of the domain wall for a wide range of the interaction parameters within the immiscible regime. We will consider general values for the coupling constants, since the scattering lengths can be tuned using Feshbach resonances (see Chapter 2). The atom–atom interactions determine the shape and features of the domain wall. Thus, the system will present different dynamical behaviors when a moving soliton encounters the domain wall depending on the strength of the interactions. We will show that the reflection and transmission of a dark soliton through the domain wall in an immiscible mixture can generate a DB soliton. This DB soliton emerges dynamically due to the interaction with the domain wall and exists in a region of interaction parameters where one cannot obtain static analytical solutions (Yan et al., 2015).

The chapter is organized as follows. In Section 6.1, we introduce bosonic binary mixtures and the theoretical mean-field framework that we use to describe this system. In Section 6.2, we present the numerical results obtained by solving the two-coupled time-dependent GPEs for an immiscible mixture. In particular, we fix the intracomponent interactions and vary the intercomponent interactions within the immiscibility regime. As the initial state, we imprint a dark soliton to one of the components of the system. Then, we analyze its reflection or transmission through the domain wall. We see that, due to the interaction of the dark soliton with the domain wall, one can generate a DB soliton for a wide range of intracomponent interactions. In Section 6.3, we study the dynamics of the DB soliton and provide a semianalytical expression for its oscillation frequency that agrees with the frequency calculated numerically. Finally, Section 6.4 gathers the results presented throughout the chapter.

6.1 Immiscible binary mixtures

To reduce the system to 1D, we assume that it is harmonically confined, and that the frequencies in the transversal[2] (y and z) directions, $\omega_\perp = \omega_y = \omega_z$, are much larger than the frequency in the longitudinal (x) direction ω_x. Since $\omega_x \ll \omega_\perp$, the motion

[2]Note that the convention used here for the term *transversal* is different to that used in Chapter 3 (and later in Chapter 7) when describing quasi-2D systems, where the transversal directions (x and y) are instead those with a shallower confinement, while the axial direction (z) refers to the tight confinement.

in the transversal directions is frozen and the excited states in those directions are not accessible (see discussion in Subsection 2.3.1, Chapter 2, for more details). Then, one can describe the system effectively by the 1D GPE we introduced in Eq. (6.1).

We consider a two-component BEC within the mean-field regime confined in an elongated harmonic potential. The system can be described by two coupled GPEs[3]:

$$i\hbar\frac{\partial\psi_\sigma(x,t)}{\partial t} = \left[-\frac{\hbar^2}{2m_\sigma}\frac{\partial^2}{\partial x^2} + \frac{1}{2}m_\sigma\omega_x^2x^2 + g_{\sigma\sigma}\left|\psi_\sigma(x,t)\right|^2 + g_{\sigma\sigma'}\left|\psi_{\sigma'}(x,t)\right|^2\right]\psi_\sigma(x,t)\,, \tag{6.5}$$

where the wavefunctions of each component, $\psi_\sigma(x,t)$ (with $\sigma = 1,2$), are normalized to 1. The number of atoms in each component is N_σ, and $g_{\sigma\sigma'}$ denote the inter- ($\sigma\sigma'$) and intracomponent ($\sigma\sigma$) 1D coupling constants, respectively.

Assuming that the two components have the same mass $m = m_1 = m_2$, the 1D coupling constants [see Eqs. (6.2) and (2.35)] are given by

$$g_{\sigma\sigma'} = 2N_{\sigma'}\frac{\hbar^2}{m}\frac{a_{\sigma\sigma'}}{a_\perp^2}\,, \tag{6.6}$$

where $a_{\sigma\sigma'}$ are the s-wave scattering lengths that characterize the atom–atom interactions within each component (a_{11} and a_{22}) and between components (a_{12}). We further assume for conceptual clarity that the two components have the same atom number $N = N_1 = N_2$ and intracomponent interactions $a_{11} = a_{22} = a_s$, such that the intracomponent coupling constants are also equal, $g_{11} = g_{22} = g$.

6.1.1 Dimensionless Gross–Pitaevskii equations

One can write the coupled GPEs (6.5) in harmonic oscillator units [see Eq. (2.26) and its derivation for more details]:

$$i\frac{\partial\psi_\sigma}{\partial t} = \left[-\frac{1}{2}\frac{\partial^2}{\partial x^2} + \frac{1}{2}x^2 + g\left|\psi_\sigma\right|^2 + g_{12}\left|\psi_{\sigma'}\right|^2\right]\psi_\sigma\,, \tag{6.7}$$

where ψ_σ, x and t are now dimensionless[4]. We have used the longitudinal oscillator length $a_x = [\hbar/(m\omega_x)]^{1/2}$ as the unit length, $\hbar\omega_x$ as the unit energy, and ω_x^{-1} as the unit time. From now on, all quantities will be given in dimensionless units unless stated otherwise. Then, the effective 1D coupling constants have units of $\hbar^2/(ma_x)$, such that

$$g = 2N\,\frac{\omega_\perp}{\omega_x}\frac{a_s}{a_x} \quad \text{and} \quad g_{12} = 2N\,\frac{\omega_\perp}{\omega_x}\frac{a_{12}}{a_x} \tag{6.8}$$

are now dimensionless.

Finally, we consider repulsive interactions, $g > 0$ and $g_{12} > 0$, such the mixture is immiscible[5] when $a_{12} > \sqrt{a_{11}a_{22}} = a_s$ (Pu and Bigelow, 1998; Timmermans, 1998). Therefore, we will focus on the regime where $g_{12} > g > 0$.

[3] See Eq. (2.34) in Subsection 2.2.1 for a 3D version.

[4] We have kept the same notation for all the quantities as in the original GPEs (6.5) for simplicity, but they are given in different units.

[5] See Subsection 2.2.1 for the miscibility condition (2.39) and discussion of the different regimes. For

6.1.2 Initial state and imprinted dark soliton

In equilibrium conditions, a two-component BEC under the conditions we described above phase separates. We choose to denote component 1 as the one located on the left (L) side of the trap and component 2 as the component on the right (R) side. Throughout this chapter, we may label the two components as 1 and 2 or, alternatively, as L and R.

The domain wall is initially situated at the center of the trap, $x = 0$. Both the ratio of the interaction strengths g_{12}/g and the motion of a soliton influence the position and shape of the domain wall, as we will discuss later. Although the mixture is immiscible, a tiny fraction of atoms from component 1 inhabits the right side of the trap as well (and equivalently for component 2). As we will see below, this small overlap between components in the vicinity of the domain wall is essential to generate DB solitons dynamically.

Imprinted dark soliton

We imprint a dark soliton at rest (6.3) in component 2 (R) at $x = x_0$. Then, one can describe the initial state by the trial wavefunction (Pitaevskii and Stringari, 2016; Tsuzuki, 1971)

$$\psi_1(x) = {\psi_1}^{(0)}(x) \quad \text{and} \quad \psi_2(x) = {\psi_2}^{(0)}(x) \tanh\left(\frac{x - x_0}{\sqrt{2}\,\xi}\right), \tag{6.9}$$

where ${\psi_1}^{(0)}(x)$ and ${\psi_2}^{(0)}(x)$ are the ground state wavefunctions of each component and $\xi = 1/(2\mu_0)^{1/2}$ is the dimensionless healing length. The chemical potential $\mu_0 = g n_0$ is also dimensionless and corresponds to the chemical potential of a scalar (i.e., single-component) and uniform condensate with density $n_0 = |{\psi_2}^{(0)}(x_0)|^2$.

We prepare the initial state numerically by evolving in imaginary time the ansatz (6.9). To imprint the dark soliton at position x_0, we first calculate the ground state of the system via imaginary-time evolution for a given value of the intercomponent interaction strength g_{12}. As indicated in the trial wavefunction (6.9), we multiply the resulting wavefunction of component 2 by a dark-soliton profile and let the system evolve again in imaginary time until the calculation converges with a reasonable tolerance (Modugno et al., 2003).

6.2 Generation of a dark–bright soliton

Let us fix from now on the dimensionless intracomponent coupling constant to $g = 3{\times}10^3$ such that the repulsion between components is strong enough. This parameter could be realized, for example, in a two-component BEC of $N = 25000$ ^{87}Rb atoms in each component with an intracomponent s-wave scattering length $a_s \simeq 100\, a_0$, where a_0 is the Bohr radius, and confined in an elongated harmonic trap of frequencies $\omega_x = 2\pi \times 1.5$

$a_{12} < -\sqrt{a_{11}a_{22}}$ with attractive intercomponent interactions ($g_{12} < 0$), on the other hand, the system collapses in the mean-field regime but can sustain self-bound droplets if beyond mean-field effects are taken into account (see Section 2.2).

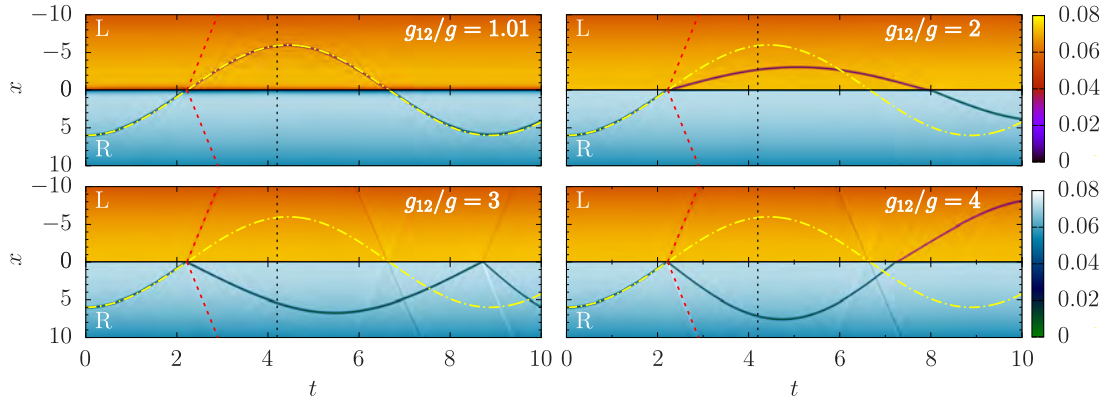

Figure 6.1: Evolution of the density profiles obtained by numerically solving the two coupled GPEs (6.7). Parameters for each panel: $g_{12}/g = 1.01$ (left, top) and $g_{12}/g = 2$ (right, top), $g_{12}/g = 3$ (left, bottom) and $g_{12}/g = 4$ (right, bottom). The point-dashed yellow line corresponds to the sinusoidal oscillation of a dark soliton in a scalar condensate, which has a frequency of $\omega_0 = 1/\sqrt{2}$ (Konotop and Pitaevskii, 2004; Pitaevskii and Stringari, 2016). The straight lines represent phonon trajectories, which travel at the speed of sound. We have only highlighted in red those generated at the first collision with the domain wall (see discussion in the main text). The dotted vertical line marks the time $t = 4.2$ considered in Fig. 6.2.

Hz and $\omega_\perp = 2\pi \times 150$ Hz (Katsimiga et al., 2020). The phenomena explored in this chapter will similarly occur as well for other parameter ranges as long as the mixture remains in the immiscible regime and the trap is effectively quasi 1D.

In this section, with the aim of studying the dynamics of the soliton in different scenarios, we perform numerical calculations of the two coupled GPEs (6.7) for different values of the intercomponent coupling constant with $g_{12}/g \in (1, 4]$, i.e., within the immiscibility regime. We will begin by studying the first collision with the domain wall (Subsection 6.2.1), when the soliton can either transmit of reflect, and describe the trajectory of the soliton in terms of the intercomponent repulsion. Afterwards, we will discuss the second collision with the domain wall (Subsection 6.2.2).

Without loss of generality, we start by imprinting the dark soliton at position $x_0 = 6$ and letting it evolve freely as described by Eq. (6.7). Due to the harmonic confinement, the density around x_0 has a local gradient that induces an initial velocity to the dark soliton. Then, the soliton follows the same trajectory of a dark soliton in a scalar condensate as it approaches the domain wall (Kivshar and Yang, 1994; Konotop and Pitaevskii, 2004); the effect of the second component will only be relevant once the soliton encounters the domain wall. One can see this behavior in Fig. 6.1, which shows the density profiles of each component as a function of time for different values of the ratio g_{12}/g. The evolution of the position of the density depletion (i.e., the center of the soliton) defines the trajectory of the soliton and corresponds to the curved black line with a piece-wise sinusoidal shape (see Fig. 6.1).

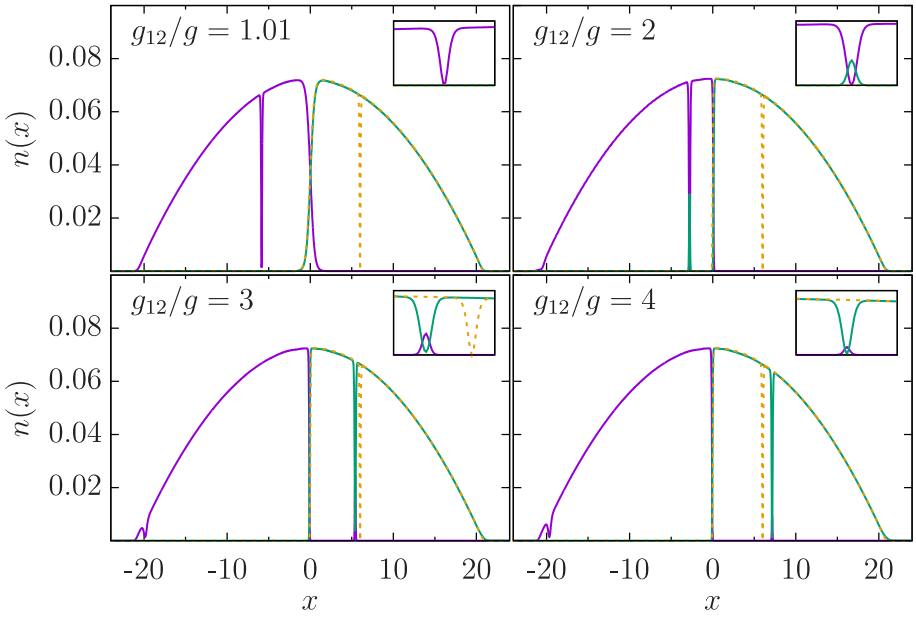

Figure 6.2: Density profiles for different values of g_{12}/g at time $t = 4.2$, which corresponds to the dotted vertical lines in Fig. 6.1. The solid green (purple) line represents the density of the right (left) component. The dashed yellow line corresponds to the initial state configuration of the right component with the dark soliton imprinted at $x_0 = 6$. The inset shows a close-up plot of the region close to the dark–bright soliton. The tiny density dip at $x \simeq -20$ in the bottom panels indicates an emitted phonon.

6.2.1 First collision with the domain wall

Before encountering the domain wall, the motion of the soliton follows the harmonic trajectory of a dark soliton in a single component. One can see this clearly in Fig. 6.1, where we plot the trajectory obtained numerically and the horizontal line at $x = 0$ corresponds to the domain wall. The point-dashed yellow line represents the harmonic trajectory of a dark soliton moving in a scalar, harmonically confined 1D BEC, which oscillates with a dimensionless frequency $\omega_0 = 1/\sqrt{2}$ (Konotop and Pitaevskii, 2004; Pitaevskii and Stringari, 2016).

Once the dark soliton reaches the domain wall, one can find two different behaviors depending on the ratio of the interaction strengths g_{12}/g, as the top and bottom panels of Fig. 6.1 show. These two distinct situations are, respectively, transmission (top panels) and reflection (bottom panels). These two scenarios agree with those described by Öhberg and Santos (2001a,b) and Zheng et al. (2019), which were obtained for fixed values of the interaction strengths and for different initial positions (i.e., initial velocity) of the dark soliton imprinted on the system. We will illustrate and discuss these two different behaviors next.

Transmission

Figure 6.2 shows the density profiles of both components at $t = 4.2$, after the dark soliton encounters the domain wall for the first time. The panels correspond to the same values

of g_{12}/g we considered in Fig. 6.1. The dashed yellow line indicates the initial density profile of the right component, with the dark soliton imprinted at position $x_0 = 6$. In the top panels of Fig. 6.2, the soliton is transferred from the right to the left component once it reaches the domain wall. If $g_{12}/g \simeq 1$, the interface is smooth and the soliton transmits to the other component with a mostly unaltered trajectory (see Fig. 6.1, top left panel). However, if the intercomponent strength slightly increases, such that $1.5 \lesssim g_{12}/g \lesssim 2$ (top right panel in Fig. 6.2), when the soliton is transmitted through the domain wall it also drags some atoms from the right component and forms a DB soliton.

The number of atoms dragged by the dark soliton, which we may call the bright component from now on, increases with the intercomponent strength g_{12}/g. This can be seen from the numerical results obtained by solving the system for different values of g_{12}/g. We will discuss this dependence in Section 6.3 (see also Fig. 6.5). The effective mass of the moving soliton increases as it fills with atoms of the bright component. Therefore, a DB soliton moves more slowly than a dark soliton, which results in a reduction of the slope of the soliton trajectory (see Fig. 6.1, top panels).

Reflection

The domain wall becomes sharper and behaves as a hard wall when the intercomponent repulsion increases further, i.e., $g_{12}/g \gtrsim 2.5$. The dark soliton does not have enough energy to be transmitted and, once it collides with the domain wall, it drags some atoms of the left component through the domain wall and then it is reflected back to the initial component as a DB soliton (see bottom panels of Fig. 6.2, which show the density profiles of the reflected DB soliton). Although the two components have a very small overlap in the domain wall due to the strongly repulsive intercomponent interaction, the density dip of the reflected soliton behaves as an effective potential and drags some atoms of the left component to the right component.

Dark–bright analytical solutions are available explicitly for $g_{12} \leq \max(g_{11}, g_{22})$ (Frantzeskakis, 2010; Yan et al., 2015). However, these DB solitons can be dynamically generated outside this regime of parameters, as we have just seen. They are dynamically generated due to the interaction of the dark soliton with the domain wall. Such DB solitons have not been observed before for the range of interaction parameters considered by Öhberg and Santos (2001a,b). Later, Zheng et al. (2019) showed that, for some values of the interaction parameters, the dark soliton can drag some atoms of the other component, although they did not analyze this fact further.

The initial position of the soliton x_0 only modifies the values of g_{12}/g that characterize the different dynamical behaviors; independently of the initial position of the soliton, one finds the same dynamical regimes. For instance, considering $x_0 = 2$ instead of $x_0 = 6$, the transition between the two regimes (transmission and reflection) takes place at values of the intercomponent interaction strength $g_{12}/g \simeq 1.14$, which is smaller since the soliton velocity (i.e., the initial position) is now lower.

Phonon emission

Either if the soliton is transmitted or reflected, it emits phonons as a result of the interaction with the domain wall. These excitations are known as *phonons* since they travel at the speed of sound $c = \sqrt{g\, n_0}$ (Muñoz Mateo et al., 2015), and are indicated in Fig. 6.1 as the tiny density perturbations (light-gray lines) that appear and propagate in each component once the soliton first collides with the domain wall. The first phonon trajectories are marked with dashed red lines. In the bottom panels of Fig. 6.2, the density depletion that corresponds to the phonon excitation can be seen, in the density profiles, close to the left boundary. Then, the phonon excitation is reflected back towards the center of the condensate once it reaches the boundary of the system.

The gray lines in Fig. 6.1 correspond to excitations that propagate from left to right (negative slope) and from right to left (positive slope). Note that the speed of the soliton (indicated by the line slope) is slower than the speed of phonons (the speed of sound). The emission of phonons leads to an acceleration of the soliton (Öhberg and Santos, 2001a,b) that is stronger when the soliton collides with a harder domain wall, as one can see in Fig. 6.1 (see also Fig. 6.3) by comparing the cases for $g_{12}/g = 3$ and 4.

6.2.2 Second collision with the domain wall

The soliton may be transmitted or reflected when it reaches the interface for the first time. Afterward, it moves towards the boundary of the system. The soliton slows down as it gets closer to the boundary until it eventually stops, and then it travels back to the domain wall. During this journey towards a second encounter with the interface, the velocity of the soliton decreases again, following a harmonic motion (we will discuss this oscillatory behavior with more detail in Section 6.3). The harmoniclike trajectories shown in Fig. 6.1 clearly depict this behavior.

Let us now discuss the second collision with the domain wall. In Fig. 6.3, we show the evolution of the center of the soliton $x_0(t)$ for different values of the intercomponent interaction strength g_{12}/g and initial position $x_0 = 6$. We plot with a solid red line the trajectory of a dark soliton in a 1D scalar condensate confined in a harmonic potential for reference. For values of the intercomponent interaction ($g_{12}/g = 1.01$) close to the Manakov limit, where the intra- and intercomponent interactions are equal, the dark soliton transmits to the other component through the domain wall. As we discussed before, the trajectory of the soliton after the first and second collision follows a harmonic trajectory in both components with frequency $\omega_0 \simeq 1/\sqrt{2}$. In this limiting case, the domain wall slightly perturbs the trajectory of the transmitted dark soliton in the other component, but otherwise its presence is negligible. We will thus refer to this case as the *unperturbed case* from now on.

The dynamics of the soliton after the second collision with the domain wall follows, in general, the same behavior as it did after the first collision. When the DB soliton reaches the interface for the second time, its interaction with the domain wall leads to the emission of phonons, and then the soliton is either transmitted or reflected. However, in some particular cases, the perturbations generated in the domain wall considerably affect the dynamics such that the soliton is transmitted instead of reflected as in the

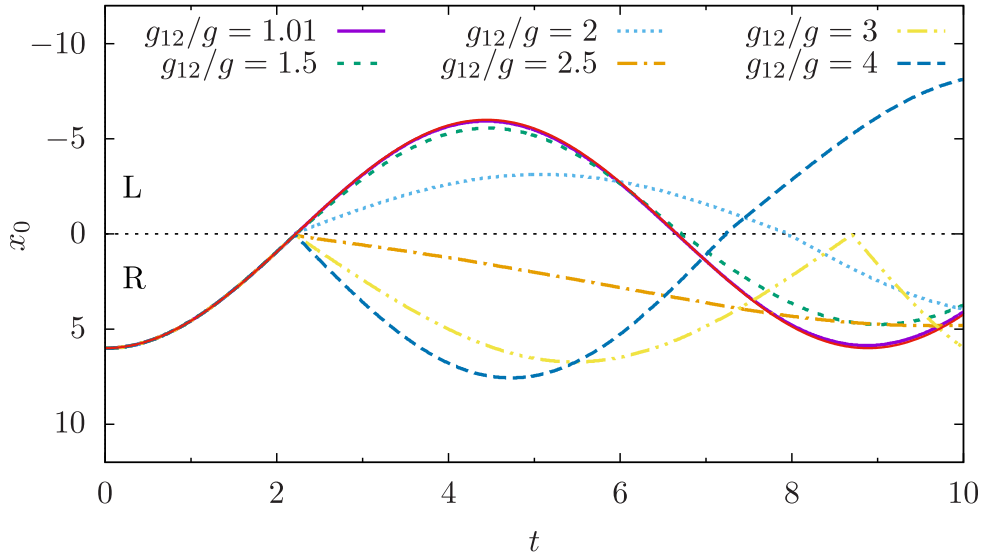

Figure 6.3: Evolution of the soliton center as a function of time for a dark soliton initially imprinted at $x_0 = 6$. The unlabeled solid red line corresponds to the trajectory of a dark soliton in a scalar condensate confined in a 1D harmonic trap (unperturbed case).

first collision (or vice versa). For example, the trajectory for $g_{12}/g = 4$ in Fig. 6.3 shows that the soliton is reflected after the first collision, while it is transferred to the other component after the second collision. We have checked that one cannot explain this behavior in terms of the critical velocity argument proposed by Öhberg and Santos (2001a,b), which indicates that the density deformations that occur in the domain wall may also play a crucial role in the dynamics after the second collision. We will discuss this point with more detail in what follows.

Interaction with the domain wall

Figure 6.4 shows a close-up of the density profile in the vicinity of the domain wall at different times, around $t \simeq 7.5$. We consider two similar values of the interaction strength, $g_{12}/g = 1.90$ (yellow lines) and $g_{12}/g = 1.91$ (blue lines). The solid lines indicate the left component and the dashed lines represent the right component. In that figure, one can see that when the domain wall and the DB soliton interact, the domain wall induces a back action into the soliton that alters its dynamics. In particular, the soliton is reflected back to the right component for $g_{12}/g = 1.90$, while it is transferred to the left component for $g_{12}/g = 1.91$. The first case, however, is an exception to the behavior we observed in the range considered, $1.5 \lesssim g_{12}/g \lesssim 2$. In addition, notice that there is no appreciable emission of phonons in both cases.

Finally, we have observed that, under certain conditions, the domain wall may trap the soliton for some time before it is either transmitted or reflected (a similar effect is discussed by Öhberg and Santos, 2001b). This behavior suggests that the interaction of the soliton with the domain wall deserves a more thorough analysis.

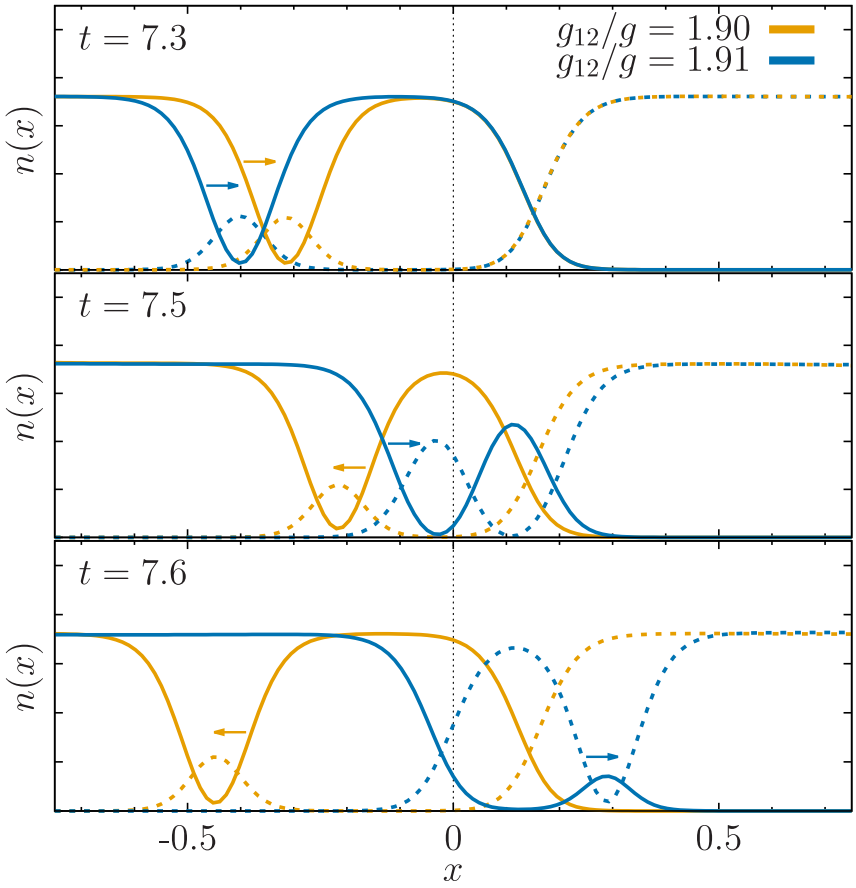

Figure 6.4: The DB soliton travels from the left component towards the domain wall. Snapshots of the density profile in the vicinity of the domain wall, for $g_{12}/g = 1.90\,(1.91)$ plotted with yellow (blue) lines. Solid (dashed) lines indicate the left (right) component. The snapshots correspond, respectively, to times $t = 7.3$, 7.5 and 7.6. The DB soliton is reflected (transmitted) for $g_{12}/g = 1.90\,(1.91)$. Arrows indicate the direction in which the dark soliton is moving. The domain wall is initially located at the center of the trap. Notice, however, that the position of the domain wall sightly varies depending on the position of the soliton. The density is given in arbitrary units.

6.3 Dynamics of the dark–bright soliton

In the previous section (Section 6.2), we observed that when the dark soliton reaches the domain wall for $g_{12}/g \lesssim 2$, it is transmitted to the other component and forms a DB soliton due to the interaction with the domain wall. The resulting DB soliton then performs a harmonic oscillation in the left component until it goes back to the interface, with which it interacts again and either transfers to the right component or, in some particular cases, is reflected back to the left component.

In this section, we will focus on the scenario where the dark soliton is transmitted after the first encounter with the domain wall, and we will investigate with more detail the oscillatory behavior of the DB soliton. One can accurately fit the trajectory of the DB soliton with a sinusoidal function; we show its characteristic frequency in Fig. 6.5.

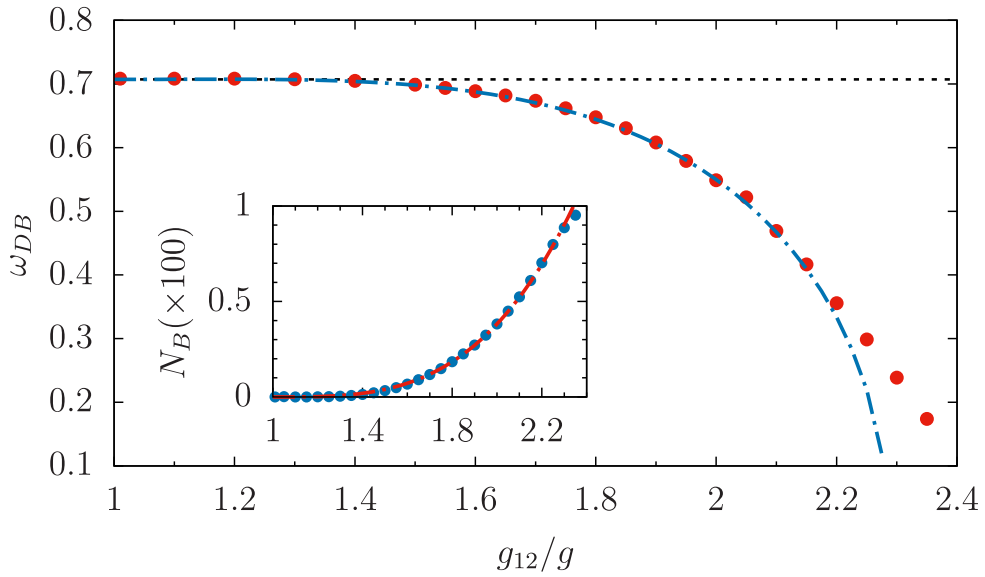

Figure 6.5: Oscillation frequency of the DB soliton transmitted to the left component as a function of the intercomponent interaction strength g_{12}/g (red points). The oscillation frequency is obtained from the numerical solution of the coupled GPEs (6.7). The horizontal dashed line indicates as reference the result for the unperturbed case, which oscillates at a frequency $\omega_0 = 1/\sqrt{2}$ as a dark soliton in a scalar condensate does. The dash-dotted line corresponds to the analytical prediction given by Eq. (6.12). The inset shows the rescaled number of atoms N_B in the bright soliton (blue points) as a function of the intercomponent interaction strength g_{12}/g. The red dashed line represents a fit of the data of the form $\alpha\,(g_{12}/g)^{\beta}$, with $\alpha \simeq 3.8 \times 10^{-3}$ and $\beta \simeq 3.3$.

6.3.1 Oscillation frequency

Close to the Manakov case (here $g_{12}/g \simeq 1$), the dark soliton is transmitted to the left component unperturbed and oscillates as a dark soliton in a scalar condensate, with a frequency $\omega_0 = 1/\sqrt{2}$ (see horizontal line in Fig. 6.5). For an interaction strength $g_{12}/g > 1.4$, the frequency of the soliton starts to depart from this unperturbed result. This signals the presence of a significant drag of atoms in the bright component, which slows down the oscillation.

Semianalytical model

We recall here that these DB solitons are dynamically generated for a regime of parameters, $g_{12} > \max(g_{11}, g_{22})$, in which explicit analytical solutions do not exist (Frantzeskakis, 2010). Then, to compare the numerical oscillation frequency with an analytical estimate, we assume that the effect of the bright component can be treated as a perturbation of the dark soliton frequency ω_0.

To construct our ansatz, we use the fact that, in the Manakov limit ($g_{12} = g = 1$), the frequency of the DB soliton is given by the following expression (Busch and Anglin,

2001; Yan et al., 2015):

$$\omega_{\mathrm{M}}^2 \simeq \frac{1}{2}\left[1 - \frac{N_{\mathrm{B}}/g}{4\sqrt{\mu + (N_{\mathrm{B}}/4g)^2}}\right], \tag{6.10}$$

where N_{B} is the rescaled number of atoms[6] in the bright soliton,

$$N_{\mathrm{B}} = \int |\psi_{\mathrm{B}}(x)|^2 \, dx \,, \tag{6.11}$$

$\psi_{\mathrm{B}}(x)$ is the density profile of the bright soliton (the total density is normalized to one as before), and μ is the chemical potential. The factor $1/g$ that rescales the number of atoms in the bright soliton comes from the fact that, in our formulation, the densities are not rescaled by $g_{11} = g$ as in the work by Yan et al. (2015).

Then, we make a continuation to $g_{12}/g > 1$ by assuming that the correction to ω_{DB}^2, which depends on the intercomponent interactions, has to be proportional (to lowest order) to g_{12}:

$$\omega_{\mathrm{DB}}^2 \simeq \frac{1}{2}\left[1 - \frac{(g_{12}/g)\, N_{\mathrm{B}}}{4\sqrt{\mu + (N_{\mathrm{B}}/4g)^2}}\right]. \tag{6.12}$$

Note that the number of dragged atoms N_{B} also depends on g_{12}.

Number of dragged atoms

One can approximate the behavior of $N_{\mathrm{B}}(g_{12})$ by fitting the bright-soliton density profile to a function of the form (Busch and Anglin, 2001; Yan et al., 2015)

$$|\psi_{\mathrm{B}}(x)|^2 = \frac{\kappa\, N_{\mathrm{B}}}{2} \operatorname{sech}^2\left[\kappa(x - x_0)\right]. \tag{6.13}$$

The width of the bright soliton is denoted by $\kappa \simeq \sqrt{\mu}$, and x_0 is the position of the DB soliton. This numerical fit starts to fail for $g_{12}/g \gtrsim 2$, since for a large enough g_{12}/g the bright component can no longer be treated as a perturbation. We have observed that, once the DB soliton forms, both N_{B} and κ do not show any significant dependence on time (until the soliton is eventually reabsorbed at the domain wall) and the DB soliton propagates across the left region of the trap without losing its shape.

The inset in Fig. 6.5 shows the behaviour of the number of dragged atoms N_{B} as a function of the interaction strength g_{12}/g. One can see in Fig. 6.5 that, for $g_{12}/g \gtrsim 1.4$, atoms from the left component start to fill the core of the dark soliton in the right component due to the interparticle repulsion. This produces a reduction of the oscillation frequency of the soliton.

Combining Eq. (6.12) with the above results, we obtain the semianalytical expression for the DB soliton frequency ω_{DB}, which we plot in Fig. 6.5 as a dashed line. For $1 \leq g_{12} \lesssim 2.3$, this simple ansatz accurately reproduces the oscillation frequency obtained from the numerical simulation of the coupled GPEs (6.7).

[6] We refer to N_{B} as *rescaled* because the wavefunction of each component ψ_σ is normalized to 1, not to the total number of atoms.

6.4 Summary of results

In this chapter, we have studied the transmission and reflection of a dark soliton through the domain wall of a quasi-1D immiscible binary mixture. Depending on the interaction strength, a dark–bright (DB) soliton is created when the initially imprinted dark soliton moves across the domain wall. We remark that such DB solitons are dynamically generated outside the regime of parameters where explicit analytical solutions exist, which opens an interesting perspective for producing DB solitons in this new dynamical regime, as it should be easily accessible in experiments with ultracold atoms (Katsimiga et al., 2020; Lee et al., 2016). Once the dark soliton reaches the domain wall and forms a DB soliton, the soliton follows a harmoniclike trajectory. The resulting DB soliton can either be transferred or reflected when it collides the domain wall for a second time.

We have shown that one can obtain a semianalytical expression for the DB soliton oscillation frequency by continuation for $g_{12}/g \gtrsim 1$ of the Manakov case discussed by Anderson et al. (2000) and Yan et al. (2015). To obtain this approximation, we have assumed that the effect of the bright component can be treated as a perturbation to the dark component. Finally, we have seen that the oscillation frequency of the DB soliton that we obtain numerically by solving the GPE is in good agreement with the predictions of this semianalytical model.

We will also investigate solitonic states in Chapter 8, where we consider a rotating quasi-1D condensate in which the effective interactions come from the current density (instead of the number density) and thus present chiral properties. Later, in Chapter 9, we will extend this study to spinor mixtures with two coherently coupled components.

7

Antiparallel dipolar mixtures and self-bound droplet crystals

Quantum droplets are self-bound states that emerge from the stabilizing effect of quantum fluctuations against the mean-field collapse[1]. For droplets to arise, the system needs to have competing interactions within the condensate such that the effective mean-field contribution is attractive and small enough to compensate for the repulsion due to quantum fluctuations. Systems with competing interactions are, for instance, bosonic binary mixtures and condensates of dipolar atoms.

In systems with strong dipole–dipole interactions, besides quantum droplets, this binding mechanism allows for the formation of crystals and supersolids. When the system is confined along the polarization direction of the dipoles, the droplets can self-assemble into arrays and, in some cases, form a supersolid, which presents both superfluid properties and a crystalline structure given by the modulation of the density. The dipolar interaction between such droplets is repulsive, so these crystals unravel in the absence of external confinement. In this chapter we will explore how one can obtain droplet crystals that are self-bound in antiparallel dipolar mixtures, where the dipoles in one component are antiparallel to those of the other component.

Solid-state crystals, for instance, present different forms of attractive and repulsive interactions between their components. The interplay between these forces binds the crystal (Kittel, 2004). The *cohesive* or *binding energy* of the crystal is a finite energy that results from the balance between these forces, and is defined as the energy that one must add to the crystal to separate its constituents infinitely apart. When the system is externally confined, crystals may still form even if they lack a genuine cohesion. Trapped ions are a good example of this effect: the combination of repulsive Coulomb interactions and the external trapping can lead to the formation of crystals (Thompson, 2015). But ion Coulomb crystals do not have a cohesive energy, and thus unravel in the absence of confinement.

The same happens for crystals of droplets in scalar dipolar condensates (Böttcher et al., 2021; Chomaz et al., 2022), as we already mentioned above. The quasi-cancellation

[1]We already introduced self-bound droplets in Chapters 2 and 3, but we will recall here the key points as a reminder. For more details of droplets in nondipolar binary mixtures, see Section 2.2. Regarding dipolar droplets, see Section 3.2; and see Subsection 3.2.3 for the particular case of droplet crystals.

of contact and dipolar interactions counterbalances the repulsive effect of quantum fluctuations, which results in self-bound droplets (Chomaz et al., 2016; Kadau et al., 2016; Petrov, 2015; Schmitt et al., 2016). These droplets elongate along the dipole direction due to the anisotropy of the dipole–dipole interactions. If the system is confined along the polarization direction (the axial direction), the droplet minimizes its energy by breaking into multiple smaller droplets. If the system is also confined in the plane perpendicular to the dipole direction (the transversal directions), the resulting droplets arrange into a crystal (Wenzel et al., 2017) that may present supersolid properties (Bland et al., 2022b; Böttcher et al., 2019a; Chomaz et al., 2019; Guo et al., 2019; Natale et al., 2019; Norcia et al., 2021; Tanzi et al., 2019a,b). However, these droplets repel each other, as in the case of ion Coulomb crystals. Therefore, the droplet crystal has no genuine cohesive energy (and neither does any other possible density pattern, see for instance Hertkorn et al., 2021b; Poli et al., 2021; Zhang et al., 2019, 2021), and the transversal trap is crucial to keep it bound.

Dipolar binary mixtures have been recently observed in experiments (Durastante et al., 2020; Politi et al., 2022; Trautmann et al., 2018). Due to the competition between intra- and intercomponent contact and dipolar interactions, dipolar mixtures present richer physics than their nondipolar counterparts, such as immiscible droplets (Bisset et al., 2021; Lee et al., 2022; Smith et al., 2021), doping-induced droplet nucleation (Politi et al., 2022; Scheiermann et al., 2023), two-fluid supersolidity (Scheiermann et al., 2023), and the formation of alternating-domain supersolids (Bland et al., 2022a; Kirkby et al., 2023; Li et al., 2022). If the dipoles of the two components are antiparallel, the inter- and intracomponent interactions have opposite sign (Bland et al., 2022a), as we will discuss later.

Our motivation in this chapter is to study the formation of crystals in an antiparallel dipolar mixture (ADM). In the absence of any confinement, an ADM may form an immiscible three-dimensionally self-bound mixture, as in the case of parallel mixtures (Bisset et al., 2021; Smith et al., 2021). However, the resulting configurations present a different topology than in the case of parallel mixtures; for instance, one of the components (i.e., the least dipolar one) may eventually form a ring around a droplet of the other component. As we mentioned before, a confinement along the polarization direction results in the formation of crystals. As opposed to the cases of single-component dipolar condensates and binary mixtures with parallel dipoles, the crystals that an ADM can form have a genuine cohesive energy. Then, these crystals remain self-bound in the absence of transversal confinement due to the mutual attraction between the components. This situation is similar to what occurs in ionic solid-state crystals: ions of opposite charge arrange in an intertwined crystalline structure and are held together by their mutual electrostatic interaction (Kittel, 2004). Self-bound ADMs, however, are not the result of two intertwined arrays of droplets. Here we will explore two possible configurations. In symmetric ADMs, where the intracomponent interactions strengths are similar, the system forms self-bound stripe/labyrinthic density patterns. If the ADM is sufficiently asymmetric instead, one of the components (i.e. the more dipolar one) forms a incoherent crystal of droplets that has an approximate triangular structure, while the second component (the least dipolar one) remains superfluid and fills in the

interstitials of the crystal[2].

The structure of the chapter is as follows. We introduce dipolar binary mixtures and the corresponding equations with a beyond mean-field correction in Section 7.1. Then, in Section 7.2 we particularize the system to the antiparallel dipolar configuration and its three-dimensionally self-bound solutions. Section 7.3 is devoted to the formation of self-bound droplet crystals in the presence of a confinement along the polarization direction, and we also discuss the interstitial superfluid and the possibility of observing crystal sublimation. In Section 7.4, we study the effect of an asymmetry in the contact interactions and explore the formation of self-bound stripe and labyrinthic phases. Finally, Section 7.5 gathers a summary of the conclusions and main results presented throughout the chapter.

7.1 Binary mixtures of dipolar atoms

A dipolar binary mixture can be described, as we saw in previous chapters, by two coupled Gross–Pitaevskii equations that include each a dipolar term that is nonlocal and long-range[3]. To account for the effect of quantum fluctuations, one can add a beyond mean-field correction to the equation.

7.1.1 Coupled Gross–Pitaevskii equations with LHY correction

The physics of the mixture is well captured by the following coupled extended GPEs (Bisset et al., 2021; Smith et al., 2021):

$$\begin{aligned} i\hbar\frac{\partial\psi_\sigma(\mathbf{r},t)}{\partial t} = \Bigg[&-\frac{\hbar^2\nabla^2}{2m} + V_{\text{ext}}(\mathbf{r}) + \sum_{\sigma'} g_{\sigma\sigma'}\,|\psi_{\sigma'}(\mathbf{r},t)|^2 + \mu^{(\sigma)}_{\text{LHY}}[n_{1,2}(\mathbf{r},t)] \\ &+ \sum_{\sigma'}\int d\mathbf{r}'\, U^{(\sigma\sigma')}_{\text{dd}}(\mathbf{r}-\mathbf{r}')\,|\psi_{\sigma'}(\mathbf{r}',t)|^2\Bigg]\psi_\sigma(\mathbf{r},t)\,, \end{aligned} \tag{7.1}$$

where $\sigma = 1, 2$ labels the components, $V_{\text{ext}}(\mathbf{r})$ is a generic external potential[4], and we have considered equal masses[5] for the atoms, $m_1 \approx m_2 \approx m$. As usual, $\psi_\sigma(\mathbf{r},t)$ is the condensate wavefunction of component σ and $n_\sigma = |\psi_\sigma|^2$ its density. The atoms may be confined along the z direction by a harmonic potential

$$V_{\text{ext}}(\mathbf{r}) = \frac{1}{2}m\omega_z^2 z^2 \tag{7.2}$$

[2]This situation resembles, to some extent, the case of superfluid helium in porous media (Reppy, 1992)

[3]See Eq. (2.34) for a nondipolar binary mixture and Eq. (3.42) for a single-component dipolar condensate with a beyond mean-field correction

[4]We will not need any external confinement to study the ground state configurations of the mixture in Section 7.2, since the mixture is self-bound, but it will be useful later for a more general case of a system confined along the polarization direction (Sections 7.3 and 7.4).

[5]This assumption is valid for most available dipolar mixtures, since they are composed either of isotopes of the same atom or by different species, in which case the species that are commonly used in dipolar experiments (erbium and dysprosium) have very similar masses. Then, one can consider the mass of two components in a mixture to be equal to the average of both masses.

that we consider to be time-independent. The atom–atom contact interactions are characterized by the coupling constants $g_{\sigma\sigma'} = 4\pi\hbar^2 a_{\sigma\sigma'}/m$, with $a_{\sigma\sigma'}$ the s-wave scattering lengths for the intra- (a_{11} and a_{22}) and intercomponent (a_{12}) interactions. The dipole–dipole interaction is given by the potential (3.2)

$$U_{\rm dd}^{(\sigma\sigma')}(\mathbf{r}) = \mu_\sigma \mu_{\sigma'} \frac{\mu_0}{4\pi} \frac{1 - 3\cos^2\theta}{r^3}\,, \tag{7.3}$$

where μ_σ is the dipole moment of component σ and θ is the angle between $\mathbf{r}$ and the direction of the dipoles (the z-axis).

To account for the effect of quantum fluctuations and study droplets in dipolar mixtures[6], one can add the Lee–Huang–Yang (LHY) correction, which is given by

$$\mu_{\rm LHY}^{(\sigma)}[n_{1,2}(\mathbf{r},t)] = \frac{\partial \mathcal{E}_{\rm LHY}}{\partial n_\sigma}\,, \tag{7.4}$$

where $\mathcal{E}_{\rm LHY}$ is the correction to the energy density,

$$\mathcal{E}_{\rm LHY} = \frac{8}{15\sqrt{2\pi}} \left(\frac{m}{4\pi\hbar^2}\right)^{3/2} \int_0^\pi d\theta_k \sin\theta_k \sum_{\lambda=\pm} V_\lambda^{5/2}(\theta_k)\,. \tag{7.5}$$

The function $V_\pm(\theta_k)$ contains the dependence on all the interactions and the densities of both components,

$$V_\pm(\theta_k) = \sum_{\sigma=1,2} \eta_{\sigma\sigma} n_\sigma \pm \sqrt{(\eta_{11} n_1 - \eta_{22} n_2)^2 + 4\eta_{12}^2 n_1 n_2}\,, \tag{7.6}$$

where θ_k is the angle between $\mathbf{k}$ and the z-axis and

$$\eta_{\sigma\sigma'} = g_{\sigma\sigma'} + g_{\rm dd}^{(\sigma\sigma')}(3\cos^2\theta_k - 1)\,, \tag{7.7}$$

with $g_{\rm dd}^{(\sigma\sigma')} = \mu_0 \mu_\sigma \mu_{\sigma'}/3$. Note that the energy correction (7.5) reduces to that of a single component (3.38) in the proper limit (i.e., when one of the densities is zero).

Finally, the total energy of the system is

$$E[\psi_1, \psi_2] = E_{\rm MF} + \int d\mathbf{r}\, \mathcal{E}_{\rm LHY}\,, \tag{7.8}$$

where $E_{\rm MF}$ is the usual mean-field energy.

[6] In dipolar binary mixtures, one can study the formation of droplets in the immiscible regime, which is not available for nondipolar mixtures [see Subsection 2.2.2 in Chapter 2 for more details]. Here droplets can remain self-bound due to the dipole–dipole interaction between the two components. In addition, a self-bound droplet may bind a second component that would not be stable by itself. One last remarkable difference with nondipolar mixtures is that the ratio between densities is no longer locked for dipolar mixtures, so one can study the effect of the atom imbalance as well as fully balanced mixtures.

Numerical considerations

The integrals in both $\mu_{\mathrm{LHY}}^{(\sigma)}$ and $\mathcal{E}_{\mathrm{LHY}}$ depend on the densities of each component. For numerical convenience, however, one can write them in terms of the total density $n(\mathbf{r},t) = n_1(\mathbf{r},t) + n_2(\mathbf{r},t)$ by introducing the dimensionless parameter A such that $n_1 = An$ and $n_2 = (1-A)n$, with $A \in [0,1]$. Then, the correction to the energy density is

$$\mathcal{E}_{\mathrm{LHY}} = \frac{8}{15\sqrt{2\pi}}\left(\frac{m}{4\pi\hbar^2}\right)^{3/2} n^{5/2}(\mathbf{r},t)\, I_{\mathcal{E}}[A(\mathbf{r})]\,, \tag{7.9}$$

and the correction to the chemical potential, using Eq. (7.4), reads

$$\mu_{\mathrm{LHY}}^{(\sigma)}[n(\mathbf{r},t), A(\mathbf{r})] = \frac{8}{15\sqrt{2\pi}}\left(\frac{m}{4\pi\hbar^2}\right)^{3/2} \frac{5}{2} n^{3/2}(\mathbf{r},t)\, I_{\mu}^{(\sigma)}[A(\mathbf{r})]\,. \tag{7.10}$$

With this transformation, one can factorize the total density such that the angular integrals do no longer contain the density and depend only on the parameter $A(\mathbf{r})$:

$$I_{\mathcal{E}} = \int d\theta_k \sin\theta_k \sum_{\lambda=\pm}\left[V_{\lambda}^{(A)}(\theta_k)\right]^{5/2}\,, \tag{7.11}$$

and

$$I_{\mu}^{(\sigma)} = \int d\theta_k \sin\theta_k \sum_{\lambda=\pm}\left[V_{\lambda}^{(A)}(\theta_k)\right]^{3/2}\left(\eta_{\sigma\sigma} \pm \frac{f_\sigma(A)}{\sqrt{\left[A\eta_{11} - (1-A)\eta_{22}\right]^2 + 4A(1-A)\eta_{12}^2}}\right), \tag{7.12}$$

with

$$V_{\pm}^{(A)}(\theta_k) = A\eta_{11} + (1-A)\eta_{22} \pm \sqrt{\left[A\eta_{11} - (1-A)\eta_{22}\right]^2 + 4A(1-A)\eta_{12}^2}\,. \tag{7.13}$$

To simplify notation, we have introduced the function f_σ for each component as

$$f_1 = A\eta_{11}^2 - (1-A)\eta_{11}\eta_{22} + 2(1-A)\eta_{12}^2 \quad \text{and} \quad f_2 = (1-A)\eta_{22}^2 - A\eta_{11}\eta_{22} + 2A\eta_{12}^2\,. \tag{7.14}$$

Since the value of A is bound between 0 and 1, one can calculate the integrals $I_{\mathcal{E}}$ (7.11) and $I_{\mu}{}^{(\sigma)}$ (7.12) for the whole range of A once at the beginning of the simulation and then interpolate for the appropriate value of A at any given density $n(\mathbf{r},t)$.

In general, both integrals are complex. However, as with the single-component dipolar case[7], the imaginary part is very small for the strengths of the dipolar interactions usually considered and thus one can neglect it.

7.2 Antiparallel dipolar mixtures

We consider a bosonic ADM with the dipoles oriented, respectively, parallel and antiparallel to the z axis. As in nondipolar mixtures, the components may belong to

[7] For more details, see Chapter 3: Eq. (3.40), Fig. 3.4 and discussion in the main text.

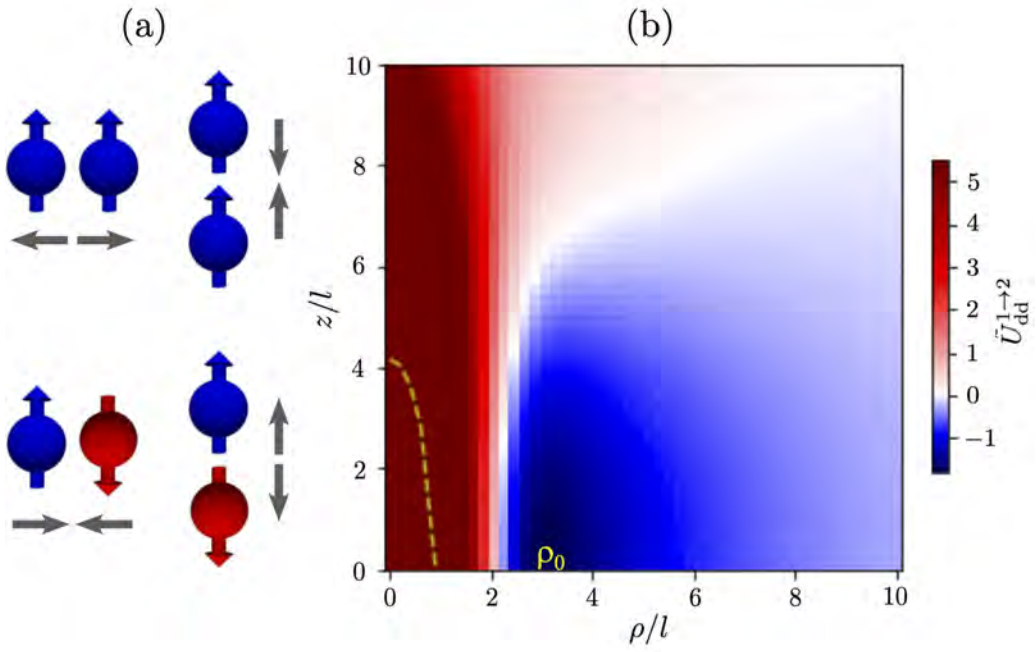

Figure 7.1: Dipole–dipole interactions in an antiparallel dipolar mixture (ADM). (a) In an ADM, intracomponent interactions are attractive when the particles are head to tail, and repulsive when they are side by side (see gray arrows); the situation is the opposite for intercomponent interactions. (b) Dipole–dipole interaction $U_{dd}^{1\to2}(\mathbf{r}) = 2\mu_0\mu_1^2/(3\pi l_z^2)\,\tilde{U}_{dd}^{1\to2}$ that component 1 exerts on component 2 in the impurity limit ($N_1 \gg N_2$) as a function of z and the radial coordinate ρ, given by $\rho^2 = x^2 + y^2$. We have assumed for simplicity a Gaussian droplet $e^{-z^2/l_z^2}e^{-\rho^2/2l^2}$, and the dashed line qualitatively indicates the half-width-at-half-maximum of the droplet. The intercomponent dipolar interaction results in an energy minimum on the xy plane at a given radius ρ_0 well outside the droplet (see dark-blue region).

the same atomic species or to two different ones. To illustrate the possible physics of the system, we consider a dysprosium mixture with magnetic dipoles $\mu_1 = 10\,\mu_B$ and $\mu_2 = -10\,\mu_B$, where μ_B is the Bohr magneton. The s-wave scattering lengths a_{11}, a_{22} and a_{12} characterize the short-range interactions, as we mentioned in the previous section, and we assume the three of them to be different.

Since the dipole moments of the components are antiparallel, the effect of the dipole–dipole interaction between components is reversed: the intercomponent dipolar potential is repulsive when the dipoles are in a head-to-tail configuration and attractive when the dipoles are side by side [see Fig. 7.1(a)]. As a result, the dipolar interaction strongly favors immiscibility, and one needs a very large and negative a_{12} to drive the system to the miscible phase. From now on, we fix the strength of the contact intercomponent interactions arbitrarily to $a_{12} = 150\,a_0$ without loss of generality, since the actual value is irrelevant as long as the intercomponent overlapping remains negligible. All the cases we will consider in this chapter are thus fully immiscible mixtures.

We will see next how the intercomponent interactions allows for the formation of

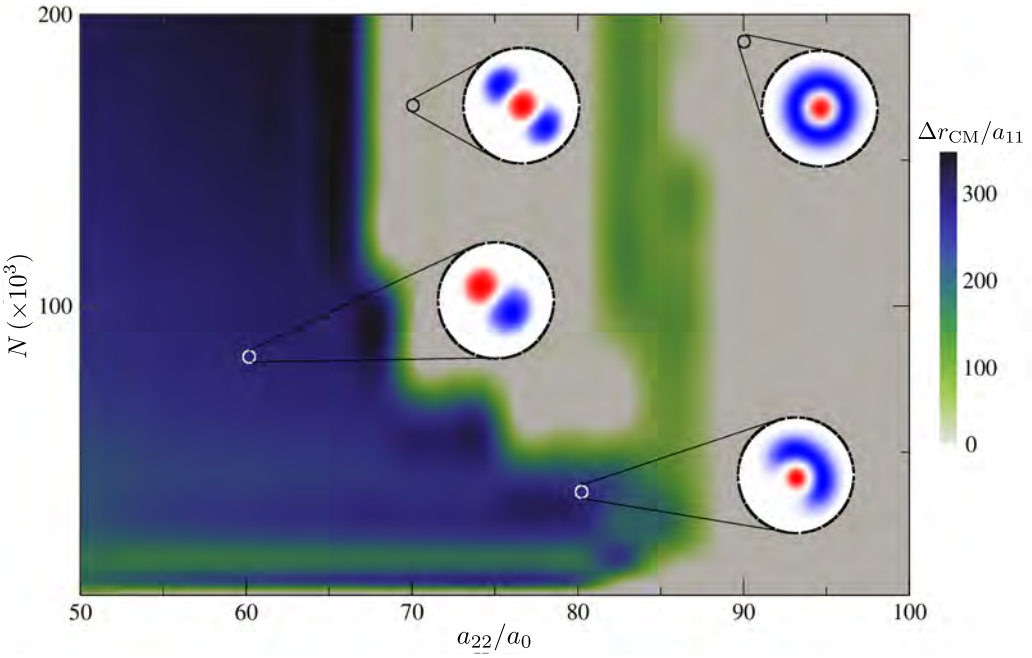

Figure 7.2: Three-dimensionally self-bound ADMs. Ground-state configuration as a function of the total number of atoms N and of a_{22}, for fixed $a_{11} = 50\,a_0$ and $N_{1,2} = N/2$ (balanced mixture). Component 1 always forms a single elongated droplet, but component 2 can acquire different topologies. We characterize the different configurations using the center-of-mass separation $\Delta r_{\rm CM}$ between two components (color code). The insets show the possible topologies, where we depict the column density (integrated over z) of each component. Red indicates component 1, and blue component 2.

self-bound droplets, so we consider first the case of a fully unconfined mixture, i.e., with $\omega_z = 0$.

7.2.1 Three-dimensional self-binding

An immiscible ADM may present a three-dimensionally self-bound solution, as in the case of parallel dipolar mixtures (Bisset et al., 2021; Smith et al., 2021), but of a very different nature (see insets in Fig. 7.2). To understand the effect of the interaction between components, let us consider the impurity limit ($N_1 \gg N_2$) and assume that component 1 (the majority component) forms a self-bound droplet with density $n_1(\mathbf{r})$. This droplet induces a dipolar potential on component 2 of the form

$$U_{\rm dd}^{1\to 2}(\mathbf{r}) = \int d\mathbf{r}'\, U_{\rm dd}^{(12)}(\mathbf{r}-\mathbf{r}')\, n_1(\mathbf{r}')\,. \tag{7.15}$$

As one can see in Fig. 7.1(b), where we plot $U_{\rm dd}^{1\to 2}(\mathbf{r})$ in terms of the axial and transversal directions (z and ρ), this potential presents a marked minimum at a given radius ρ_0 that is well outside the droplet. Then, the atoms in component 2 (the minority component) are trapped in this mexican-hat potential.

The argument remains valid if the mixture is more balanced ($N_1 \sim N_2$), but now component 2 also exerts a similar potential $U_{\rm dd}^{2\to1}(\mathbf{r})$ on component 1. Therefore, the two components confine each other mutually on the xy plane, which results in self-bound ADMs. Figure 7.2 illustrates these self-bound solutions for balanced mixtures ($N_{1,2} = N/2$) with the intracomponent interactions of component 1 fixed[8] to $a_{11} = 50\,a_0$ and different values of a_{22} and N. If the intracomponent interactions are asymmetric and $a_{11} < a_{22}$, component 1 remains a compact droplet while the second component accommodates on the ring potential around the droplet. On the other hand, for low enough a_{22} (such that $a_{11} \sim a_{22}$), the system minimizes the energy by also forming a single droplet in component 2. Then, for growing N and a_{22}, the droplet on component 2 spreads around the mexican-hat minimum until it eventually forms a ring-like configuration. Note that, for intermediate values of a_{22}, there is a second possible topology where two droplets of component 2 sit at opposite sides of the ring potential.

7.3 Self-bound droplet crystals

In unconfined mixtures (i.e., when $\omega_z = 0$), increasing the number of atoms N elongates the droplet along the z direction. As occurs for scalar (single-component) dipolar condensates (Böttcher et al., 2021), the presence of an axial trap along z ($\omega_z > 0$) frustrates the elongation of the droplet, which breaks into multiple droplets. These droplets repel each other, but a transversal confinement on the xy plane allows for the creation of 2D droplet crystals (Bland et al., 2022b; Norcia et al., 2021). However, the resulting crystals have no intrinsic cohesion, and thus unravel in the absence of the in-plane (xy) confinement.

This is not the case in an ADM. Droplet crystals of ADMs do no longer need any transversal confinement since the intercomponent interaction is attractive and binds the two components together. From now on, we will consider an ADM confined along the polarization direction ($\omega_z > 0$) but unconfined in the transversal plane ($\omega_x = \omega_y = 0$). Then, in this section we will study how a 3D self-bound mixture may form a self-bound crystal by increasing the axial frequency ω_z. We will denote all lengths in units of a_z, the harmonic oscillator length associated with ω_z, unless when stated otherwise.

7.3.1 Three-dimensionally self-bound ADMs to self-bound crystals

Figure 7.3(a) shows the phase diagram of ground-state configurations in terms of the atom number N and axial frequency $f_z = \omega_z/(2\pi)$ for a balanced mixture $N_1 = N_2 = N/2$ with asymmetric intracomponent interactions, $a_{11} = 50\,a_0$ and $a_{22} = 70\,a_0$. Figures 7.3(b–g) illustrate some particular cases. The three-dimensionaly self-bound solution, with a single droplet in the first component[9], remains valid for a low enough ω_z [see Fig. 7.3(b)].

[8] We consider this particular value to ensure that component 1 is "dipolar enough" such that it forms a droplet regardless of the intracomponent interaction strength of component 2.

[9] Note that in the phase diagram [Fig. 7.3(a)] we only show the number of droplets of the first component. Close to the untrapped case (in the region of $N_D = 1$), however, the second component may either form one or two droplets, or a ring-like structure around the droplet in the first component, as in the

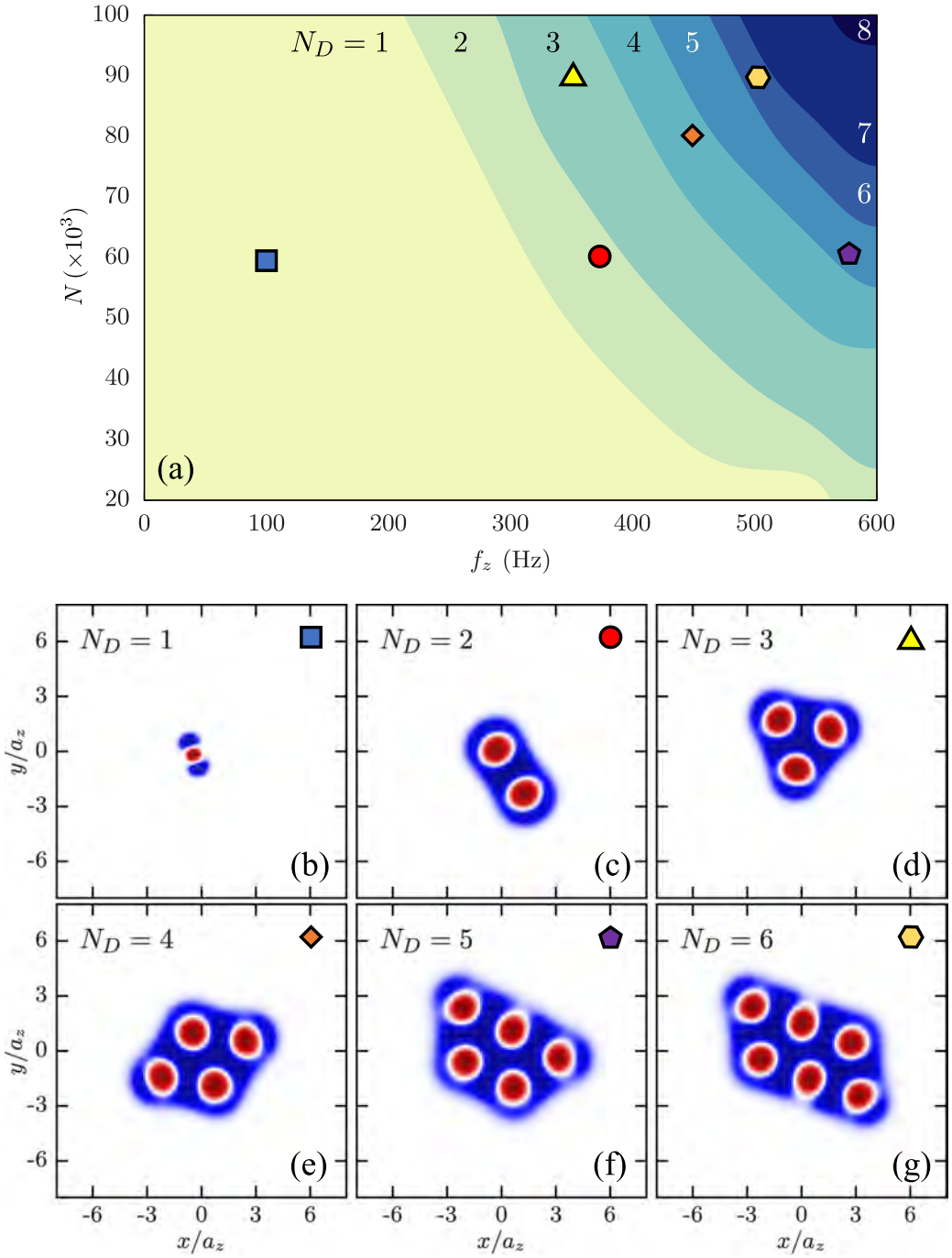

Figure 7.3: Self-bound droplet crystals. (a) Phase diagram as a function of the atom number N and the axial trap frequency $f_z = \omega_z/(2\pi)$ for $a_{11} = 50\,a_0$ and $a_{22} = 70\,a_0$. The colors correspond to configurations with a different number of droplets N_D in component 1. Figures (b–g) show the column magnetization $n_1 - n_2$ (integrated along z) of the lowest-energy solution for selected cases and are indicated with the corresponding symbol in Fig. (a). Component 1 populates the red regions, and 2 the blue ones.

Increasing the frequency, there is a critical ω_z that depends on the number of atoms N for which the droplet splits into two. Each of the droplets induces a mexican-hat potential on the second component, which gets trapped in the combined energy minimum. At the same time, the second component glues the two droplets together and thus the system forms a self-bound ADM [see Fig. 7.3(c)]. If one increases ω_z further [see Fig. 7.3(d–g)], the number of droplets of the first component grows, and the resulting crystal is surrounded by a bath of the second component. In scalar condensates, each individual droplet requires a minimal number of atoms to remain self-bound; otherwise, the kinetic energy unbinds it. This limits drastically the total number of droplets in a scalar condensate. In an ADM, on the other hand, the droplets remain confined due to the intercomponent interactions, such that droplets can have a much smaller number of atoms (Bland et al., 2022a; Li et al., 2022). Then, as a result, the 2D crystals that form for increasing ω_z contain much more droplets than scalar condensates with the same total atom number would have.

Note that the distance between droplets is approximately $3\,a_z$, where a_z is the oscillator length associated with ω_z [see for instance Figs. 7.3(e–g)]. This feature indicates that the roton instability may be the origin of these density modulations, as we will revisit again later in Subsection 7.3.2.

Shot-to-shot variability

We obtained the numerical results presented in this chapter by evolving the extended GPE (7.1) in imaginary time with initial random conditions[10]. For the droplet crystals shown in Fig. 7.3, we found many possible solutions for each case all with very similar energy and which only differ in the exact number of droplets and their arrangement. Therefore, we expect a similar shot-to-shot variability in experiments, similarly to what has been experimentally observed recently with 2D supersolids (Norcia et al., 2021).

We illustrate this large shot-to-shot variability of the exact number of droplets and their arrangement in the droplet crystal in Fig. 7.4. We consider $a_{11} = 50\,a_0$, $a_{22} = 70\,a_0$, $\omega_z/2\pi = 1200$ Hz, and $N_{1,2} = 5 \times 10^4$, and show different configurations obtained for those parameters. All the states we obtain have an energy per particle $E/N \simeq 0.22\,\hbar\omega_z$ which differs by less than 1%, and their number of droplets ranges from 23 to 31.

Note that the arrangement of droplets is only approximately triangular. The actual distribution is in general nonuniform and may significantly depart from a triangular lattice. The structure of the interstitial component reflects this nonuniformity as well, which shows in a distorted momentum distribution, as we will discuss in the next subsection (7.3.2). Finally, we observed also a similar shot-to-shot variability in the stripe/labyrinthic phase of Section 7.4.

---

three-dimensionaly self-bound solution (see Fig. 7.2).

[10] In particular, we start from Gaussian functions with a small amount of noise that is seeded randomly such that it differs in each realization. To determine the ground-state configuration for a given set of parameters, we perform several realizations and keep the state with the lowest energy.

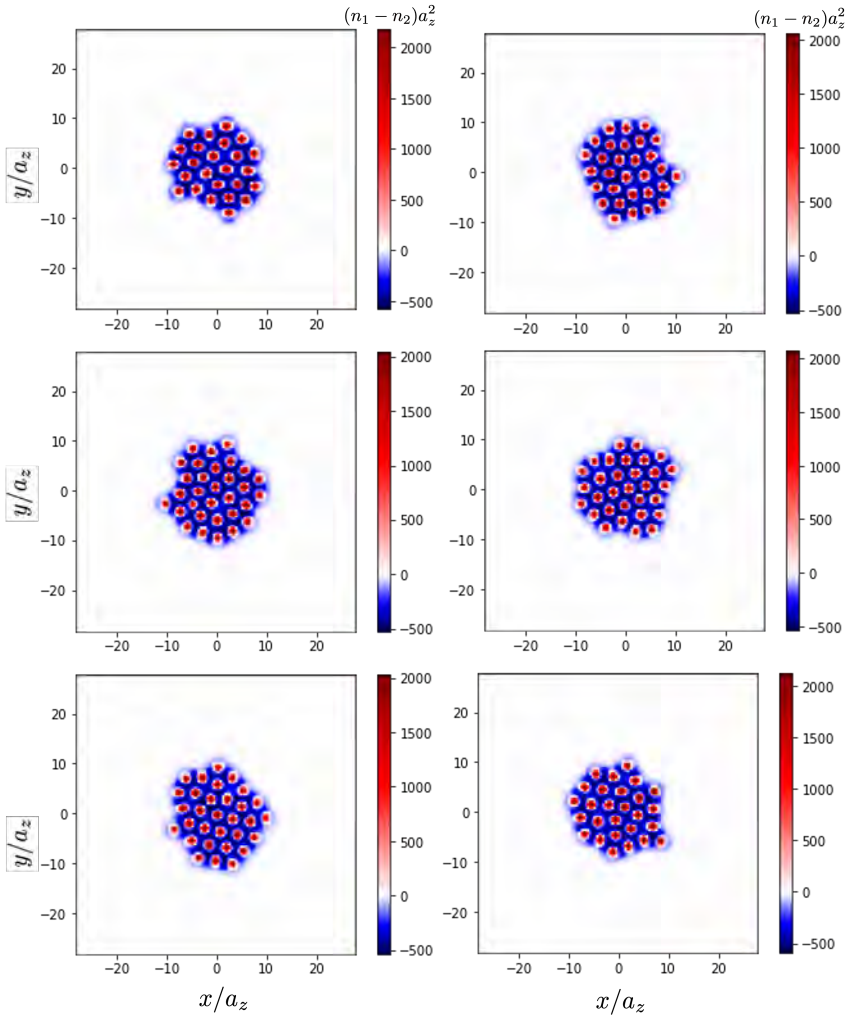

Figure 7.4: Shot-to-shot variability. Different droplet-crystal configurations obtained for the same parameters: $a_{11} = 50\,a_0$, $a_{22} = 70\,a_0$, $\omega_z/2\pi = 1200$ Hz, $N_{1,2} = 5 \times 10^4$. As usual, the plots show the column magnetization, with red indicating component 1 and blue component 2.

7.3.2 Interstitial superfluid and crystal sublimation

The droplets of the crystal are mutually incoherent (i.e., their densities do not overlap), but the component that fills the crystal interstitials may form a superfluid[11]. This behavior resembles, to some extent, the case of helium in a porous medium; in the system we consider, though, the droplets of the first component do not form a rigid structure.

[11]One may expect this from the seminal work of Leggett (1970), which provides a clear correlation between the superfluid fraction and the possibility that two points in the fluid may be linked without crossing a region of zero density (i.e., that the fluid remains connected). In the mixture we are considering, the bath (component 2) contains holes that are induced by the presence of the droplets (component 1), but still remains connected. A thorough analysis of superfluidity of the interstitial component is beyond the scope of this chapter, though one would expect the bath to present a large superfluid fraction.

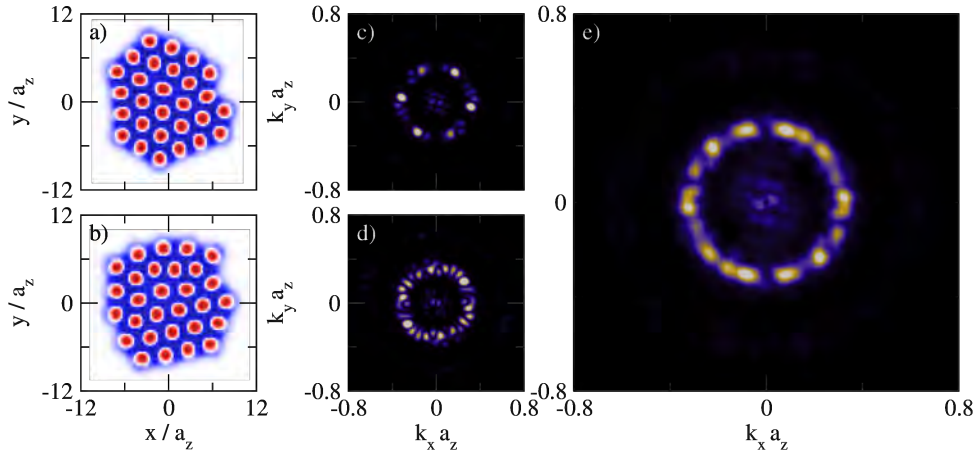

Figure 7.5: [(a,b)] Single-shot realizations of the column magnetization for $a_{11} = 50\,a_0$, $a_{22} = 70\,a_0$, $N_{1,2} = 5\times10^4$ and $\omega_z/2\pi = 1300$ Hz. Red regions are populated by component 1, and blue ones by component 2. [(c,d)] Corresponding momentum distribution for the second component $\tilde{n}_2(k_x, k_y)$ in the $k_z = 0$ plane, for the cases of (a) and (b), respectively. (e) Momentum distribution $\tilde{n}_2(k_x, k_y)$ averaged over 10 different realizations.

The droplets of component 1 present an approximately triangular crystalline structure that the interstitial component 2 inherits as well. Then, the resulting system forms a peculiar form of supersolid. Time-of-flight measurements may reveal the coherence and spatial density modulation of component 2. In Fig. 7.5 we show the momentum distribution $\tilde{n}_2(k_x, k_y)$ in the $k_z = 0$ plane.

The approximate triangular structure in real space [see Fig. 7.5(a)] translates to an hexagonal pattern in momentum space [see the momentum distribution $\tilde{n}_2$ in Fig. 7.5(c)]. However, there is a significant shot-dependent distortion in the momentum distribution due to the shot-to-shot variability of the exact arrangement of the droplets [see Figs. 7.5(b,d)] that we mentioned in the previous subsection. Note also that, since the system is not confined in the xy plane, the patterns spontaneously break the polar symmetry and, as a result, experience a random rotation from shot to shot.

As one may expect from the theory of roton immiscibility (Bland et al., 2022a; Lee et al., 2022; Wilson et al., 2012), the oscillator length $a_z = \sqrt{\hbar/m\omega_z}$ fixes the interdroplet distance R. In particular, for the case of Fig. 7.3, the interdroplet distance is $R \simeq 3\,a_z$ for all values of the atom number N and the axial frequency ω_z. One can also see this periodicity in the average of the momentum distribution over many realizations, which shows a ring at $1/R$ [see Fig. 7.5(e)].

Evaporation of the droplet crystal

For very large crystals, the interstitial component may evaporate partially or even totaly. Figure 7.6 illustrates this effect: for scattering lengths[12] $a_{11} = 50\,a_0$ and $a_{22} = 70\,a_0$, and

[12]The particular values we consider for a_{11} and a_{22} are small and thus give a mean-field contribution that is very negative, so the density has to be large to stabilize the system. This may result in peak densities for the droplets that are too high to lie within the experimental possibilities because high densities reduce

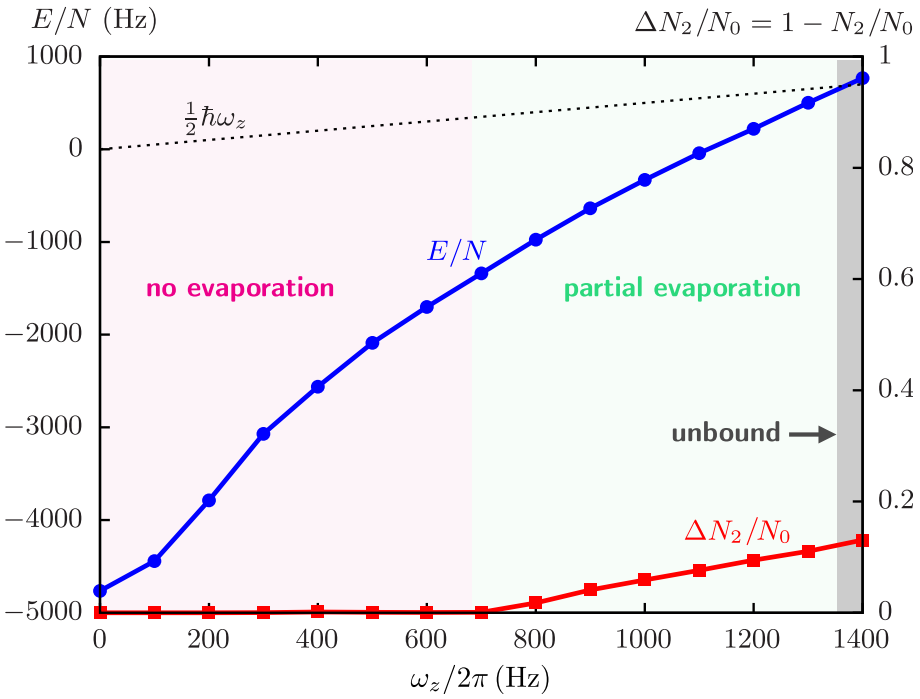

Figure 7.6: Energy per particle (blue circles) as a function of the axial trap frequency $f_z = \omega_z/2\pi$ for $a_{11} = 50\,a_0$, $a_{22} = 70\,a_0$ and $N_{1,2} = 5 \times 10^4$. The dashed line corresponds to the energy per particle ($\hbar\omega_z/2$) for a mixture infinitely spread on the xy plane and marks the border between self-bound and unbound solutions. The red squares are the proportion of atoms of component 2 that evaporate, with N_0 the initial number of atoms.

atom number $N_{1,2} = 5 \times 10^4$, we plot the energy per particle of the system and the ratio of particles lost by the second component as a function of the axial frequency.

For a fixed total number of atoms, the cohesive energy $|E/N|$ decreases when the droplet number grows (i.e., when the frequency grows). This occurs because increasing the number of droplets reduces the density, which in turns lowers the intercomponent dipolar attraction. Then, if the cohesive energy decreases enough, the self-bound solution eventually unbinds.

At a critical frequency $\omega_z^{\rm cr}$, the crystal unbinds and both components evaporate; for the case we show in Fig. 7.6, this frequency is $\omega_z^{\rm cr}/2\pi \simeq 1400$ Hz[13]. One can approximately determine this critical value as the frequency for which the energy per particle reaches $\hbar\omega_z/2$, which corresponds to the energy of an infinitely spread solution

drastically the lifetime of the system due to three-body losses. However, one could avoid this problem by considering larger values of the scattering length (for instance, $a_{11} = 70\,a_0$ and $a_{22} = 90\,a_0$), which results in equivalent physics but with lower peak densities.

[13]This value corresponds to the case with $N/2 = 5 \times 10^4$ but, in general, if the total number of atoms N is large enough, then the threshold between the self-bound and unbound regimes does not change significantly with N. The energy per particle is approximately independent of N; what changes instead is the number of droplets, since the peak density of the droplet is fixed for the interaction parameters. Therefore, increasing N results in more droplets, but the critical frequency should be approximately the same.

on the xy plane[14] (with axial confinement).

Note that when the frequency ω_z approaches the critical frequency ω_z^{cr}, the mutual attraction between components may still be enough to maintain a stable crystal, but insufficient to bind the whole interstitial superfluid. In this case, the second component partially evaporates[15], as we show in Fig. 7.6 (red line): the proportion of the interstitial component that evaporates grows with increasing frequency, as one may expect. On the opposite limit of very low frequencies, the cohesive energy is very large and there is no evaporation.

The situation is a bit more nuanced in imbalanced mixtures ($N_1 \neq N_2$). The mixture is fully self-bound for low enough frequencies: neither component evaporates, so the mixture keeps the original imbalance. In the vicinity of ω_z^{cr}, however, the component with a higher population may lose particles[16] and the mixture stabilizes into a smaller imbalance. Above ω_z^{cr}, the whole system unbinds, as in balanced mixtures.

7.4 Self-bound stripe/labyrinthic patterns

Thus far, we have considered a mixture with significantly asymmetric intracomponent interactions. However, the mixture arranges in a different form of self-bound pattern when the interactions are almost symmetric ($a_{11} \simeq a_{22}$).

In this section, we will begin by considering the case of strictly symmetric mixtures (Subsection 7.4.1) and then study more generally the effect of the asymmetry in the possible ground-state configurations of the system (Subsection 7.4.2).

7.4.1 Symmetric mixtures

When the interactions are symmetric[17] ($a_{11} = a_{22}$), the mixture forms stripes[18] in both components that are incoherent[19]. Figure 7.7 shows three selected cases of the scattering

[14] We do not find well defined self-bound solutions in our simulations beyond that value. However, one can still find numerically self-bound solutions above the critical frequency due to finite size effects. This happens because, for a finite-size box, the energy of the homogeneous solution may be much larger than $\hbar\omega_z/2$.

[15] To take into account this partial evaporation of the crystal, we add absorbing boundary conditions in our imaginary-time simulations. We fix a radius ρ_c on the xy plane such that the crystal lies well within a circle of radius $\rho < \rho_c$. Then, we consider as evaporated all particles that reach $\rho > \rho_c$ during the imaginary-time evolution. In the unbound regime, the whole mixture eventually leaves (in imaginary time) this region $\rho < \rho_c$.

[16] We have seen, for instance, that in the case when $N_1 > N_2$, it may be the first component (the droplet crystal) that evaporates partially until the imbalance is small enough to sustain a self-bound mixture.

[17] Note that $a_{11} = a_{22}$ when one considers a mixture of two maximally stretched magnetic states of the same atomic species.

[18] Actually, the system forms incoherent patterns when all the interactions, including the dipole–dipole interactions, are identical.

[19] We recall here that, while the droplets of the crystals we previously considered are incoherent as well (there is no overlap between them), the interstitial component is superfluid (and thus coherent). This is not the case in self-bound stripes.

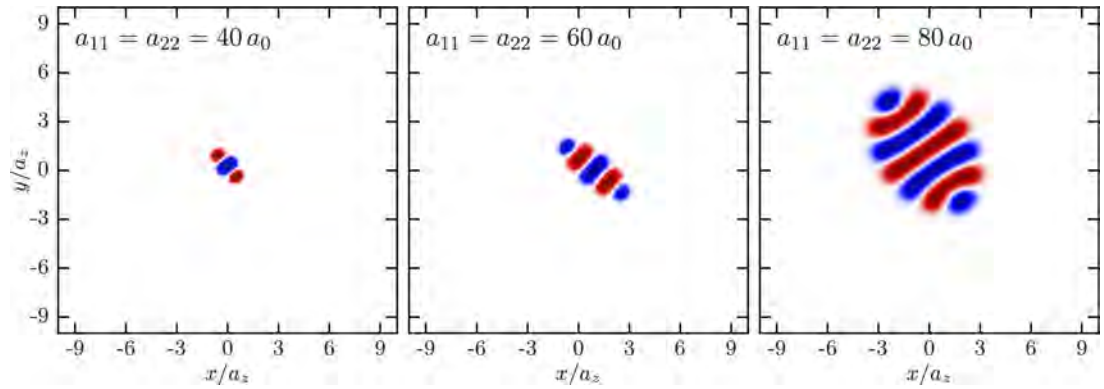

Figure 7.7: Self-bound stripe phase in a symmetric mixture ($a_{11} = a_{22}$) for $N_{1,2} = 5 \times 10^4$ (balanced mixture) and axial frequency $\omega_z/2\pi = 180$ Hz. As in previous figures, we plot the column magnetization (integrated along z) such that the red and blue regions correspond to component 1 and 2, respectively. For these low frequencies, the mixture shows a well-defined stripe phase.

lengths $a_{11} = a_{22}$ for a balanced mixture with $N_{1,2} = 5 \times 10^4$ atoms for each component and axial confinement with frequency $\omega_z/2\pi = 180$ Hz.

For very small values of the scattering length and when the dipolar interactions are dominant, the formation of droplets is more favorable for the system (see Fig. 7.7, left panel). Increasing the scattering length (and thus reducing the relative strength of the dipolar interactions) favors the formation of stripes instead. Therefore, the system will form more stripes the larger the scattering lengths are (see Fig. 7.7, central and right panels).

The axial frequency also affects the pattern in which the stripes arrange. In the case of droplet crystals (see Section 7.3), low frequencies result in well-defined crystals with a given number of droplets that depends on the frequency and the number of atoms. For large frequencies, on the other hand, we found a huge variability in the possible configurations that increases further with the axial confinement. This also happens for symmetric mixtures: for low frequencies, the stripes are well defined (see Fig. 7.7), but large frequencies will result in more complex configurations, as we will discuss in the next subsection.

7.4.2 Self-bound droplet crystals to self-bound stripes

To discuss with more detail the effect of the asymmetry in the interactions, we show in Fig. 7.8(a) the phase diagram in terms of the scattering lengths, a_{11} and a_{22}, for a balanced mixture with $N_{1,2} = 5 \times 10^4$ and an axial frequency $\omega_z/2\pi = 1200$ Hz that is much larger than the one we considered previously.

For a large enough asymmetry $|a_{11} - a_{22}|$, we obtain the droplet crystals from Section 7.3 [see Fig. 7.8(a), inset with the yellow square]. As we mentioned before, the interstitial component of these crystals partially evaporates in the vicinity of the unbinding threshold. When the interactions are similar ($a_{11} \simeq a_{22}$), in contrast, the system arranges in a labyrinthic phase that also has a large shot-to-shot variability. In

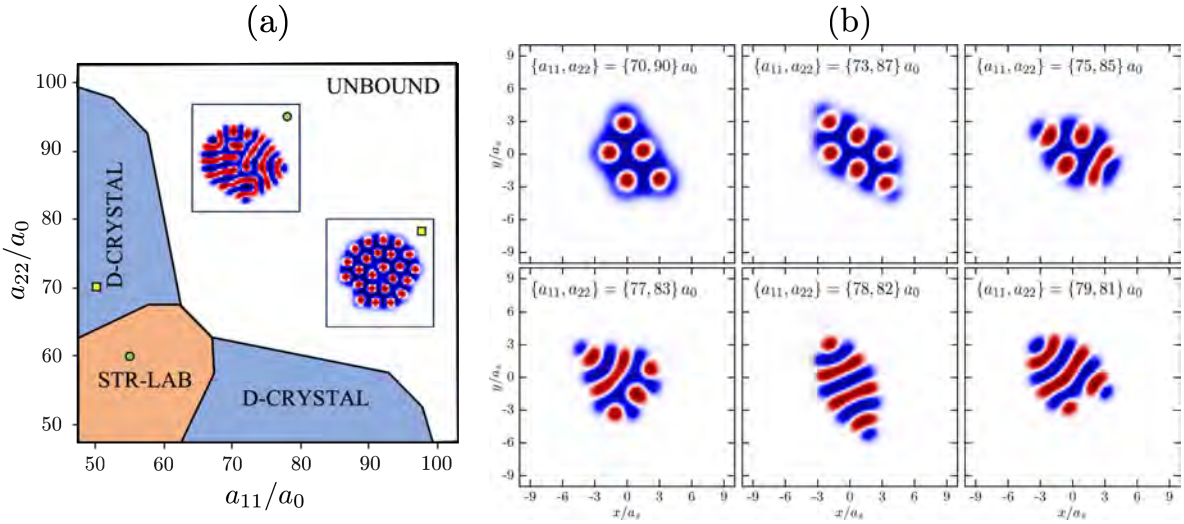

Figure 7.8: Droplet crystals and stripe/labyrinthic phases for $N_{1,2} = 5 \times 10^4$. (a) Phase diagram for $\omega_z/2\pi = 1200$ Hz. We find two different self-bound solutions: a droplet crystal (D-CRYSTAL), illustrated in the inset for $a_{11} = 50\, a_0$ and $a_{22} = 70\, a_0$ (yellow square), and a stripe/labyrinthic (STR-LAB) phase, illustrated in the inset for $a_{11} = 55\, a_0$ and $a_{22} = 60\, a_0$ (green circle). (b) Transition from droplet crystal to stripe phase for $\omega_z/2\pi = 180$ Hz, with the scattering lengths indicated in the labels. The red and blue regions, as before, are populated respectively by components 1 and 2.

this phase, the stripes present different orientations [see Fig. 7.8(a), inset with the green circle].

The phase diagram is similar for lower frequencies but, in this case, the ground-state configuration presents a well-defined stripe crystal, as we discussed in the previous subsection. In Fig. 7.8(b), we show selected cases in the vicinity of the droplet-crystal–stripe transition for a small frequency $\omega_z/2\pi = 180$ Hz (the same as in Fig. 7.7). These cases illustrate how the ground-state configuration may range from a droplet crystal (for markedly asymmetric mixtures) to a stripe crystal (for symmetric mixtures) with intermediate situations. In addition, independently of how strong the axial confinement is, both components form mutually incoherent domains in the labyrinthic/stripe phase.

Finally, the effect of an imbalance in the number of atoms is similar to what we observed in droplet crystals. Starting from a mixture with $N_1 \neq N_2$, the system eventually stabilizes into a mixture with almost no imbalance ($N_1 \sim N_2$) after some evaporation. We observed in our calculations that this effect is more pronounced for high frequencies. For lower frequencies, as in the case of droplet crystals, unbalanced mixtures may be stable as long as they are well below the unbinding threshold.

7.5 Summary of results

In this chapter, we have studied antiparallel dipolar mixtures and how they can form self-bound crystals[20] when confined along the polarization direction. These crystals differ from those of parallel mixtures in that they have a genuine cohesive energy and thus remain self-bound in the absence of a transversal trap. The mutual confinement between components comes from the intercomponent interactions, which are attractive. As a result, the system can form incoherent stripe/labyrinthic crystals in mixtures with symmetric intracomponent interactions, and self-bound droplet crystals in asymmetric mixtures. In the last case, one of the components forms an array of incoherent droplets that arranges in an approximately triangular structure, while the other component remains superfluid and fills in the interstitials. Thus, the whole mixture forms a peculiar form of supersolid that could be probed using time-of-flight measurements. We have considered the particular case of a dysprosium mixture, but the results presented in this chapter could be extended to other antiparallel (either magnetic or electric) dipolar mixtures including, for instance, mixtures of polar molecules.

Creating such self-bound dipolar crystals opens new avenues for future studies. For instance, analyzing the character of lattice excitations, which may remain self-bound or result in phonon evaporation[21]; proving the superfluidity of the interstitial superfluid by, for example, vortex formation; or exploring, in general, the dynamics of self-bound crystals.

[20] One could address antiparallel dipolar mixtures experimentally in a dysprosium gas, for example. For that, one should first create a dipolar condensate in the magnetic state $|m = -8\rangle$, and then transfer part of the atoms to the $|m = 8\rangle$ state using, for instance, optical pumping, Raman or STIRAP techniques. Finally, after some time, one would remove the transversal trapping to prove the self-bound nature of the mixture.

[21] Similar to the self-evaporation observed in the case of nondipolar mixtures (Petrov, 2015).

8

Chiral states in rotating Bose–Einstein condensates with current-density interactions

The chiral theory proposed by Aglietti et al. (1996) describes a system with effective current-density interactions, as we explored in Subsection 4.2 (Chapter 4). These interactions have chiral properties and can emerge from a gauge potential such as $\mathcal{A}(x,t) = -(\hbar\kappa/2)\, n(x,t)$ (4.41), which depends linearly on the number density $n(x,t)$ with a strength κ. The theory has been experimentally realized in ultracold atoms in the last years (Clark et al., 2018; Frölian et al., 2022; Görg et al., 2019; Yao et al., 2022) using light-induced density-dependent gauge potentials (Chisholm et al., 2022; Dalibard et al., 2011; Edmonds et al., 2013a; Goldman et al., 2014).

One can map this theory into a 1D Gross–Pitaevskii-like equation where the nonlinearity comes from the number density, as usual, but also from the current density $J(x,t)$. The effective GPE that describes the system is

$$i\hbar\frac{\partial\psi}{\partial t} = \frac{\hat{p}^2}{2m}\,\psi + \left(gn + \hbar\kappa J\right)\psi\,, \tag{8.1}$$

where g is the coupling constant of the mean-field contact interactions and κ characterizes the strength of the current-density interactions. We derived this equation in detail in Chapter 4 [see Eq. (4.50) and Section 4.2] for a system where, in general, both current-density and contact interactions can be present. In this chapter, we will consider the theory as originally proposed (Aglietti et al., 1996; Jackiw, 1997), with the current-density term in the interactions replacing the number-density term. The effective contact interactions may not be negligible in realistic settings, but here we will assume $g = 0$ to isolate the effect of the current-density interactions. We will use as a reference the case with only contact interactions (i.e., $g \neq 0$ and $\kappa = 0$) to discuss the results presented in this chapter as well as in Chapter 9, and we will refer to it as the *nonchiral case* from now on.

The chiral properties of Eq. (8.1) can be observed in current-carrying states (Edmonds et al., 2013a, 2015; Xu et al., 2023) and, more particularly, in chiral solitons (Aglietti et al., 1996; Bhat et al., 2021; Dingwall and Öhberg, 2019; Dingwall et al., 2018; Gao et al., 2022; Griguolo and Seminara, 1998; Jia et al., 2022b), as already discussed in Chapter 4. Setting $g = 0$, the equation supports dark-soliton solutions for $\hbar\kappa J > 0$ and

bright-soliton solutions for $\hbar\kappa J < 0$. These solitons can be analytically described by means of hyperbolic functions [see, for instance, Eqs. (6.3) and (6.4) in Chapters 2 and 6], with the proper normalization.

We will consider a system with periodic boundary conditions and under rotation, i.e., a quasi-1D gas trapped in a ring potential that rotates around its symmetry axis at a frequency Ω. BECs confined in ring geometries present persistent currents (i.e., quantized vortices) when rotating as a result of their superfluid character. The aim of this chapter is to explore how these currents become chiral when the nonlinearity of the system comes from a density-dependent gauge potential (so that the interactions depend on the current-density) and which types of stationary solutions these systems may support.

Kanamoto et al. (2009) presented a detailed study of the families of solutions and their dynamical stability for the nonchiral case. In particular, they study how the different branches of stationary states (i.e., plane waves and solitons) connect when varying the rotation frequency, both for a fixed attractive and repulsive contact-interaction strength. The resulting diagrams of energy as a function of rotation for a given interaction strength are symmetric with respect to the rotation frequency Ω as a result of the symmetry with respect to Galilean transformations. However, this is not the case in a chiral condensate.

In the presence of current-density interactions, the Galilean symmetry is broken and thus the strength and nature of the interactions is determined by the modulus and sign of the rotation rate Ω: clockwise or counterclockwise rotations are not equivalent, and increasing rotation rates translate into increasing interaction strengths. As a result, the energy diagrams are no longer symmetric with Ω and unexpected trajectories appear in the dispersion relations. The two characters of the interactions (attractive and repulsive) will then appear in the same diagram due to the chiral properties of the system: the interactions will be attractive for negative rotation rates, and repulsive for positive rotation rates. Therefore, one can already anticipate that, in such a situation, the nonrotating case ($\Omega = 0$) becomes a singular point where the effective interactions change sign due to the chiral nature of the system.

In this chapter, we will focus on the general solutions to the equation of motion in a ring geometry and generalize what has been done for the nonchiral case (Kanamoto et al., 2009) to a system with current-density interactions. The differences between the chiral and nonchiral cases are observable in the density profiles as well as in the trajectories of the stationary states. In general, soliton-like branches connect with plane waves for varying rotation rates. However, for negative rotation frequencies above (in modulus) a velocity threshold, some bright-soliton families may detach from the expected path and follow instead the dispersion of a free particle. We will analyze the stability of these stationary states for a particular case both by linearizing the GPE as well as by performing a nonlinear time evolution.

The chapter is structured in four sections. In Section 8.1, we introduce the equations of motion and conserved quantities in a ring geometry that describe the system for a ring geometry. We also discuss plane-wave solutions and particular solitonic states. In Section 8.2, we derive more general solutions to the equations of motion that allow us to connect different stationary states. In Section 8.3, we consider a particular case and

analyze the different families of solutions available, the parameters for their existence and their dynamical stability. Finally, in Section 8.4, we summarize all the results presented throughout the chapter.

8.1 Chiral condensates in a ring geometry

In this section, we present the theoretical model that describes the system[1]. We first introduce the equation of motion of the system and the conserved energy, as well as discuss the ring units and other particularities of this geometry (Subsection 8.1.1). Afterwards, we explore the simplest sationary states that the system supports (Subsection 8.1.2) to prepare the ground for the study of more general stationary states in Section 8.2.

8.1.1 Gross–Pitaevskii equation in the rotating frame

Consider a quasi-1D ring of radius R (i.e., a 1D system with periodic boundary conditions) rotating at an angular frequency Ω around its perpendicular axis. The generalized 1D chiral GPE (8.1) translates to the rotating frame as (4.64)

$$i\hbar\frac{\partial\psi}{\partial t} = \left(\frac{\hat{\Pi}^2}{2m} + \hbar\kappa J\right)\psi\,, \tag{8.2}$$

where m is the mass of the atoms and $\psi(x,t)$ is the condensate wavefunction, with $n(x,t) = |\psi(x,t)|^2$ its (number) density. We recall that the momentum operator in the rotating frame is defined as $\hat{\Pi} = \hat{p} - m\Omega R$ (4.63), where $\hat{p}$ is the canonical momentum operator.

The current-density interactions have a (dimensionless) strength κ, and depend on the current density $J(x,t)$ measured in the laboratory frame (4.47),

$$J = \frac{\hbar}{2mi}\left(\psi^*\frac{\partial\psi}{\partial x} - \psi\frac{\partial\psi^*}{\partial x}\right). \tag{8.3}$$

From now on, we set $\kappa > 0$ for simplicity and consider both positive and negative rotation rates.

The current density can be rewritten in terms of the canonical momentum $\hat{p}$ as $J = [\psi^*\hat{p}\psi + (\psi^*\hat{p}\psi)^*]/(2m)$. Then, the average canonical momentum $\langle\hat{p}\rangle$ is defined as

$$\langle\hat{p}\rangle = \oint \psi^*\hat{p}\psi\,dx = m\oint J\,dx\,. \tag{8.4}$$

The number density is related to the current density (8.3) by means of the continuity equation (4.48),

$$\frac{\partial n}{\partial t} + \frac{\partial\mathcal{J}}{\partial x} = 0\,, \tag{8.5}$$

[1]For more details on the derivation of the equation of motion and conserved quantities, see Subsection 4.2.2 in Chapter 4.

where $\mathcal{J} = J - n\Omega R$ is the current density in the rotating frame: we will naturally obtain this expression from the usual 1D continuity equation when looking for general solutions in Section 8.2.

The wavefunction is normalized to the number of atoms N in the condensate, $N = \oint dx\, |\psi|^2$, and the average number density is $n_0 = N/(2\pi R)$. We also introduce the wavenumber associated with rotation,

$$k_\Omega = \frac{m|\Omega|R}{\hbar}\,, \tag{8.6}$$

for notational convenience.

To rewrite the equations of motion and physical quantities that describe the system in dimensionless units, one refers to the characteristic scales of the system. Due to the absence of external trapping and the periodic boundary conditions we are considering, a natural choice of unit length is the ring radius R, such that the unit energy is $\hbar^2/(mR^2)$. Then, we can introduce the dimensionless quantity $\tilde{n} = n_0\, R$ for the density and $\tilde{\Omega} = \Omega\, mR^2/\hbar$ for the angular rotation frequency.

Conserved energy

From the chiral GPE (8.2) one can identify the nonlinear Hamiltonian operator that effectively describes the system in the rotating frame [see Eq. (4.62)],

$$\mathcal{H} = \frac{\hat{\Pi}^2}{2m} + \hbar\kappa J\,, \tag{8.7}$$

and thus $i\hbar\,\partial_t\psi = \mathcal{H}\psi$ gives the evolution of the system. The expectation value of the first term of $\mathcal{H}$ (8.7) gives the conserved energy (4.65),

$$E = \frac{1}{2m}\oint \psi^*\hat{\Pi}^2\psi\, dx\,. \tag{8.8}$$

As we discussed in Chapter 4, the conserved energy E (8.8) does not depend on the current-density interactions (Aglietti et al., 1996; Jia et al., 2022b).

Constraint of the ring geometry

Before discussing the stationary states of the system, let us remark an important consequence of the periodic boundary conditions on the elimination of the density-dependent gauge potential.

In open geometries, the chiral model can be mapped into a theory with a density-dependent gauge field such as $\mathcal{A}(x,t) = -(\hbar\kappa/2)\, n(x,t)$. However, as we anticipated in Chapter 4 (see Subsection 4.2.2 and discussion therein), the ring geometry may frustrate the mapping between the density-dependent gauge equation into the GPE with chiral interactions. Since the density has a single value in both theories and the density profile has to be the same, the periodic boundary conditions impose a $2\pi l$ phase jump when winding around the ring (l is an integer).

This constraint affects the Jordan–Wigner-like transformation (4.46) that one performs to eliminate the gauge from the equation of motion,

$$\psi(x,t) = \varphi(x,t) \exp\left[i\frac{\kappa}{2} \int^{x} |\varphi(y,t)|^2 \, dy \right] , \tag{8.9}$$

where x is now bounded as $x \in [0, 2\pi R]$. The wavefunction for the current-density interaction theory (i.e., the transformed wavefunction) is $\psi(x,t)$, with phase $\theta(x,t) = \arg[\psi(x,t)]$, and the wavefunction for the gauge-dependent theory (i.e., the nontransformed wavefunction) is $\varphi(x,t)$, with phase $\vartheta(x,t) = \arg[\varphi(x,t)]$. Then, using Eq. (8.9), the phase of the transformed wavefunction can be written as

$$\theta(x,t) = \vartheta(x,t) + \frac{\kappa}{2} \int^{x} |\varphi(y,t)|^2 \, dy \, , \tag{8.10}$$

and the phase difference for a given time t when winding around the ring, $\Delta\theta = \theta(2\pi R) - \theta(0)$, is given by

$$\Delta\theta = \Delta\vartheta + \frac{\kappa}{2} \oint |\varphi(y)|^2 \, dy = \Delta\vartheta + \frac{\kappa N}{2} \, , \tag{8.11}$$

with $\Delta\vartheta = \vartheta(2\pi R) - \vartheta(0)$. Since the periodic boundary conditions impose that both $\Delta\theta = 2\pi l$ and $\Delta\vartheta = 2\pi l'$, where l and l' are integers, $\kappa N/2$ has to jump in integer multiples of 2π as well. Thus, the mapping between theories is only allowed for quantized values of the total number of particles,

$$N = \frac{4\pi}{\kappa} j \, , \tag{8.12}$$

where j is an integer.

This feature of the ring geometry will be particularly relevant when comparing results obtained for each theory, since the mapping between the two theories exists only when the quantization condition (8.12) is satisfied.

8.1.2 Stationary states

The stationary states of the system $\psi(x,t) = \phi(x) \, \exp(-i\mu t/\hbar)$ fulfill the time-independent equation

$$\mathcal{H} \, \phi = \mu \, \phi, \tag{8.13}$$

where μ is the energy eigenvalue of the Hamiltonian operator $\mathcal{H}$ (8.7). Note that this eigenenergy is not the conserved energy of the system (8.8). From the corresponding definitions, one can see that the energy eigenvalue μ and the conserved energy E are related by

$$\mu = \frac{E}{N} + \hbar\kappa \frac{\langle J \rangle}{N} \, , \tag{8.14}$$

where $\langle J(x,t) \rangle = \oint dx \, J(x,t) \, |\phi(x,t)|^2$ is the expectation value of the current (8.3).

Plane-wave solutions

Due to the translational invariance of the system, the time-independent equation (8.2) admits plane-wave solutions

$$\psi_q(x,t) = \sqrt{n_0}\, e^{iqx}\, e^{-i\mu_q t/\hbar}\,, \tag{8.15}$$

where q is the wavenumber, which is quantized and, in dimensionless units, takes integer values ($qR = 0, \pm 1, \pm 2, \ldots$). The current density (8.3) is constant,

$$J_q = \frac{\hbar}{m}\, q n_0\,, \tag{8.16}$$

such that $\langle J_q \rangle = J_q\, N$. Using that $\hat{\Pi}^2\, \psi_q = (\hbar q - m\Omega R)^2\, \psi_q$ and substituting the current density J_q from Eq. (8.16), the energy eigenvalue μ_q (8.14) is

$$\mu_q = \frac{(\hbar q - m\Omega R)^2}{2m} + \frac{\hbar^2 q \kappa n_0}{m}\,. \tag{8.17}$$

Comparing with the noninteracting system ($\kappa = 0$), the energy eigenvalue for plane waves μ_q (8.17) has an energy shift of $|\hbar^2 q\kappa n_0/m|$ that increases with the average number density n_0.

Quasi-linear states for the nonrotating case

For the particular case of $\Omega = 0$, the equation of motion (8.2) reduces to

$$i\hbar \frac{\partial \psi}{\partial t} = \left(\frac{\hat{p}^2}{2m} + \hbar \kappa J \right) \psi\,, \tag{8.18}$$

which becomes linear for a vanishing current, $J = 0$. Other than plane waves, which have a zero current for $q = 0$, the system admits the same solutions as the Schrödinger equation, which are standing waves such as $\sin(qx)$ and $\cos(qx)$. Therefore, linear superpositions of these states with real coefficients are a solution of the equation (8.18) as well. In addition, complex superpositions with a general nonvanishing current J, of the form $\cos(qx) + i\alpha \sin(qx)$, are also a solution at $\Omega = 0$. One can write these complex superpositions as

$$\psi_{\alpha q}(x,t) = \frac{1}{2}\sqrt{n_\alpha}\, \left[(1-\alpha) e^{-iqx} + (1+\alpha) e^{iqx} \right]\, e^{-i\mu_{\alpha q} t/\hbar}\,, \tag{8.19}$$

where α is a real number. The current (8.3) of these quasi-linear states (8.19) is

$$J_{\alpha q} = \frac{\hbar}{m}\, \alpha q n_\alpha\,, \tag{8.20}$$

and the eigenenergy $\mu_{\alpha q}$ (8.14) is

$$\mu_{\alpha q} = \frac{(\hbar q)^2}{2m} + \alpha\, \frac{\hbar^2 q \kappa n_\alpha}{m}\,. \tag{8.21}$$

Asymptotic soliton solutions

Besides plane waves and their superpositions, one can also find in the literature (Aglietti et al., 1996) dark- and bright-soliton solutions described in terms of hyperbolic functions (see Chapters 2, 4 and 6). We denote these solutions by ψ_{D} and ψ_{B}, respectively, and rewrite them here for a ring rotating with angular velocity Ω as approximate stationary states when their characteristic lengths, ξ_{D} and ξ_{B}, are small compared to the radius. Thus, these asymptotic solutions are only exact for infinite rings, i.e., $\xi_{\mathrm{D,B}} \ll \pi R$.

For positive rotation rates ($\Omega > 0$), the equation of motion (8.2) admits dark-soliton solutions:

$$\psi_{\mathrm{D}}(x,t) \approx \sqrt{\frac{N}{2(\pi R - \xi_{\mathrm{D}})}}\, \tanh\left(\frac{x}{\xi_{\mathrm{D}}}\right) e^{ik_\Omega x}\, e^{-i\mu_{\mathrm{D}} t/\hbar}\,. \tag{8.22}$$

The normalizing prefactor can be obtained by normalization of ψ_{D} to the number of atoms N, and assuming that $\xi_{\mathrm{D}} \ll \pi R$ such that $\tanh(\pi R/\xi_{\mathrm{D}}) \approx 1$. We recall that $k_\Omega = m|\Omega|R/\hbar$ (8.6) is the wavenumber related to rotation. Similarly, bright solitons are solution of the equation for negative velocities ($\Omega < 0$) instead:

$$\psi_{\mathrm{B}}(x,t) \approx \sqrt{\frac{N}{2\xi_{\mathrm{B}}}}\, \mathrm{sech}\left(\frac{x}{\xi_{\mathrm{B}}}\right) e^{-ik_\Omega x}\, e^{-i\mu_{\mathrm{B}} t/\hbar}\,. \tag{8.23}$$

The characteristic lengths of the solitons are

$$\xi_{\mathrm{D}} = \frac{\xi_{\mathrm{B}}}{2}\left[\sqrt{1 + \frac{4\pi R}{\xi_{\mathrm{B}}}} - 1\right] \quad \text{and} \quad \xi_{\mathrm{B}} = \frac{2}{\kappa N k_\Omega}\,, \tag{8.24}$$

and the energy eigenvalues, assuming $\xi_{\mathrm{D,B}} \ll \pi R$, are

$$\mu_{\mathrm{D}} \approx \frac{\hbar^2}{m\xi_{\mathrm{D}}^2} = \frac{\hbar\,\pi R}{\pi R - \xi_{\mathrm{D}}}\,\kappa\Omega R n_0 = \frac{\kappa N}{2}\,\frac{\hbar\,\Omega R}{\pi R - \xi_{\mathrm{D}}}\,, \tag{8.25}$$

and

$$\mu_{\mathrm{B}} \approx -\frac{\hbar^2}{2m\xi_{\mathrm{B}}^2} = -\frac{m(\pi R)^2}{2}\,(\kappa\Omega R n_0)^2 = -\left(\frac{\kappa N}{2}\right)^2 \frac{m(\Omega R)^2}{2}. \tag{8.26}$$

Note that the energy eigenvalues show a different scaling: μ_{D} (8.25) varies linearly with $\kappa\Omega R n_0$, while μ_{B} (8.26) scales quadratically with $\kappa\Omega R n_0$.

Dark and bright solitons differ as well in their domains of existence. In the regime we are considering, the bright soliton exists for arbitrary values of Ω (with $\Omega < 0$), as occurs for a classical particle. However, the dark soliton (with $\Omega > 0$) in the ring has to fulfill a particular boundary condition: dark solitons are characterized by a π-phase jump across their profile. Therefore, the background constant velocity ΩR has to cancel this π-phase jump,

$$\frac{m\Omega R}{\hbar}\, 2\pi R = \pi + 2\pi l\,, \tag{8.27}$$

with $l = 0, \pm 1, \pm 2, \ldots$ an integer that labels, in units of 2π, the phase difference acquired as winding around the ring. As a result, the possible rotation rates are restricted to

$$\Omega_{\mathrm{D}} = \left(\frac{1}{2} + l\right) \frac{\hbar}{mR^2} \,. \tag{8.28}$$

This constraint denotes the wave character of the dark soliton, as opposed to the particle nature of the bright soliton.

In the next section (Section 8.2), we will consider a given average density n_0 (or particle number N) and search for analytical stationary solutions to the equation of motion (8.13) that generalize the solutions we have explored so far: Eqs. (8.15), (8.22) and (8.23). The last two correspond to the asymptotic limit for large rings; before moving to more general solutions, we will next give particular dark- and bright-soliton solutions that are exact for a ring geometry.

Soliton solutions for generic rings

Equations (8.22) and (8.23) give approximate solutions for a large ring of radius R ($\xi_{\mathrm{D,B}} \ll \pi R$), but one can make them exact for generic rings using Jacobi elliptic functions. As we mentioned on Chapter 4 (Subsection 4.2.2; for details, see Appendix A), Jacobi elliptic functions are periodic functions that generalize the trigonometric functions (Abramowitz and Stegun, 1968), which allows one to account for the periodic boundary conditions of a ring geometry when describing solitonic states.

In particular, we will consider the Jacobi sine and cosine functions, $\mathrm{sn}(x/\xi, \mathfrak{m})$ and $\mathrm{cn}(x/\xi, \mathfrak{m})$ [see Eq. (A.1)], with characteristic width ξ and parameter $\mathfrak{m} \in [0, 1]$. If $\Omega > 0$, the function $\mathrm{sn}(x/\xi, \mathfrak{m})$ generalizes the dark-soliton solution (8.22),

$$\psi_{\mathrm{sn}}(x,t) = \sqrt{\frac{\mathfrak{m}}{\kappa\, \xi^2 k_\Omega}}\, \mathrm{sn}\left(\frac{x}{\xi},\, \mathfrak{m}\right) e^{ik_\Omega x}\, e^{-i\mu_{\mathrm{sn}} t/\hbar} \,. \tag{8.29}$$

On the other hand, if $\Omega < 0$, the function $\mathrm{cn}(x/\xi, \mathfrak{m})$ generalizes the bright-soliton solution (8.23),

$$\psi_{\mathrm{cn}}(x,t) = \sqrt{\frac{\mathfrak{m}}{\kappa\, \xi^2 k_\Omega}}\, \mathrm{cn}\left(\frac{x}{\xi},\, \mathfrak{m}\right) e^{-ik_\Omega x}\, e^{-i\mu_{\mathrm{cn}} t/\hbar} \,. \tag{8.30}$$

The characteristic length ξ is the same for both ψ_{sn} (8.29) and ψ_{cn} (8.30), and the corresponding eigenergies are

$$\mu_{\mathrm{sn}} = \frac{\hbar^2}{2m\xi^2}\,(1 + \mathfrak{m}), \tag{8.31}$$

if $\Omega > 0$, and

$$\mu_{\mathrm{cn}} = -\frac{\hbar^2}{2m\xi^2}\,(2\mathfrak{m} - 1), \tag{8.32}$$

if $\Omega < 0$. The phase $\pm k_\Omega x$ [see Eqs. (8.29) and (8.30)] is linear with the position and follows the motion of the ring in both cases, and thus the current density vanishes in the co-moving reference frame.

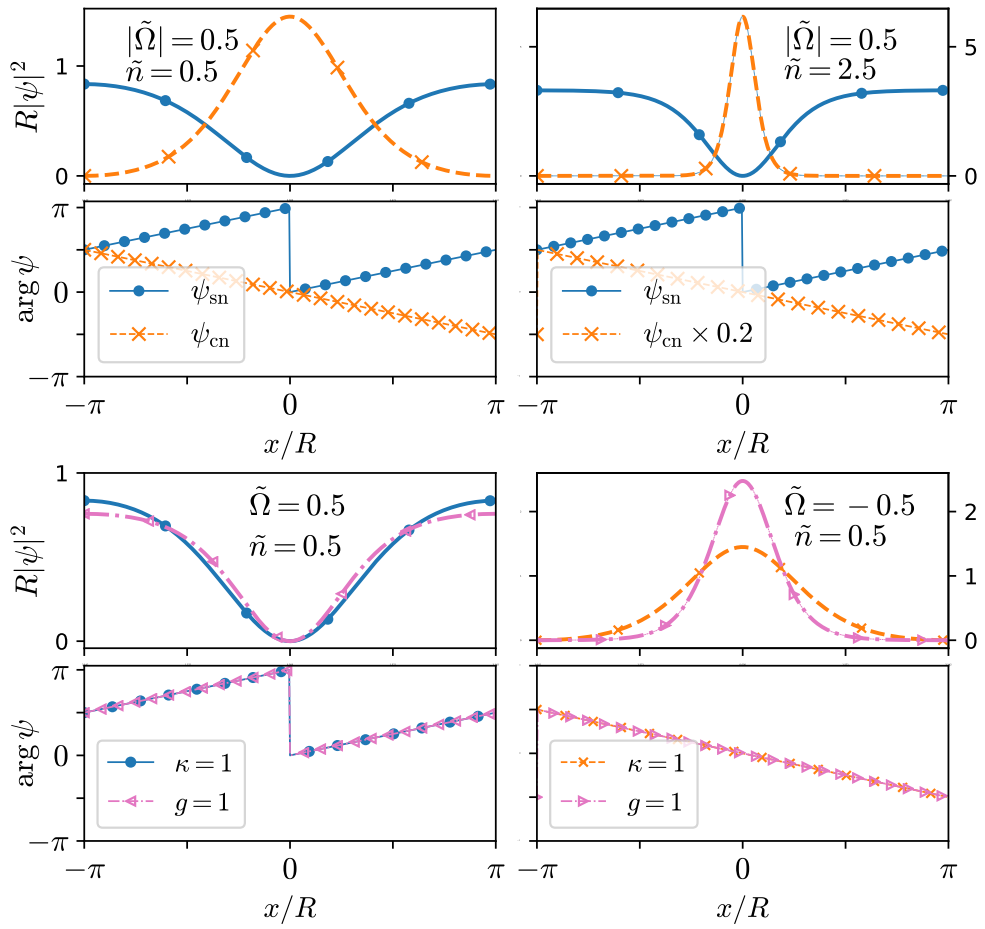

Figure 8.1: Stationary solitonic states defined by Eqs. (8.29) and (8.30) for rotating rate $|\Omega| = 0.5\hbar/(mR^2)$. Top panels: states with a low $n_0 = 0.5/R$ (left panels) versus high $n_0 = 2.5/R$ (right panels) number density; they correspond to the black solid symbols in Fig. 8.3. Bottom panels: comparison with equivalent states of the nonchiral case with $n_0 = 0.5/R$ and obtained with a contact interaction of dimensionless strength g that corresponds to the same interaction strength, i.e., $|g| = \kappa = 1$; dark soliton with $\Omega = 0.5\hbar/(mR^2)$ (left panel) and bright soliton with $\Omega = -0.5\hbar/(mR^2)$ (right panel). The labels $\tilde{\Omega}$ and $\tilde{n}$ indicate the dimensionless values of Ω and n_0, with units $\hbar/(mR^2)$ and $1/R$, respectively.

Figure 8.1 (top panels) shows as an example the stationary states given by Eqs. (8.29) and (8.30) for a single node (one soliton) along the ring, rotation rate $|\Omega| = 0.5\hbar/(mR^2)$, and two different values of the average number density: $n_0 = 0.5/R$ (left panels) and $n_0 = 2.5/R$ (right panels). As one can see in the figure, increasing the number of particles (such that the interactions increase) translates to narrower solitons. For a given average density and rotation rate, these states are clearly different from the stationary states that are solution of the usual Gross–Pitaevskii equation with only contact interactions (i.e., the nonchiral case), as we show in the bottom panels of Fig. 8.1. This occurs because the effective interactions that result from the current density are not constant but depend on the position, unlike the contact interactions in the nonchiral case.

The parameter $\mathfrak{m}$ is bound between 0 and 1, which gives the two limits of the elliptic functions (see Appendix A for more details). The wavefunctions (8.29) and (8.30) tend to the hyperbolic functions, (8.22) and (8.23), respectively, for $\mathfrak{m} \to 1$. In the opposite limit, $\mathfrak{m} \to 0$, one recovers the trigonometric functions $\sin(x/\xi)$ and $\cos(x/\xi)$.

The complete elliptic integral of the first kind $\mathrm{K} = \mathrm{K}(\mathfrak{m})$ (A.4) gives the spatial period of the elliptic functions (Abramowitz and Stegun, 1968). The functions sn and cn have a period of 4K, but the period of the squared functions is 2K, which is what we use to define the solitonic solutions. Then, since the period of these functions has to be a divisor of the ring length ($2\pi R$), it fulfills that

$$j\,\mathrm{K}(\mathfrak{m})\,\xi = \pi R\,, \tag{8.33}$$

where $j = 1, 2, 3, \ldots$ is a positive integer that labels the number of nodes (solitons) in the ring.

Equation (8.33) also defines the characteristic length ξ of the corresponding nonlinear wave. Finally, imposing that the phase has to be periodic, one finds the possible rotation rates where these solutions can exist:

$$|\Omega| = \frac{j}{2}\,\frac{\hbar}{mR^2}\,. \tag{8.34}$$

This condition is obtained as a generalization of the expression for the asymptotic dark soliton in an infinite ring (8.28) with $l = 0$.

Normalizing the dark-soliton wavefunction ψ_{sn} (8.29) and using the condition for the period (8.33) gives an implicit equation for the parameter $\mathfrak{m}$,

$$\frac{N_{\mathrm{sn}}}{2\pi R}\,k_\Omega = \frac{\mathrm{L}(\mathfrak{m})}{\kappa\xi^2}\,, \tag{8.35}$$

and equivalently for the bright soliton, ψ_{cn} (8.30),

$$\frac{N_{\mathrm{cn}}}{2\pi R}\,k_\Omega = \frac{\mathfrak{m} - \mathrm{L}(\mathfrak{m})}{\kappa\xi^2}\,. \tag{8.36}$$

We have defined the function $\mathrm{L}(\mathfrak{m}) = 1 - \mathrm{E}(\mathfrak{m})/\mathrm{K}(\mathfrak{m})$, where $\mathrm{E}(\mathfrak{m})$ is the complete integral of the second kind [see Eq. (A.5) and discussion in Appendix A]. $\mathrm{L}(\mathfrak{m})$ takes values in the range $[0, 1]$ when $\mathfrak{m}$ varies in $[0, 1]$.

8.2 General current-carrying states

In the present section we will look for more general solutions to the equation of motion (8.2) that interpolate between plane waves (8.15) and soliton-like states [(8.29) and (8.30)]. We consider generic stationary states,

$$\psi(x,t) = \sqrt{n(x)}\,e^{i\theta(x)}\,e^{-i\mu t/\hbar}\,, \tag{8.37}$$

where the phase $\theta(x)$ and number density $n(x)$ are given in terms of the system parameters $\{R, N, \Omega, \kappa\}$. The current density in the laboratory frame (8.3) can be written in terms of the phase and the density as (4.52)

$$J(x) = n(x)\,\frac{\hbar}{m}\,\frac{\partial\theta(x)}{\partial x}\,. \tag{8.38}$$

8.2.1 Phase and density equations

Introducing the generic state (8.37) into the chiral GPE (8.2), one can separate the real and imaginary parts and obtain two equations. The imaginary part yields the stationary continuity equation in the moving reference frame [Eq. (8.5) with $\partial_t n = 0$],

$$\frac{\partial}{\partial x}\left(J - n\Omega R\right) = 0\,, \tag{8.39}$$

where $\mathcal{J} = J - n\Omega R$ is the current in the rotating frame. Using Eq. (8.38), the continuity equation (8.39) relates the phase of the condensate with its number density, and gives rise to a constant current density

$$\mathcal{J} = n\left(\frac{\hbar}{m}\frac{\partial\theta}{\partial x} - \Omega R\right)\,, \tag{8.40}$$

since $\partial_x \mathcal{J} = 0$. Note that the current in the rotating frame vanishes (i.e., $\mathcal{J} = 0$) for plane waves (8.15) with $\hbar q = m\Omega R$ and also for the particular soliton solutions [(8.29) and (8.30)].

After replacing $\psi(x,t)$ by the stationary state (8.37) and using Eq. (8.40), the real part of the chiral GPE (8.2) gives an equation for the density,

$$\mu = -\frac{\hbar^2}{2m}\frac{\partial_x^2\sqrt{n}}{\sqrt{n}} + \frac{m}{2}\left(\frac{\mathcal{J}}{n}\right)^2 + \kappa\hbar\left(\mathcal{J} + \Omega R n\right). \tag{8.41}$$

Premultiplying Eq. (8.41) by $\partial_x\sqrt{n}$ gives

$$\frac{\partial}{\partial x}\left[2n\left(\mu - \hbar\kappa\mathcal{J}\right) + \frac{\hbar^2}{m}\left(\partial_x\sqrt{n}\right)^2 + \frac{m\mathcal{J}^2}{n} - \hbar\kappa\Omega R n^2\right] = 0\,, \tag{8.42}$$

and subsequent integration brings the density equation (8.41) to the form

$$(\partial_x n)^2 = \frac{4m}{\hbar^2}\left[\hbar\kappa\Omega R n^3 - 2\left(\mu - \hbar\kappa\mathcal{J}\right)n^2 - 2Cn - m\mathcal{J}^2\right]\,, \tag{8.43}$$

where C is an integration constant with units of energy per unit length.

The right-hand side of the density equation (8.43) is a cubic polynomial in the density. The formal, complex general solution of this equation is the Weierstrass $\wp$ function (Abramowitz and Stegun, 1968). However, to obtain solutions that are real and

normalizable, one can write the Weierstrass function in terms of Jacobi elliptic functions by means of the transformation

$$n(x) = \alpha + \beta f^2(x)\,, \tag{8.44}$$

where α and β are constants, and the constraint[2]

$$m\mathcal{J}^2 - 2\kappa\hbar\alpha^2\mathcal{J} - \left(\kappa\hbar\Omega R\alpha^3 - 2\mu\alpha^2 - 2C\alpha\right) = 0\,, \tag{8.45}$$

as we will discuss next.

8.2.2 Solutions as Jacobi elliptic functions

Transforming the density as Eq. (8.44), the density equation (8.43) in terms of the function $f(x)$ takes the form

$$\begin{aligned}\left(\frac{\partial}{\partial x} f\right)^2 &= \frac{m\kappa\Omega R\beta}{\hbar} f^4 - \frac{2m}{\hbar^2}\left(\mu - \hbar\kappa\mathcal{J} - \frac{3\hbar\kappa\Omega R\alpha}{2}\right) f^2 \\ &\quad - \frac{4m\alpha}{\hbar^2\beta}\left(\mu - \hbar\kappa\mathcal{J} + \frac{C}{2\alpha} - \frac{3\hbar\kappa\Omega R\alpha}{4}\right)\end{aligned} \tag{8.46}$$

as long as the condition in Eq. (8.45) is fulfilled. We follow Carr et al. (2000a,b) and Kanamoto et al. (2009), and choose the Jacobi $\mathrm{dn}(z, \mathfrak{m})$ function, which satisfies the differential equation

$$\left[\frac{\partial}{\partial z}\,\mathrm{dn}(z,\mathfrak{m})\right]^2 = (\mathfrak{m}-1) + (2-\mathfrak{m})\,\mathrm{dn}^2(z,\mathfrak{m}) - \mathrm{dn}^4(z,\mathfrak{m})\,. \tag{8.47}$$

Then, $f(x) = \mathrm{dn}(x/\xi, \mathfrak{m})$, with characteristic width ξ, argument x/ξ and parameter $\mathfrak{m}$.

Comparison between Eqs. (8.46) and (8.47) eventually gives that the $\mathrm{dn}(x/\xi, \mathfrak{m})$ Jacobi elliptic function solves the generalized GPE (8.2) when the parameters of the system satisfy the following expressions for the characteristic width,

$$\xi = \frac{\hbar}{\sqrt{m\kappa\hbar|\Omega\beta|R}}\,, \tag{8.48}$$

for the current in the rotating frame,

$$\mathcal{J} = \pm\frac{\hbar\beta}{m\xi}\sqrt{(\mathfrak{m}-1)\frac{\alpha}{\beta} + (\mathfrak{m}-2)\frac{\alpha^2}{\beta^2} - \frac{\alpha^3}{\beta^3}}\,, \tag{8.49}$$

for the eigenenergy,

$$\mu = \left(\mathfrak{m} - 2 - 3\frac{\alpha}{\beta}\right)\frac{\hbar^2}{2m\xi^2} + \kappa\hbar\mathcal{J}\,, \tag{8.50}$$

[2]This constraint comes from introducing the density transformation (8.44) into the density equation (8.43) and setting $f = 0$. The sum of the constant terms that remain should be zero, which imposes that C fulfills Eq. (8.45).

and for the integration constant,

$$C = \frac{\hbar^2\beta}{2m\xi^2}\left[1 - \mathfrak{m} + 2(2-\mathfrak{m})\frac{\alpha}{\beta} + 3\frac{\alpha^2}{\beta^2}\right] . \tag{8.51}$$

The rotation rate Ω and the parameter β should also satisfy that $\Omega\beta < 0$ for the general solution to give dark-soliton (bright-soliton) solutions for positive (negative) velocities, as we will discuss in Subsection 8.2.3 with more detail.

Combining the condition for the periodicity of the density (8.33) that we introduced for particular soliton solutions, $j\,\mathrm{K}(\mathfrak{m})\,\xi = \pi R$, with the equation for the characteristic width ξ (8.48) yields

$$|\beta| = \left(\frac{j\,\mathrm{K}(\mathfrak{m})}{\pi R}\right)^2 \frac{1}{\kappa k_\Omega} , \tag{8.52}$$

where $j = 1, 2, 3, \ldots$ corresponds, as before, to the number of solitons along the ring. In addition, one can find the relation between the coefficients α and β by normalization,

$$\alpha + [1 - \mathrm{L}(\mathfrak{m})]\,\beta = n_0 , \tag{8.53}$$

with n_0 the average density.

From the equation for the current in the rotating frame (8.40), one finds $\partial_x\theta = \mathrm{sgn}(\Omega)\,k_\Omega + m\mathcal{J}/(\hbar n)$ such that the phase is

$$\theta(x) = \mathrm{sgn}(\Omega)\,k_\Omega\,x + \frac{m\mathcal{J}}{\hbar}\int_0^x \frac{dx'}{\alpha + \beta\,\mathrm{dn}^2(x'/\xi, \mathfrak{m})} . \tag{8.54}$$

We write the last integral in terms of the incomplete elliptic integral of the third kind $\mathrm{P}(\eta; x/\xi, \mathfrak{m})$ [see Eq. (A.7), and Abramowitz and Stegun (1968)], where $\eta = \mathfrak{m}\beta/(\alpha+\beta)$. Then, the phase can be written as

$$\theta(x) = \mathrm{sgn}(\Omega)\,k_\Omega\,x + \frac{m\xi\mathcal{J}}{\hbar\,(\alpha+\beta)}\,\mathrm{P}(\eta; x/\xi, \mathfrak{m}) . \tag{8.55}$$

The elliptic integral is complete $\mathrm{P}(\eta; \mathfrak{m})$ for $x = 2\pi R$, and the phase becomes periodic in the ring, $\theta(x) = \theta(x + 2\pi R) + 2\pi l$, where l is an integer. Imposing the phase periodicity to Eq. (8.55) gives

$$2j\frac{m\xi\mathcal{J}}{\hbar\,(\alpha+\beta)}\,\mathrm{P}(\eta; \mathfrak{m}) + \mathrm{sgn}(\Omega)\,k_\Omega\,2\pi R = 2\pi l . \tag{8.56}$$

Introducing into Eq. (8.56) the expressions for ξ (8.48), α (8.53), β (8.52), μ (8.50) and $\mathcal{J}$ (8.49) results in an implicit equation for the parameter $\mathfrak{m}$. Then, substituting backwards one can obtain all the constants in Eqs. (8.37) and (8.44).

Finally, the conserved energy (8.8) per particle of these general solutions is

$$\frac{E}{N} = \frac{\hbar^2}{2m\xi^2}\left\{\mathfrak{m} - 2\mathrm{L}(\mathfrak{m}) - \frac{\alpha}{\beta} - \frac{2\beta}{3n_0}\left[\mathfrak{m} - 2\,(\mathfrak{m}+1)\,\mathrm{L}(\mathfrak{m}) + 3\mathrm{L}^2(\mathfrak{m})\right]\right\} . \tag{8.57}$$

We recall that $\mathrm{L}(\mathfrak{m}) = 1 - \mathrm{E}(\mathfrak{m})/\mathrm{K}(\mathfrak{m})$ such that $\mathrm{L}(\mathfrak{m}) \in [0, 1]$.

8.2.3 General solutions

To summarize, we write the density as $n(x) = \alpha + \beta f^2(x)$ (8.44) and choose $f(x) = \mathrm{dn}(x/\xi, \mathfrak{m})$ such that the wavefunction for the general solution is

$$\psi(x,t) = \sqrt{\alpha + \beta\,\mathrm{dn}^2(x/\xi,\mathfrak{m})}\, e^{i\theta(x)} e^{-i\mu t/\hbar}\,. \tag{8.58}$$

As we saw in the previous subsection, it has a characteristic width ξ that satisfies Eq. (8.48) and the phase $\theta(x)$ is defined by Eq. (8.55). From the expression for the period of the wavefunction (8.33) one can determine β, which is implicit in ξ, and then obtain α from the normalization of the wavefunction [see Eqs. (8.52) and (8.53)]. With these two coefficients, one obtains the energy eigenvalue μ by means of Eq. (8.50), which resembles (and, in the proper limits, reduces to) the eigenenergies obtained for the particular soliton solutions [(8.31) and (8.32)], and the constant current density $\mathcal{J}$ as Eq. (8.49). Finally, the periodicity of the phase results in an implicit equation for the parameter $\mathfrak{m}$ in terms of the system quantities $\{R, N, \Omega, \kappa\}$.

In the $\mathfrak{m} \to 0$ limit, the function $\mathrm{dn}(x/\xi, \mathfrak{m})$ tends to 1 such that the wavefunction (8.58) approaches plane-wave solutions (8.15). On the opposite limit ($\mathfrak{m} \to 1$), $\mathrm{dn}(x/\xi, \mathfrak{m})$ tends to $\mathrm{sech}(x/\xi)$ and thus the wavefunction can approach the solitonic solutions [Eqs. (8.22) and (8.23)] depending on the values of the coefficients α and β. Particularly, the general solution (8.58) gives dark-soliton states ($\Omega > 0$) for $\beta < 0$ and bright-soliton states ($\Omega < 0$) for $\beta > 0$, and thus $\Omega\beta < 0$ for all cases.

Figure 8.2 shows the density profile of Eq. (8.58) for these two limit cases of the parameter $\mathfrak{m}$. Using the general solution (8.58), one can smoothly connect soliton solutions ($\mathfrak{m} \to 1$) with plane waves ($\mathfrak{m} \to 0$) by adjusting the value of the parameter $\mathfrak{m}$. In addition, we plot two different situations with different sign for the coefficient β to show how the general solution describes dark solitons if $\beta < 0$ (Fig. 8.2, right) and bright solitons if $\beta > 0$ (Fig. 8.2, left). Due to this, since dark solitons exist only for a positive rotating rate Ω and bright solitons for a negative one, the condition $\beta\Omega < 0$ has to be fullfiled in both cases.

The general solution (8.58) leads to soliton states only if $\Omega \neq 0$. When the rotation rate approaches zero, the length scale ξ associated with the soliton grows infinitely, and so the general solution only gives plane-wave solutions. The Weierstrass $\wp$ function is the formal solution as $\Omega \to 0$, but it diverges in this case, and such a solution with infinite density has no physical meaning. In any case, the nonrotating scenario is actually a singular case of the density equation (8.43), since the cubic term of the equation vanishes for $\Omega = 0$ and the Weierstrass and Jacobi elliptic functions are no longer its solution. However, as we show later (and discussed in the previous section), one can always find solutions to the resulting linear equation with $\mathcal{J} = 0$.

8.3 Case study

To analyze the general solutions introduced in Section 8.2, we focus here on a particular case with number density $n_0 = 0.5/R$ and current-density interaction strength $\kappa = 1$.

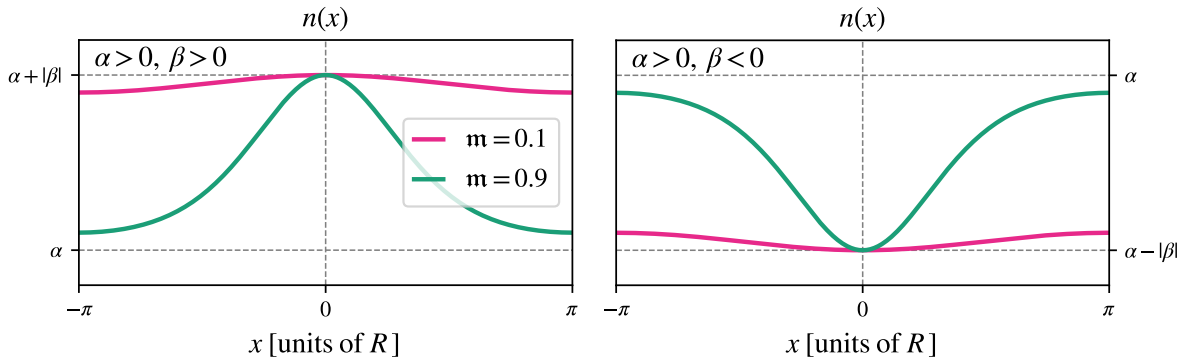

Figure 8.2: Schematic density profile of the general solution for a single node with different values of the parameter $\mathfrak{m}$ and the coefficient α. The two values of $\mathfrak{m}$ correspond to the hyperbolic limit ($\mathfrak{m} \to 1$), which yields solitonic-like solutions, and to the trigonometric limit ($\mathfrak{m} \to 0$), where one recovers plane waves. The sign of the coefficient β allows one to obtain dark solitons if $\beta < 0$ (right) and bright solitons if $\beta > 0$ (left). The density is given in arbitrary units for clarity, and the x coordinate is in units of the ring radius R. We also set the number of nodes to $j = 1$ for simplicity.

We already showed in Fig. 8.1 how changing the average density n_0 on the particular soliton solutions [(8.29) and (8.30)] modifies the width of the resulting soliton, and such change will have a similar effect in the states described by the general solution. Similarly, varying the strength of the current-density interactions κ alters the shape and phase gradient of the soliton, since it modifies the strength of the nonlinearity, as we will discuss later.

In Subsection 8.3.1, we will study the stationary states that the equation of motion (8.2) supports and how these states connect when changing the rotation rate Ω. To understand the different families of trajectories and compare with the nonchiral case, we consider the following quantities: the eigenenergy μ [(8.14) and (8.50)], the conserved energy per particle E/N [(8.8) and (8.57)] and the average (canonical) momentum per particle $\langle \hat{p}/N \rangle$ (8.4). Finally, in Subsection 8.3.2 we will discuss the dynamical stability of these states by means of a linear excitation analysis as well as a nonlinear time evolution.

8.3.1 Stationary states

Figure 8.3 collects the energy eigenvalue μ (8.14), the average momentum per particle $\langle \hat{p}/N \rangle = (m/N) \oint J\, dx$ (8.4) and the energy per particle E/N (8.8), as a function of the angular velocity Ω. The states shown in the plot are plane waves (thick lines) and soliton states (thin lines with symbols); dark and bright solitons belong to trajectories with positive and negative angular velocities, respectively.

All the trajectories show bifurcation points that interconnect families of plane-wave and soliton states. Generally, in contrast to nonchiral systems (i.e., with only contact interactions), these connections are not smooth and give rise to tangent trajectories. This occurs because neither μ nor $\langle \hat{p} \rangle$ retain here their usual meaning of chemical potential and conserved momentum, respectively. However, the trajectories do connect smoothly

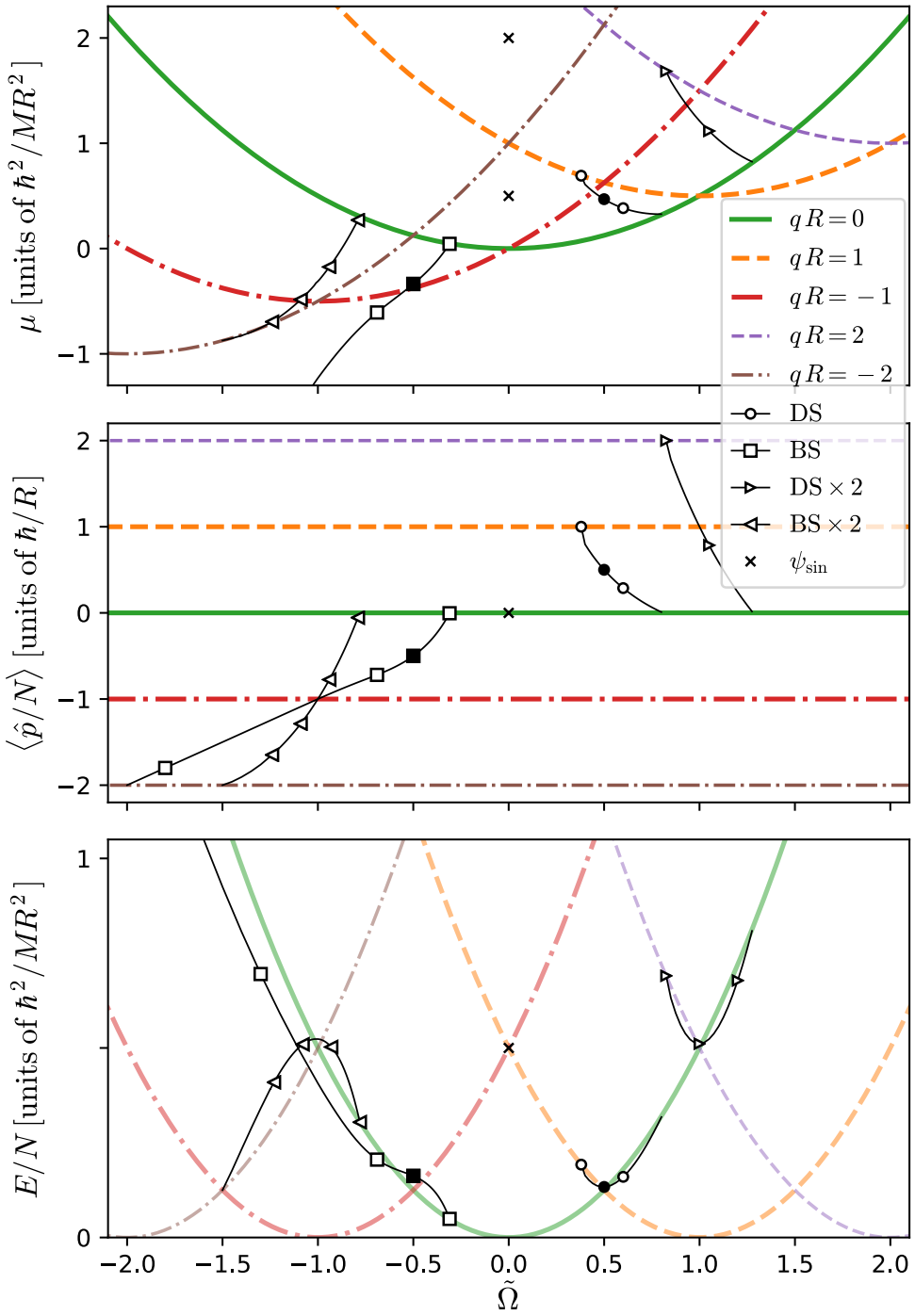

Figure 8.3: Energy eigenvalues μ (top panel), average momentum per particle $\langle \hat{p}/N \rangle$ (middle panel) and energy per particle E/N (bottom panel), as a function of the angular frequency $\tilde{\Omega}$, for plane-wave states (thick lines) with wavenumbers $q \in [-2, 2] \times 1/R$, and dark (DS) and bright (BS) soliton-like states (thin lines with symbols) in a rotating ring with number density $n_0 = 0.5/R$ and current-density interaction strength $\kappa = 1$. We also show the isolated states $\psi_{\sin} \propto \sin(qx)$ (crosses) at $\Omega = 0$. The states labeled as DS × 2 (BS × 2) have two dark (bright) solitons. Note that in the energy diagram (bottom panel), the trajectories of solitonic states (thin lines with symbols) connect smoothly with the plane-wave trajectories (thick faded lines).

in the energy versus rotation plot, which is a conserved quantity of the system.

Families of solutions and trajectories

Plane-wave solutions (8.15), with eigenenergy μ (8.17) and conserved energy defined as $E/N = (\hbar q - m\Omega R)^2/(2m)$, trace parabolas centered at $\Omega/(\hbar/mR^2) = qR$. In the eigenenergy graph (Fig. 8.3, top panel), these parabolas have an energy shift of $\kappa\hbar^2 q n_0/m$ due to the current-density interactions. This asymmetry stems from the chirality of the system and shows as well in the soliton trajectories[3].

Regarding solitons, families of states with one or two dark solitons connect two plane-wave trajectories whose dimensionless wavenumbers, qR, differ in one or two units, respectively. For positive angular velocities ($\Omega > 0$), for example, the one-dark-soliton family (thin line with circles) makes the connection between plane waves that have $qR = 0$ and those with $qR = 1$, while the two-dark-soliton family (thin lines with right-pointing triangles) connects $qR = 0$ and $qR = 2$. Thus, in general, solutions with j solitons connect plane-wave states with a difference of j in the dimensionless wavenumber qR, as one may expect. The filled circle in Fig. 8.3 corresponds to the particular solution (8.29), which only exists for $\Omega = 0.5\,\hbar/(mR^2)$.

For negative angular velocities ($\Omega < 0$), one would expect bright solitons to play a similar connecting role. We show in Fig. 8.3 the trajectories for states with one bright soliton (thin line with squares) and two bright solitons (thin line with left-pointing triangles). As one can see in the plot, the two-soliton family indeed connects plane waves with $qR = 0$ and $qR = -2$. However, the single-soliton trajectory shows a different behavior: instead of connecting the cases with $qR = 0$ and $qR = -1$, it detaches from the expected path as $|\Omega|$ increases (i.e., as the interaction becomes more attractive). The filled square corresponds to the particular solution (8.30) for $\Omega = -0.5\,\hbar/(mR^2)$. Then, for high rotating rates, the one-soliton trajectory behaves as a free particle, with energy and momentum that vary quadratically and linearly, respectively, with the angular velocity. This free-particle behavior does not happen for the two-soliton trajectory, in the present case, because the total attractive interaction (or number of particles) is not large enough for each soliton to attain free-particle features, but this may eventually occur with a different choice of parameters. Therefore, the threshold velocity (and interaction) above which bright-soliton states show a free-particle dispersion will mainly depend on the number of solitons and on the particular parameters of the system, i.e., the number density and the strength of the current-density interactions.

Nonzero current in the rotating frame

Figure 8.4 shows the typical details of the general solitonic states (8.58). We plot the density and phase profiles of two selected positive and negative values of the rotation frequency for a state with one soliton (left panels) and two solitons (right panels). As opposed to the particular solutions plotted in Fig. 8.1, which do not have current in

[3]Note that the conserved energy E/N (Fig. 8.3, bottom panel), on the other hand, does not show this asymmetry since it does not depend on the current-density interactions.

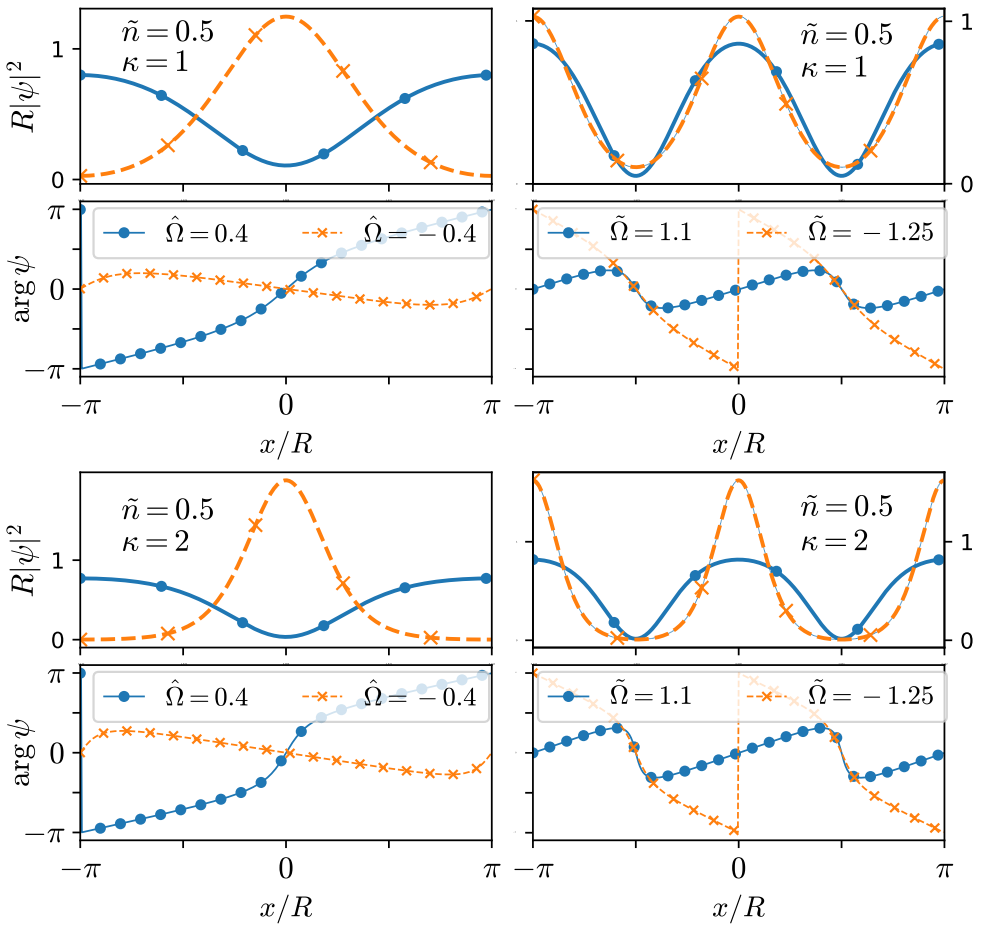

Figure 8.4: General solitonic states (8.58), which have a nonzero current $\mathcal{J} \neq 0$ in the rotating frame. One-soliton (left panels) and two-soliton states (right panels) with a number density $n_0 = 0.5/R$ and two different rotating rates (positive for dark solitons and negative for bright solitons). We consider the interaction strengths $\kappa = 1$ (top panels) and $\kappa = 2$ (bottom panels). See Fig. 8.5 for the spectrum of linear excitations of some cases from the top panels.

the rotating frame, the general states present a nonvanishing constant current in the rotating frame.

The constant current density $\mathcal{J}$ can be written in terms of the average momentum $\langle \hat{p} \rangle$ (8.4) using Eq. (8.40) so that

$$2\pi R\mathcal{J} = \frac{\langle \hat{p} \rangle}{m} - \Omega RN \,. \tag{8.59}$$

From the central panel of Fig. 8.3, and by means of Eq. (8.59), one can see that the current $\mathcal{J}$ vanishes for a family of j solitons for the particular solitonic solutions [(8.30) and (8.29)] and also once a bright-soliton family reaches the free-particle dispersion, as occurs to the one-bright-soliton family in the case considered here. Departing from these particular cases, the current in the rotating frame $\mathcal{J}$ decreases (increases) for increasing

(decreasing) rotation frequency when Ω is positive (negative). This fact reflects the production of backflow currents in response to the soliton phase jumps.

One can see the effect of the strength of the interactions by comparing the top ($\kappa = 1$) and bottom ($\kappa = 2$) panels of Fig. 8.4. As the interaction increases, the density profiles narrow (as we show in Fig. 8.1 for the particular solitonic solutions with different densities), and the phase gradient becomes also steeper, which increases the constant current density $\mathcal{J}$ (8.40).

Nonrotating case

In the absence of rotation ($\Omega = 0$), the system supports plane-wave solutions as well as the isolated, sinusoidal solutions $\psi_{\sin} \propto \sin(qx)$ and $\psi_{\cos} \propto \cos(qx)$. These solutions correspond to the crosses in Fig. 8.3 and, due to the absence of current, are degenerate solutions of the Schrödinger equation[4]. Therefore, superpositions of these states with real amplitudes are also possible solutions. As we discussed before (see Subsection 8.2.3), the general solution that we considered in this chapter (8.58) gives plane waves when $\Omega = 0$ and the more general solution (the Weierstrass $\wp$ function) is not physically valid.

This means that one cannot connect plane-wave families with wavenumbers of different signs, $qR > 0$ and $qR < 0$, as doing so would provide a means of adiabatically changing the chirality of the states. As opposed to nonchiral systems, where one can connect plane-wave trajectories of positive and negative wavenumber, this path does not exist in the presence of current-density interactions, and the sinusoidal solutions that should be part of it (at $\Omega = 0$) remain unconnected as isolated states.

8.3.2 Dynamical stability

We have performed the analysis of linear excitations and the nonlinear time evolution of the stationary states to check their dynamical stability. For the linear analysis, we have solved numerically the Bogoliubov equations for the linear excitations of solitonic states and searched for complex excitation frequencies that may point to dynamical instabilities. For the nonlinear analysis, we have simulated numerically Eq. (8.2) to obtain the time evolution of the system.

One can calculate the linear excitation modes $\delta\psi_j = [u_j,\, v_j]^T$ of a given stationary state ψ as solutions to the Bogoliubov equations[5]. These equations are obtained by introducing the perturbed state

$$\psi(x,t) = e^{-i\mu t/\hbar} \left\{ \phi(x) + \sum_j \left[u_j(x)\, e^{-i\omega_j t} + v_j^*(x)\, e^{i\omega_j^* t} \right] \right\}, \tag{8.60}$$

[4] If both $J = 0$ and $\Omega = 0$, the chiral Gross–Pitaevskii equation (8.2) reduces to the Schrödinger equation and thus supports its usual solutions.

[5] In Chapter 2, we obtained the Bogoliubov equations for the nonchiral case. See Eq. (2.29) and discussion for more details.

where j now indexes the excitation modes, into the GPE (8.2). This yields the following system of equations:

$$\hat{B}\,\delta\psi_j = \hbar\omega_j\,\delta\psi_j. \tag{8.61}$$

The Bogoliubov operator is defined as

$$\hat{B} = \begin{pmatrix} \mathcal{H}-\mu & 0 \\ 0 & -\mathcal{H}^*+\mu \end{pmatrix} + \frac{\hbar\kappa}{2m}\begin{pmatrix} \phi\left[\phi^*\hat{p}-(\hat{p}\,\phi^*)\right] & -\phi\left[\phi\,\hat{p}-(\hat{p}\,\phi)\right] \\ -\phi^*\left[\phi^*\hat{p}-(\hat{p}\,\phi^*)\right] & \phi^*\left[\phi\,\hat{p}-(\hat{p}\,\phi)\right] \end{pmatrix}, \tag{8.62}$$

where $\mathcal{H}$ is the energy operator in Eq. (8.13) and $\hat{p}$ is the momentum operator. The dynamical instabilities correspond to modes with complex frequencies, i.e., $\mathrm{Im}(\omega_j) \neq 0$.

Linear analysis of plane waves

For the excitation modes of plane waves with wavenumber q, we choose plane-wave solutions of the form

$$u(x) = u\,e^{i\,(k+q)\,x} \quad \text{and} \quad v(x) = v\,e^{i\,(k-q)\,x}, \tag{8.63}$$

where k is the wavenumber of the excitation. Then, the dispersion relation for the linear excitation modes of plane waves has the analytical expression

$$\omega_k = \frac{\hbar k}{m}\left[q + \frac{\kappa n_0}{2} \pm \sqrt{q\kappa n_0 + \frac{(\kappa n_0)^2 + k^2}{4}} - \mathrm{sgn}(\Omega)\,k_\Omega\right]. \tag{8.64}$$

All positive values of q lead to real frequencies; however, negative values of q for which $|q| > \kappa n_0/4$ give complex frequencies and are thus unstable. For the parameters we are considering, this threshold corresponds to $|q|R > 1/8$. Therefore, for this case, all the plane waves with negative wavenumber are unstable.

This result indicates that solitonic states connecting plane-wave families with negative wavenumber may also contain unstable states, at least close to the connection points of the corresponding trajectories in the μ versus Ω diagram.

Stable and unstable states

We have not found unstable modes in the spectrum of excitations neither for solitonic states with positive rotation rate (i.e., dark solitons) nor for the family of one-bright-soliton states (with negative rotation rate). We show in Fig. 8.5 two typical examples of the corresponding dispersion of such cases, which present only real frequencies. Regarding one-bright-soliton states, our results for the ring geometry agree with the findings of Dingwall and Öhberg (2019); despite the model being nonintegrable, their results also account for contact interactions on their stability against small perturbations.

As one may expect from the analysis of plane waves discussed above, we have found that, for negative rotation rates, the states with two bright solitons have excitation modes with complex frequencies when $|\tilde{\Omega}| \geq 1$ and thus are linearly unstable, while states in the same family are stable when $|\tilde{\Omega}| < 1$. Figures 8.6 and 8.7 show the results

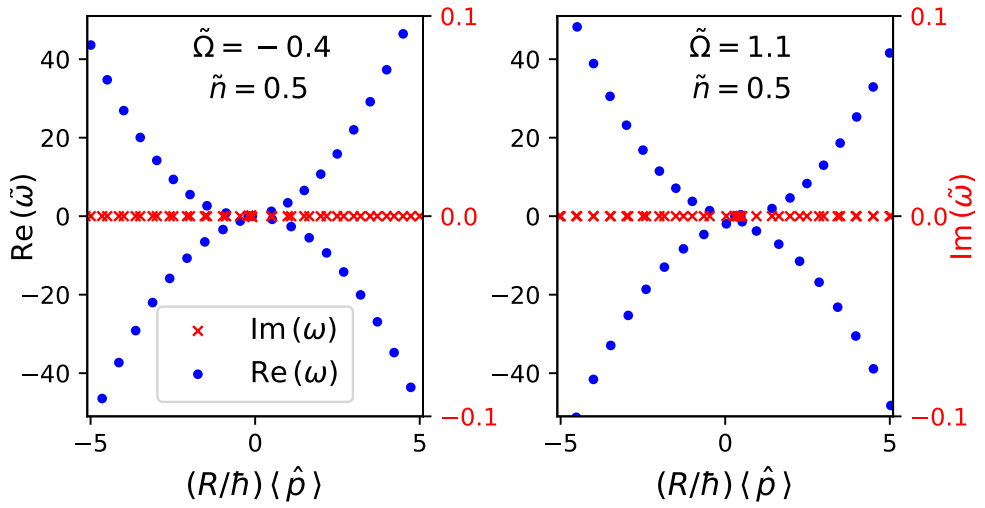

Figure 8.5: Spectrum of linear excitations for one-bright-soliton (left) and two-dark-soliton (right) states with $\kappa = 1$ and frequency ω in units of $\hbar/(mR^2)$. The dispersion relations only present real frequencies, which indicates that both cases are linearly stable. Density and phase profiles of these two cases are shown in the top panels in Fig. 8.4.

of the linear analysis and the nonlinear time evolution, respectively, for two of these two-bright-soliton states. We have obtained the nonlinear evolution after seeding a perturbative amount of white noise on the initial stationary states. One can see in Fig. 8.7 that the equilibrium configuration is preserved for a long time when $\tilde{\Omega} = -0.9$ (left panel). However, when $\tilde{\Omega} = -1.25$, the real-time evolution shows the decay of the initial state with two solitons (right panel). These results agree with the predictions of the linear analysis.

8.4 Summary of results

In this chapter, we have studied persistent currents in quasi-1D Bose–Einstein condensates loaded in a rotating ring trap, which become chiral in the presence of current-density interactions. The current-carrying states that this chiral system supports, plane waves and soliton-like states, show clear differences with respect to nonchiral systems (i.e., with the usual contact interactions between the particles).

The eigenenergy versus rotation rate diagram is asymmetric against the direction of the rotation rate Ω. Then, due to this asymmetry, there are no solitonic trajectories that cross $\Omega = 0$, so it is not possible to adiabatically connect plane-wave states with different chirality.

Concerning the dynamical stability of the stationary states, we have seen that the predictions obtained from the linear analysis of excitations agree with the nonlinear analysis. In our tests of dynamical stability, we find stable currents for positive-velocity states with both constant and modulated density profiles, while decaying currents appear only beyond a unidirectional (negative) velocity threshold. This last instability points to alternative stable states (i.e., moving and strongly localized bright solitons)

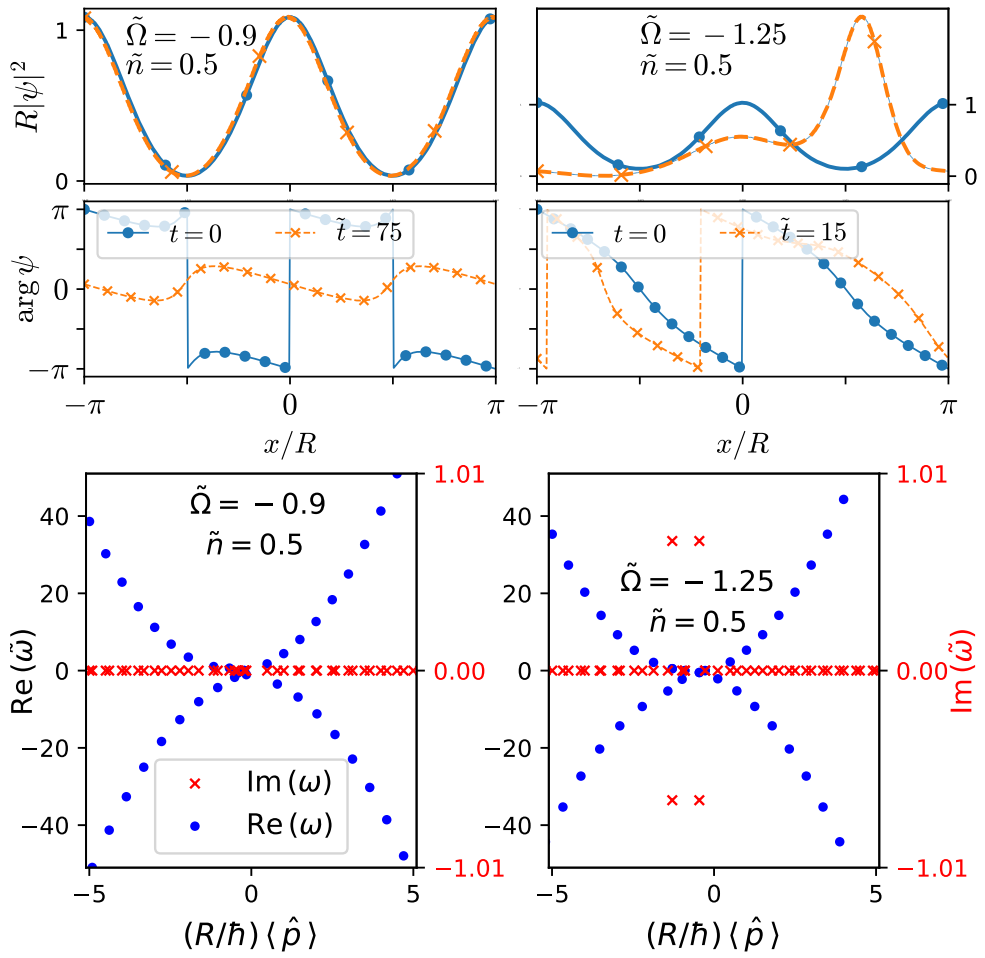

Figure 8.6: Stable (left panels) and unstable (right panels) states with two bright solitons. Top: initial stationary states and final states after a nonlinear time evolution; see Fig. 8.7 for more details. Bottom: spectra of linear excitations. Note that the state with rotating frequency $|\tilde{\Omega}| > 1$ is unstable, as discussed in the main text.

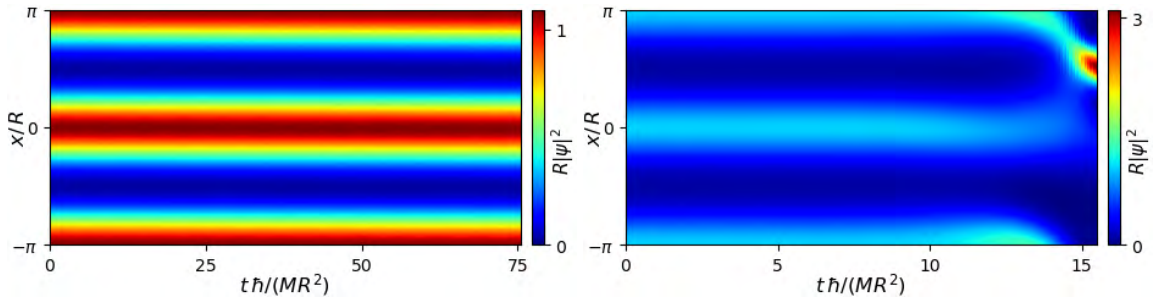

Figure 8.7: Nonlinear time evolution in the rotating frame of the two-bright-soliton states from Fig. 8.6, for two different rotating rates: $\tilde{\Omega} = -0.9$ (left), which is stable, and $\tilde{\Omega} = -1.25$ (right), which is unstable. We perform the time evolution after adding a perturbative amount of white noise over the initial stationary state that changes the energy a 2%.

whose dynamics resemble the energy and momentum features of classical particles.

These results open prospects of new work in the search of equivalent current-carrying states within the 3D framework of the recently realized effective 1D chiral theory (Frölian et al., 2022). They also broaden the phenomenology of BEC dynamics in ring geometries, which lies at the basis for the exploration of atomtronic technologies. Finally, we will generalize this study to a BEC with two coherently coupled components in Chapter 9.

9

Spinor Bose–Einstein condensates with current-density interactions

In this chapter, we extend the study of Chapter 8 to spinor condensates in the presence of current-density interactions[1]. BECs of ultracold gases subject to interactions that are proportional to the local atomic current density were experimentally realized very recently (Frölian et al., 2022), as we discussed in Chapters 4 and 8. Obtaining these condensates involves systems of neutral atoms coupled to laser fields that give rise to artificial electromagnetism. The gauge fields that emerge in such systems turn out to be the effect of geometrical phases accumulated in the adiabatic path of the optically dressed atomic states (see for more details Chapter 4 and Dalibard et al., 2011; Edmonds et al., 2013a). Then, the resulting systems exhibit chiral properties (Chisholm et al., 2022) when restricted to their lowest energy bands and when they can be described by an effective Hamiltonian that includes a current-density term and operates on a scalar order parameter. This theoretical model can be mapped into a density-dependent gauge theory, and was predicted to host chiral solitons (Aglietti et al., 1996; Jackiw, 1997) that were later observed experimentally (Frölian et al., 2022).

Our aim is to implement a spinor system[2] from the effective chiral scalar condensate in a ring geometry and explore a long Josephson bosonic junction with chiral properties. To this end, we consider a double-well potential across the direction transverse to the chiral axis[3], such that one can model an effective two-component, linearly coupled system, as realized in regular extended bosonic junctions (Pigneur et al., 2018; Schweigler et al., 2017). In this setting, as a generalization of a chiral point-like Josephson junction (Edmonds et al., 2013b), we study the Josephson dynamics of extended chiral states.

The chapter is organized as follows. We begin in Section 9.1 by presenting the equations of motion and conserved quantities of the system as well as the different types of stationary solutions that one can find. In Section 9.2, we analyze in detail plane-wave solutions and their superpositions, as well as the dynamical stability of linear excitations.

[1] A spinor condensate is a two-component BEC with particle exchange between components due to a linear coupling (see Chapter 2).

[2] For more details on the nonchiral case, see review by Recati and Stringari (2022) and references therein.

[3] The rotation axis of the ring.

We consider nonlinear excited states with density- and phase-modulated profiles in Section 9.3, which can be the regular solitons we discussed in previous chapters or Josephson vortices, that are particular to spinor systems. Finally, we conclude with a summary of results in Section 9.4.

9.1 Chiral spinor condensates in a ring geometry

In this section, we provide the theoretical description of spinor condensates with current-density interactions. We begin by defining the equations of motion of the system and other quantities (Subsection 9.1.1). Then, we introduce the general equations for the linear excitations of stationary states (Subsection 9.1.2), and finally we discuss the type of solutions that the system supports (Subsection 9.1.3). We may point out relevant differences with both the chiral scalar case (Chapter 8) and the nonchiral spinor case (Abad and Recati, 2013; Recati and Stringari, 2022) when needed.

9.1.1 Coupled Gross–Pitaevskii equations

Let us consider a linearly (i.e., coherently) coupled, two-component BEC in a ring geometry of radius R rotating with angular velocity Ω. We label each component by $\uparrow$ and $\downarrow$, and both of them are subject to the same (intracomponent) current-density interaction of dimensionless strength κ. As we did in Chapter 8, here we assume $\kappa > 0$ without loss of generality and, to isolate the effect of the current-density interactions, we assume as well that there are no contact interparticle interactions in the system, $g_{\uparrow\uparrow} = g_{\downarrow\downarrow} = g_{\uparrow\downarrow} = 0$.

The system can be effectively described by the mean-field Gross–Pitaevskii-like equation

$$i\hbar\frac{\partial\Psi}{\partial t} = \begin{pmatrix} \frac{\hat{\Pi}^2}{2m} + \hbar\kappa J_\uparrow & -\nu \\ -\nu & \frac{\hat{\Pi}^2}{2m} + \hbar\kappa J_\downarrow \end{pmatrix}\Psi \tag{9.1}$$

for the pseudospin-1/2 wavefunction $\Psi = [\psi_\uparrow,\ \psi_\downarrow]^T$. As usual, m is the atomic mass, $\hat{\Pi} = \hat{p} - m\Omega R$ is the mechanical momentum operator in the frame rotating with angular velocity Ω, and $\hat{p} = -i\hbar\partial_x$ is the canonical momentum operator. The energy of the linear coupling is ν (with $\nu > 0$), and the current density for each component measured with respect to the laboratory frame [see Eq. (8.3) for the scalar case] is

$$J_\sigma = \frac{\hbar}{2mi}\left(\psi_\sigma^*\frac{\partial\psi_\sigma}{\partial x} - \psi_\sigma\frac{\partial\psi_\sigma^*}{\partial x}\right), \tag{9.2}$$

where $\sigma = \uparrow, \downarrow$ labels the component. Similarly, the (number) density for each component is given by $n_\sigma = |\psi_\sigma|^2$.

As for the scalar case, we introduce for further use the average number density

$n_0 = N/(2\pi R)$, with N the total number of atoms, the rotation wavenumber[4] $k_\Omega = m\Omega R/\hbar$, and the normalized interaction strength $\tilde{\kappa} = \kappa n_0 R = \kappa N/(2\pi)$. In addition, we use as length, time, and energy units the ring units: R, $1/\Omega_0 = mR^2/\hbar$ and $\hbar\Omega_0$. All dimensionless quantities are denoted by tildes.

The wavefunction Ψ is normalized to the total number of atoms $N = \oint \Psi^\dagger \Psi \, dx$ in the ring and, as we discussed in the scalar case (see Chapter 8), is quantized due to the periodic boundary conditions. The number of atoms N is a conserved quantity of the system, and so is the total energy E, as we discuss next.

Conserved energy

The energy density for a condensate with two coherently coupled components[5] with no interparticle interactions is (Son and Stephanov, 2002)

$$\mathcal{E} = \frac{1}{2m}\left[|\hat{\Pi}\psi_\uparrow|^2 + |\hat{\Pi}\psi_\downarrow|^2\right] - \nu\left[\psi_\uparrow^*\psi_\downarrow + \psi_\downarrow^*\psi_\uparrow\right]. \tag{9.3}$$

Writing the wavefunctions ψ_σ in terms of their densities and phases, n_σ and θ_σ, the energy density (9.3) reads

$$\mathcal{E} = \frac{1}{2m}\left[\left|\hat{\Pi}\psi_\uparrow\right|^2 + \left|\hat{\Pi}\psi_\downarrow\right|^2\right] - 2\nu\sqrt{n_\uparrow n_\downarrow}\cos\varphi\,, \tag{9.4}$$

where $\varphi = \theta_\uparrow - \theta_\downarrow$ is the relative phase.

Integration of Eq. (9.4) gives the total energy of the system. Using $\oint |\hat{p}\psi_\sigma|^2\, dx = \oint \psi^* \hat{p}^2\psi \, dx$, the energy is

$$E = \frac{1}{2m}\oint dx\left[\psi_\uparrow^*\left(\hat{\Pi}^2\psi_\uparrow\right) + \psi_\downarrow^*\left(\hat{\Pi}^2\psi_\downarrow\right)\right] - 2\nu\oint dx\,\sqrt{n_\uparrow n_\downarrow}\cos\varphi\,. \tag{9.5}$$

As in the scalar case, E (9.5) is the conserved energy and does not depend explicitly on the interaction strength κ. This total energy corresponds to the energy contribution of each component, as given by the expression for the scalar case (8.8), with the extra term

$$\mathcal{E}_\varphi = -2\nu\sqrt{n_\uparrow n_\downarrow}\cos\varphi = -2\nu\,\mathrm{Re}\left[\psi_\uparrow^*\psi_\downarrow\right], \tag{9.6}$$

which is the Josephson energy. The scaling of $\mathcal{E}_\varphi$ with the cosine of the relative phase φ reflects the pendulum-like dynamics of the junction.

[4] The notation now is slightly different and k_Ω includes the sign of Ω for clarity (we defined it as $k_\Omega = m|\Omega|R/\hbar$ in Chapter 8).

[5] The energy is a conserved quantity in the scalar case, as we discussed in Chapters 4 and 8 (see in particular Chapter 4 for a detailed derivation). Therefore, the energy of the spinor system is a conserved quantity as well, since now we start from the chiral scalar case (Chapter 8) and split the system into two coherently coupled condensates by means of a double-well potential. The expression we give here for the energy assumes that the double well removes the nonlinear terms (which come from the current density) in the potential barrier such that only the linear coupling remains.

Continuity equations

Premultiplying the GPE (9.1) for each component by ψ_σ^* and subtracting from each other its complex conjugate gives

$$2i\hbar\,\mathrm{Re}\left[\psi_\sigma^*\,\frac{\partial\psi_\sigma}{\partial t}\right] = \frac{i}{m}\,\mathrm{Im}\left[\psi_\sigma^*\,\hat{\Pi}^2\psi_\sigma\right] - 2i\nu\,\mathrm{Im}\left[\psi_\sigma^*\,\psi_{\sigma'}\right]\,. \tag{9.7}$$

Then, we write the wavefunction of each component in terms of its density and phase, $\psi_\sigma = \sqrt{n_\sigma}\exp(i\theta_\sigma)$, such that the current density (9.2) is

$$J_\sigma = n_\sigma\frac{\hbar}{m}\frac{\partial\theta_\sigma}{\partial x}\,. \tag{9.8}$$

As a result, Eq. (9.7) gives two coupled equations:

$$\frac{\partial n_\sigma}{\partial t} = -\frac{\partial}{\partial x}\left(J_\sigma - n_\sigma\Omega R\right) + \frac{2\nu}{\hbar}\sqrt{n_\sigma n_{\sigma'}}\sin\left(\theta_\sigma - \theta_{\sigma'}\right)\,. \tag{9.9}$$

Adding the two Eqs. (9.9) for $\sigma =\uparrow$ and $\sigma =\downarrow$, one gets the continuity equation for the total number density $n(x,t) = n_\uparrow(x,t) + n_\downarrow(x,t)$ and the total current density $J(x,t) = J_\uparrow(x,t) + J_\downarrow(x,t)$,

$$\frac{\partial n}{\partial t} + \frac{\partial}{\partial x}\left(J - n\Omega R\right) = 0\,. \tag{9.10}$$

Equation (9.10) guarantees the conservation of the total number of particles $N = \oint n(x,t)\,dx$ in the ring.

Similarly, one can find a second continuity equation by subtracting the two Eqs. (9.9) for each component. Introducing the spin number density, $n_s(x,t) = n_\uparrow(x,t) - n_\downarrow(x,t)$, which is the local population imbalance between components, and the spin current density, $J_s(x,t) = J_\uparrow(x,t) - J_\downarrow(x,t)$, these densities fulfill the continuity equation

$$\frac{\partial n_s}{\partial t} + \frac{\partial}{\partial x}\left(J_s - n_s\Omega R\right) = \frac{4\nu}{\hbar}\sqrt{n_\uparrow n_\downarrow}\sin\varphi\,. \tag{9.11}$$

We rewrite the right-hand side of Eq. (9.11) as

$$\mathcal{I}_\varphi = \frac{4\nu}{\hbar}\sqrt{n_\uparrow n_\downarrow}\sin\varphi\,, \tag{9.12}$$

where $\mathcal{I}_\varphi$ is twice the Josephson current flowing between components (Barone, 1982).

In the spinor case, it is not possible to find general analytical solutions to the coupled equations as we did in Chapter 8 due to the fact that the right-hand side of Eq. (9.11) is, in general, nonzero[6].

[6] In this case, one cannot remove the phase dependency on the equations of motion and write the equations for the density, as we did for the scalar case.

Stationary states

The steady states of the system, $\Psi(x,t) = \Phi(x)\,\exp(-i\mu t/\hbar)$, satisfy the time-independent equation

$$\mathcal{H}\,\Phi = \mu\,\Phi \tag{9.13}$$

with energy eigenvalue μ, where $\mathcal{H}$ is the nonlinear Hamiltonian matrix in the coupled GPEs (9.1). These states also fulfill the stationary versions of the continuity equations [(9.10) and (9.11) with $\partial_t n = 0$ and $\partial_t n_s = 0$, respectively]. The first continuity equation (9.10) gives the total current in the rotating frame,

$$\mathcal{J} = J - n\Omega R\,, \tag{9.14}$$

which is always constant. From the second equation (9.11), $\partial_x\,(J_s - n_s\Omega R) = \mathcal{I}_\varphi$, one can find a second current,

$$\mathcal{J}_s = J_s - n_s\Omega R\,, \tag{9.15}$$

that is constant only when $\varphi = j\pi$ (where j is an integer) such that $\mathcal{I}_\varphi = 0$.

9.1.2 Bogoliubov equations of linear excitations

To calculate the linear excitations of the stationary states $\Psi = [\psi_\uparrow,\ \psi_\downarrow]^T$, we follow the standard procedure and introduce the perturbed state

$$\psi_\sigma(x,t) = e^{-i\mu t/\hbar}\left\{\phi_\sigma(x) + \sum_j \left[u_{j\sigma}(x)\,e^{-i\omega_j t} + v^*_{j\sigma}(x)\,e^{i\omega^*_j t}\right]\right\} \tag{9.16}$$

in the GPE (9.1), where j indexes the excitations modes and σ the component. Note that μ is the same for both components because the total number of atoms is conserved. The amplitudes of the linear excitation modes, which we write as the vector $\delta\psi_j = [u_{j\uparrow},\ v_{j\uparrow},\ u_{j\downarrow},\ v_{j\downarrow}]^T$, are solution of the Bogoliubov equations[7]:

$$\begin{pmatrix} \hat{B}_\uparrow & -\nu\sigma_z \\ -\nu\sigma_z & \hat{B}_\downarrow \end{pmatrix}\delta\psi_j = \hbar\omega_j\,\delta\psi_j\,, \tag{9.17}$$

where σ_z is the Pauli matrix,

$$\sigma_z = \begin{pmatrix} 1 & 0 \\ 0 & -1 \end{pmatrix}, \tag{9.18}$$

and $\hat{B}_\sigma$ is the 2×2 Bogoliubov operator,

$$\hat{B}_\sigma = \begin{pmatrix} \mathcal{H}_\sigma & 0 \\ 0 & -\mathcal{H}^*_\sigma \end{pmatrix} + \frac{\hbar\kappa}{2m}\begin{pmatrix} \phi_\sigma\,C(\phi^*_\sigma,\hat{p}) & -\phi_\sigma\,C(\phi_\sigma,\hat{p}) \\ -\phi^*_\sigma\,C(\phi^*_\sigma,\hat{p}) & \phi^*_\sigma\,C(\phi_\sigma,\hat{p}) \end{pmatrix}. \tag{9.19}$$

The single-component energy operator is $\mathcal{H}_\sigma = \hat{\Pi}^2/(2m) + \hbar\kappa J_\sigma - \mu$, and we have introduced the operator $C(\phi_\sigma,\hat{p}) = \phi_\sigma\hat{p} - (\hat{p}\phi_\sigma)$ to simplify notation.

As in the scalar case, pure real modes $\delta\psi_j$ are stable excitations, while complex modes will signal instabilities.

[7] See Chapters 2 and 8 for the nonchiral and scalar cases, respectively.

9.1.3 Types of solutions

One can write the nonlinear Hamiltonian $\mathcal{H}$ of the GPE (9.1) in terms of the total and spin current densities, J and J_s, using that $J_\uparrow = (J + J_s)/2$ and $J_\downarrow = (J - J_s)/2$. Then,

$$\mathcal{H} = \left(\frac{\hat{\Pi}^2}{2m} + \frac{\hbar\kappa J}{2}\right)\mathbb{I}_2 + \frac{\hbar\kappa J_s}{2}\,\sigma_z - \nu\,\sigma_x\,, \tag{9.20}$$

where σ_i are the Pauli matrices, σ_z (9.18) and

$$\sigma_x = \begin{pmatrix} 0 & 1 \\ 1 & 0 \end{pmatrix}, \tag{9.21}$$

and $\mathbb{I}_2$ is the 2×2 identity matrix. Besides the coherent-coupling term, $-\nu\sigma_x$, this Hamiltonian also includes an effective spin–orbit coupling, which is the term that goes with σ_z. This spin–orbit-coupling term shifts the energies of the spin components according to J_s, the axial (orbital) current. Then, one can find two different types of stationary states depending on whether $J_s = 0$ or $J_s \neq 0$.

States with no spin current

If $J_s = 0$, the Hamiltonian (9.20) commutes with the Pauli matrix σ_x, $[\mathcal{H}, \sigma_x] = 0$, and one can find common eigenstates that satisfy $\psi_\downarrow(x,t) = \pm\psi_\uparrow(x,t)$, i.e., solutions with the same density for each component ($n_\uparrow = n_\downarrow$) and a relative phase φ of either 0 or π. Then, the coupled equations in Eq. (9.1) reduce into a single equation:

$$i\hbar\frac{\partial\psi_\uparrow}{\partial t} = \left(\frac{\hat{\Pi}^2}{2m} + \hbar\kappa J_\uparrow \mp \nu\right)\psi_\uparrow\,. \tag{9.22}$$

In this case, the two components have equal currents $J_\uparrow = J_\downarrow = J/2$ and one recovers all the stationary states known for a single-component condensate (see Chapter 8 and Arazo et al., 2023b). Particularly, the general solution (8.37) in terms of the Jacobi dn function now reads

$$\psi_\uparrow(x,t) = \sqrt{\alpha + \beta\,\mathrm{dn}^2(x/\xi, \mathfrak{m})}\,e^{i\theta_\uparrow(x)}e^{-i\mu t/\hbar}\,, \tag{9.23}$$

with phase (8.55)

$$\theta_\uparrow(x) = \mathrm{sgn}(\Omega)\,k_\Omega x + \frac{m\xi\mathcal{J}}{2\hbar\,(\alpha+\beta)}\,\Pi(\eta; x/\xi, \mathfrak{m})\,, \tag{9.24}$$

where $\mathcal{J}$ (9.14) is the total current in the rotating frame. We recall that the function $\mathrm{dn}(x/\xi, \mathfrak{m})$ depends on the parameter $\mathfrak{m} \in [0,1]$ and has a characteristic length (8.48) $\xi = \hbar/(m\kappa\hbar|\Omega\beta|R)^{1/2}$. In addition, the incomplete elliptic integral of the third kind $\Pi(\eta; x/\xi, \mathfrak{m})$, with $\eta = \mathfrak{m}\beta/(\alpha+\beta)$, is complete $\Pi(\eta; \mathfrak{m})$ for $x = 2\pi R$.

Then, one determines the real parameters $\mathfrak{m}$, α and β self-consistently for a particular system with a given R, N and Ω (see Subsection 8.2.2 in Chapter 8). The energy eigenvalues μ,

$$\mu = \left(\mathfrak{m} - 2 - 3\frac{\alpha}{\beta}\right)\frac{\hbar^2}{2m\xi^2} + \frac{\hbar\kappa\mathcal{J}}{2} \mp \nu\,, \tag{9.25}$$

are now shifted with respect to the scalar case (8.50) by $\mp\nu$ due to the coherent coupling.

States with spin current

In the general case with $J_s \neq 0$, one has to deal with the full Hamiltonian (9.20) that includes an effective spin–orbit coupling, which yields the two coupled GPEs (9.1). Then, one finds a double degeneracy in the energy eigenvalue μ for a given $|J_s|$ depending on the sign of the spin current.

However, in the limit of $\nu \to 0$, the σ_z symmetry (which results from $[\mathcal{H}, \sigma_z] = 0$) is just slightly broken by a very small coherent coupling $\nu \neq 0$. In this situation, one expects the stationary states to approach the eigenstates of σ_z and realize a population *self-trapping*, i.e., with $\psi_\sigma \approx 0$ for one of the components. We will show later that our numerical simulations depict this scenario.

9.2 Plane-wave states

As for the scalar case [Chapter 8, see Eq. (8.15)], the system is translationally invariant and thus plane waves of the form

$$\Psi_q(x,t) = \begin{pmatrix} \sqrt{n_{0\uparrow}} \\ \pm\sqrt{n_{0\downarrow}} \end{pmatrix} e^{iqx}\, e^{-i\mu_q t/\hbar} \tag{9.26}$$

are solutions of the coupled GPEs (9.1). Each component has a constant density $n_{0\sigma}$, and the $\pm$ sign accounts for the relative phase φ between components, which can be either 0 or π (Abad and Recati, 2013). The common wavenumber q is quantized in the ring and, in dimensionless units, takes integer values ($qR = 0, \pm1, \pm2, \ldots$).

The component current density in the laboratory frame (9.2) is $J_\sigma = (\hbar/m)\, q n_{0\sigma}$, such that the total and spin current densities are constant as well,

$$J_q = \frac{\hbar}{m}\, q n_0 \quad \text{and} \quad J_{qs} = \frac{\hbar}{m}\, q n_{0s}\,, \tag{9.27}$$

with $n_0 = n_{0\uparrow} + n_{0\downarrow}$ and $n_{0s} = n_{0\uparrow} - n_{0\downarrow}$ the total and spin densities, as before. Note that the currents relate as

$$\frac{J_q}{n_0} = \frac{J_{qs}}{n_{0s}} = \frac{\hbar}{m}\, q\,. \tag{9.28}$$

9.2.1 Polarized and unpolarized cases

Introducing the ansatz for Ψ_q (9.26) into the equations of motion (9.1) and multiplying each of the coupled equations by $\sqrt{n_{0\sigma}}$ gives the following two equations:

$$\mu_q n_{0\sigma} = \left[\frac{(\hbar q - m\Omega R)^2}{2m} + \hbar\kappa J_\sigma\right] n_{0\sigma} \mp \nu\sqrt{n_{0\sigma} n_{0\sigma'}}\,, \tag{9.29}$$

for $\sigma = \uparrow, \downarrow$. After some manipulation, one eventually gets

$$\left(\hbar\kappa \frac{J_{qs}}{n_{0s}} \pm \frac{\nu}{\sqrt{n_{0\uparrow} n_{0\downarrow}}}\right) n_{0s} = 0\,, \tag{9.30}$$

which, for convenience, we rewrite as

$$\hbar\kappa J_{qs} = \mp\nu \frac{n_{0s}}{\sqrt{n_{0\uparrow} n_{0\downarrow}}}\,. \tag{9.31}$$

Equation (9.30) admits two possible solutions, as we already anticipated: waves with or without a local population imbalance between components. The imbalance or spin density n_{0s} is also known as *polarization*, so we will refer to the solutions without population imbalance ($n_{0s} = 0$), which thus have no spin current ($J_{qs} = 0$), as the *unpolarized* (or balanced) states, and to the more general solutions with imbalance ($n_{0s} \neq 0$ and $J_{qs} \neq 0$) as the *polarized* (or imbalanced) states.

Unpolarized states

In the absence of imbalance and spin current[8], $n_{0s} = 0$ and $J_{qs} = 0$, the two components have the same density $n_{0\uparrow} = n_{0\downarrow} = n_0/2$ and current density $J_\uparrow = J_\downarrow = J_q/2$. Then, using Eq. (9.29), one can find the eigenenergies

$$\mu_q^{(\mp)} = \frac{(\hbar q - m\Omega R)^2}{2m} + \frac{\hbar\kappa J_q}{2} \mp \nu\,, \tag{9.32}$$

which describe two different branches of the dispersion, and the corresponding conserved energy (9.5) per particle is

$$\frac{E_q^{(\mp)}}{N} = \frac{(\hbar q - m\Omega R)^2}{2m} \mp \nu\,. \tag{9.33}$$

These balanced states exist for any (integer) value of qR, unlike in the polarized case, as we will see next.

[8]These states are particular cases of the general solution (9.23) when $\mathfrak{m} = 0$ (i.e., when the general solution tends to plane-wave solutions).

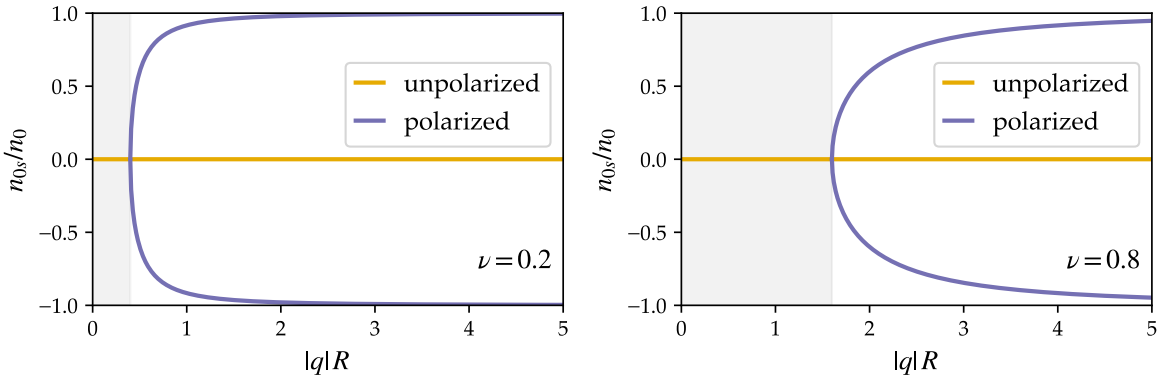

Figure 9.1: Spin density (9.37) of stationary plane waves with wavenumber q in a ring trap of radius R for two values of the linear coupling ν [in units of $\hbar^2/(mR^2)$] at $\Omega = 0$ and for $\kappa n_0 = 1/R$. Unpolarized states exist for $|\gamma_q| < 1$ (see discussion in the main text). Within the shaded region, however, only the balanced states are available. We recall that the wavenumber q is quantized on the ring and only integer values of qR are valid.

Polarized states

In the presence of spin current, to find the eigenenergies one can divide Eq. (9.29) by $n_{0\sigma}$, add the two resulting equations (for each component), and relate the component densities to the total and spin densities by $4n_{0\uparrow}n_{0\downarrow} = n_0^2 - n_{0s}^2$, which gives

$$\mu_q^{(s)} = \frac{(\hbar q - m\Omega R)^2}{2m} + \frac{\hbar\kappa J_q}{2} \mp \frac{\nu n_0}{\sqrt{n_0^2 - n_{0s}^2}} \,. \tag{9.34}$$

Then, using Eq. (9.31) and that the total and spin currents are related as Eq. (9.28), one finally gets

$$\mu_q^{(s)} = \frac{(\hbar q - m\Omega R)^2}{2m} + \hbar\kappa J_q \,. \tag{9.35}$$

The energy (9.5) per particle in this case is

$$\frac{E_q^{(s)}}{N} = \frac{(\hbar q - m\Omega R)^2}{2m} \mp \nu\sqrt{1 - \left(\frac{n_{0s}}{n_0}\right)^2} \,. \tag{9.36}$$

Then, for the polarized states one finds two degenerate energy branches [see Eq. (9.35)] for opposite signs of the polarization n_{0s}. Equations (9.31) and (9.28) give the polarization or spin density[9] n_{0s} and the spin current J_{qs},

$$n_{0s} = \pm n_0\sqrt{1 - \gamma_q^2} \quad \text{and} \quad J_{qs} = \pm J_q\sqrt{1 - \gamma_q^2} \,, \tag{9.37}$$

[9]Note that the spin density n_{0s} [see Eq. (9.37)] depends on ν, κ and, particularly, in the wavenumber q, which is quantized in the ring. See Fig. 9.1 for more details.

where the parameter γ_q contains the ratio between the linear coupling and the interactions,

$$\gamma_q = \frac{2\nu}{\hbar\kappa J_q}\,. \tag{9.38}$$

This overlap is however not trivial. Equation (9.31) can be rewritten as

$$\hbar\kappa\frac{J_q}{n_0} = \mp\frac{\nu}{\sqrt{n_{0\uparrow}n_{0\downarrow}}}\,, \tag{9.39}$$

such that $\nu/\sqrt{n_{0\uparrow}n_{0\downarrow}}$ is always positive. Then, since we set $\kappa > 0$, $J_q \propto q$ and q is the only parameter that may change sign, the values of q for which polarized states exist are restricted: states with a negative q exist only in the in-phase branch (which corresponds to the "−" sign), while states with a positive q do so in the out-of-phase branch (the "+" sign).

The existence of the polarized states is further limited by the parameter γ_q, which marks the transition between polarized and unpolarized solutions. While balanced (unpolarized) states can exist for arbitrary values of γ_q, the polarized solutions exist only for high interactions, $|\gamma_q| < 1$ [see Eq. (9.37), where $1 - \gamma_q^2 \geq 0$]. This implies that, for $q \neq 0$, the wavenumber q must fulfill the condition that

$$|q| > \frac{2\nu m}{\hbar^2\kappa n_0}\,. \tag{9.40}$$

One can thus think of the polarized states as nonlinear bifurcations of the unpolarized states at $|\gamma_q| = 1$. Note from Eq. (9.40) that the range of possible wavenumbers q is reduced as the coherent coupling ν increases. Figure 9.1 shows the polarization n_{0s} as a function of the wavenumber q for two different values of the coherent coupling, $\nu = 0.2$ and 0.8, to illustrate this point.

Ground state of the system

To compare the two different types of solutions, we plot in Fig. 9.2 the energy eigenvalues [top panel, Eqs. (9.32) and (9.35)] and the conserved energies per particle [bottom panel, Eqs. (9.33) and (9.36)] of plane waves in the absence of rotation ($\Omega = 0$).

In the nonchiral case (with only contact interactions), the ground state of the system can either be balanced or polarized depending on the relative strength of the coherent coupling compared to the interactions (Abad and Recati, 2013). This is not the case in coherently coupled BECs with only current-density interactions. Here, the polarized states are never the ground state (when they exist at $|\gamma_q| < 1$), since the current-density interactions do not contribute to the conserved energy in the chiral case.

Introducing the parameter γ_q (9.38), we rewrite here the conserved energies of polarized (9.36) and unpolarized (9.33) states as

$$\frac{E_q^{(\mp)}}{N} = \epsilon_q \mp \nu \quad \text{and} \quad \frac{E_q^{(s)}}{N} = \epsilon_q \mp \nu|\gamma_q|\,, \tag{9.41}$$

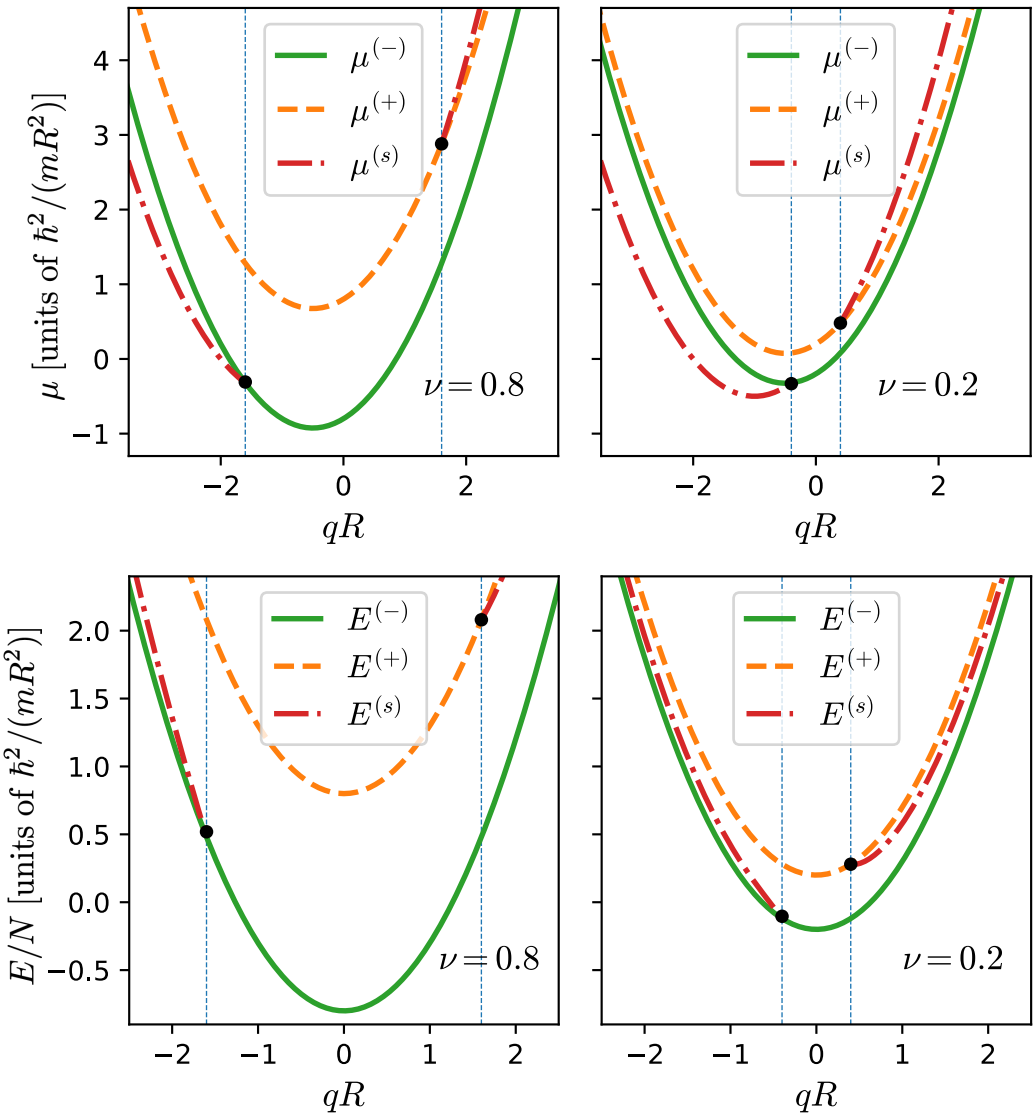

Figure 9.2: Energy eigenvalue (top) and energy per particle (bottom) of stationary plane waves with wavenumber q in a ring trap of radius R for two values of the linear coupling ν [in units of $\hbar^2/(mR^2)$] at $\Omega = 0$ and for $\kappa n_0 = 1/R$, as in Fig. 9.1. The solid circles indicate the bifurcation points of states with nonvanishing spin current density J_s (thick dot-dashed lines), so that they do not exist within the region limited by the vertical dashed lines. Note that q is quantized on a ring and only the integer values of qR exist.

where $\epsilon_q = (\hbar q - m\Omega R)^2/2m$ is the energy per particle in the absence of coherent coupling ($\nu = 0$). Since $|\gamma_q| < 1$ for the polarized states to exist, one can see by comparing both expressions in Eq. (9.41) that the splitting due to the coherent coupling ν will always be larger for the unpolarized states. Despite the fact that the energy eigenvalue ${\mu_q}^{(s)}$ of states with nonvanishing spin current density may become the lowest for negative wavenumbers (see Fig. 9.2, top panel), the conserved energy does not (see Fig. 9.2, bottom panel), and hence the polarized states are not the ground state of the system.

9.2.2 Stability of plane waves

Let us now consider the linear excitations of plane waves (9.26) to analyze their stability. As the unperturbed state $\Phi(x)$, we consider plane waves with wavenumber q and in-phase components,

$$\Phi_q(x) = \begin{pmatrix} \sqrt{n_{0\uparrow}} \\ \sqrt{n_{0\downarrow}} \end{pmatrix} e^{iqx} \,, \tag{9.42}$$

since the out-of-phase states will be unstable[10]. Independently of the relative phase between components of the unperturbed state, which we set to zero, the excitation modes for each component may also be in or out of phase, which will result in two dispersion branches[11].

As we introduced in Subsection 9.1.2, the amplitudes of the linear excitations[12] $\delta\psi = [u_\uparrow, v_\uparrow, u_\downarrow, v_\downarrow]^T$ are solution of the Bogoliubov equations (9.17). Due to the translational invariance of the system, one can choose the amplitudes $u_\sigma(x)$ and $v_\sigma(x)$ to be plane-wave solutions of the form,

$$u_\uparrow(x) = u_\uparrow\, e^{i(k+q)\,x},\ v_\uparrow(x) = v_\uparrow\, e^{i(k-q)\,x} \ \text{ and } \ u_\downarrow(x) = \pm\, u_\downarrow\, e^{i(k+q)\,x},\ v_\downarrow(x) = \pm\, v_\downarrow\, e^{i(k-q)\,x} \,, \tag{9.43}$$

where the ± sign accounts for the relative phase between components of the excitations.

Here we will first consider the simpler case of unpolarized states, where the Bogoliubov equations reduce to two equations that one can solve analytically in a way similar to the scalar case. Later, we will calculate the dispersion relations numerically for the more general case of polarized states[13].

Unpolarized plane waves

For unpolarized plane waves with wavenumber q, which have $n_{0\uparrow} = n_{0\downarrow} = n_0/2$, one can find linear excitations with equal phase, $u_\uparrow = u_\downarrow = u$ and $v_\uparrow = v_\downarrow = v$, known as *density modes*, and out-of-phase excitations, $u_\uparrow = -u_\downarrow = u$ and $v_\uparrow = -v_\downarrow = v$, or *spin modes*. The dispersion relation for the density modes is

$$\omega_k^{(\mathrm{d})} = \frac{\hbar k}{m}\left(q + \frac{\kappa n_0}{4}\right) \pm \sqrt{\left(\frac{\hbar k}{m}\right)^2 \left[\left(\frac{\kappa n_0}{4}\right)^2 + \frac{2\kappa n_0 q + k^2}{4}\right]} - \Omega R k \,, \tag{9.44}$$

and for the spin modes it is

$$\omega_k^{(\mathrm{s})} = \frac{\hbar k}{m}\left(q + \frac{\kappa n_0}{4}\right) \pm \sqrt{\left(\frac{\hbar k}{m}\right)^2 \left[\left(\frac{\kappa n_0}{4}\right)^2 + \frac{2\kappa n_0 q + k^2}{4}\right] + 2\nu\left(\frac{k^2 + \kappa n_0 q}{m} + \frac{2\nu}{\hbar^2}\right)} - \Omega R k \,. \tag{9.45}$$

[10] The stability of the system resembles that of a pendulum: while both in-phase ($\varphi = 0$) and out-of-phase ($\varphi = \pi$) states are stationary, the out-of-phase case is not stable against perturbations.

[11] For more details, see Chapter 2, Subsection 2.2.1, where we discuss the excitations of a nonchiral binary mixture. Regarding excitations in nonchiral spinor condensates, see for instance the works by Abad and Recati (2013) and by Cominotti et al. (2022).

[12] We drop the index of the excitations j from now on for simplicity.

[13] One can also find the dispersion relations for polarized states analytically, but the procedure is much less straightforward.

Introducing the energy term

$$\hbar\omega_q = \frac{(\hbar\kappa n_0)^2}{4m} + 2\kappa\hbar J_q \tag{9.46}$$

and the wavenumber associated to rotation, $k_\Omega = m\Omega R/\hbar$, the energies of the density modes (9.44) and of the spin modes (9.45) read

$$\hbar\omega_k^{(\mathrm{d})} = \frac{\hbar^2 k}{m}\left(q + \frac{\kappa n_0}{4} - k_\Omega \pm \frac{1}{2}\sqrt{k^2 + \frac{m\omega_q}{\hbar}}\right), \tag{9.47}$$

and

$$\hbar\omega_k^{(\mathrm{s})} = \frac{\hbar^2 k}{m}\left(q + \frac{\kappa n_0}{4} - k_\Omega\right) \pm \sqrt{\frac{\hbar^2 k^2}{2m}\left(\frac{\hbar^2 k^2}{2m} + \frac{\hbar\omega_q}{2} + 4\nu\right) + 4\nu^2\left(1 + \frac{1}{\gamma_q}\right)}. \tag{9.48}$$

The dispersion relation of the density modes, $\omega_k^{(\mathrm{d})}$ (9.47), does not depend on the coherent coupling ν and reproduces the linear excitations of the scalar case (see Chapter 8 and Arazo et al., 2023b). For low wavenumbers, $\omega_k^{(\mathrm{d})}$ is linear in k, while it tends to zero in the $k \to 0$ limit. On the other hand, the dispersion of spin modes, $\omega_k^{(\mathrm{s})}$ (9.48), shows an energy gap[14] due to the presence of the coherent coupling ν. This gap appears (not at $k = 0$, in general, but) at the wavenumber that solves $\partial_k \omega_k^{(\mathrm{s})} = 0$.

The spectrum associated with $\omega_k^{(\mathrm{d})}$ (9.47) and $\omega_k^{(\mathrm{s})}$ (9.48) contains unstable modes[15] when either $\omega_q < 0$ and/or $\gamma_q \in [-1, 0]$. Both types of instabilities appear only for negative wavenumbers: $\omega_q < 0$, as in scalar condensates, produces modulation instabilities of the total density if $q < -\kappa n_0/8$, while the spin-density instabilities arise for states that present $2\nu < \kappa\hbar|J_q|$. The last condition is the same as for the existence of polarized plane waves (with negative wavenumber q), whose bifurcation point occurs at $\gamma_q = -1$. This value also indicates the first crossing of the two dispersion branches [Eqs. (9.47) and (9.48)] at $k = 0$, while further crossings take place in the dispersion of unstable states[16] (i.e., for $-1 < \gamma_q < 0$) at

$$\hbar k = \pm\sqrt{-2m\nu\left(1 + \frac{1}{\gamma_q}\right)} = \pm\sqrt{-m\left(2\nu + \hbar\kappa J_q\right)}. \tag{9.49}$$

The fact that spin-density instabilities are associated with the existence of polarized plane waves seems an intriguing feature, since these states have higher energy than the unpolarized plane waves, as we show in Fig. 9.2 (see discussion in the main text as well).

Figure 9.3 shows the excitation spectra of plane waves with $qR = -1$ and interaction parameter $\tilde{\kappa}$ for two values of the coherent coupling ν, where we have introduced

[14] If $\nu = 0$, one recovers the expression for $\omega_k^{(\mathrm{d})}$ [see Eq. (9.47)], since only density excitations exist.

[15] For the density modes, setting $k = 0$ in the equation for $\omega_k^{(\mathrm{d})}$ (9.47) gives the condition that $\omega_q < 0$ for $\omega_k^{(\mathrm{d})}$ to become imaginary. Similarly for the spin modes, one can see in the dispersion relation $\omega_k^{(\mathrm{s})}$ (9.48) for $k = 0$ that the modes will be unstable when $1 + 1/\gamma_q < 0$, which means both that $\gamma_q < 0$ and $\gamma_q > -1$ for $\omega_k^{(\mathrm{s})}$ to be imaginary.

[16] There are no crossings for $\gamma_q > 0$.

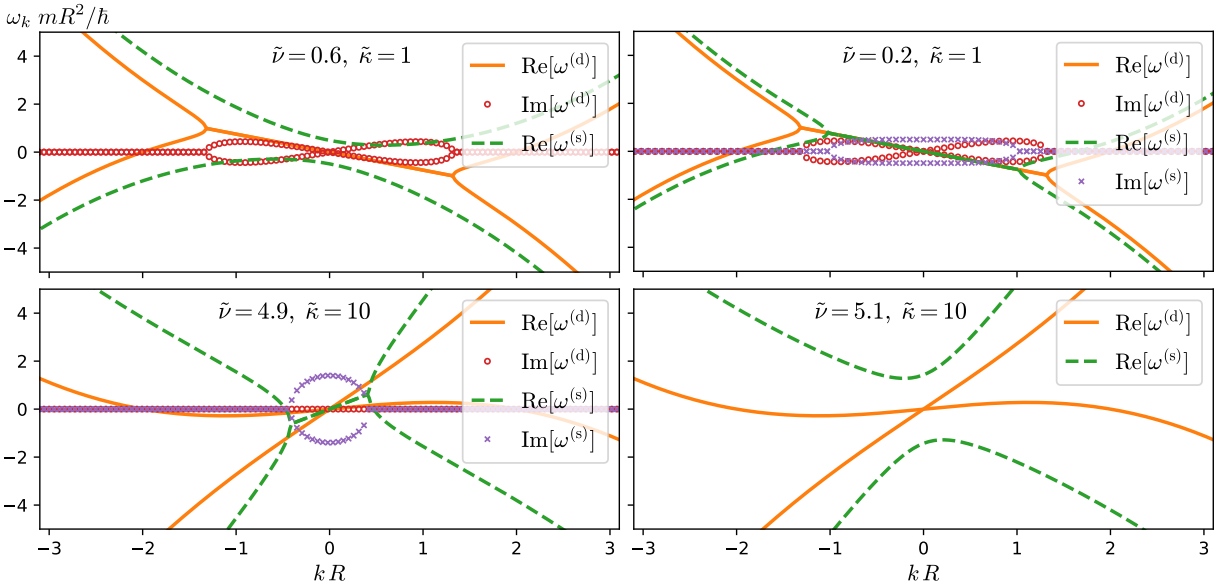

Figure 9.3: Excitation spectrum of unpolarized plane waves with dimensionless wavenumber $qR = -1$ for two different values of the coherent coupling ν as given by Eqs. (9.47) and (9.48). The interaction parameter is $\kappa N = 2\pi$ (top) and $\kappa N = 20\pi$ (bottom). The coherent coupling ν has the usual units of energy, $\hbar^2/(mR^2)$, and the interaction parameter labelled in the plots is $\tilde{\kappa} = \kappa n_0 R$, where $\tilde{n}_0 = n_0 R$ is dimensionless and we recall that $n_0 = N/(2\pi R)$.

the interaction parameter $\tilde{\kappa} = \kappa n_0 R$ and the dimensionless coherent coupling energy $\tilde{\nu} = \nu\, mR^2/\hbar^2$.

Let us first focus on the case of a low interaction parameter, $\tilde{\kappa} = 1$ (top panels), for which $\omega_q = -1.75\,\hbar/(mR^2)$ and $\gamma_q = -2\tilde{\nu}$, such that $\omega_q < 0$ for any value of ν. At a high coupling $\tilde{\nu} = 0.6$ (left panel), the unstable spin modes are suppressed; note that $\gamma_q < -1$ for these parameters. However, there are unstable density modes, since $\omega_q < 0$, as the existence of complex frequencies $\mathrm{Im}[\omega_k^{(\mathrm{d})}] \neq 0$ (open circles) indicates. For lower couplings such as $\tilde{\nu} = 0.2$ (right panel), both types of instabilities occur, since $\gamma_q = -0.4$ ($\gamma_q > -1$) in this case.

Due to the constant energy term $(\hbar\kappa n_0)^2/(4m)$ in $\hbar\omega_q$ (9.46), high densities[17] can suppress the unstable density modes. We illustrate this point in the bottom panels of Fig. 9.3, which show the dispersion of plane waves with $qR = -1$ and $\tilde{\kappa} = 10$ for two different values of the coherent coupling. However, unstable spin modes can still appear if the coherent coupling is not high enough, as depicted in the left panel at $\tilde{\nu} = 4.9$.

Polarized plane waves

For the general, polarized plane waves with wavenumber q, the states have a nonzero imbalance and spin current ($n_{0s} \neq 0$ and $J_{qs} \neq 0$) and thus one has to diagonalize the full 4×4 matrix in the Bogoliubov equations (9.17). We solve the system of

[17] We have defined $\tilde{\kappa} = \kappa n_0 R$, so high densities translate to a higher interaction parameter $\tilde{\kappa}$.

equations numerically, although these equations still support analytical solutions as in the unpolarized case but of a more complex nature.

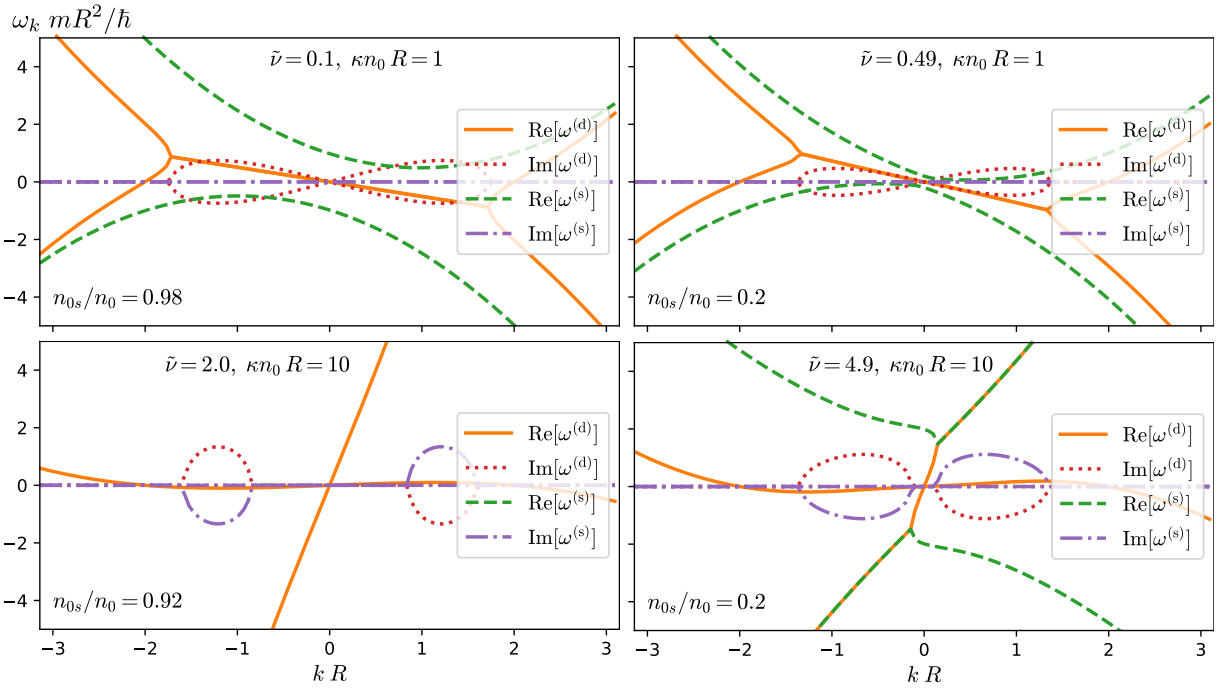

Figure 9.4: Excitation spectrum of polarized plane waves with dimensionless wavenumber $qR = -1$ for two different values of the coherent coupling ν, which we obtain by solving the Bogoliubov equations (9.17) numerically. As for the unpolarized case (see Fig. 9.3), we consider two strengths of the interactions: $\kappa N = 2\pi$ (top) and $\kappa N = 20\pi$ (bottom). The dimensionless coherent coupling is $\tilde{\nu} = \nu\, mR^2/\hbar^2$, and we have defined the interaction parameter as $\tilde{\kappa} = \kappa n_0 R$. We recall that $\tilde{n}_0 = n_0 R$ is dimensionless, with the average density given by $n_0 = N/(2\pi R)$. The imbalance or spin density is n_{0s} and $|n_{0s}| \in [0, n_0]$.

Polarized states present notable differences in the dispersion of linear excitations with respect to the unpolarized states. Now, the splitting between total-density and spin-density branches is not meaningful in general cases. For negative wavenumbers, however, low number densities trigger instabilities that closely resemble those of the density modes in unpolarized states, while instabilities similar to those of the spin modes are suppressed. Thus, we keep here the notation from the unpolarized case and refer to the two possible instabilities as the *density* or *spin* modes.

In Fig. 9.4, we plot the dispersion charts of polarized plane waves with dimensionless wavenumber $qR = -1$ for two interaction parameters, $\tilde{\kappa} = 1$ and 10, and two different values of the coherent coupling ν for each $\tilde{\kappa}$.

For a low interaction parameter such as $\tilde{\kappa} = 1$ (see top panels in Fig. 9.4), the density modes are unstable while spin modes are stable for all possible values of ν (see top panels in Fig. 9.4), which means $\tilde{\nu} \leq 0.5$ for the parameters considered here. The threshold value $\tilde{\nu} = 0.5$ corresponds to the bifurcation point between polarized and unpolarized states, $|\gamma_q| = 1$, and has zero imbalance ($n_{0s} = 0$). If $\tilde{\nu} \geq 0.5$, the polarized states can no longer exist, since $|\gamma_q| > 1$. When the coherent coupling is very strong and close to

the bifurcation, $\tilde{\nu} \approx 0.5$, the spin density is almost zero, $n_{0s} \approx 0$, and one recovers the excitation spectrum for a balanced mixture (see top right panel in Fig. 9.4). The spin density n_{0s} then increases as the coherent coupling ν decreases. Eventually, when the coherent coupling is weak enough, such as $\tilde{\nu} = 0.1$, the system presents population self-trapping, with $n_{0s} \approx n_0$ (see top left panel in Fig. 9.4).

The disctinctive feacture of polarized states appears at higher densities, and it is related to instabilities (for $q < 0$) produced by the collision of excitation branches at $k \neq 0$. For an interaction parameter $\tilde{\kappa} = 10$ (see bottom panels in Fig. 9.4), both density and spin modes are now unstable for the whole possible range of ν, which for the parameters considered corresponds to $\tilde{\nu} \leq 5$. Exceptionally, all modes are stable in the two extreme situations of a very strong or weak coherent coupling. In the self-trapping limit, $\tilde{\nu} \to 0$ and $|\gamma_q| \to 0$, and all the population locates in one of the components, $n_{0s} \approx n_0$ (see bottom left panel in Fig. 9.4). On the other hand, in the balanced case, $\tilde{\nu} \to 5$ and $|\gamma_q| \to 1$, such that $n_{0s} \approx 0$, and one recovers the excitation spectrum of the unpolarized states (see bottom right panel in Fig. 9.4; for reference, see bottom panels in Fig. 9.3).

In the unpolarized case, we discussed that a high density (or interaction) could prevent the density modes from being unstable. Although the same argument applies to the polarized states, the collision of the different dispersion branches gives rise to new instabilities, so there are always unstable modes for higher densities. Note however that one could choose the system parameters in a way that these instabilities appear exclusively for noninteger values of the dimensionless wavenumber qR. Since only integer values of qR are valid for the ring geometry, all the excitation modes in this case would be stable.

9.2.3 Quasi-linear states for the nonrotating case

Although the equation of motion (9.1) is a nonlinear equation due to the current-density term, it becomes linear when the current density for each component vanishes, $J_\sigma = 0$. Then, it admits the same solutions as the free Schrödinger equation for a spin-1/2 particle; for the nonrotating case ($\Omega = 0$), the usual standing waves $\sin(qx)$ and $\cos(qx)$ fulfill this condition. Thus, as we discussed in Chapter 8 [see Eq. (8.19)], linear superpositions of these waves with real coefficients are also stationary states, and complex superpositions with nonzero current,

$$\psi_{\alpha q}(x,t) = \begin{pmatrix} \sqrt{n_{\alpha\uparrow}} \\ \pm\sqrt{n_{\alpha\downarrow}} \end{pmatrix} \left[\frac{1-\alpha}{2} e^{-iqx} + \frac{1+\alpha}{2} e^{i\beta} e^{iqx} \right] e^{-i\mu_{\alpha q} t/\hbar} , \tag{9.50}$$

with α and β real numbers and q the wavenumber, solve the GPE as well. These states have the constant component current density (8.20) $J_\sigma = (\hbar/m)\, \alpha q n_{\alpha\sigma}$, and total current density

$$J_\alpha = \frac{\hbar}{m} \alpha q n_\alpha = \frac{2\alpha}{1+\alpha^2} J_q , \tag{9.51}$$

with J_q the total current for plane-wave states (9.27). Normalization to the total number of atoms N gives

$$n_\alpha = n_{\alpha\uparrow} + n_{\alpha\downarrow} = \frac{2n_0}{1+\alpha^2}\,. \tag{9.52}$$

As for plane waves, one can find solutions of the type of Eq. (9.50) with either zero or nonzero spin current, $J_{\alpha s} = 0$ and $J_{\alpha s} \neq 0$. For the unpolarized states ($J_{\alpha s} = 0$), the energy eigenvalue[18] is

$$\mu^{(\mp)}_{\alpha q} = \frac{\hbar^2 q^2}{2m} + \frac{\alpha}{1+\alpha^2}\,\hbar\kappa J_q \mp \nu\,. \tag{9.53}$$

There is no restriction for α other than normalization, and the conserved energy is

$$\frac{E^{(\mp)}_{\alpha q}}{N} = \frac{\hbar^2 q^2}{2m} \mp \nu\,\frac{2}{1+\alpha^2}\,, \tag{9.54}$$

such that one recovers the energy of plane waves with the same wavenumber q, as given by Eq. (9.33), for $\alpha = \pm 1$. For polarized states ($J_{\alpha s} \neq 0$), the imbalance $n_{\alpha s} = n_{\alpha\uparrow} - n_{\alpha\downarrow}$ is given by

$$n_{\alpha s} = \pm n_0 \sqrt{\left(\frac{2}{1+\alpha^2}\right)^2 - \left(\frac{\gamma_q}{\alpha}\right)^2}\,. \tag{9.55}$$

Unlike in the case of balanced states, the value of α is now constrained since $n_{\alpha s}$ has to be real, which leads to the condition that

$$|\alpha| \in \left[1 - \sqrt{1-\gamma_q^2},\, 1 + \sqrt{1-\gamma_q^2}\right]\,\frac{1}{|\gamma_q|}\,. \tag{9.56}$$

The energy eigenvalue in this case is

$$\mu^{(s)}_{\alpha q} = \frac{\hbar^2 q^2}{2m} + \frac{2\alpha}{1+\alpha^2}\,\hbar\kappa J_q\,, \tag{9.57}$$

and the conserved energy is

$$\frac{E^{(s)}_{\alpha q}}{N} = \frac{\hbar^2 q^2}{2m} \mp \nu\,\frac{|\gamma_q|}{\alpha}\,. \tag{9.58}$$

Figure 9.5 shows two examples for the same linear coupling $\nu = 0.3\,\hbar^2/(mR^2)$ and interaction parameter $\kappa N = 20\pi$: an in-phase, unpolarized state with $\alpha = 0.8$ (left panel), and a polarized state with $\alpha = 6$ and a π-relative phase.

9.3 Nonlinear excited states

Superpositions of plane waves present a non-homogeneous density profile and constant current densities, as we discussed in Subsection 9.2.3. Besides plane-wave superpositions, one can also find generic nonlinear excited states with modulated density and current profiles; we will thus refer to such states as *solitonic states*.

[18] The energy eigenvalue of these complex superpositions have the same expression as those for plane-wave solutions (9.32) with the total current J_q replaced by J_α.

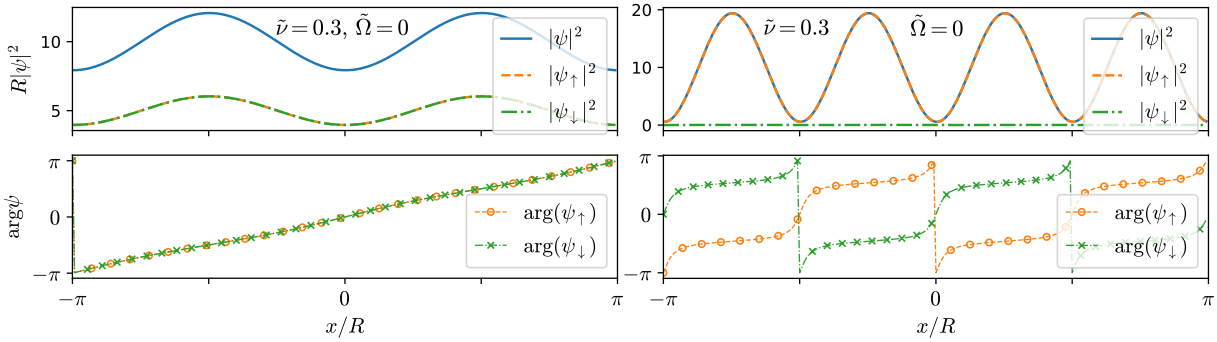

Figure 9.5: Linear superpositions of plane waves with (dimensionless) linear coupling $\tilde{\nu} = 0.3$ and interaction parameter $\tilde{\kappa} = 10$ in the absence of rotation ($\Omega = 0$), as given by Eq. (9.50). We show two different cases: unpolarized state with wavenumber $qR = 1$, vanishing spin current $J_{\alpha s} = 0$ and coefficient $\alpha = 0.8$ (left); and polarized state with wavenumber $qR = 2$, nonvanishing spin currrent $J_{\alpha s} \neq 0$ and coefficient $\alpha = 6$ (right). We recall that the dimensionless parameters are $\tilde{\kappa} = \kappa n_0 R$ and $\tilde{\nu} = \nu\, mR^2/\hbar^2$.

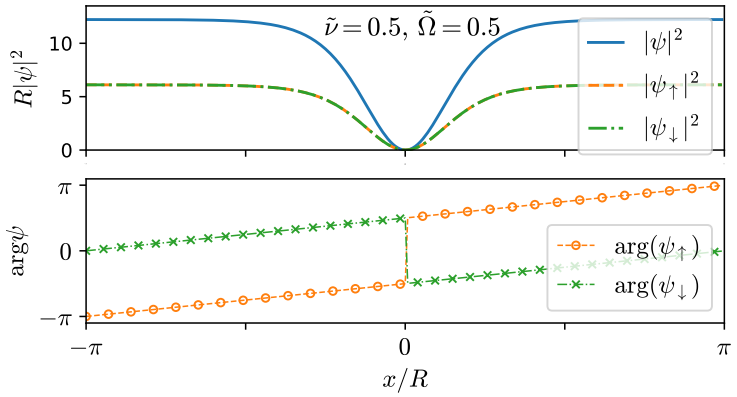

Figure 9.6: Nonlinear state with one dark soliton in a chiral spinor condensate with interaction parameter $\kappa N = 20\pi$, linear coupling $\tilde{\nu} = 0.5$ and relative phase $\varphi = \pi$ at rotation rate $\tilde{\Omega} = 0.5$.

9.3.1 Solitons

The simplest of these states replicates the solutions of the scalar (chiral) system in the spinor system, as we already introduced in Subsection 9.1.3 [see Eq. (9.23)]. We illustrate this case in Fig. 9.6 for unpolarized, out-of-phase ($\psi_\uparrow = -\psi_\downarrow$) dark solitons[19] at rotating rate $\Omega = 0.5\,\Omega_0$. The usual hyperbolic functional form for infinite systems, $\tanh(x/\xi)$, transforms to a ring trap into the Jacobi $\mathrm{sn}(x/\xi, \mathfrak{m})$ function, which is a particular case of Eq. (9.23) (see Chapter 8).

The spinor system allows also for more complex structures involving dark solitons. As an example, in Fig. 9.7 we show a two-soliton state with a strong polarization at rotation rate $\Omega = \Omega_0$. In this case, the density profile of the minority component is highly irregular (see inset), and is sustained by sudden π jumps in the phase profile.

[19] Dark solitons are characterized by a density dip and a π-phase jump across their profile.

These phase jumps produce alternate regions of either in-phase ($\varphi = 0$) or out-of-phase ($\varphi = \pi$) spin components.

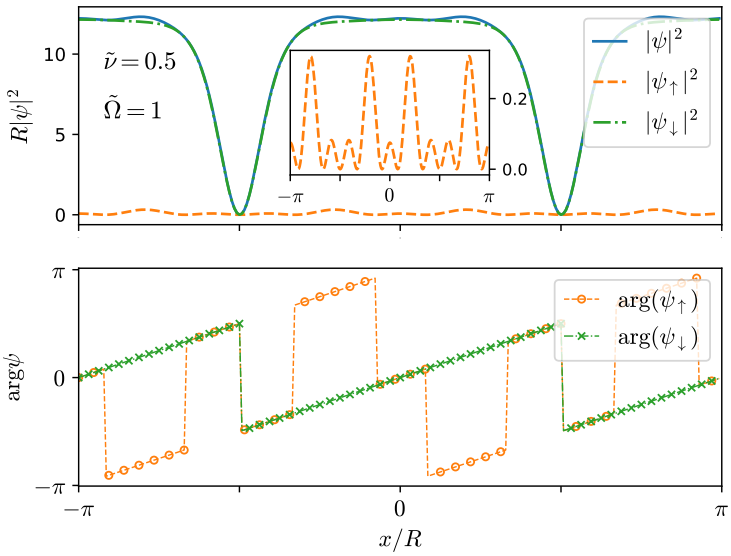

Figure 9.7: Nonlinear state with two dark solitons in a chiral spinor condensate with interaction parameter $\kappa N = 20\pi$, linear coupling $\tilde{\nu} = 0.5$ at rotation rate $\tilde{\Omega} = 1$ in a highly imbalanced state with non-constant relative phase. The inset zooms in the density of the minority component.

9.3.2 Josephson vortices

In spinor condensates, in general, one can have two types of solitonic states, as in nonchiral systems: regular (dark and bright) solitons, and Josephson vortices[20] (Kaurov and Kuklov, 2005). Soliton solutions do not have Josephson currents and are well known in scalar condensates (see for instance Pitaevskii and Stringari, 2016). Josephson vortices, however, are characterized by the presence of Josephson currents and appear only in spinor systems (Baals et al., 2018; Qadir et al., 2012; Shamailov and Brand, 2018). In nonchiral systems with repulsive contact interparticle interactions, dark solitons and Josephson vortices can be considered as domain walls of the total and relative phase with corresponding healing lengths $\xi = \hbar^2/(m\mu)$ and $\xi_\nu = \hbar^2/(4m\nu)$, respectively (Son and Stephanov, 2002), and the interconversion between them takes place at $\xi = \xi_\nu$ (Kaurov and Kuklov, 2005, 2006).

Figure 9.8 shows our numerical results for a stationary Josephson-vortex state in a chiral spinor system with the same parameters as for the dark solitons shown in Fig. 9.6. The total density profile resembles the dark-soliton state, but the 2π jump in the relative phase stands out as the main signature of the Josephson vortex (see central panel). Additionally, the nonvanishing Josephson current $\mathcal{I}_\varphi$ [defined in Eqs. (9.11)

[20] Josephson vortices have a density profile similar to two overlapped dark solitons (one in each component) but with a nonzero density at the core.

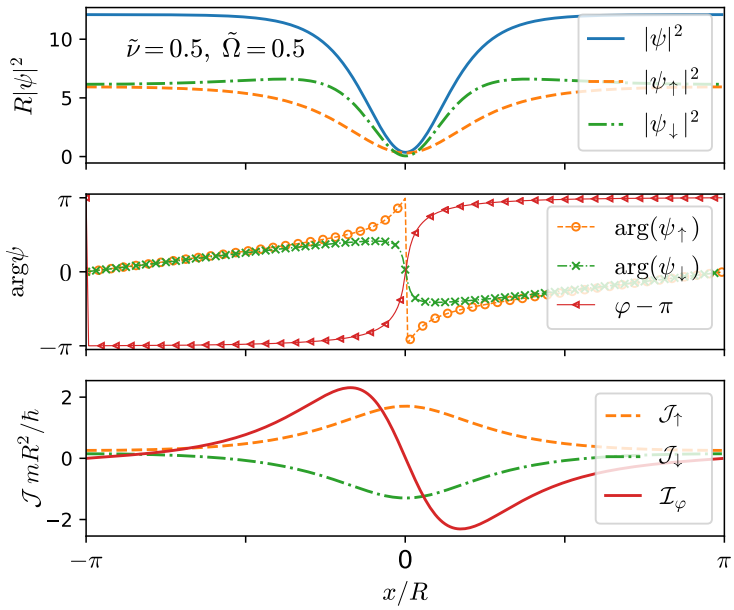

Figure 9.8: Josephson-vortex state in a chiral spinor condensate. Density profiles (top), phase profiles (middle), and currents (bottom) for a system with interaction parameter $\kappa N = 20\pi$, linear coupling $\tilde{\nu} = 0.5$, and rotation rate $\tilde{\Omega} = 0.5$, as in Fig. 9.7.

and (9.12)] changes sign around the vortex core, as the density minimum reflects (see bottom panel). The current densities that we represent are measured with respect to the rotating frame, $\mathcal{J}_\sigma = J_\sigma - n_\sigma \Omega R$, and show opposite directions as measured with respect an average nonzero current. Regular (nonchiral) Josephson vortices are analytically described as (Kaurov and Kuklov, 2005)

$$\psi_{\uparrow,\downarrow} \propto \tanh(x/\xi_\nu) \pm i\frac{\beta}{\cosh(x/\xi_\nu)}\,. \tag{9.59}$$

An important difference in chiral spinor condensates is the uneven spin density profiles, which arise from differences in the effective interactions induced by the chiral currents, and are closer to those of regular moving Josephson vortices (Shamailov and Brand, 2018).

Regarding states with multiple Josephson vortices, configurations with co- and counter-rotating vortices are possible. Figure 9.9 shows a state with two co-rotating Josephson vortices, which have smooth 2π jumps in the relative phase for each vortex (see central panel), and with a nonzero density at the vortex core (see top panel). Note that these cores are located in the junction at the spatial position of the density minima of both spin components, and that the Josephson current changes sign (vanishes) also at half distance between them. The situation is more involved however for counter-rotating Josephson vortices, as we show in Fig. 9.10. Although one can identify the sign change of Josephson currents around the vortex cores, which are now signaled by minima in the total density, the relative phase presents just π (opposite) jumps across them. These π jumps are caused by staggered dark-soliton-like phase profiles in the spin components. The features of counter-rotating Josephson vortices are in sharp contrast with the case

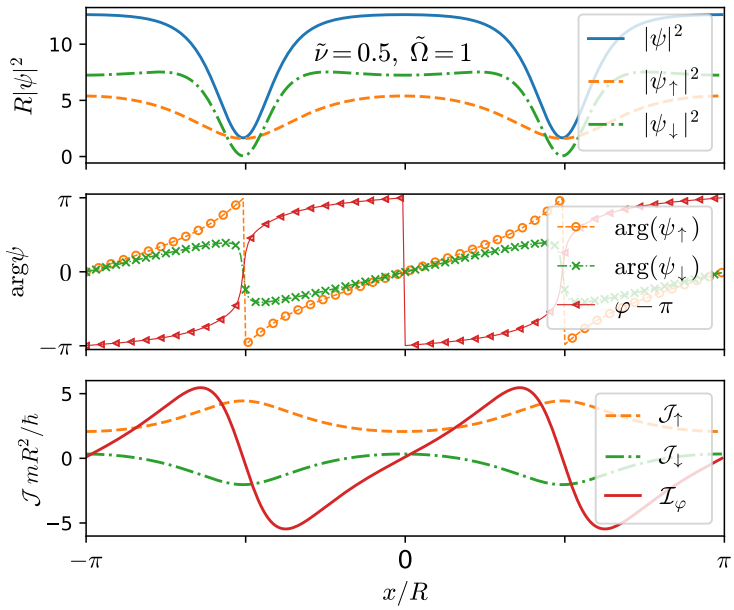

Figure 9.9: Co-rotating Josephson vortices in a chiral spinor condensate with interaction parameter $\kappa N = 20\pi$ at $\tilde{\Omega} = 1$ and $\tilde{\nu} = 0.5$. We plot the density profiles (top), the phase profiles (middle), and the currents (bottom).

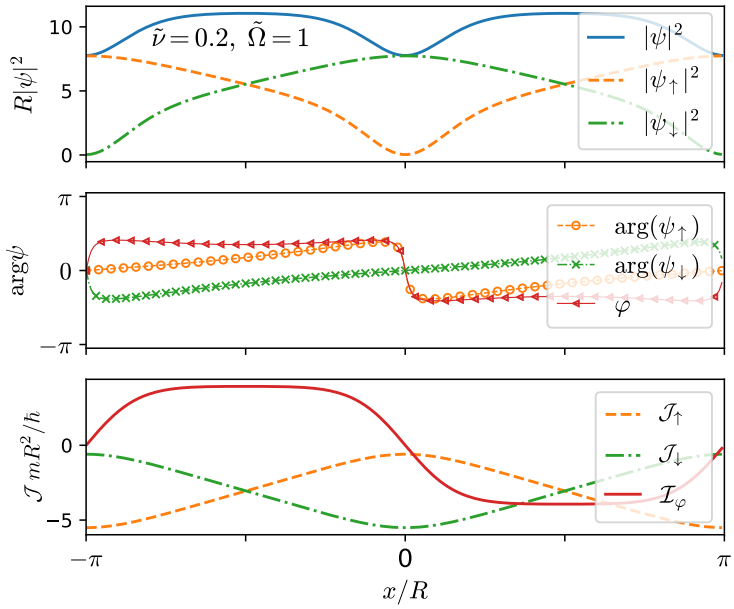

Figure 9.10: Counter-rotating Josephson vortices in a chiral spinor condensate with interaction parameter $\kappa N = 20\pi$ at $\tilde{\Omega} = 1$ and $\tilde{\nu} = 0.2$. As in Fig. 9.9, we plot the density profiles (top), the phase profiles (middle), and the currents (bottom).

of static counter-rotating Josephson vortices in regular spinor condensates (Qiu et al., 2021), and present common features with other moving solitonic structures, such as staggered dark solitons or Manakov solitons (see for instance Shamailov and Brand, 2018).

9.4 Summary of results

In this chapter, we have studied the stationary states of quasi-1D spinor condensates in a rotating ring geometry with current-density interactions. The two spin components can exchange particles due to the linear coupling, which we implement by considering a double well in the direction transversal to the chiral axis.

The Hamiltonian that describes the system contains a coherent coupling term, but it also includes an effective spin–orbit coupling that does not appear in equivalent nonchiral spinor condensates. This additional term originates from an axial current between the spin components. Thus, we find that the absence or presence of a spin current determines the two possible types of solutions that the system supports.

As for the chiral scalar case, the most simple possible solutions are plane waves. Then, depending on whether the spin current is nonzero, the system may present either unpolarized (with zero spin current) or polarized (with nonzero spin current) plane-wave solutions analogously to the nonchiral spinor case. In particular, we have analyzed the regime of parameters in which polarized states can exist. A distinct feature of polarized states in the chiral spinor system is that now polarized states are never the ground state of the system, as opposed to nonchiral spinor condensates, where states with a nonvanishing spin current may be the ground state for the appropriate values of the interparticle interaction strength.

We have also studied the stability of plane waves (with negative wavenumber) by analyzing their linear excitations. The excitation spectra of unpolarized states (without spin current) show two branches of excitations, called spin or density modes, as for the nonchiral case. We have studied the effect of the number density on the stability of plane waves since a high density (i.e., a strong interaction) may suppress density modes that are unstable at lower densities. Polarized states present a similar situation at low densities as unpolarized states. For higher densities, however, the polarized states present instabilities that arise by the collision of excitation branches at nonzero momenta.

Besides plane waves, the system also supports complex superpositions of plane-wave solutions, which have constant currents and spatially modulated density and phase profiles. We have finally studied more general solutions with space-dependent profiles, namely nonlinear excited states, which we refer to as solitonic states. Among these states, one can find similar states as those we already discussed in the scalar case (see Chapter 8), which are regular dark and bright solitons that can now appear with or without spin currents. Interestingly, we have seen that the system may also host Josephson vortices, a particular feature of spinor condensates, which present Josephson currents flowing between components.

10

Conclusions

Bose–Einstein condensation of ultradilute and weakly interacting gases has been the leitmotiv of this thesis. We have employed a theoretical mean-field description of Bose–Einstein condensates (BECs) and explored two main interconnected themes: anisotropic interactions and self-bound solutions. First, we have dealt with long-range dipolar interactions, which may dominate in systems of highly magnetic atoms, and with the effective short-range chiral interactions that can emerge in a condensate when subject to an artificial gauge field. Second, we have focused on two types of states that self-bind due to the interacting nature of the system: quantum droplets, stabilized by quantum fluctuations, and solitons, which owe their existence to the dispersion of the medium.

In the present chapter, we summarize the main results of this work and examine the possible future lines of research that may derive from this thesis.

The initial part of this thesis was devoted to the development of the theoretical foundations of the subsequent research, and was detailed in Chapters 2, 3, and 4.

In *Chapter 2*, we reviewed the fundamental concepts behind Bose–Einstein condensation. First, we introduced basic ideas such as the quantum statistical origin of this transition, the condensate fraction, quantum depletion, the role of dimensionality, and two-body interactions. Since BECs are generally weakly interacting and very dilute, one can deal with the many-body problem using a mean-field approach that yields the Gross–Pitaevskii equation (GPE). However, when these conditions are not met, the mean-field approach is no longer valid, and quantum fluctuations start to contribute significantly. We gave an overview of both the mean-field treatment and the beyond-mean correction that takes into account these quantum fluctuations. Second, we moved to bosonic binary mixtures and discussed their stability and excitations. In particular, we introduced the effective single-component model commonly used to study quantum nondipolar droplets. Later, we discussed the binding mechanism of such droplets and outlined their main properties, such as the critical number of atoms, saturation, and self-evaporation. Finally, we reduced the GPE to 1D and introduced the formalism that describes solitonic solutions, focusing, in particular, on dark and bright solitons and their main features.

In *Chapter 3*, we focused on BECs of atoms with a high dipolar moment. First, we described the dipole–dipole interactions and the mean-field formalism for dipolar atoms, which adds a nonlocal term to the GPE. We discussed the effect of these interactions on

the ground state, and then we examined the excitations and instabilities of the system, especially the roton instability. Second, we introduced a beyond mean-field correction to the dipolar GPE to include the effect of quantum fluctuations and studied the formation of self-bound droplets. We discussed the role of confinement in such droplets, which may break into several droplets when the confinement along the dipole direction is strong enough. We concluded by discussing how these smaller droplets can form crystals due to the in-plane confinement and that, in some cases, the resulting crystals may exhibit supersolid properties.

In *Chapter 4*, we dealt with current-density interactions, which are chiral. First, we introduced artificial gauge fields and density-dependent gauge potentials, which give rise to the chiral interactions we considered. Then, we explored how these density-dependent gauge potentials could be obtained in optically coupled condensates, starting from the simple case of a two-level atom to develop the main ideas and later discussing a two-component condensate with asymmetric contact interactions. Second, we presented the current-density theory in 1D by deriving its equation of motion, which has a nonlinear term that comes from the current density and results in effective chiral interactions. Finally, we added periodic boundary conditions to the system to write the chiral GPE for a rotating ring and discussed the possible states of the system.

The remaining chapters of this thesis explored ultracold bosonic gases in different configurations within the mean-field framework. In particular, we studied shell-shaped BECs (Chapter 5), bosonic binary mixtures (Chapters 6 and 7), and BECs in a rotating ring (Chapters 8 and 9).

In *Chapter 5*, we studied the ground-state configurations and dynamical behavior of shell-shaped BECs under a small gravitational force. We considered nondipolar and dipolar condensates and used gravities above microgravity but well below terrestrial gravity, which would drag all the atoms to the bottom of the trap. First, we examined the static properties of the system both in the absence of gravity and with a tiny gravitational sag and compared the nondipolar and dipolar cases. Also, we considered both the case of complete alignment between the gravitational axis and the dipoles and the case of a small misalignment. Then, we described how the strength of the gravitational force determines the ground-state shape of the condensate, a full or half shell, and thus critically affects the dynamics of the system. Second, we characterized the dynamical oscillations when varying perturbatively the orientation or the strength of gravity. We showed how the two ground-state regimes result in two different behaviors: the oscillation frequency increases (decreases) with the strength of gravity for the half shell (full shell). Finally, we discussed that oscillations, whether from variations in angle or magnitude, are similar in nondipolar condensates, but they show distinct behaviors in dipolar BECs since the dipolar interactions counterbalance the gravitational sag and reduce its effect. As a result, dipolar shells are much more robust against perturbations to gravity.

We explored in depth the sensitivity of both dipolar and nondipolar condensates to variations in the angle and the strength of gravity, and found that one cannot discern the origin of the oscillations from the dynamics alone. A potential line of inquiry would be to reduce the geometry and study instead a toroidal BEC (Guo et al., 2022), where it may

be possible to distinguish between the two effects. Additionally, one could explore the effect of quantum fluctuations, as recently done in dipolar shell-shaped BECs (Ciardi et al., 2024; Sánchez-Baena et al., 2023a), and study the formation of droplet arrays and supersolids.

In *Chapter 6*, we considered a quasi-1D immiscible mixture of two nondipolar components, and we characterized the transmission and reflection of a dark soliton through the domain wall that separates them. First, we saw that a dark soliton imprinted in one of the components may generate a dark–bright (DB) soliton when crossing the domain wall depending on the strength of the interactions. The resulting DB solitons are generated dynamically outside the regime of parameters for which explicit analytical solutions exist. Once the DB forms, it follows a harmonic-like trajectory; when it reaches the domain wall again, it is transferred or reflected. Second, we obtained a semianalytical expression for the oscillation frequency of the DB soliton by treating the bright component, which is the minority component, as a perturbation to the dark component. We finally checked that this semianalytical prediction agrees with the numerical frequency obtained by solving the GPE.

A natural extension of this work would be to examine the interaction and back-action between the DB soliton and the domain wall to understand better their interplay. Furthermore, one could consider the case of higher dimensions (Aioi et al., 2012), in which case a more complex picture and instabilities due to the dimensionality would arise.

In *Chapter 7*, we dealt with binary dipolar mixtures with antiparallel dipoles. First, we observed that the mixture can form three-dimensionally self-bound structures, while confinement along the polarization (axial) direction can give rise to the formation of droplet crystals. These crystals are self-bound in the transversal plane since the intercomponent interactions are attractive and the two components confine each other. Then, we analyzed these crystals, where one of the components forms an array of droplets and the other fills in the interstitials of the crystal. We argued the incoherent nature of the droplets, observed how they arrange in an approximately triangular structure, and discussed that the superfluidity of the interstitial component may be probed using time-of-flight measurements. Finally, we also examined the effect of the contact interactions and showed that the system may form stripe/labyrinthic crystals or droplet crystals when the intracomponent interactions are symmetric or asymmetric, respectively.

This work leaves several open questions. For example, one could study the excitations of the system, and investigating wether they evaporate would be a possible course to follow. Additionally, one could also explore the formation of quantized vortices in the interstitial component as a means to prove its superfluid character. Lastly, one could also explore the dynamical formation of these crystals by starting with a single dipolar component and adiabatically transferring population to the other component.

In *Chapter 8*, we moved to quasi-1D BECs confined in a rotating-ring trap and subject to current-density interactions. Persistent currents become chiral in such a system, and the stationary states of the system (plane waves and solitonic states) are also markedly different compared to the nonchiral case. First, we showed that the eigenenergy is

asymmetric in the angular frequency; thus, solitonic trajectories cannot cross the non-rotating case. Second, we analyzed the dynamical stability of the stationary states and started by verifying that the time evolution agrees with the predictions of the linear analysis of excitations. For a positive velocity, we found stable currents with either constant or modulated density profiles. For a negative velocity, on the other hand, we observed unstable currents above a velocity threshold. This instability indicates that moving and strongly localized bright solitons, which behave as classical particles regarding their energy and momentum, may be stable instead.

In *Chapter 9*, we generalized the system of Chapter 8 to a 1/2-spinor condensate resembling a long Josephson junction and studied the stationary states of the system. To split the condensate into two components, we proposed using a double-well potential in the direction transversal to the chiral axis such that there can be an interchange of particles between components due to the linear coupling. First, we examined the Hamiltonian of the system, which contains, besides a coherent coupling term, an effective spin–orbit coupling. We discussed that this new term does not appear in nonchiral spinor condensates since it comes from the current between spin components. Then, we saw that the two possible types of solutions depend on the absence or presence of spin current. Second, we analyzed plane-wave solutions thoroughly and discussed the two scenarios that arise in the absence or presence of a spin current: unpolarized or polarized plane waves. We analyzed the conditions of the existence of polarized states, and we pointed out that, unlike in nonchiral spinor condensates, the polarized states in the chiral case cannot be the ground state. Later, we examined the stability of plane-wave solutions via linear analysis of excitations for both the unpolarized and the polarized cases. We showed that the unpolarized states present two excitation branches and that high densities may suppress unstable density modes, while polarized states exhibit instabilities stemming from the collision of different branches. Third, we studied solitonic-like solutions of the system, which are more general solutions and, in contrast to plane waves, present a modulated density profile. In particular, we considered solitons, which were already solutions of the scalar case, and Josephson vortices, which are distinctive of spinor condensates since they emerge from the current between components.

Instead of the long Josephson junction of Chapter 9, one could consider a point-like junction (Edmonds et al., 2013b), with the double-well potential along the chiral axis. It would be worth doing a thorough analysis of how the current-density interactions affect the Josephson dynamics of the system and checking the validity of the two-mode approximation by performing full 3D mean-field calculations.

Connecting with the previous lines of research discussed through this thesis, another natural extension of the scalar chiral model would be to consider a dipolar condensate in a 1D geometry with open boundary conditions (or in a very large ring). First, one should consider the experimental feasibility of a dipolar condensate with these effective chiral interactions, since dipolar relaxation may limit the lifetime of the system. Then, one could study the interplay between the orientation of the dipoles and the short-range chiral interactions, and explore the ground-state configurations and excitations of the system.

Other possible continuations to the 1D chiral case would be to include the effect of quantum fluctuations to study the formation of droplets when the interactions are chiral. For instance, one could consider a 1D nondipolar and miscible mixture with current-density interactions, which may be achieved by mixing two chiral condensates of different atomic species. The beyond mean-field correction to the mean-field formalism would now have a chiral nature as well, and as a result, the binding mechanism of the droplets would also show a dependence on the motion of the atoms. Droplets of nondipolar (and nonchiral) mixtures exist only for a particular ratio of the components' densities. For this reason, this setup raises the question of whether such chiral droplets could exist or a moving droplet would evaporate to reach a new density ratio as the effective interactions change due to chirality.

Finally, building on the last two scenarios, one could explore the effect of quantum fluctuations in a 1D chiral scalar condensate with dipole–dipole interactions. In this system, when quantum fluctuations are no longer negligible, droplets and supersolids with chiral properties could emerge.

A

JACOBI ELLIPTIC FUNCTIONS

The Jacobi elliptic[1] functions allow one to generalize the hyperbolic functions to a geometry with periodic boundary conditions (see Abramowitz and Stegun, 1968, for more details). There are twelve elliptic functions denoted as pq$(x, \mathfrak{m})$, with p and q any of the letters c, s, n and d[2]. However, all twelve of them can be derived and expressed in terms of the three main functions: cn$(x, \mathfrak{m})$, sn$(x, \mathfrak{m})$ and dn$(x, \mathfrak{m})$ (see Fig. A.1), which are defined as

$$\mathrm{sn}(x, \mathfrak{m}) = \sin(\varpi)\,, \quad \mathrm{cn}(x, \mathfrak{m}) = \cos(\varpi)\,, \quad \mathrm{dn}(x, \mathfrak{m}) = \sqrt{1 - \mathfrak{m}\sin^2\varpi}\,. \tag{A.1}$$

The angle ϖ is called the *amplitude*, and is the angle for which the cartesian coordinate x can be written in integral form as

$$x = \int_0^{\varpi} \left(1 - \mathfrak{m}\sin^2\vartheta\right)^{-1/2} d\vartheta\,. \tag{A.2}$$

The first variable in these functions is, in our case, the spatial coordinate x; the second variable is the parameter $\mathfrak{m}$[3], which is a real scalar. The value of $\mathfrak{m}$ is bounded between 0 and 1, which leads to two limiting cases:

- *Trigonometric limit*. The functions sn$(x, 0)$ and cn$(x, 0)$ yield the trigonometric functions $\sin(x)$ and $\cos(x)$, respectively, while dn$(x, 0) = 1$ (see Fig. A.1, left).
- *Hyperbolic limit*. The elliptic functions cn$(x, \mathfrak{m} \to 1)$ and dn$(x, \mathfrak{m} \to 1)$ tend both to the hyperbolic function $\mathrm{sech}(x)$, while sn$(x, \mathfrak{m} \to 1)$ tends to $\tanh(x)$ instead (see Fig. A.1, right).

[1] The term *elliptic* refers to the fact that these functions are defined with the ellipse as reference, while the trigonometric and hyperbolic functions use instead the circle and the hyperbola, respectively.

[2] When the two letters are the same, for instance p, the corresponding function pp$(x, \mathfrak{m})$ is set to unity for completeness.

[3] The notation used to characterize the elliptic functions is not particularly uniform in the literature: the first variable can also be given in terms of the amplitude ϖ, and the second variable is sometimes expressed in terms of the *elliptic modulus* k, with $\mathfrak{m} = k^2$. The cartesian coordinate and the amplitude are usually denoted in the literature by u and φ, but here we will use x and ϖ instead to avoid confusion.

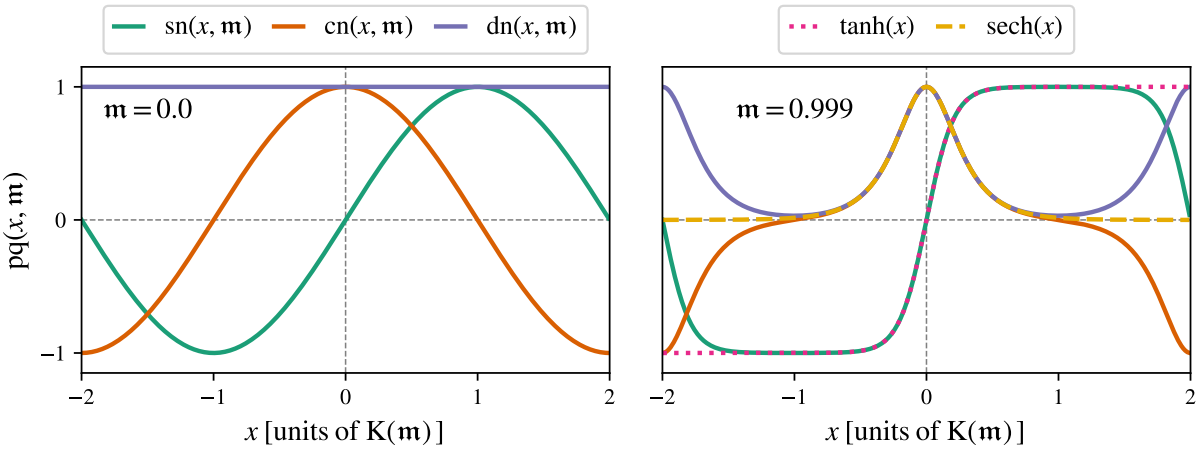

Figure A.1: Jacobi elliptic functions $\mathrm{sn}(x,\mathfrak{m})$, $\mathrm{cn}(x,\mathfrak{m})$ and $\mathrm{dn}(x,\mathfrak{m})$ [see (A.1)] as a function of x for the trigonometric limit (left) and the hyperbolic limit (right). The spatial coordinate x is given in units of $\mathrm{K} = \mathrm{K}(\mathfrak{m})$ (A.4), the integral of the first kind. In the right panel, dotted and dashed lines correspond to the hyperbolic functions $\tanh(x)$ and $\mathrm{sech}(x)$, respectively.

The usual trigonometric identity $\sin^2 x + \cos^2 x = 1$ generalizes to elliptic functions as

$$-\,\mathrm{dn}^2(x,\mathfrak{m}) + (1-\mathfrak{m}) = -\mathfrak{m}\,\mathrm{cn}^2(x,\mathfrak{m}) = \mathfrak{m}\,\mathrm{sn}^2(x,\mathfrak{m}) - \mathfrak{m}\,, \tag{A.3}$$

such that, in the $\mathfrak{m} = 0$ case, one recovers the trigonometric expression $\mathrm{sn}^2(x,0) + \mathrm{cn}^2(x,0) = 1$. Similarly, one gets the hyperbolic relation $\mathrm{sech}^2(x) = 1 - \tanh^2(x)$ in the $\mathfrak{m} \to 1$ limit.

The period of the elliptic functions is given in terms of the complete elliptic integral of the first kind,

$$\mathrm{K} = \mathrm{K}(\mathfrak{m}) = \int_0^{\pi/2} \left(1 - \mathfrak{m}\sin^2\vartheta\right)^{-1/2} d\vartheta\,, \tag{A.4}$$

which corresponds to Eq. (A.2) with amplitude $\varpi = \pi/2$. Then, as one can see by plotting the elliptic functions (Fig. A.1), the period of $\mathrm{sn}(x,\mathfrak{m})$ and $\mathrm{cn}(x,\mathfrak{m})$ is 4K, while $\mathrm{dn}(x,\mathfrak{m})$ has a period of 2K when $\mathfrak{m} \neq 0$.

The stationary soliton solutions that we study in Chapters 8 and 9 are given in terms of these elliptic functions. To calculate the norm and phase of these solutions, we need to introduce the incomplete elliptic integrals. The incomplete elliptic integral of the second kind is defined as

$$\mathrm{E}(x,\mathfrak{m}) = \int_0^x \mathrm{dn}^2(u,\mathfrak{m})\,du\,, \tag{A.5}$$

which becomes complete when $x = \mathrm{K}$, which we denote as $\mathrm{E}(\mathfrak{m}) = \mathrm{E}(\mathrm{K},\mathfrak{m})$, and has the property

$$\mathrm{E}(x + a\mathrm{K},\mathfrak{m}) = \mathrm{E}(x,\mathfrak{m}) + a\mathrm{E}(\mathfrak{m})\,, \tag{A.6}$$

where a is an integer. Lastly, we introduce the incomplete integral of the third kind[4],

$$\mathrm{P}(\eta; x, \mathfrak{m}) = \int_0^x \left[1 - \eta\, \mathrm{sn}^2(x, \mathfrak{m})\right]^{-1} du\,, \tag{A.7}$$

where η may be complex and take on any value. As we did for the integral of the second kind, we now define the complete integral as $\mathrm{P}(\eta; \mathfrak{m}) = \mathrm{P}(\eta; \mathrm{K}, \mathfrak{m})$.

[4]The elliptic integral of the third kind is usually denoted by Π in the literature and most numerical libraries, but here we will use P to differentiate it from the momentum operator in the rotating frame, $\hat{\Pi}$, which we use in Chapters 8 and 9.

Bibliography

M. Abad. Persistent currents in coherently coupled bose-einstein condensates in a ring trap. *Physical Review A*, 93:033603, Mar 2016. doi: 10.1103/PhysRevA.93.033603. URL https://link.aps.org/doi/10.1103/PhysRevA.93.033603. (Cited on page 2.)

M. Abad and A. Recati. A study of coherently coupled two-component Bose-Einstein condensates. *The European Physical Journal D*, 67:1–11, Jul 2013. doi: 10.1140/epjd/e2013-40053-2. URL https://doi.org/10.1140/epjd/e2013-40053-2. (Cited on pages 4, 29, 154, 159, 162, and 164.)

M. Abad, M. Guilleumas, R. Mayol, M. Pi, and D. M. Jezek. Vortices in Bose-Einstein condensates with dominant dipolar interactions. *Physical Review A*, 79(6):063622, Jun 2009. doi: 10.1103/PhysRevA.79.063622. URL https://link.aps.org/doi/10.1103/PhysRevA.79.063622. (Cited on page 83.)

M. Abad, M. Guilleumas, R. Mayol, M. Pi, and D. M. Jezek. Dipolar condensates confined in a toroidal trap: Ground state and vortices. *Physical Review A*, 81(4):043619, Apr 2010. doi: 10.1103/PhysRevA.81.043619. URL https://link.aps.org/doi/10.1103/PhysRevA.81.043619. (Cited on page 84.)

M. Abad, M. Guilleumas, R. Mayol, M. Pi, and D. M. Jezek. A dipolar self-induced bosonic Josephson junction. *Europhysics Letters*, 94(1):10004, Apr 2011. doi: 10.1209/0295-5075/94/10004. URL https://dx.doi.org/10.1209/0295-5075/94/10004. (Cited on page 84.)

M. Abad, A. Sartori, S. Finazzi, and A. Recati. Persistent currents in two-component condensates in a toroidal trap. *Physical Review A*, 89:053602, May 2014. doi: 10.1103/PhysRevA.89.053602. URL https://link.aps.org/doi/10.1103/PhysRevA.89.053602. (Cited on page 2.)

M. Abad, M. Guilleumas, R. Mayol, F. Piazza, D. M. Jezek, and A. Smerzi. Phase slips and vortex dynamics in Josephson oscillations between Bose-Einstein condensates. *Europhysics Letters*, 109(4):40005, Feb 2015. doi: 10.1209/0295-5075/109/40005. URL https://dx.doi.org/10.1209/0295-5075/109/40005. (Cited on page 84.)

M. J. Ablowitz, B. Prinari, and A. D. Trubatch. *Discrete and continuous nonlinear Schrödinger systems*, volume 302. Cambridge University Press, 2004. doi: 10.1017/CBO9780511546709. URL https://doi.org/10.1017/CBO9780511546709. (Cited on page 6.)

M. Abramowitz and I. A. Stegun. *Handbook of mathematical functions with formulas, graphs, and mathematical tables*, volume 55. US Government printing office, 1968. ISBN 9780486612720. (Cited on pages 136, 138, 139, 141, and 181.)

V. Achilleos, P. G. Kevrekidis, V. M. Rothos, and D. J. Frantzeskakis. Statics and dynamics of atomic dark-bright solitons in the presence of impurities. *Physical Review A*, 84:053626, Nov 2011. doi: 10.1103/PhysRevA.84.053626. URL https://doi.org/10.1103/PhysRevA.84.053626. (Cited on page 7.)

S. K. Adhikari. Dipolar Bose-Einstein condensate in a ring or in a shell. *Physical Review A*, 85(5):053631, May 2012. doi: 10.1103/PhysRevA.85.053631. URL https://link.aps.org/doi/10.1103/PhysRevA.85.053631. (Cited on pages 80 and 84.)

V. Afanasyev, Y. S. Kivshar, V. Konotop, and V. Serkin. Dynamics of coupled dark and bright optical solitons. *Optics letters*, 14(15):805–807, 1989. doi: 10.1364/OL.14.000805. URL https://opg.optica.org/ol/abstract.cfm?uri=ol-14-15-805. (Cited on page 7.)

U. Aglietti, L. Griguolo, R. Jackiw, S.-Y. Pi, and D. Seminara. Anyons and chiral solitons on a line. *Physical Review Letters*, 77(21):4406–4409, Nov 1996. doi: 10.1103/PhysRevLett.77.4406. URL https://link.aps.org/doi/10.1103/PhysRevLett.77.4406. (Cited on pages 5, 7, 72, 73, 74, 75, 129, 132, 135, and 153.)

Y. Aharonov and D. Bohm. Significance of electromagnetic potentials in the quantum theory. *Physical Review*, 115(3):485–491, Aug 1959. doi: 10.1103/PhysRev.115.485. URL https://link.aps.org/doi/10.1103/PhysRev.115.485. (Cited on page 67.)

M. Aidelsburger, S. Nascimbene, and N. Goldman. Artificial gauge fields in materials and engineered systems. *Comptes Rendus Physique*, 19(6):394–432, Nov 2018. doi: 10.1016/j.crhy.2018.03.002. URL https://doi.org/10.1016/j.crhy.2018.03.002. (Cited on pages 64, 65, and 69.)

K. Aikawa, A. Frisch, M. Mark, S. Baier, A. Rietzler, R. Grimm, and F. Ferlaino. Bose-Einstein condensation of erbium. *Physical Review Letters*, 108(21):210401, May 2012. doi: 10.1103/PhysRevLett.108.210401. URL https://link.aps.org/doi/10.1103/PhysRevLett.108.210401. (Cited on pages 4 and 95.)

T. Aioi, T. Kadokura, and H. Saito. Penetration of a vortex dipole across an interface of Bose-Einstein condensates. *Physical Review A*, 85(2):023618, Feb 2012. doi: 10.1103/PhysRevA.85.023618. URL https://link.aps.org/doi/10.1103/PhysRevA.85.023618. (Cited on page 177.)

N. Akhmediev, W. Królikowski, and A. W. Snyder. Partially coherent solitons of variable shape. *Physical Review Letters*, 81:4632–4635, Nov 1998. doi: 10.1103/PhysRevLett.81.4632. URL https://link.aps.org/doi/10.1103/PhysRevLett.81.4632. (Cited on page 7.)

M. Albiez, R. Gati, J. Fölling, S. Hunsmann, M. Cristiani, and M. K. Oberthaler. Direct observation of tunneling and nonlinear self-trapping in a single bosonic josephson junction. *Physical Review Letters*, 95:010402, Jun 2005. doi: 10.1103/PhysRevLett.95.010402. URL https://link.aps.org/doi/10.1103/PhysRevLett.95.010402. (Cited on page 2.)

M. O. D. Alotaibi and L. D. Carr. Scattering of a dark-bright soliton by an impurity. *Journal of Physics B: Atomic, Molecular and Optical Physics*, 52(16):165301, Jul 2019. doi: 10.1088/1361-6455/ab2cfb. URL https://dx.doi.org/10.1088/1361-6455/ab2cfb. (Cited on page 7.)

L. Amico, M. Boshier, G. Birkl, A. Minguzzi, C. Miniatura, L.-C. Kwek, D. Aghamalyan, V. Ahufinger, D. Anderson, N. Andrei, et al. Roadmap on Atomtronics: State of the art and perspective. *AVS Quantum Science*, 3(3):039201, 08 2021. ISSN 2639-0213. doi: 10.1116/5.0026178. URL https://doi.org/10.1116/5.0026178. (Cited on page 3.)

L. Amico, D. Anderson, M. Boshier, J.-P. Brantut, L.-C. Kwek, A. Minguzzi, and W. von Klitzing. Colloquium: Atomtronic circuits: From many-body physics to quantum technologies. *Rev. Mod. Phys.*, 94:041001, Nov 2022. doi: 10.1103/RevModPhys.94.041001. URL https://link.aps.org/doi/10.1103/RevModPhys.94.041001. (Cited on page 3.)

M. F. Andersen, C. Ryu, P. Cladé, V. Natarajan, A. Vaziri, K. Helmerson, and W. D. Phillips. Quantized rotation of atoms from photons with orbital angular momentum. *Physical Review Letters*, 97:170406, Oct 2006. doi: 10.1103/PhysRevLett.97.170406. URL https://link.aps.org/doi/10.1103/PhysRevLett.97.170406. (Cited on page 2.)

B. P. Anderson, P. C. Haljan, C. E. Wieman, and E. A. Cornell. Vortex precession in Bose-Einstein condensates: Observations with filled and empty cores. *Physical Review Letters*, 85(14):2857–2860, Oct 2000. doi: 10.1103/PhysRevLett.85.2857. URL https://link.aps.org/doi/10.1103/PhysRevLett.85.2857. (Cited on pages 7 and 110.)

B. P. Anderson, P. C. Haljan, C. A. Regal, D. L. Feder, L. A. Collins, C. W. Clark, and E. A. Cornell. Watching dark solitons decay into vortex rings in a bose-einstein condensate. *Physical Review Letters*, 86:2926–2929, Apr 2001. doi: 10.1103/PhysRevLett.86.2926. URL https://link.aps.org/doi/10.1103/PhysRevLett.86.2926. (Cited on page 6.)

M. H. Anderson, J. R. Ensher, M. R. Matthews, C. E. Wieman, and E. A. Cornell. Observation of Bose-Einstein condensation in a dilute atomic vapor. *Science*, 269(5221):198–201, 1995. doi: 10.1126/science.269.5221.198. URL https://www.science.org/doi/abs/10.1126/science.269.5221.198. (Cited on pages 1 and 11.)

P. W. Anderson and J. M. Rowell. Probable observation of the josephson superconducting tunneling effect. *Physical Review Letters*, 10:230–232, Mar 1963. doi: 10.1103/PhysRevLett.10.230. URL https://link.aps.org/doi/10.1103/PhysRevLett.10.230. (Cited on page 2.)

M. Andrews, C. Townsend, H.-J. Miesner, D. Durfee, D. Kurn, and W. Ketterle. Observation of interference between two bose condensates. *Science*, 275(5300):637–641, 1997. doi: 10.1126/science.275.5300.637. URL https://www.science.org/doi/10.1126/science.275.5300.637. (Cited on page 2.)

P. Ao and S. T. Chui. Binary Bose-Einstein condensate mixtures in weakly and strongly segregated phases. *Physical Review A*, 58(6):4836–4840, Dec 1998. doi: 10.1103/PhysRevA.58.4836. URL https://link.aps.org/doi/10.1103/PhysRevA.58.4836. (Cited on page 27.)

M. Arazo, M. Guilleumas, R. Mayol, and M. Modugno. Dynamical generation of dark-bright solitons through the domain wall of two immiscible Bose-Einstein condensates. *Physical Review A*, 104(4):043312, Oct 2021a. doi: 10.1103/PhysRevA.104.043312. URL https://link.aps.org/doi/10.1103/PhysRevA.104.043312. (Cited on pages xv and 9.)

M. Arazo, R. Mayol, and M. Guilleumas. Shell-shaped condensates with gravitational sag: contact and dipolar interactions. *New Journal of Physics*, 23(11):113040, nov 2021b. doi: 10.1088/1367-2630/ac37c9. URL https://dx.doi.org/10.1088/1367-2630/ac37c9. (Cited on pages xv and 8.)

M. Arazo, A. Gallemí, M. Guilleumas, R. Mayol, and L. Santos. Self-bound crystals of antiparallel dipolar mixtures. *Physical Review Research*, 5(4):043038, Oct 2023a. doi: 10.1103/PhysRevResearch.5.043038. URL https://link.aps.org/doi/10.1103/PhysRevResearch.5.043038. (Cited on pages xv and 9.)

M. Arazo, M. Guilleumas, R. Mayol, V. Delgado, and A. Muñoz Mateo. Chiral currents in Bose-Einstein condensates subject to current-density interactions. *Physical Review A*, 108(5):053302, Nov 2023b. doi: 10.1103/PhysRevA.108.053302. URL https://link.aps.org/doi/10.1103/PhysRevA.108.053302. (Cited on pages xv, 9, 158, and 165.)

A. S. Arnold. Extending dark optical trapping geometries. *Optics letters*, 37(13):2505–2507, 2012. doi: 10.1364/OL.37.002505. URL https://opg.optica.org/ol/abstract.cfm?uri=ol-37-13-2505. (Cited on page 3.)

D. C. Aveline et al. Observation of Bose–Einstein condensates in an Earth-orbiting research lab. *Nature*, 582:193–197, Jun 2020. URL http://www.nature.com/articles/s41586-020-2346-1. (Cited on page 80.)

M. C. Bañuls, R. Blatt, J. Catani, A. Celi, J. I. Cirac, M. Dalmonte, L. Fallani, K. Jansen, M. Lewenstein, S. Montangero, et al. Simulating lattice gauge theories within quantum technologies. *The European physical journal D*, 74:1–42, 2020. doi: 10.1140/epjd/e2020-100571-8. URL https://link.springer.com/article/10.1140/epjd/e2020-100571-8. (Cited on page 3.)

C. Baals, H. Ott, J. Brand, and A. Muñoz Mateo. Nonlinear standing waves in an array of coherently coupled Bose-Einstein condensates. *Physical Review A*, 98(5):053603, Nov 2018. doi: 10.1103/PhysRevA.98.053603. URL https://link.aps.org/doi/10.1103/PhysRevA.98.053603. (Cited on page 171.)

D. Baillie and P. B. Blakie. Droplet crystal ground states of a dipolar bose gas. *Physical Review Letters*, 121(19):195301, Nov 2018. doi: 10.1103/PhysRevLett.121.195301. URL https://link.aps.org/doi/10.1103/PhysRevLett.121.195301. (Cited on pages 6 and 59.)

D. Baillie, R. M. Wilson, R. N. Bisset, and P. B. Blakie. Self-bound dipolar droplet: A localized matter wave in free space. *Physical Review A*, 94(2):021602, Aug 2016. doi: 10.1103/PhysRevA.94.021602. URL https://link.aps.org/doi/10.1103/PhysRevA.94.021602. (Cited on page 56.)

D. Baillie, R. M. Wilson, and P. B. Blakie. Collective excitations of self-bound droplets of a dipolar quantum fluid. *Physical Review Letters*, 119(25):255302, Dec 2017. doi: 10.1103/PhysRevLett.119.255302. URL https://link.aps.org/doi/10.1103/PhysRevLett.119.255302. (Cited on page 58.)

M. Baranov. Theoretical progress in many-body physics with ultracold dipolar gases. *Physics Reports*, 464(3):71–111, 2008. ISSN 0370-1573. doi: https://doi.org/10.1016/j.physrep.2008.04.007. URL https://www.sciencedirect.com/science/article/pii/S0370157308001385. (Cited on page 4.)

M. Baranov, L. Dobrek, K. Góral, L. Santos, and M. Lewenstein. Ultracold dipolar gases – a challenge for experiments and theory. *Physica Scripta*, 2002(T102):74, jan 2002. doi: 10.1238/Physica.Topical.102a00074. URL https://dx.doi.org/10.1238/Physica.Topical.102a00074. (Cited on page 4.)

M. A. Baranov, M. Dalmonte, G. Pupillo, and P. Zoller. Condensed matter theory of dipolar quantum gases. *Chemical Reviews*, 112(9):5012–5061, 2012. doi: 10.1021/cr2003568. URL https://doi.org/10.1021/cr2003568. (Cited on page 4.)

C. F. Barenghi and N. G. Parker. *A primer on quantum fluids*. Springer, 2016. doi: 10.1007/978-3-319-42476-7. URL https://doi.org/10.1007/978-3-319-42476-7. (Cited on pages 6, 35, and 98.)

A. Barone. *Physics and Applications of the Josephson Effect*. John Wiley and Sons, Ltd, 1982. ISBN 9783527602780. doi: 10.1002/352760278X.ch10. URL https://doi.org/10.1002/352760278X.ch10. (Cited on page 156.)

S. Beattie, S. Moulder, R. J. Fletcher, and Z. Hadzibabic. Persistent currents in spinor condensates. *Physical Review Letters*, 110:025301, Jan 2013. doi: 10.1103/PhysRevLett.110.025301. URL https://link.aps.org/doi/10.1103/PhysRevLett.110.025301. (Cited on page 2.)

Q. Beaufils, R. Chicireanu, T. Zanon, B. Laburthe-Tolra, E. Maréchal, L. Vernac, J.-C. Keller, and O. Gorceix. All-optical production of chromium bose-einstein condensates. *Physical Review A*, 77:061601, Jun 2008. doi: 10.1103/PhysRevA.77.061601. URL https://link.aps.org/doi/10.1103/PhysRevA.77.061601. (Cited on page 4.)

C. Becker, S. Stellmer, P. Soltan-Panahi, S. Dörscher, M. Baumert, E.-M. Richter, J. Kronjager, K. Bongs, and K. Sengstock. Oscillations and interactions of dark and dark–bright solitons in Bose–Einstein condensates. *Nature Physics*, 4:496–501, 2008. doi: 10.1038/nphys962. URL https://doi.org/10.1038/nphys962. (Cited on pages 3, 7, 98, and 99.)

D. Becker, M. D. Lachmann, S. T. Seidel, H. Ahlers, A. N. Dinkelaker, J. Grosse, O. Hellmig, H. Müntinga, V. Schkolnik, T. Wendrich, et al. Space-borne Bose–Einstein condensation for precision interferometry. *Nature*, 562(7727):391–395, 2018. (Cited on page 80.)

T. A. Bell, J. A. P. Glidden, L. Humbert, M. W. J. Bromley, S. A. Haine, M. J. Davis, T. W. Neely, M. A. Baker, and H. Rubinsztein-Dunlop. Bose–einstein condensation in large time-averaged optical ring potentials. *New Journal of Physics*, 18(3):035003, mar 2016. doi: 10.1088/1367-2630/18/3/035003. URL https://dx.doi.org/10.1088/1367-2630/18/3/035003. (Cited on page 3.)

S. J. Bereta, L. Madeira, V. S. Bagnato, and M. A. Caracanhas. Bose–Einstein condensation in spherically symmetric traps. *American Journal of Physics*, 87(11):924–934, Nov 2019. ISSN 0002-9505. doi: 10.1119/1.5125092. URL https://doi.org/10.1119/1.5125092. (Cited on page 79.)

S. J. Bereta, M. A. Caracanhas, and A. L. Fetter. Superfluid vortex dynamics on a spherical film. *Physical Review A*, 103(5):053306, May 2021. doi: 10.1103/PhysRevA.103.053306. URL https://link.aps.org/doi/10.1103/PhysRevA.103.053306. (Cited on page 79.)

M. V. Berry. Quantal phase factors accompanying adiabatic changes. *Proceedings of the Royal Society of London. A. Mathematical and Physical Sciences*, 392(1802):45–57, Mar 1984. doi: 10.1098/rspa.1984.0023. URL https://royalsocietypublishing.org/doi/10.1098/rspa.1984.0023. (Cited on pages 4, 64, and 66.)

I. A. Bhat, S. Sivaprakasam, and B. A. Malomed. Modulational instability and soliton generation in chiral Bose-Einstein condensates with zero-energy nonlinearity. *Physical Review E*, 103(3):032206, Mar 2021. doi: 10.1103/PhysRevE.103.032206. URL https://link.aps.org/doi/10.1103/PhysRevE.103.032206. (Cited on pages 7 and 129.)

R. N. Bisset, R. M. Wilson, D. Baillie, and P. B. Blakie. Ground-state phase diagram of a dipolar condensate with quantum fluctuations. *Physical Review A*, 94(3):033619, Sep 2016. doi: 10.1103/PhysRevA.94.033619. URL https://link.aps.org/doi/10.1103/PhysRevA.94.033619. (Cited on pages 5, 56, and 58.)

R. N. Bisset, L. A. P. n. Ardila, and L. Santos. Quantum droplets of dipolar mixtures. *Physical Review Letters*, 126(2):025301, Jan 2021. doi: 10.1103/PhysRevLett.126.025301. URL https://link.aps.org/doi/10.1103/PhysRevLett.126.025301. (Cited on pages 4, 112, 113, and 117.)

T. Bland, E. Poli, L. A. P. n. Ardila, L. Santos, F. Ferlaino, and R. N. Bisset. Alternating-domain supersolids in binary dipolar condensates. *Physical Review A*, 106(5):053322, Nov 2022a. doi: 10.1103/PhysRevA.106.053322. URL https://link.aps.org/doi/10.1103/PhysRevA.106.053322. (Cited on pages 112, 120, and 122.)

T. Bland, E. Poli, C. Politi, L. Klaus, M. A. Norcia, F. Ferlaino, L. Santos, and R. N. Bisset. Two-dimensional supersolid formation in dipolar condensates. *Physical Review Letters*, 128(19):195302, May 2022b. doi: 10.1103/PhysRevLett.128.195302. URL https://link.aps.org/doi/10.1103/PhysRevLett.128.195302. (Cited on pages 112 and 118.)

I. Bloch, J. Dalibard, and W. Zwerger. Many-body physics with ultracold gases. *Rev. Mod. Phys.*, 80:885–964, Jul 2008. doi: 10.1103/RevModPhys.80.885. URL https://link.aps.org/doi/10.1103/RevModPhys.80.885. (Cited on page 3.)

N. Bogoliubov. On the theory of superfluidity. *J. Phys*, 11(1):23, 1947. doi: 10.1016/B978-0-08-015816-7.50020-1. URL https://www.sciencedirect.com/science/article/pii/B9780080158167500201. (Cited on pages 22 and 48.)

J. L. Bohn, R. M. Wilson, and S. Ronen. How does a dipolar Bose-Einstein condensate collapse? *Laser Physics*, 19:547–549, Apr 2009. doi: 10.1134/S1054660X09040021. URL https://doi.org/10.1134/S1054660X09040021. (Cited on page 47.)

J. L. Bohn, A. M. Rey, and J. Ye. Cold molecules: Progress in quantum engineering of chemistry and quantum matter. *Science*, 357(6355):1002–1010, 2017. doi: 10.1126/science.aam6299. URL https://www.science.org/doi/abs/10.1126/science.aam6299. (Cited on page 4.)

K. Bongs and K. Sengstock. Physics with coherent matter waves. *Reports on Progress in Physics*, 67(6):907, may 2004. doi: 10.1088/0034-4885/67/6/R03. URL https://dx.doi.org/10.1088/0034-4885/67/6/R03. (Cited on page 20.)

M. Boninsegni and N. V. Prokof'ev. Colloquium: Supersolids: What and where are they? *Reviews of Modern Physics*, 84(2):759–776, May 2012. doi: 10.1103/RevModPhys.84.759. URL https://link.aps.org/doi/10.1103/RevModPhys.84.759. (Cited on page 59.)

S. N. Bose. Plancks gesetz und lichtquantenhypothese. *Zeitschrift für Physik*, 26(1):178–181, 1924. (Cited on page 1.)

F. Böttcher, J.-N. Schmidt, M. Wenzel, J. Hertkorn, M. Guo, T. Langen, and T. Pfau. Transient supersolid properties in an array of dipolar quantum droplets. *Physical Review X*, 9(1):011051, Mar 2019a. doi: 10.1103/PhysRevX.9.011051. URL https://link.aps.org/doi/10.1103/PhysRevX.9.011051. (Cited on pages 6, 59, and 112.)

F. Böttcher, M. Wenzel, J.-N. Schmidt, M. Guo, T. Langen, I. Ferrier-Barbut, T. Pfau, R. Bombín, J. Sánchez-Baena, J. Boronat, and F. Mazzanti. Dilute dipolar quantum droplets beyond the extended gross-pitaevskii equation. *Physical Review Res.*, 1:033088, Nov 2019b. doi: 10.1103/PhysRevResearch.1.033088. URL https://link.aps.org/doi/10.1103/PhysRevResearch.1.033088. (Cited on page 5.)

C. C. Bradley, C. A. Sackett, J. J. Tollett, and R. G. Hulet. Evidence of bose-einstein condensation in an atomic gas with attractive interactions. *Physical Review Letters*, 75: 1687–1690, Aug 1995. doi: 10.1103/PhysRevLett.75.1687. URL https://link.aps.org/doi/10.1103/PhysRevLett.75.1687. (Cited on page 1.)

C. C. Bradley, C. A. Sackett, and R. G. Hulet. Analysis of in situ images of bose-einstein condensates of lithium. *Physical Review A*, 55:3951–3953, May 1997a. doi: 10.1103/PhysRevA.55.3951. URL https://link.aps.org/doi/10.1103/PhysRevA.55.3951. (Cited on page 1.)

C. C. Bradley, C. A. Sackett, and R. G. Hulet. Bose-einstein condensation of lithium: Observation of limited condensate number. *Physical Review Letters*, 78:985–989, Feb 1997b. doi: 10.1103/PhysRevLett.78.985. URL https://link.aps.org/doi/10.1103/PhysRevLett.78.985. (Cited on page 1.)

J. Brand and W. P. Reinhardt. Generating ring currents, solitons and svortices by stirring a bose-einstein condensate in a toroidal trap. *Journal of Physics B: Atomic, Molecular and Optical Physics*, 34(4):L113, feb 2001. doi: 10.1088/0953-4075/34/4/105. URL https://dx.doi.org/10.1088/0953-4075/34/4/105. (Cited on page 7.)

V. A. Brazhnyi and V. V. Konotop. Evolution of a dark soliton in a parabolic potential: Application to Bose-Einstein condensates. *Physical Review A*, 68(4), Oct 2003a. doi: 10.1103/PhysRevA.68.043613. URL http://dx.doi.org/10.1103/PhysRevA.68.043613. (Cited on page 6.)

V. A. Brazhnyi and V. V. Konotop. Publisher's note: Evolution of a dark soliton in a parabolic potential: Application to bose-einstein condensates [physical review a 68, 043613 (2003)]. *Physical Review A*, 68:059902, Nov 2003b. doi: 10.1103/PhysRevA.68.059902. URL https://link.aps.org/doi/10.1103/PhysRevA.68.059902. (Cited on page 6.)

S. Bresolin, A. Roy, G. Ferrari, A. Recati, and N. Pavloff. Oscillating solitons and ac josephson effect in ferromagnetic bose-bose mixtures. *Physical Review Letters*, 130: 220403, May 2023. doi: 10.1103/PhysRevLett.130.220403. URL https://link.aps.org/doi/10.1103/PhysRevLett.130.220403. (Cited on page 7.)

N. Q. Burdick, K. Baumann, Y. Tang, M. Lu, and B. L. Lev. Fermionic suppression of dipolar relaxation. *Physical Review Letters*, 114(2):023201, Jan 2015. doi: 10.1103/PhysRevLett.114.023201. URL https://link.aps.org/doi/10.1103/PhysRevLett.114.023201. (Cited on page 40.)

S. Burger, K. Bongs, S. Dettmer, W. Ertmer, K. Sengstock, A. Sanpera, G. V. Shlyapnikov, and M. Lewenstein. Dark solitons in bose-einstein condensates. *Physical Review Letters*, 83:5198–5201, Dec 1999. doi: 10.1103/PhysRevLett.83.5198. URL https://link.aps.org/doi/10.1103/PhysRevLett.83.5198. (Cited on page 6.)

E. A. Burt, R. W. Ghrist, C. J. Myatt, M. J. Holland, E. A. Cornell, and C. E. Wieman. Coherence, correlations, and collisions: What one learns about Bose-Einstein condensates from their decay. *Physical Review Letters*, 79(3):337–340, Jul 1997. doi: 10.1103/PhysRevLett.79.337. URL https://link.aps.org/doi/10.1103/PhysRevLett.79.337. (Cited on page 15.)

A. V. Buryak, Y. S. Kivshar, and D. F. Parker. Coupling between dark and bright solitons. *Physics Letters A*, 215(1-2):57–62, 1996. doi: 10.1016/0375-9601(96)00208-3. URL https://www.sciencedirect.com/science/article/abs/pii/0375960196002083. (Cited on page 7.)

T. Busch and J. R. Anglin. Motion of dark solitons in trapped Bose-Einstein condensates. *Physical Review Letters*, 84(11):2298–2301, Mar 2000. doi: 10.1103/PhysRevLett.84.2298. URL https://link.aps.org/doi/10.1103/PhysRevLett.84.2298. (Cited on page 98.)

T. Busch and J. R. Anglin. Dark-bright solitons in inhomogeneous Bose-Einstein condensates. *Physical Review Letters*, 87(1):010401, Jun 2001. doi: 10.1103/PhysRevLett.87.010401. URL http://dx.doi.org/10.1103/PhysRevLett.87.010401. (Cited on pages 7, 99, 108, and 109.)

S. Butera, M. Valiente, and P. Öhberg. Quantized vortices in interacting gauge theories. *Journal of Physics B: Atomic, Molecular and Optical Physics*, 49(1):015304, dec 2015. doi: 10.1088/0953-4075/49/1/015304. URL https://dx.doi.org/10.1088/0953-4075/49/1/015304. (Cited on page 5.)

S. Butera, M. Valiente, and P. Öhberg. Vortex dynamics in superfluids governed by an interacting gauge theory. *New Journal of Physics*, 18(8):085001, aug 2016. doi: 10.1088/1367-2630/18/8/085001. URL https://dx.doi.org/10.1088/1367-2630/18/8/085001. (Cited on page 5.)

F. Böttcher, J.-N. Schmidt, J. Hertkorn, K. S. H. Ng, S. D. Graham, M. Guo, T. Langen, and T. Pfau. New states of matter with fine-tuned interactions: quantum droplets and dipolar supersolids. *Reports on Progress in Physics*, 84(1):012403, dec 2021. doi: 10.1088/1361-6633/abc9ab. URL https://dx.doi.org/10.1088/1361-6633/abc9ab. (Cited on pages 5, 30, 37, 56, 58, 111, and 118.)

C. R. Cabrera, L. Tanzi, J. Sanz, B. Naylor, P. Thomas, P. Cheiney, and L. Tarruell. Quantum liquid droplets in a mixture of Bose-Einstein condensates. *Science*, 359(6373):301–304, 2018. doi: 10.1126/science.aao5686. URL https://www.science.org/doi/abs/10.1126/science.aao5686. (Cited on pages 5, 6, 30, 31, and 33.)

M. A. Caracanhas, P. Massignan, and A. L. Fetter. Superfluid vortex dynamics on an ellipsoid and other surfaces of revolution. *Physical Review A*, 105(2):023307, Feb 2022. doi: 10.1103/PhysRevA.105.023307. URL https://link.aps.org/doi/10.1103/PhysRevA.105.023307. (Cited on page 79.)

R. A. Carollo, D. C. Aveline, B. Rhyno, S. Vishveshwara, C. Lannert, J. D. Murphree, E. R. Elliott, J. R. Williams, R. J. Thompson, and N. Lundblad. Observation of ultracold atomic bubbles in orbital microgravity. *Nature*, 606(7913):281–286, May 2022. doi: 10.1038/s41586-022-04639-8. URL https://www.nature.com/articles/s41586-022-04639-8. (Cited on page 80.)

L. D. Carr and Y. Castin. Dynamics of a matter-wave bright soliton in an expulsive potential. *Physical Review A*, 66:063602, Dec 2002. doi: 10.1103/PhysRevA.66.063602. URL https://link.aps.org/doi/10.1103/PhysRevA.66.063602. (Cited on page 6.)

L. D. Carr, C. W. Clark, and W. P. Reinhardt. Stationary solutions of the one-dimensional nonlinear schrödinger equation. i. case of repulsive nonlinearity. *Physical Review A*, 62 (6):063610, Nov 2000a. doi: 10.1103/PhysRevA.62.063610. URL https://link.aps.org/doi/10.1103/PhysRevA.62.063610. (Cited on page 140.)

L. D. Carr, C. W. Clark, and W. P. Reinhardt. Stationary solutions of the one-dimensional nonlinear schrödinger equation. ii. case of attractive nonlinearity. *Physical Review A*, 62(6):063611, Nov 2000b. doi: 10.1103/PhysRevA.62.063611. URL https://link.aps.org/doi/10.1103/PhysRevA.62.063611. (Cited on page 140.)

L. D. Carr, M. A. Leung, and W. P. Reinhardt. Dynamics of the bose-einstein condensate: quasi-one-dimension and beyond. *Journal of Physics B: Atomic, Molecular and Optical Physics*, 33(19):3983, oct 2000c. doi: 10.1088/0953-4075/33/19/312. URL https://dx.doi.org/10.1088/0953-4075/33/19/312. (Cited on pages 6 and 7.)

L. D. Carr, D. DeMille, R. V. Krems, and J. Ye. Cold and ultracold molecules: science, technology and applications. *New Journal of Physics*, 11(5):055049, may 2009. doi: 10.1088/1367-2630/11/5/055049. URL https://dx.doi.org/10.1088/1367-2630/11/5/055049. (Cited on page 4.)

P. Cheiney, C. R. Cabrera, J. Sanz, B. Naylor, L. Tanzi, and L. Tarruell. Bright soliton to quantum droplet transition in a mixture of Bose-Einstein condensates. *Physical Review Letters*, 120(13):135301, Mar 2018. doi: 10.1103/PhysRevLett.120.135301. URL https://link.aps.org/doi/10.1103/PhysRevLett.120.135301. (Cited on pages 5, 7, 31, and 33.)

Z. Chen and H. Zhai. Collective-mode dynamics in a spin-orbit-coupled bose-einstein condensate. *Physical Review A*, 86:041604, Oct 2012. doi: 10.1103/PhysRevA.86.041604. URL https://link.aps.org/doi/10.1103/PhysRevA.86.041604. (Cited on page 5.)

Z. Chen, M. Segev, T. H. Coskun, D. N. Christodoulides, and Y. S. Kivshar. Coupled photorefractive spatial-soliton pairs. *JOSA B*, 14(11):3066–3077, 1997. doi:

10.1364/JOSAB.14.003066. URL https://opg.optica.org/josab/abstract.cfm?uri=josab-14-11-3066. (Cited on page 7.)

C. Chin, R. Grimm, P. Julienne, and E. Tiesinga. Feshbach resonances in ultracold gases. *Reviews of Modern Physics*, 82(2):1225–1286, Apr 2010. doi: 10.1103/RevModPhys.82.1225. URL https://link.aps.org/doi/10.1103/RevModPhys.82.1225. (Cited on pages 3, 16, and 71.)

C. S. Chisholm, A. Frölian, E. Neri, R. Ramos, L. Tarruell, and A. Celi. Encoding a one-dimensional topological gauge theory in a raman-coupled Bose-Einstein condensate. *Physical Review Research*, 4(4):043088, Nov 2022. doi: 10.1103/PhysRevResearch.4.043088. URL https://link.aps.org/doi/10.1103/PhysRevResearch.4.043088. (Cited on pages 4, 5, 68, 72, 73, 129, and 153.)

L. Chomaz, S. Baier, D. Petter, M. J. Mark, F. Wächtler, L. Santos, and F. Ferlaino. Quantum-fluctuation-driven crossover from a dilute Bose-Einstein condensate to a macrodroplet in a dipolar quantum fluid. *Physical Review X*, 6(4):041039, Nov 2016. doi: 10.1103/PhysRevX.6.041039. URL https://link.aps.org/doi/10.1103/PhysRevX.6.041039. (Cited on pages 5 and 112.)

L. Chomaz, D. Petter, P. Ilzhöfer, G. Natale, A. Trautmann, C. Politi, G. Durastante, R. M. W. van Bijnen, A. Patscheider, M. Sohmen, M. J. Mark, and F. Ferlaino. Long-lived and transient supersolid behaviors in dipolar quantum gases. *Physical Review X*, 9(2):021012, Apr 2019. doi: 10.1103/PhysRevX.9.021012. URL https://link.aps.org/doi/10.1103/PhysRevX.9.021012. (Cited on pages 6, 59, and 112.)

L. Chomaz, I. Ferrier-Barbut, F. Ferlaino, B. Laburthe-Tolra, B. L. Lev, and T. Pfau. Dipolar physics: a review of experiments with magnetic quantum gases. *Reports on Progress in Physics*, 86(2):026401, Dec 2022. doi: 10.1088/1361-6633/aca814. URL https://dx.doi.org/10.1088/1361-6633/aca814. (Cited on pages 4, 5, 37, 38, 39, 40, 56, 57, 58, and 111.)

S. Chu. Nobel lecture: The manipulation of neutral particles. *Rev. Mod. Phys.*, 70:685–706, Jul 1998. doi: 10.1103/RevModPhys.70.685. URL https://link.aps.org/doi/10.1103/RevModPhys.70.685. (Cited on page 1.)

M. Ciardi, F. Cinti, G. Pellicane, and S. Prestipino. Supersolid phases of bosonic particles in a bubble trap. *Physical Review Letters*, 132(2):026001, Jan 2024. doi: 10.1103/PhysRevLett.132.026001. URL https://link.aps.org/doi/10.1103/PhysRevLett.132.026001. (Cited on pages 81 and 177.)

F. Cinti and M. Boninsegni. Classical and quantum filaments in the ground state of trapped dipolar bose gases. *Physical Review A*, 96:013627, Jul 2017. doi: 10.1103/PhysRevA.96.013627. URL https://link.aps.org/doi/10.1103/PhysRevA.96.013627. (Cited on page 6.)

L. W. Clark, B. M. Anderson, L. Feng, A. Gaj, K. Levin, and C. Chin. Observation of density-dependent gauge fields in a Bose-Einstein condensate based on micromotion control in a shaken two-dimensional lattice. *Physical Review Letters*, 121(3):030402, Jul 2018. doi: 10.1103/PhysRevLett.121.030402. URL https://link.aps.org/doi/10.1103/PhysRevLett.121.030402. (Cited on pages 5 and 129.)

C. N. Cohen-Tannoudji. Nobel lecture: Manipulating atoms with photons. *Rev. Mod. Phys.*, 70:707–719, Jul 1998. doi: 10.1103/RevModPhys.70.707. URL https://link.aps.org/doi/10.1103/RevModPhys.70.707. (Cited on page 1.)

Y. Colombe, E. Knyazchyan, O. Morizot, B. Mercier, V. Lorent, and H. Perrin. Ultracold atoms confined in rf-induced two-dimensional trapping potentials. *Europhysics Letters*, 67(4):593–599, Aug 2004. doi: 10.1209/epl/i2004-10095-7. URL https://dx.doi.org/10.1209/epl/i2004-10095-7. (Cited on page 80.)

M. Cominotti, D. Rossini, M. Rizzi, F. Hekking, and A. Minguzzi. Optimal persistent currents for interacting bosons on a ring with a gauge field. *Physical Review Letters*, 113:025301, Jul 2014. doi: 10.1103/PhysRevLett.113.025301. URL https://link.aps.org/doi/10.1103/PhysRevLett.113.025301. (Cited on page 2.)

M. Cominotti, M. Rizzi, D. Rossini, D. Aghamalyan, L. Amico, L. C. Kwek, F. Hekking, and A. Minguzzi. Optimal scaling of persistent currents for interacting bosons on a ring. *The European Physical Journal Special Topics*, 224:519–524, 2015. doi: 10.1140/epjst/e2015-02381-3. URL https://link.springer.com/article/10.1140/epjst/e2015-02381-3. (Cited on page 2.)

R. Cominotti, A. Berti, A. Farolfi, A. Zenesini, G. Lamporesi, I. Carusotto, A. Recati, and G. Ferrari. Observation of massless and massive collective excitations with faraday patterns in a two-component superfluid. *Physical Review Letters*, 128(21):210401, May 2022. doi: 10.1103/PhysRevLett.128.210401. URL https://link.aps.org/doi/10.1103/PhysRevLett.128.210401. (Cited on page 164.)

G. Condon, M. Rabault, B. Barrett, L. Chichet, R. Arguel, H. Eneriz-Imaz, D. Naik, A. Bertoldi, B. Battelier, P. Bouyer, and A. Landragin. All-optical Bose-Einstein condensates in microgravity. *Physical Review Letters*, 123(24):240402, Dec 2019. doi: 10.1103/PhysRevLett.123.240402. URL https://link.aps.org/doi/10.1103/PhysRevLett.123.240402. (Cited on page 80.)

N. Cooper. Rapidly rotating atomic gases. *Advances in Physics*, 57(6):539–616, 2008. doi: 10.1080/00018730802564122. URL https://doi.org/10.1080/00018730802564122. (Cited on pages 64 and 77.)

E. A. Cornell and C. E. Wieman. Nobel lecture: Bose-einstein condensation in a dilute gas, the first 70 years and some recent experiments. *Rev. Mod. Phys.*, 74:875–893, Aug 2002. doi: 10.1103/RevModPhys.74.875. URL https://link.aps.org/doi/10.1103/RevModPhys.74.875. (Cited on page 1.)

S. L. Cornish, N. R. Claussen, J. L. Roberts, E. A. Cornell, and C. E. Wieman. Stable ^{85}Rb bose-einstein condensates with widely tunable interactions. *Physical Review Letters*, 85:1795–1798, Aug 2000. doi: 10.1103/PhysRevLett.85.1795. URL https://link.aps.org/doi/10.1103/PhysRevLett.85.1795. (Cited on page 3.)

S. L. Cornish, S. T. Thompson, and C. E. Wieman. Formation of bright matter-wave solitons during the collapse of attractive bose-einstein condensates. *Physical Review Letters*, 96:170401, May 2006. doi: 10.1103/PhysRevLett.96.170401. URL https://link.aps.org/doi/10.1103/PhysRevLett.96.170401. (Cited on page 6.)

F. Dalfovo, S. Giorgini, L. P. Pitaevskii, and S. Stringari. Theory of Bose-Einstein condensation in trapped gases. *Reviews of Modern Physics*, 71(3):463–512, Apr 1999. doi: 10.1103/RevModPhys.71.463. URL https://link.aps.org/doi/10.1103/RevModPhys.71.463. (Cited on pages 1, 2, 7, 11, 21, and 22.)

J. Dalibard. Introduction to the physics of artificial gauge fields. In *Proceedings of the International School of Physics "Enrico Fermi", Course 191 "Quantum Matter at Ultralow Temperatures"*, 2016. doi: 10.3254/978-1-61499-694-1-1. (Cited on pages 4, 62, 63, 64, 65, 68, and 69.)

J. Dalibard, F. Gerbier, G. Juzeliūnas, and P. Öhberg. Colloquium: Artificial gauge potentials for neutral atoms. *Reviews of Modern Physics*, 83(4):1523–1543, Nov 2011. doi: 10.1103/RevModPhys.83.1523. URL https://link.aps.org/doi/10.1103/RevModPhys.83.1523. (Cited on pages 4, 5, 68, 69, 70, 129, and 153.)

K. B. Davis, M. O. Mewes, M. R. Andrews, N. J. van Druten, D. S. Durfee, D. M. Kurn, and W. Ketterle. Bose-Einstein condensation in a gas of sodium atoms. *Physical Review Letters*, 75(22):3969–3973, Nov 1995. doi: 10.1103/PhysRevLett.75.3969. URL https://link.aps.org/doi/10.1103/PhysRevLett.75.3969. (Cited on pages 1 and 11.)

N. Defenu, T. Donner, T. Macrì, G. Pagano, S. Ruffo, and A. Trombettoni. Long-range interacting quantum systems. *Rev. Mod. Phys.*, 95:035002, Aug 2023. doi: 10.1103/RevModPhys.95.035002. URL https://link.aps.org/doi/10.1103/RevModPhys.95.035002. (Cited on page 4.)

J. Denschlag, J. E. Simsarian, D. L. Feder, C. W. Clark, L. A. Collins, J. Cubizolles, L. Deng, E. W. Hagley, K. Helmerson, W. P. Reinhardt, et al. Generating solitons by phase engineering of a bose-einstein condensate. *Science*, 287(5450):97–101, 2000. doi: 10.1126/science.287.5450.97. URL https://www.science.org/doi/10.1126/science.287.5450.97. (Cited on page 6.)

C. D'Errico, A. Burchianti, M. Prevedelli, L. Salasnich, F. Ancilotto, M. Modugno, F. Minardi, and C. Fort. Observation of quantum droplets in a heteronuclear bosonic mixture. *Physical Review Res.*, 1:033155, Dec 2019. doi: 10.1103/PhysRevResearch.1.033155. URL https://link.aps.org/doi/10.1103/PhysRevResearch.1.033155. (Cited on page 5.)

A. S. Desyatnikov, Y. S. Kivshar, K. Motzek, F. Kaiser, C. Weilnau, and C. Denz. Multicomponent dipole-mode spatial solitons. *Optics letters*, 27(8):634–636, 2002. doi: 10.1364/OL.27.000634. URL https://opg.optica.org/ol/abstract.cfm?uri=ol-27-8-634. (Cited on page 7.)

R. J. Dingwall and P. Öhberg. Stability of matter-wave solitons in a density-dependent gauge theory. *Physical Review A*, 99(2):023609, Feb 2019. doi: 10.1103/PhysRevA.99.023609. URL https://link.aps.org/doi/10.1103/PhysRevA.99.023609. (Cited on pages 7, 129, and 148.)

R. J. Dingwall, M. J. Edmonds, J. L. Helm, B. A. Malomed, and P. Öhberg. Non-integrable dynamics of matter-wave solitons in a density-dependent gauge theory. *New Journal of Physics*, 20(4):043004, Apr 2018. doi: 10.1088/1367-2630/aab29e. URL https://doi.org/10.1088/1367-2630/aab29e. (Cited on pages 7 and 129.)

P. C. Diniz, E. A. B. Oliveira, A. R. P. Lima, and E. A. L. Henn. Ground state and collective excitations of a dipolar Bose-Einstein condensate in a bubble trap. *Scientific Reports*, 10:4831, Mar 2020. doi: 10.1038/s41598-020-61657-0. URL http://www.nature.com/articles/s41598-020-61657-0. (Cited on pages 80 and 84.)

E. A. Donley, N. R. Claussen, S. L. Cornish, J. L. Roberts, E. A. Cornell, and C. E. Wieman. Dynamics of collapsing and exploding bose–einstein condensates. *Nature*, 412(6844):295–299, 2001. doi: 10.1038/35085500. URL https://www.nature.com/articles/35085500. (Cited on page 6.)

R. Dum and M. Olshanii. Gauge structures in atom-laser interaction: Bloch oscillations in a dark lattice. *Phys. Rev. Lett.*, 76:1788–1791, Mar 1996. doi: 10.1103/PhysRevLett.76.1788. URL https://link.aps.org/doi/10.1103/PhysRevLett.76.1788. (Cited on page 4.)

G. Durastante, C. Politi, M. Sohmen, P. Ilzhöfer, M. J. Mark, M. A. Norcia, and F. Ferlaino. Feshbach resonances in an erbium-dysprosium dipolar mixture. *Physical Review A*, 102(3):033330, Sep 2020. doi: 10.1103/PhysRevA.102.033330. URL https://link.aps.org/doi/10.1103/PhysRevA.102.033330. (Cited on pages 4 and 112.)

Z. Dutton, M. Budde, C. Slowe, and L. V. Hau. Observation of quantum shock waves created with ultra-compressed slow light pulses in a bose-einstein condensate. *Science*, 293(5530):663–668, 2001. doi: 10.1126/science.1062527. URL https://www.science.org/doi/10.1126/science.1062527. (Cited on page 6.)

C. Eberlein, S. Giovanazzi, and D. H. J. O'Dell. Exact solution of the thomas-fermi equation for a trapped Bose-Einstein condensate with dipole-dipole interactions. *Physical Review A*, 71(3):033618, Mar 2005. doi: 10.1103/PhysRevA.71.033618. URL https://link.aps.org/doi/10.1103/PhysRevA.71.033618. (Cited on page 45.)

M. J. Edmonds, M. Valiente, G. Juzeliūnas, L. Santos, and P. Öhberg. Simulating an interacting gauge theory with ultracold bose gases. *Physical Review Letters*, 110(8):

085301, Feb 2013a. doi: 10.1103/PhysRevLett.110.085301. URL https://link.aps.org/doi/10.1103/PhysRevLett.110.085301. (Cited on pages 4, 5, 7, 68, 70, 71, 72, 74, 129, and 153.)

M. J. Edmonds, M. Valiente, and P. Öhberg. On the josephson effect in a Bose–Einstein condensate subject to a density-dependent gauge potential. *Journal of Physics B: Atomic, Molecular and Optical Physics*, 46(13):134013, Jun 2013b. doi: 10.1088/0953-4075/46/13/134013. URL https://dx.doi.org/10.1088/0953-4075/46/13/134013. (Cited on pages 153 and 178.)

M. J. Edmonds, M. Valiente, and P. Öhberg. Elementary excitations of chiral Bose-Einstein condensates. *Europhysics Letters*, 110(3):36004, May 2015. doi: 10.1209/0295-5075/110/36004. URL https://doi.org/10.1209/0295-5075/110/36004. (Cited on pages 5 and 129.)

A. Einstein. Quanten theorie des einatomigen idealen gases. *Sitzungsberichte der Königlich Preussischen Akademie der Wissenschaften zu Berlin*, pages 261–267, 1924. (Cited on page 1.)

A. Einstein. Quanten theorie des einatomigen idealen gase. *Sitzungsberichte der Königlich Preussischen Akademie der Wissenschaften zu Berlin*, pages 3–14, 1925. (Cited on page 1.)

E. R. Elliott, M. C. Krutzik, J. R. Williams, R. J. Thompson, and D. C. Aveline. NASA's Cold Atom Lab (CAL): system development and ground test status. *npj Microgravity*, 4:16, May 2018. doi: 10.1038/s41526-018-0049-9. URL http://www.nature.com/articles/s41526-018-0049-9. (Cited on page 80.)

P. J. Everitt, M. A. Sooriyabandara, M. Guasoni, P. B. Wigley, C. H. Wei, G. D. McDonald, K. S. Hardman, P. Manju, J. D. Close, C. C. N. Kuhn, S. S. Szigeti, Y. S. Kivshar, and N. P. Robins. Observation of a modulational instability in Bose-Einstein condensates. *Physical Review A*, 96(4):041601, Oct 2017. doi: 10.1103/PhysRevA.96.041601. URL https://link.aps.org/doi/10.1103/PhysRevA.96.041601. (Cited on page 7.)

D. L. Feder, M. S. Pindzola, L. A. Collins, B. I. Schneider, and C. W. Clark. Dark-soliton states of bose-einstein condensates in anisotropic traps. *Physical Review A*, 62:053606, Oct 2000. doi: 10.1103/PhysRevA.62.053606. URL https://link.aps.org/doi/10.1103/PhysRevA.62.053606. (Cited on page 7.)

P. O. Fedichev, Y. Kagan, G. V. Shlyapnikov, and J. T. M. Walraven. Influence of nearly resonant light on the scattering length in low-temperature atomic gases. *Physical Review Letters*, 77:2913–2916, Sep 1996. doi: 10.1103/PhysRevLett.77.2913. URL https://link.aps.org/doi/10.1103/PhysRevLett.77.2913. (Cited on page 3.)

G. Ferioli, G. Semeghini, L. Masi, G. Giusti, G. Modugno, M. Inguscio, A. Gallemí, A. Recati, and M. Fattori. Collisions of self-bound quantum droplets. *Physical Review Letters*, 122:090401, Mar 2019. doi: 10.1103/PhysRevLett.122.090401. URL https://link.aps.org/doi/10.1103/PhysRevLett.122.090401. (Cited on page 5.)

G. Ferioli, G. Semeghini, S. Terradas-Briansó, L. Masi, M. Fattori, and M. Modugno. Dynamical formation of quantum droplets in a ^{39}K mixture. *Physical Review Research*, 2(1):013269, Mar 2020. doi: 10.1103/PhysRevResearch.2.013269. URL https://link.aps.org/doi/10.1103/PhysRevResearch.2.013269. (Cited on pages 5 and 33.)

I. Ferrier-Barbut, M. Delehaye, S. Laurent, A. T. Grier, M. Pierce, B. S. Rem, F. Chevy, and C. Salomon. A mixture of bose and fermi superfluids. *Science*, 345(6200):1035–1038, 2014. doi: 10.1126/science.1255380. URL https://www.science.org/doi/10.1126/science.1255380. (Cited on page 3.)

I. Ferrier-Barbut, H. Kadau, M. Schmitt, M. Wenzel, and T. Pfau. Observation of quantum droplets in a strongly dipolar bose gas. *Physical Review Letters*, 116(21):215301, May 2016a. doi: 10.1103/PhysRevLett.116.215301. URL https://link.aps.org/doi/10.1103/PhysRevLett.116.215301. (Cited on pages 5, 6, 56, and 57.)

I. Ferrier-Barbut, M. Schmitt, M. Wenzel, H. Kadau, and T. Pfau. Liquid quantum droplets of ultracold magnetic atoms. *Journal of Physics B: Atomic, Molecular and Optical Physics*, 49(21):214004, Oct 2016b. doi: 10.1088/0953-4075/49/21/214004. URL https://dx.doi.org/10.1088/0953-4075/49/21/214004. (Cited on pages 5 and 56.)

I. Ferrier-Barbut, M. Wenzel, F. Böttcher, T. Langen, M. Isoard, S. Stringari, and T. Pfau. Scissors mode of dipolar quantum droplets of dysprosium atoms. *Physical Review Letters*, 120:160402, Apr 2018a. doi: 10.1103/PhysRevLett.120.160402. URL https://link.aps.org/doi/10.1103/PhysRevLett.120.160402. (Cited on page 5.)

I. Ferrier-Barbut, M. Wenzel, M. Schmitt, F. Böttcher, and T. Pfau. Onset of a modulational instability in trapped dipolar Bose-Einstein condensates. *Physical Review A*, 97(1):011604, Jan 2018b. doi: 10.1103/PhysRevA.97.011604. URL https://link.aps.org/doi/10.1103/PhysRevA.97.011604. (Cited on page 59.)

G. Ferrini, A. Minguzzi, and F. W. J. Hekking. Number squeezing, quantum fluctuations, and oscillations in mesoscopic bose josephson junctions. *Physical Review A*, 78:023606, Aug 2008. doi: 10.1103/PhysRevA.78.023606. URL https://link.aps.org/doi/10.1103/PhysRevA.78.023606. (Cited on page 2.)

G. Ferrini, D. Spehner, A. Minguzzi, and F. W. J. Hekking. Noise in bose josephson junctions: Decoherence and phase relaxation. *Physical Review A*, 82:033621, Sep 2010. doi: 10.1103/PhysRevA.82.033621. URL https://link.aps.org/doi/10.1103/PhysRevA.82.033621. (Cited on page 2.)

A. L. Fetter. Rotating trapped Bose-Einstein condensates. *Reviews of Modern Physics*, 81 (2):647–691, May 2009. doi: 10.1103/RevModPhys.81.647. URL https://link.aps.org/doi/10.1103/RevModPhys.81.647. (Cited on pages 64 and 77.)

R. P. Feynman. Simulating physics with computers. *International Journal of Theoretical Physics*, 21:467–488, 1982. (Cited on page 3.)

M. Fierz. Über die relativistische theorie kräftefreier teilchen mit beliebigem spin. *Helvetica Physica Acta*, 12:3–37, 1939. (Cited on page 12.)

M. P. A. Fisher, P. B. Weichman, G. Grinstein, and D. S. Fisher. Boson localization and the superfluid-insulator transition. *Physical Review B*, 40:546–570, Jul 1989. doi: 10.1103/PhysRevB.40.546. URL https://link.aps.org/doi/10.1103/PhysRevB.40.546. (Cited on page 3.)

C. J. Foot. *Atomic physics*, volume 7. Oxford University Press, Nov 2004. (Cited on page 11.)

C. Fort and M. Modugno. Self-evaporation dynamics of quantum droplets in a 41k-87rb mixture. *Applied Sciences*, 11(2), Jan 2021. ISSN 2076-3417. doi: 10.3390/app11020866. URL https://www.mdpi.com/2076-3417/11/2/866. (Cited on pages 30 and 33.)

D. J. Frantzeskakis. Dark solitons in atomic Bose–Einstein condensates: from theory to experiments. *Journal of Physics A: Mathematical and Theoretical*, 43(21):213001, May 2010. doi: 10.1088/1751-8113/43/21/213001. URL https://dx.doi.org/10.1088/1751-8113/43/21/213001. (Cited on pages 6, 35, 97, 104, and 108.)

M. Frigo and S. Johnson. The design and implementation of fftw3. *Proceedings of the IEEE*, 93(2):216–231, 2005. doi: 10.1109/JPROC.2004.840301. (Cited on pages 41 and 83.)

A. Frölian, C. S. Chisholm, E. Neri, C. R. Cabrera, R. Ramos, A. Celi, and L. Tarruell. Realizing a 1d topological gauge theory in an optically dressed bec. *Nature*, 608(7922):293–297, Aug 2022. doi: 10.1038/s41586-022-04943-3. URL https://doi.org/10.1038/s41586-022-04943-3. (Cited on pages 4, 5, 68, 72, 73, 74, 129, 151, and 153.)

K. Frye, S. Abend, W. Bartosch, A. Bawamia, D. Becker, H. Blume, C. Braxmaier, S.-W. Chiow, M. A. Efremov, W. Ertmer, et al. The Bose-Einstein Condensate and Cold Atom Laboratory. *EPJ Quantum Technology*, 8:1–38, Jan 2021. doi: 10.1140/epjqt/s40507-020-00090-8. URL https://epjquantumtechnology.springeropen.com/articles/10.1140/epjqt/s40507-020-00090-8. (Cited on pages 80 and 85.)

A. Gallemí, S. M. Roccuzzo, S. Stringari, and A. Recati. Quantized vortices in dipolar supersolid Bose-Einstein-condensed gases. *Physical Review A*, 102(2):023322, Aug 2020. doi: 10.1103/PhysRevA.102.023322. URL https://link.aps.org/doi/10.1103/PhysRevA.102.023322. (Cited on page 6.)

A. Gallemí, A. M. Mateo, R. Mayol, and M. Guilleumas. Coherent quantum phase slip in two-component bosonic atomtronic circuits. *New Journal of Physics*, 18(1):015003, dec 2015. doi: 10.1088/1367-2630/18/1/015003. URL https://dx.doi.org/10.1088/1367-2630/18/1/015003. (Cited on page 2.)

A. Gammal, T. Frederico, and L. Tomio. Critical number of atoms for attractive bose-einstein condensates with cylindrically symmetrical traps. *Physical Review A*, 64:055602, Oct 2001. doi: 10.1103/PhysRevA.64.055602. URL https://link.aps.org/doi/10.1103/PhysRevA.64.055602. (Cited on page 6.)

R. Gao, X. Qiao, Y.-E. Ma, Y. Jian, A.-X. Zhang, and J.-K. Xue. Chiral matter-wave soliton in a Bose-Einstein condensate under density-dependent gauge potential. *Physics Letters A*, 446:128283, Sep 2022. ISSN 0375-9601. doi: 10.1016/j.physleta.2022.128283. URL https://www.sciencedirect.com/science/article/pii/S0375960122003656. (Cited on pages 7 and 129.)

B. M. Garraway and H. Perrin. Recent developments in trapping and manipulation of atoms with adiabatic potentials. *Journal of Physics B: Atomic, Molecular and Optical Physics*, 49(17):172001, Aug 2016. doi: 10.1088/0953-4075/49/17/172001. URL https://dx.doi.org/10.1088/0953-4075/49/17/172001. (Cited on pages 3 and 79.)

I. M. Georgescu, S. Ashhab, and F. Nori. Quantum simulation. *Rev. Mod. Phys.*, 86: 153–185, Mar 2014. doi: 10.1103/RevModPhys.86.153. URL https://link.aps.org/doi/10.1103/RevModPhys.86.153. (Cited on page 3.)

J. M. Gerton, D. Strekalov, I. Prodan, and R. G. Hulet. Direct observation of growth and collapse of a bose–einstein condensate with attractive interactions. *Nature*, 408(6813): 692–695, 2000. doi: 10.1038/35047030. URL https://www.nature.com/articles/35047030. (Cited on page 6.)

N. S. Ginsberg, J. Brand, and L. V. Hau. Observation of hybrid soliton vortex-ring structures in bose-einstein condensates. *Physical Review Letters*, 94:040403, Jan 2005. doi: 10.1103/PhysRevLett.94.040403. URL https://link.aps.org/doi/10.1103/PhysRevLett.94.040403. (Cited on page 6.)

S. Giorgini, L. P. Pitaevskii, and S. Stringari. Thermodynamics of a trapped Bose-condensed gas. *Journal of Low Temperature Physics*, 109(1-2):309–355, Oct 1997. ISSN 0022-2291. doi: 10.1007/BF02396737. URL http://link.springer.com/10.1007/BF02396737. (Cited on page 14.)

S. Giovanazzi, A. Görlitz, and T. Pfau. Tuning the dipolar interaction in quantum gases. *Physical Review Letters*, 89(13):130401, Sep 2002. doi: 10.1103/PhysRevLett.89.130401. URL https://link.aps.org/doi/10.1103/PhysRevLett.89.130401. (Cited on page 41.)

S. Giovanazzi, A. Görlitz, and T. Pfau. Ballistic expansion of a dipolar condensate. *Journal of Optics B: Quantum and Semiclassical Optics*, 5(2):S208, apr 2003. doi: 10.1088/1464-4266/5/2/381. URL https://dx.doi.org/10.1088/1464-4266/5/2/381. (Cited on page 47.)

R. J. Glauber. The quantum theory of optical coherence. *Physical Review*, 130:2529–2539, Jun 1963. doi: 10.1103/PhysRev.130.2529. URL https://link.aps.org/doi/10.1103/PhysRev.130.2529. (Cited on page 2.)

N. Goldman, G. Juzeliūnas, P. Öhberg, and I. B. Spielman. Light-induced gauge fields for ultracold atoms. *Reports on Progress in Physics*, 77(12):126401, Nov 2014. doi: 10.1088/0034-4885/77/12/126401. URL https://dx.doi.org/10.1088/0034-4885/77/12/126401. (Cited on pages 4, 5, 62, 64, 65, 67, 68, 69, 70, and 129.)

K. Góral and L. Santos. Ground state and elementary excitations of single and binary Bose-Einstein condensates of trapped dipolar gases. *Physical Review A*, 66(2):023613, Aug 2002. doi: 10.1103/PhysRevA.66.023613. URL https://link.aps.org/doi/10.1103/PhysRevA.66.023613. (Cited on page 47.)

K. Góral, K. Rzążewski, and T. Pfau. Bose-Einstein condensation with magnetic dipole-dipole forces. *Physical Review A*, 61(5):051601, Mar 2000. doi: 10.1103/PhysRevA.61.051601. URL https://link.aps.org/doi/10.1103/PhysRevA.61.051601. (Cited on pages 4 and 47.)

F. Görg, K. Sandholzer, J. Minguzzi, R. Desbuquois, M. Messer, and T. Esslinger. Realization of density-dependent peierls phases to engineer quantized gauge fields coupled to ultracold matter. *Nature Physics*, 15(11):1161–1167, Aug 2019. doi: 10.1038/s41567-019-0615-4. URL https://doi.org/10.1038/s41567-019-0615-4. (Cited on pages 5 and 129.)

S. A. Gredeskul and Y. S. Kivshar. Generation of dark solitons in optical fibers. *Physical Review Letters*, 62:977–977, Feb 1989. doi: 10.1103/PhysRevLett.62.977. URL https://link.aps.org/doi/10.1103/PhysRevLett.62.977. (Cited on page 6.)

S. A. Gredeskul, Y. S. Kivshar, and M. V. Yanovskaya. Dark-pulse solitons in nonlinear-optical fibers. *Physical Review A*, 41:3994–4008, Apr 1990. doi: 10.1103/PhysRevA.41.3994. URL https://link.aps.org/doi/10.1103/PhysRevA.41.3994. (Cited on page 6.)

M. Greiner, O. Mandel, T. Esslinger, T. W. Hänsch, and I. Bloch. Quantum phase transition from a superfluid to a mott insulator in a gas of ultracold atoms. *nature*, 415 (6867):39–44, 2002. (Cited on page 3.)

S. Greschner, G. Sun, D. Poletti, and L. Santos. Density-dependent synthetic gauge fields using periodically modulated interactions. *Physical Review Letters*, 113:215303, Nov 2014. doi: 10.1103/PhysRevLett.113.215303. URL https://link.aps.org/doi/10.1103/PhysRevLett.113.215303. (Cited on page 5.)

A. Griesmaier, J. Werner, S. Hensler, J. Stuhler, and T. Pfau. Bose-einstein condensation of chromium. *Physical Review Letters*, 94:160401, Apr 2005. doi: 10.1103/PhysRevLett.94.160401. URL https://link.aps.org/doi/10.1103/PhysRevLett.94.160401. (Cited on page 4.)

L. Griguolo and D. Seminara. Chiral solitons from dimensional reduction of chern-simons gauged non-linear schrödinger equation: classical and quantum aspects. *Nuclear Physics B*, 516(1):467–498, 1998. ISSN 0550-3213. doi: https://doi.org/10.1016/S0550-3213(97)00810-9. URL https://www.sciencedirect.com/science/article/pii/S0550321397008109. (Cited on pages 7, 75, and 129.)

R. Grimm, M. Weidemüller, and Y. B. Ovchinnikov. Optical dipole traps for neutral atoms. volume 42 of *Advances In Atomic, Molecular, and Optical Physics*, pages 95–170. Academic

Press, 2000. doi: https://doi.org/10.1016/S1049-250X(08)60186-X. URL https://www.sciencedirect.com/science/article/pii/S1049250X0860186X. (Cited on page 3.)

C. Gross and I. Bloch. Quantum simulations with ultracold atoms in optical lattices. *Science*, 357(6355):995–1001, 2017. doi: 10.1126/science.aal3837. URL https://www.science.org/doi/10.1126/science.aal3837. (Cited on page 3.)

E. P. Gross. Structure of a quantized vortex in boson systems. *Il Nuovo Cimento (1955-1965)*, 20(3):454–477, May 1961. doi: 10.1007/BF02731494. URL https://doi.org/10.1007/BF02731494. (Cited on pages 2 and 21.)

D. Guéry-Odelin and S. Stringari. Scissors mode and superfluidity of a trapped Bose-Einstein condensed gas. *Physical Review Letters*, 83(22):4452–4455, Nov 1999. doi: 10.1103/PhysRevLett.83.4452. URL https://link.aps.org/doi/10.1103/PhysRevLett.83.4452. (Cited on page 2.)

M. Guo, F. Böttcher, J. Hertkorn, J.-N. Schmidt, M. Wenzel, H. P. Büchler, T. Langen, and T. Pfau. The low-energy Goldstone mode in a trapped dipolar supersolid. *Nature*, 574:386, Sep 2019. doi: 10.1038/s41586-019-1569-5. URL https://doi.org/10.1038/s41586-019-1569-5. (Cited on page 112.)

Y. Guo, E. M. Gutierrez, D. Rey, T. Badr, A. Perrin, L. Longchambon, V. S. Bagnato, H. Perrin, and R. Dubessy. Expansion of a quantum gas in a shell trap. *New Journal of Physics*, 24(9):093040, oct 2022. doi: 10.1088/1367-2630/ac919f. URL https://dx.doi.org/10.1088/1367-2630/ac919f. (Cited on page 176.)

Z. Guo, F. Jia, L. Li, Y. Ma, J. M. Hutson, X. Cui, and D. Wang. Lee-huang-yang effects in the ultracold mixture of ^{23}Na and ^{87}Rb with attractive interspecies interactions. *Physical Review Res.*, 3:033247, Sep 2021. doi: 10.1103/PhysRevResearch.3.033247. URL https://link.aps.org/doi/10.1103/PhysRevResearch.3.033247. (Cited on page 5.)

S. Gupta, K. W. Murch, K. L. Moore, T. P. Purdy, and D. M. Stamper-Kurn. Bose-einstein condensation in a circular waveguide. *Physical Review Letters*, 95:143201, Sep 2005. doi: 10.1103/PhysRevLett.95.143201. URL https://link.aps.org/doi/10.1103/PhysRevLett.95.143201. (Cited on page 3.)

D. S. Hall, M. R. Matthews, J. R. Ensher, C. E. Wieman, and E. A. Cornell. Dynamics of component separation in a binary mixture of Bose-Einstein condensates. *Physical Review Letters*, 81(8):1539–1542, Aug 1998. doi: 10.1103/PhysRevLett.81.1539. URL https://link.aps.org/doi/10.1103/PhysRevLett.81.1539. (Cited on pages 3 and 7.)

C. Hamner, J. J. Chang, P. Engels, and M. A. Hoefer. Generation of dark-bright soliton trains in superfluid-superfluid counterflow. *Physical Review Letters*, 106(6):065302, Feb 2011. doi: 10.1103/PhysRevLett.106.065302. URL https://link.aps.org/doi/10.1103/PhysRevLett.106.065302. (Cited on pages 7 and 98.)

T. L. Harte, E. Bentine, K. Luksch, A. J. Barker, D. Trypogeorgos, B. Yuen, and C. J. Foot. Ultracold atoms in multiple radio-frequency dressed adiabatic potentials. *Physical Review A*, 97(1):013616, Jan 2018. doi: 10.1103/PhysRevA.97.013616. URL https://link.aps.org/doi/10.1103/PhysRevA.97.013616. (Cited on pages 3 and 79.)

K. Henderson, C. Ryu, C. MacCormick, and M. G. Boshier. Experimental demonstration of painting arbitrary and dynamic potentials for bose–einstein condensates. *New Journal of Physics*, 11(4):043030, apr 2009. doi: 10.1088/1367-2630/11/4/043030. URL https://dx.doi.org/10.1088/1367-2630/11/4/043030. (Cited on page 3.)

J. Hertkorn, F. Böttcher, M. Guo, J. N. Schmidt, T. Langen, H. P. Büchler, and T. Pfau. Fate of the amplitude mode in a trapped dipolar supersolid. *Physical Review Letters*, 123(19):193002, Nov 2019. doi: 10.1103/PhysRevLett.123.193002. URL https://link.aps.org/doi/10.1103/PhysRevLett.123.193002. (Cited on page 6.)

J. Hertkorn, J.-N. Schmidt, M. Guo, F. Böttcher, K. S. H. Ng, S. D. Graham, P. Uerlings, H. P. Büchler, T. Langen, M. Zwierlein, and T. Pfau. Supersolidity in two-dimensional trapped dipolar droplet arrays. *Physical Review Letters*, 127(15):155301, Oct 2021a. doi: 10.1103/PhysRevLett.127.155301. URL https://link.aps.org/doi/10.1103/PhysRevLett.127.155301. (Cited on page 60.)

J. Hertkorn, J.-N. Schmidt, M. Guo, F. Böttcher, K. S. H. Ng, S. D. Graham, P. Uerlings, T. Langen, M. Zwierlein, and T. Pfau. Pattern formation in quantum ferrofluids: From supersolids to superglasses. *Physical Review Research*, 3(3):033125, Aug 2021b. doi: 10.1103/PhysRevResearch.3.033125. URL https://link.aps.org/doi/10.1103/PhysRevResearch.3.033125. (Cited on pages 60 and 112.)

F. T. Hioe. Solitary waves for N coupled nonlinear schrödinger equations. *Physical Review Letters*, 82:1152–1155, Feb 1999. doi: 10.1103/PhysRevLett.82.1152. URL https://link.aps.org/doi/10.1103/PhysRevLett.82.1152. (Cited on page 7.)

M. A. Hoefer, J. J. Chang, C. Hamner, and P. Engels. Dark-dark solitons and modulational instability in miscible two-component Bose-Einstein condensates. *Physical Review A*, 84(4):041605, Oct 2011. doi: 10.1103/PhysRevA.84.041605. URL https://link.aps.org/doi/10.1103/PhysRevA.84.041605. (Cited on pages 7 and 98.)

H. Hu and X.-J. Liu. Collective excitations of a spherical ultradilute quantum droplet. *Physical Review A*, 102(5):053303, Nov 2020. doi: 10.1103/PhysRevA.102.053303. URL https://link.aps.org/doi/10.1103/PhysRevA.102.053303. (Cited on page 33.)

D. A. W. Hutchinson and E. Zaremba. Excitations of a bose-condensed gas in anisotropic traps. *Phys. Rev. A*, 57:1280–1285, Feb 1998. doi: 10.1103/PhysRevA.57.1280. URL https://link.aps.org/doi/10.1103/PhysRevA.57.1280. (Cited on page 2.)

M. Šindik, A. Recati, S. M. Roccuzzo, L. Santos, and S. Stringari. Creation and robustness of quantized vortices in a dipolar supersolid when crossing the superfluid-to-supersolid transition. *Phys. Rev. A*, 106(6):L061303, Dec 2022. doi: 10.1103/PhysRevA.

106.L061303. URL https://link.aps.org/doi/10.1103/PhysRevA.106.L061303. (Cited on page 6.)

R. Inoue, Y. Miyazawa, and M. Kozuma. Magneto-optical trapping of optically pumped metastable europium. *Physical Review A*, 97:061607, Jun 2018. doi: 10.1103/PhysRevA.97.061607. URL https://link.aps.org/doi/10.1103/PhysRevA.97.061607. (Cited on page 4.)

R. Jackiw. A nonrelativistic chiral soliton in one dimension. *Nonlinear Math. Phys.*, 4 (3-4):261–270, Nov 1997. doi: 10.2991/jnmp.1997.4.3-4.2. URL https://doi.org/10.2991/jnmp.1997.4.3-4.2. (Cited on pages 73, 75, 76, 129, and 153.)

J. D. Jackson and L. B. Okun. Historical roots of gauge invariance. *Reviews of Modern Physics*, 73(3):663–680, Sep 2001. doi: 10.1103/RevModPhys.73.663. URL https://link.aps.org/doi/10.1103/RevModPhys.73.663. (Cited on page 67.)

D. Jaksch, C. Bruder, J. I. Cirac, C. W. Gardiner, and P. Zoller. Cold bosonic atoms in optical lattices. *Physical Review Letters*, 81:3108–3111, Oct 1998. doi: 10.1103/PhysRevLett.81.3108. URL https://link.aps.org/doi/10.1103/PhysRevLett.81.3108. (Cited on page 3.)

D. M. Jezek, M. Barranco, M. Guilleumas, R. Mayol, and M. Pi. K-rb Fermi-Bose mixtures: Vortex states and sag. *Physical Review A*, 70(4):043630, Oct 2004. doi: 10.1103/PhysRevA.70.043630. URL https://link.aps.org/doi/10.1103/PhysRevA.70.043630. (Cited on page 85.)

F. Jia, Z. Huang, L. Qiu, R. Zhou, Y. Yan, and D. Wang. Expansion dynamics of a shell-shaped Bose-Einstein condensate. *Physical Review Letters*, 129(24):243402, Dec 2022a. doi: 10.1103/PhysRevLett.129.243402. URL https://link.aps.org/doi/10.1103/PhysRevLett.129.243402. (Cited on page 80.)

Q. Jia, H. Qiu, and A. Muñoz Mateo. Soliton collisions in Bose-Einstein condensates with current-dependent interactions. *Physical Review A*, 106(6):063314, Dec 2022b. doi: 10.1103/PhysRevA.106.063314. URL https://link.aps.org/doi/10.1103/PhysRevA.106.063314. (Cited on pages 7, 129, and 132.)

D. S. Jin, J. R. Ensher, M. R. Matthews, C. E. Wieman, and E. A. Cornell. Collective excitations of a bose-einstein condensate in a dilute gas. *Physical Review Letters*, 77:420–423, Jul 1996. doi: 10.1103/PhysRevLett.77.420. URL https://link.aps.org/doi/10.1103/PhysRevLett.77.420. (Cited on page 2.)

B. Josephson. Possible new effects in superconductive tunnelling. *Physics Letters*, 1(7):251–253, 1962. ISSN 0031-9163. doi: https://doi.org/10.1016/0031-9163(62)91369-0. URL https://www.sciencedirect.com/science/article/pii/0031916362913690. (Cited on page 2.)

H. Kadau, M. Schmitt, M. Wenzel, C. Wink, T. Maier, I. Ferrier-Barbut, and T. Pfau. Observing the Rosensweig instability of a quantum ferrofluid. *Nature*, 530(7589):

194–197, Feb 2016. doi: 10.1038/nature16485. URL https://doi.org/10.1038/nature16485. (Cited on pages 5, 6, 56, 58, and 112.)

Y. Kagan, B. Svistunov, and G. Shlyapnikov. Effect of bose condensation on inelastic processes in gases. *JETP Lett*, 42(4), 1985. (Cited on page 15.)

R. Kanamoto, L. D. Carr, and M. Ueda. Metastable quantum phase transitions in a periodic one-dimensional bose gas: Mean-field and bogoliubov analyses. *Physical Review A*, 79(6):063616, Jun 2009. doi: 10.1103/PhysRevA.79.063616. URL https://link.aps.org/doi/10.1103/PhysRevA.79.063616. (Cited on pages 130 and 140.)

G. C. Katsimiga, S. I. Mistakidis, T. M. Bersano, M. K. H. Ome, S. M. Mossman, K. Mukherjee, P. Schmelcher, P. Engels, and P. G. Kevrekidis. Observation and analysis of multiple dark-antidark solitons in two-component Bose-Einstein condensates. *Physical Review A*, 102(2):023301, Aug 2020. ISSN 2469-9926. doi: 10.1103/PhysRevA.102.023301. URL https://link.aps.org/doi/10.1103/PhysRevA.102.023301. (Cited on pages 3, 7, 102, and 110.)

V. M. Kaurov and A. B. Kuklov. Josephson vortex between two atomic Bose-Einstein condensates. *Physical Review A*, 71(1):011601, Jan 2005. doi: 10.1103/PhysRevA.71.011601. URL https://link.aps.org/doi/10.1103/PhysRevA.71.011601. (Cited on pages 7, 171, and 172.)

V. M. Kaurov and A. B. Kuklov. Atomic josephson vortices. *Physical Review A*, 73(1):013627, Jan 2006. doi: 10.1103/PhysRevA.73.013627. URL https://link.aps.org/doi/10.1103/PhysRevA.73.013627. (Cited on pages 7 and 171.)

Y. Kawaguchi and M. Ueda. Spinor Bose–Einstein condensates. *Physics Reports*, 520(5):253–381, 2012. doi: 10.1016/j.physrep.2012.07.005. URL https://www.sciencedirect.com/science/article/abs/pii/S0370157312002098. (Cited on page 3.)

T. Keilmann, S. Lanzmich, I. McCulloch, and M. Roncaglia. Statistically induced phase transitions and anyons in 1d optical lattices. *Nature communications*, 2(1):361, Jun 2011. doi: 10.1038/ncomms1353. URL https://www.nature.com/articles/ncomms1353. (Cited on page 68.)

W. Ketterle. Nobel lecture: When atoms behave as waves: Bose-einstein condensation and the atom laser. *Rev. Mod. Phys.*, 74:1131–1151, Nov 2002. doi: 10.1103/RevModPhys.74.1131. URL https://link.aps.org/doi/10.1103/RevModPhys.74.1131. (Cited on page 1.)

W. Ketterle and N. Van Druten. Evaporative cooling of trapped atoms. In *Advances in atomic, molecular, and optical physics*, volume 37, pages 181–236. Elsevier, 1996. doi: 10.1016/S1049-250X(08)60101-9. URL https://doi.org/10.1016/S1049-250X(08)60101-9. (Cited on page 1.)

P. Kevrekidis and D. Frantzeskakis. Solitons in coupled nonlinear schrödinger models: A survey of recent developments. *Reviews in Physics*, 1:140–153, 2016. ISSN 2405-4283.

doi: 10.1016/j.revip.2016.07.002. URL https://www.sciencedirect.com/science/article/pii/S2405428316300132. (Cited on page 98.)

P. G. Kevrekidis, D. J. Frantzeskakis, and R. Carretero-González. *Emergent Nonlinear Phenomena in Bose-Einstein Condensates: Theory and Experiment*. Springer Series on Atomic, Optical and Plasma Physics, 45. Springer-Verlag, Nov 2010. doi: 10.1007/978-3-540-73591-5. URL https://doi.org/10.1007/978-3-540-73591-5. (Cited on pages 6 and 97.)

P. G. Kevrekidis, D. J. Frantzeskakis, and R. Carretero-González. *The defocusing nonlinear Schrödinger equation: from dark solitons to vortices and vortex rings*. SIAM, 2015. (Cited on page 6.)

L. Khaykovich, F. Schreck, G. Ferrari, T. Bourdel, J. Cubizolles, L. D. Carr, Y. Castin, and C. Salomon. Formation of a matter-wave bright soliton. *Science*, 296(5571):1290–1293, 2002. doi: 10.1126/science.1071021. URL https://www.science.org/doi/10.1126/science.1071021. (Cited on page 6.)

H. Kiehn, S. I. Mistakidis, G. C. Katsimiga, and P. Schmelcher. Spontaneous generation of dark-bright and dark-antidark solitons upon quenching a particle-imbalanced bosonic mixture. *Physical Review A*, 100(2):023613, Aug 2019. ISSN 2469-9926. doi: 10.1103/PhysRevA.100.023613. URL https://link.aps.org/doi/10.1103/PhysRevA.100.023613. (Cited on page 7.)

W. Kirkby, T. Bland, F. Ferlaino, and R. N. Bisset. Spin rotons and supersolids in binary antidipolar condensates. *SciPost Phys. Core*, 6:084, Dec 2023. doi: 10.21468/SciPostPhysCore.6.4.084. URL https://scipost.org/10.21468/SciPostPhysCore.6.4.084. (Cited on pages 41 and 112.)

C. Kittel. *Introduction to Solid State Physics*. Wiley, 8 edition, 2004. ISBN 9780471415268. (Cited on pages 111 and 112.)

Y. S. Kivshar and S. K. Turitsyn. Vector dark solitons. *Optics letters*, 18(5):337–339, 1993. doi: 10.1364/OL.18.000337. URL https://opg.optica.org/ol/abstract.cfm?uri=ol-18-5-337. (Cited on page 7.)

Y. S. Kivshar and X. Yang. Perturbation-induced dynamics of dark solitons. *Physical Review E*, 49(2):1657–1670, Feb 1994. doi: 10.1103/PhysRevE.49.1657. URL https://link.aps.org/doi/10.1103/PhysRevE.49.1657. (Cited on page 102.)

L. Klaus, T. Bland, E. Poli, C. Politi, G. Lamporesi, E. Casotti, R. N. Bisset, M. J. Mark, and F. Ferlaino. Observation of vortices and vortex stripes in a dipolar condensate. *Nature Physics*, 18(12):1453–1458, Oct 2022. doi: 10.1038/s41567-022-01793-8. URL https://www.nature.com/articles/s41567-022-01793-8. (Cited on page 6.)

T. Koch, T. Lahaye, J. Metz, B. Fröhlich, A. Griesmaier, and T. Pfau. Stabilization of a purely dipolar quantum gas against collapse. *Nature physics*, 4(3):218–222, Feb

2008. doi: 10.1038/nphys887. URL https://doi.org/10.1038/nphys887. (Cited on pages 47, 50, and 95.)

V. V. Konotop and L. Pitaevskii. Landau dynamics of a grey soliton in a trapped condensate. *Physical Review Letters*, 93(24):240403, 2004. doi: 10.1103/PhysRevLett.93.240403. URL http://dx.doi.org/10.1103/PhysRevLett.93.240403. (Cited on pages 102 and 103.)

V. V. Konotop and V. E. Vekslerchik. Direct perturbation theory for dark solitons. *Physical Review E*, 49:2397–2407, Mar 1994. doi: 10.1103/PhysRevE.49.2397. URL https://link.aps.org/doi/10.1103/PhysRevE.49.2397. (Cited on page 6.)

A. Kumar, R. Dubessy, T. Badr, C. De Rossi, M. de Goër de Herve, L. Longchambon, and H. Perrin. Producing superfluid circulation states using phase imprinting. *Physical Review A*, 97:043615, Apr 2018. doi: 10.1103/PhysRevA.97.043615. URL https://link.aps.org/doi/10.1103/PhysRevA.97.043615. (Cited on page 2.)

T. Lahaye, T. Koch, B. Fröhlich, M. Fattori, J. Metz, A. Griesmaier, S. Giovanazzi, and T. Pfau. Strong dipolar effects in a quantum ferrofluid. *Nature*, 448(7154):672–675, Aug 2007. doi: 10.1038/nature06036. URL https://www.nature.com/articles/nature06036. (Cited on page 95.)

T. Lahaye, C. Menotti, L. Santos, M. Lewenstein, and T. Pfau. The physics of dipolar bosonic quantum gases. *Reports on Progress in Physics*, 72(12):126401, Nov 2009. doi: 10.1088/0034-4885/72/12/126401. URL https://dx.doi.org/10.1088/0034-4885/72/12/126401. (Cited on pages 4, 37, 38, 39, 40, 52, 80, and 84.)

T. Lancaster and S. J. Blundell. *Quantum Field Theory for the Gifted Amateur*. Oxford University Press, 2014. doi: 10.1093/acprof:oso/9780199699322.001.0001. URL https://doi.org/10.1093/acprof:oso/9780199699322.001.0001. (Cited on page 62.)

C. Lannert, T.-C. Wei, and S. Vishveshwara. Dynamics of condensate shells: Collective modes and expansion. *Physical Review A*, 75(1):013611, Jan 2007. doi: 10.1103/PhysRevA.75.013611. URL https://link.aps.org/doi/10.1103/PhysRevA.75.013611. (Cited on page 79.)

K. J. H. Law, P. G. Kevrekidis, and L. S. Tuckerman. Stable vortex–bright-soliton structures in two-component Bose-Einstein condensates. *Physical Review Letters*, 105 (16):160405, Oct 2010. doi: 10.1103/PhysRevLett.105.160405. URL https://link.aps.org/doi/10.1103/PhysRevLett.105.160405. (Cited on page 7.)

A.-C. Lee, D. Baillie, P. B. Blakie, and R. N. Bisset. Miscibility and stability of dipolar bosonic mixtures. *Physical Review A*, 103:063301, Jun 2021. doi: 10.1103/PhysRevA.103.063301. URL https://link.aps.org/doi/10.1103/PhysRevA.103.063301. (Cited on page 4.)

A.-C. Lee, D. Baillie, and P. B. Blakie. Stability of a flattened dipolar binary condensate: Emergence of the spin roton. *Physical Review Research*, 4(3):033153, Aug

2022. doi: 10.1103/PhysRevResearch.4.033153. URL https://link.aps.org/doi/10.1103/PhysRevResearch.4.033153. (Cited on pages 112 and 122.)

K. L. Lee, N. B. Jørgensen, I.-K. Liu, L. Wacker, J. J. Arlt, and N. P. Proukakis. Phase separation and dynamics of two-component Bose-Einstein condensates. *Physical Review A*, 94(1):013602, Jul 2016. doi: 10.1103/PhysRevA.94.013602. URL https://link.aps.org/doi/10.1103/PhysRevA.94.013602. (Cited on page 110.)

T. D. Lee and C. N. Yang. Many-body problem in quantum mechanics and quantum statistical mechanics. *Phys. Rev.*, 105(3):1119–1120, Feb 1957. doi: 10.1103/PhysRev.105.1119. URL https://link.aps.org/doi/10.1103/PhysRev.105.1119. (Cited on page 24.)

T. D. Lee, K. Huang, and C. N. Yang. Eigenvalues and eigenfunctions of a bose system of hard spheres and its low-temperature properties. *Phys. Rev.*, 106(6):1135–1145, Jun 1957. doi: 10.1103/PhysRev.106.1135. URL https://link.aps.org/doi/10.1103/PhysRev.106.1135. (Cited on page 24.)

A. J. Leggett. Can a solid be "superfluid"? *Physical Review Letters*, 25(22):1543–1546, Nov 1970. doi: 10.1103/PhysRevLett.25.1543. URL https://link.aps.org/doi/10.1103/PhysRevLett.25.1543. (Cited on page 121.)

A. J. Leggett. Bose-Einstein condensation in the alkali gases: Some fundamental concepts. *Reviews of Modern Physics*, 73(2):307–356, Apr 2001. doi: 10.1103/RevModPhys.73.307. URL https://link.aps.org/doi/10.1103/RevModPhys.73.307. (Cited on pages 1, 7, 11, and 20.)

S. Levy, E. Lahoud, I. Shomroni, and J. Steinhauer. The ac and dc josephson effects in a bose–einstein condensate. *Nature*, 449(7162):579–583, 2007. (Cited on page 2.)

M. Lewenstein, A. Sanpera, and V. Ahufinger. *Ultracold Atoms in Optical Lattices: Simulating quantum many-body systems*. Oxford University Press, Mar 2012. ISBN 9780199573127. doi: 10.1093/acprof:oso/9780199573127.001.0001. URL https://doi.org/10.1093/acprof:oso/9780199573127.001.0001. (Cited on pages 3 and 14.)

J.-R. Li, J. Lee, W. Huang, S. Burchesky, B. Shteynas, F. Ç. Top, A. O. Jamison, and W. Ketterle. A stripe phase with supersolid properties in spin–orbit-coupled Bose–Einstein condensates. *Nature*, 543(7643):91–94, Mar 2017. doi: 10.1038/nature21431. URL https://doi.org/10.1038/nature21431. (Cited on pages 6 and 60.)

S. Li, U. N. Le, and H. Saito. Long-lifetime supersolid in a two-component dipolar Bose-Einstein condensate. *Physical Review A*, 105(6):L061302, Jun 2022. doi: 10.1103/PhysRevA.105.L061302. URL https://link.aps.org/doi/10.1103/PhysRevA.105.L061302. (Cited on pages 112 and 120.)

A. R. P. Lima and A. Pelster. Quantum fluctuations in dipolar bose gases. *Physical Review A*, 84(4):041604, Oct 2011. doi: 10.1103/PhysRevA.84.041604. URL https://link.aps.org/doi/10.1103/PhysRevA.84.041604. (Cited on pages 6 and 55.)

A. R. P. Lima and A. Pelster. Beyond mean-field low-lying excitations of dipolar bose gases. *Physical Review A*, 86(6):063609, Dec 2012. doi: 10.1103/PhysRevA.86.063609. URL https://link.aps.org/doi/10.1103/PhysRevA.86.063609. (Cited on pages 6 and 55.)

Y.-J. Lin, R. L. Compton, K. Jiménez-García, J. V. Porto, and I. B. Spielman. Synthetic magnetic fields for ultracold neutral atoms. *Nature*, 462(7273):628–632, 2009. doi: 10.1038/nature08609. URL https://www.nature.com/articles/nature08609. (Cited on page 5.)

Y.-J. Lin, K. Jiménez-García, and I. B. Spielman. Spin–orbit-coupled bose–einstein condensates. *Nature*, 471(7336):83–86, 2011. doi: 10.1038/nature09887. URL https://www.nature.com/articles/nature09887. (Cited on pages 3 and 5.)

H.-Y. Lu, H. Lu, J.-N. Zhang, R.-Z. Qiu, H. Pu, and S. Yi. Spatial density oscillations in trapped dipolar condensates. *Physical Review A*, 82(2):023622, Aug 2010a. doi: 10.1103/PhysRevA.82.023622. URL https://link.aps.org/doi/10.1103/PhysRevA.82.023622. (Cited on page 42.)

M. Lu, S. H. Youn, and B. L. Lev. Trapping ultracold dysprosium: A highly magnetic gas for dipolar physics. *Physical Review Letters*, 104:063001, Feb 2010b. doi: 10.1103/PhysRevLett.104.063001. URL https://link.aps.org/doi/10.1103/PhysRevLett.104.063001. (Cited on page 4.)

M. Lu, N. Q. Burdick, S. H. Youn, and B. L. Lev. Strongly dipolar Bose-Einstein condensate of dysprosium. *Physical Review Letters*, 107(19):190401, Oct 2011. doi: 10.1103/PhysRevLett.107.190401. URL https://link.aps.org/doi/10.1103/PhysRevLett.107.190401. (Cited on pages 4 and 95.)

N. Lundblad, R. A. Carollo, C. Lannert, M. J. Gold, X. Jiang, D. Paseltiner, N. Sergay, and D. C. Aveline. Shell potentials for microgravity Bose-Einstein condensates. *npj Microgravity*, 5:30, Dec 2019. doi: 10.1038/s41526-019-0087-y. URL http://www.nature.com/articles/s41526-019-0087-y. (Cited on pages 80 and 85.)

R. Löw, H. Weimer, J. Nipper, J. B. Balewski, B. Butscher, H. P. Büchler, and T. Pfau. An experimental and theoretical guide to strongly interacting rydberg gases. *Journal of Physics B: Atomic, Molecular and Optical Physics*, 45(11):113001, may 2012. doi: 10.1088/0953-4075/45/11/113001. URL https://dx.doi.org/10.1088/0953-4075/45/11/113001. (Cited on page 4.)

M. Ma and Z. Huang. Bright soliton solution of a gross–pitaevskii equation. *Applied Mathematics Letters*, 26(7):718–724, 2013. ISSN 0893-9659. doi: https://doi.org/10.1016/j.aml.2013.02.002. URL https://www.sciencedirect.com/science/article/pii/S0893965913000591. (Cited on page 6.)

A. Macia, J. Sánchez-Baena, J. Boronat, and F. Mazzanti. Droplets of trapped quantum dipolar bosons. *Physical Review Letters*, 117:205301, Nov 2016. doi: 10.1103/

PhysRevLett.117.205301. URL https://link.aps.org/doi/10.1103/PhysRevLett.117.205301. (Cited on page 6.)

S. Manakov. Nonlinear fraunhofer diffraction. *Soviet Physics JETP*, 65(4):10, 1973. (Cited on page 7.)

O. M. Maragò, S. A. Hopkins, J. Arlt, E. Hodby, G. Hechenblaikner, and C. J. Foot. Observation of the scissors mode and evidence for superfluidity of a trapped Bose-Einstein condensed gas. *Physical Review Letters*, 84(10):2056–2059, Mar 2000. doi: 10.1103/PhysRevLett.84.2056. URL https://link.aps.org/doi/10.1103/PhysRevLett.84.2056. (Cited on page 2.)

A. L. Marchant, T. P. Billam, T. P. Wiles, M. M. H. Yu, S. A. Gardiner, and S. L. Cornish. Controlled formation and reflection of a bright solitary matter-wave. *Nature Communications*, 4:1865, May 2013. doi: 10.1038/ncomms2893. URL https://doi.org/10.1038/ncomms2893. (Cited on page 6.)

A. D. Martin and P. B. Blakie. Stability and structure of an anisotropically trapped dipolar Bose-Einstein condensate: Angular and linear rotons. *Physical Review A*, 86(5):053623, Nov 2012. doi: 10.1103/PhysRevA.86.053623. URL https://link.aps.org/doi/10.1103/PhysRevA.86.053623. (Cited on page 48.)

E. A. Martinez, C. A. Muschik, P. Schindler, D. Nigg, A. Erhard, M. Heyl, P. Hauke, M. Dalmonte, T. Monz, P. Zoller, et al. Real-time dynamics of lattice gauge theories with a few-qubit quantum computer. *Nature*, 534(7608):516–519, 2016. doi: 10.1038/nature18318. URL https://www.nature.com/articles/nature18318. (Cited on page 5.)

G. I. Martone, Y. Li, and S. Stringari. Approach for making visible and stable stripes in a spin-orbit-coupled bose-einstein superfluid. *Physical Review A*, 90:041604, Oct 2014. doi: 10.1103/PhysRevA.90.041604. URL https://link.aps.org/doi/10.1103/PhysRevA.90.041604. (Cited on page 6.)

M. R. Matthews, B. P. Anderson, P. C. Haljan, D. S. Hall, M. J. Holland, J. E. Williams, C. E. Wieman, and E. A. Cornell. Watching a superfluid untwist itself: Recurrence of rabi oscillations in a Bose-Einstein condensate. *Physical Review Letters*, 83(17):3358–3361, Oct 1999. doi: 10.1103/PhysRevLett.83.3358. URL https://link.aps.org/doi/10.1103/PhysRevLett.83.3358. (Cited on pages 3 and 29.)

J. J. McClelland and J. L. Hanssen. Laser cooling without repumping: A magneto-optical trap for erbium atoms. *Physical Review Letters*, 96:143005, Apr 2006. doi: 10.1103/PhysRevLett.96.143005. URL https://link.aps.org/doi/10.1103/PhysRevLett.96.143005. (Cited on page 4.)

M. Meister, A. Roura, E. M. Rasel, and W. P. Schleich. The space atom laser: an isotropic source for ultra-cold atoms in microgravity. *New Journal of Physics*, 21:013039, Jan 2019. doi: 10.1088/1367-2630/aaf7b5. URL https://iopscience.iop.org/article/10.1088/1367-2630/aaf7b5. (Cited on page 80.)

M. Melé-Messeguer, B. Juliá-Díaz, M. Guilleumas, A. Polls, and A. Sanpera. Weakly linked binary mixtures of f= 1 87rb bose–einstein condensates. *New Journal of Physics*, 13(3):033012, 2011. (Cited on page 2.)

K. Merloti, R. Dubessy, L. Longchambon, A. Perrin, P.-E. Pottie, V. Lorent, and H. Perrin. A two-dimensional quantum gas in a magnetic trap. *New Journal of Physics*, 15:033007, Mar 2013. doi: 10.1088/1367-2630/15/3/033007. URL https://iopscience.iop.org/article/10.1088/1367-2630/15/3/033007. (Cited on page 79.)

H. J. Metcalf and P. Van der Straten. *Laser cooling and trapping*. Springer Science & Business Media, 1999. doi: 10.1007/978-1-4612-1470-0. URL https://link.springer.com/book/10.1007/978-1-4612-1470-0. (Cited on page 1.)

M.-O. Mewes, M. R. Andrews, N. J. van Druten, D. M. Kurn, D. S. Durfee, C. G. Townsend, and W. Ketterle. Collective excitations of a bose-einstein condensate in a magnetic trap. *Physical Review Letters*, 77:988–991, Aug 1996. doi: 10.1103/PhysRevLett.77.988. URL https://link.aps.org/doi/10.1103/PhysRevLett.77.988. (Cited on page 2.)

J. Miao, J. Hostetter, G. Stratis, and M. Saffman. Magneto-optical trapping of holmium atoms. *Physical Review A*, 89:041401, Apr 2014. doi: 10.1103/PhysRevA.89.041401. URL https://link.aps.org/doi/10.1103/PhysRevA.89.041401. (Cited on page 4.)

S. Middelkamp, J. J. Chang, C. Hammer, R. Carretero-González, P. G. Kevrekidis, V. Achilleos, D. J. Frantzeskakis, P. Schmelcher, and P. Engels. Dynamics of dark–bright solitons in cigar shaped Bose–Einstein condensates. *Physics Letters A*, 375(3):642–646, Jan 2011. ISSN 0375-9601. doi: https://doi.org/10.1016/j.physleta.2010.11.025. URL https://www.sciencedirect.com/science/article/pii/S0375960110014738. (Cited on pages 7, 98, and 99.)

F. Migliaccio et al. Mocass: A satellite mission concept using cold atom interferometry for measuring the earth gravity field. *Surveys in Geophysics*, 40:1029–1053, Aug 2019. doi: 10.1007/s10712-019-09566-4. URL http://link.springer.com/10.1007/s10712-019-09566-4. (Cited on page 96.)

M. Mitchell and M. Segev. Self-trapping of incoherent white light. *Nature*, 387(6636):880–883, 1997. doi: 10.1038/43136. URL https://www.nature.com/articles/43136. (Cited on page 7.)

G. Modugno, M. Modugno, F. Riboli, G. Roati, and M. Inguscio. Two atomic species superfluid. *Physical Review Letters*, 89:190404, Oct 2002. doi: 10.1103/PhysRevLett.89.190404. URL https://link.aps.org/doi/10.1103/PhysRevLett.89.190404. (Cited on page 3.)

M. Modugno, L. Pricoupenko, and Y. Castin. Bose-Einstein condensates with a bent vortex in rotating traps. *Eur. Phys. J. D*, 22(2):235–257, Feb 2003. ISSN 1434-6079. doi: 10.1140/epjd/e2003-00015-y. URL https://doi.org/10.1140/epjd/e2003-00015-y. (Cited on page 101.)

A. J. Moerdijk, B. J. Verhaar, and A. Axelsson. Resonances in ultracold collisions of ^{6}Li, ^{7}Li, and ^{23}Na. *Physical Review A*, 51(6):4852–4861, Jun 1995. doi: 10.1103/PhysRevA.51.4852. URL https://link.aps.org/doi/10.1103/PhysRevA.51.4852. (Cited on page 16.)

N. S. Móller, F. E. A. dos Santos, V. S. Bagnato, and A. Pelster. Bose–Einstein condensation on curved manifolds. *New Journal of Physics*, 22:063059, Jun 2020. doi: 10.1088/1367-2630/ab91fb. URL https://doi.org/10.1088/1367-2630/ab91fb. (Cited on page 79.)

I. Morera, A. Muñoz Mateo, A. Polls, and B. Juliá-Díaz. Dark-dark-soliton dynamics in two density-coupled Bose-Einstein condensates. *Physical Review A*, 97(4):043621, Apr 2018. doi: 10.1103/PhysRevA.97.043621. URL https://link.aps.org/doi/10.1103/PhysRevA.97.043621. (Cited on page 7.)

I. Morera-Navarro, M. Guilleumas, R. Mayol, and A. Muñoz Mateo. Bound states of dark solitons and vortices in trapped multidimensional Bose-Einstein condensates. *Physical Review A*, 98(4):043612, Oct 2018. doi: 10.1103/PhysRevA.98.043612. URL https://link.aps.org/doi/10.1103/PhysRevA.98.043612. (Cited on page 7.)

O. Morizot, Y. Colombe, V. Lorent, H. Perrin, and B. M. Garraway. Ring trap for ultracold atoms. *Physical Review A*, 74:023617, Aug 2006. doi: 10.1103/PhysRevA.74.023617. URL https://link.aps.org/doi/10.1103/PhysRevA.74.023617. (Cited on page 3.)

S. A. Moses, J. P. Covey, M. T. Miecnikowski, D. S. Jin, and J. Ye. New frontiers for quantum gases of polar molecules. *Nature Physics*, 13(1):13–20, 2017. doi: 10.1038/nphys3985. URL https://www.nature.com/articles/nphys3985. (Cited on page 4.)

A. Mosk, S. Kraft, M. Mudrich, K. Singer, W. Wohlleben, R. Grimm, and M. Weidemüller. Mixture of ultracold lithium and cesium atoms in an optical dipole trap. *Applied Physics B*, 73:791–799, 2001. doi: 10.1007/s003400100743. URL https://link.springer.com/article/10.1007/s003400100743. (Cited on page 3.)

A. Muñoz Mateo, A. Gallemí, M. Guilleumas, and R. Mayol. Persistent currents supported by solitary waves in toroidal Bose-Einstein condensates. *Physical Review A*, 91(6):063625, Jun 2015. doi: 10.1103/PhysRevA.91.063625. URL https://link.aps.org/doi/10.1103/PhysRevA.91.063625. (Cited on pages 2 and 105.)

K. Mukherjee, M. N. Tengstrand, T. A. Cardinale, and S. M. Reimann. Supersolid stacks in antidipolar bose-einstein condensates. *Physical Review A*, 108:023302, Aug 2023. doi: 10.1103/PhysRevA.108.023302. URL https://link.aps.org/doi/10.1103/PhysRevA.108.023302. (Cited on page 41.)

H. Müntinga, H. Ahlers, M. Krutzik, A. Wenzlawski, S. Arnold, D. Becker, K. Bongs, H. Dittus, H. Duncker, N. Gaaloul, et al. Interferometry with Bose-Einstein condensates in microgravity. *Physical Review Letters*, 110(9):093602, Feb 2013. doi: 10.1103/PhysRevLett.110.093602. URL https://link.aps.org/doi/10.1103/PhysRevLett.110.093602. (Cited on page 80.)

A. Muryshev, G. V. Shlyapnikov, W. Ertmer, K. Sengstock, and M. Lewenstein. Dynamics of dark solitons in elongated bose-einstein condensates. *Physical Review Letters*, 89: 110401, Aug 2002. doi: 10.1103/PhysRevLett.89.110401. URL https://link.aps.org/doi/10.1103/PhysRevLett.89.110401. (Cited on page 6.)

A. E. Muryshev, H. B. van Linden van den Heuvell, and G. V. Shlyapnikov. Stability of standing matter waves in a trap. *Physical Review A*, 60:R2665–R2668, Oct 1999. doi: 10.1103/PhysRevA.60.R2665. URL https://link.aps.org/doi/10.1103/PhysRevA.60.R2665. (Cited on page 7.)

C. J. Myatt, E. A. Burt, R. W. Ghrist, E. A. Cornell, and C. E. Wieman. Production of two overlapping Bose-Einstein condensates by sympathetic cooling. *Physical Review Letters*, 78(4):586–589, Jan 1997. doi: 10.1103/PhysRevLett.78.586. URL https://link.aps.org/doi/10.1103/PhysRevLett.78.586. (Cited on pages 3 and 7.)

P. Naidon and D. S. Petrov. Mixed bubbles in bose-bose mixtures. *Physical Review Letters*, 126:115301, Mar 2021. doi: 10.1103/PhysRevLett.126.115301. URL https://link.aps.org/doi/10.1103/PhysRevLett.126.115301. (Cited on page 5.)

G. Natale, R. M. W. van Bijnen, A. Patscheider, D. Petter, M. J. Mark, L. Chomaz, and F. Ferlaino. Excitation spectrum of a trapped dipolar supersolid and its experimental evidence. *Physical Review Letters*, 123(5):050402, Aug 2019. doi: 10.1103/PhysRevLett.123.050402. URL https://link.aps.org/doi/10.1103/PhysRevLett.123.050402. (Cited on page 112.)

J. H. V. Nguyen, D. Luo, and R. G. Hulet. Formation of matter-wave soliton trains by modulational instability. *Science*, 356(6336):422–426, Apr 2017. ISSN 0036-8075. doi: 10.1126/science.aal3220. URL http://science.sciencemag.org/content/356/6336/422. (Cited on page 7.)

M. A. Norcia, C. Politi, L. Klaus, E. Poli, M. Sohmen, M. J. Mark, R. N. Bisset, L. Santos, and F. Ferlaino. Two-dimensional supersolidity in a dipolar quantum gas. *Nature*, 596 (7872):357–361, Aug 2021. doi: 10.1038/s41586-021-03725-7. URL https://doi.org/10.1038/s41586-021-03725-7. (Cited on pages 60, 112, 118, and 120.)

M. A. Norcia, E. Poli, C. Politi, L. Klaus, T. Bland, M. J. Mark, L. Santos, R. N. Bisset, and F. Ferlaino. Can angular oscillations probe superfluidity in dipolar supersolids? *Physical Review Letters*, 129(4):040403, Jul 2022. doi: 10.1103/PhysRevLett.129.040403. URL https://link.aps.org/doi/10.1103/PhysRevLett.129.040403. (Cited on page 6.)

D. H. J. O'Dell, S. Giovanazzi, and G. Kurizki. Rotons in gaseous Bose-Einstein condensates irradiated by a laser. *Physical Review Letters*, 90(11):110402, Mar 2003. doi: 10.1103/PhysRevLett.90.110402. URL https://link.aps.org/doi/10.1103/PhysRevLett.90.110402. (Cited on page 51.)

D. H. J. O'Dell, S. Giovanazzi, and C. Eberlein. Exact hydrodynamics of a trapped dipolar Bose-Einstein condensate. *Physical Review Letters*, 92(25):250401, Jun 2004. doi: 10.1103/PhysRevLett.92.250401. URL https://link.aps.org/doi/10.1103/PhysRevLett.92.250401. (Cited on page 45.)

P. Öhberg and L. Santos. Dark solitons in a two-component Bose-Einstein condensate. *Physical Review Letters*, 86(14):2918–2921, Apr 2001a. doi: 10.1103/PhysRevLett.86.2918. URL https://link.aps.org/doi/10.1103/PhysRevLett.86.2918. (Cited on pages 99, 103, 104, 105, and 106.)

P. Öhberg and L. Santos. Solitons in two-component Bose-Einstein condensates. *Journal of Physics B: Atomic, Molecular and Optical Physics*, 34(23):4721, nov 2001b. doi: 10.1088/0953-4075/34/23/316. URL https://dx.doi.org/10.1088/0953-4075/34/23/316. (Cited on pages 99, 103, 104, 105, and 106.)

P. Öhberg and E. M. Wright. Quantum time crystals and interacting gauge theories in atomic Bose-Einstein condensates. *Physical Review Letters*, 123(25):250402, Dec 2019. doi: 10.1103/PhysRevLett.123.250402. URL https://doi.org/10.1103/PhysRevLett.123.250402. (Cited on page 7.)

K. Padavić, K. Sun, C. Lannert, and S. Vishveshwara. Physics of hollow Bose-Einstein condensates. *Europhysics Letters*, 120:20004, Jan 2018. doi: 10.1209/0295-5075/120/20004. URL https://iopscience.iop.org/article/10.1209/0295-5075/120/20004. (Cited on pages 79 and 83.)

K. Padavić, K. Sun, C. Lannert, and S. Vishveshwara. Vortex-antivortex physics in shell-shaped Bose-Einstein condensates. *Physical Review A*, 102(4):043305, Oct 2020. doi: 10.1103/PhysRevA.102.043305. URL https://link.aps.org/doi/10.1103/PhysRevA.102.043305. (Cited on page 79.)

S. B. Papp and C. E. Wieman. Observation of heteronuclear feshbach molecules from a ^{85}Rb – –^{87}Rb gas. *Physical Review Letters*, 97:180404, Oct 2006. doi: 10.1103/PhysRevLett.97.180404. URL https://link.aps.org/doi/10.1103/PhysRevLett.97.180404. (Cited on page 3.)

Q.-H. Park and H. J. Shin. Systematic construction of multicomponent optical solitons. *Physical Review E*, 61:3093–3106, Mar 2000. doi: 10.1103/PhysRevE.61.3093. URL https://link.aps.org/doi/10.1103/PhysRevE.61.3093. (Cited on page 7.)

N. G. Parker and D. H. J. O'Dell. Thomas-fermi versus one- and two-dimensional regimes of a trapped dipolar Bose-Einstein condensate. *Physical Review A*, 78(4):041601, Oct 2008. doi: 10.1103/PhysRevA.78.041601. URL https://link.aps.org/doi/10.1103/PhysRevA.78.041601. (Cited on page 45.)

W. Pauli. The connection between spin and statistics. *Physical Review*, 58(8):716–722, Oct 1940. doi: 10.1103/PhysRev.58.716. URL https://link.aps.org/doi/10.1103/PhysRev.58.716. (Cited on page 12.)

G. Pecci, G. Aupetit-Diallo, M. Albert, P. Vignolo, and A. Minguzzi. Persistent currents in a strongly interacting multicomponent bose gas on a ring. *Comptes Rendus Physique*, 24(S3):1–13, 2023. doi: 10.5802/crphys.157. URL https://doi.org/10.5802/crphys.157. (Cited on page 2.)

D. E. Pelinovsky and Y. S. Kivshar. Stability criterion for multicomponent solitary waves. *Physical Review E*, 62:8668–8676, Dec 2000. doi: 10.1103/PhysRevE.62.8668. URL https://link.aps.org/doi/10.1103/PhysRevE.62.8668. (Cited on page 7.)

V. M. Pérez-García, H. Michinel, and H. Herrero. Bose-einstein solitons in highly asymmetric traps. *Physical Review A*, 57:3837–3842, May 1998. doi: 10.1103/PhysRevA.57.3837. URL https://link.aps.org/doi/10.1103/PhysRevA.57.3837. (Cited on page 6.)

H. Perrin and B. M. Garraway. Chapter four: Trapping atoms with radio frequency adiabatic potentials. volume 66 of *Advances In Atomic, Molecular, and Optical Physics*, pages 181–262. Academic Press, 2017. doi: https://doi.org/10.1016/bs.aamop.2017.03.002. URL https://www.sciencedirect.com/science/article/pii/S1049250X17300137. (Cited on pages 3, 79, and 82.)

C. J. Pethick and H. Smith. *Bose-Einstein condensation in dilute gases*. Cambridge University Press, Sep 2008. ISBN 9780521846516. doi: 10.1017/CBO9780511802850. URL https://doi.org/10.1017/CBO9780511802850. (Cited on pages 1, 11, 15, 20, 21, 22, 27, 35, and 36.)

D. S. Petrov. Quantum mechanical stabilization of a collapsing Bose-bose mixture. *Physical Review Letters*, 115(15):155302, Oct 2015. doi: 10.1103/PhysRevLett.115.155302. URL https://link.aps.org/doi/10.1103/PhysRevLett.115.155302. (Cited on pages 6, 25, 29, 30, 31, 33, 112, and 127.)

D. S. Petrov and G. E. Astrakharchik. Ultradilute low-dimensional liquids. *Physical Review Letters*, 117:100401, Sep 2016. doi: 10.1103/PhysRevLett.117.100401. URL https://link.aps.org/doi/10.1103/PhysRevLett.117.100401. (Cited on page 5.)

D. Petter, G. Natale, R. M. W. van Bijnen, A. Patscheider, M. J. Mark, L. Chomaz, and F. Ferlaino. Probing the roton excitation spectrum of a stable dipolar bose gas. *Physical Review Letters*, 122:183401, May 2019. doi: 10.1103/PhysRevLett.122.183401. URL https://link.aps.org/doi/10.1103/PhysRevLett.122.183401. (Cited on page 6.)

W. D. Phillips. Nobel lecture: Laser cooling and trapping of neutral atoms. *Rev. Mod. Phys.*, 70:721–741, Jul 1998. doi: 10.1103/RevModPhys.70.721. URL https://link.aps.org/doi/10.1103/RevModPhys.70.721. (Cited on page 1.)

M. Pigneur, T. Berrada, M. Bonneau, T. Schumm, E. Demler, and J. Schmiedmayer. Relaxation to a phase-locked equilibrium state in a one-dimensional bosonic josephson junction. *Physical Review Letters*, 120:173601, Apr 2018. doi: 10.1103/PhysRevLett.120.173601. URL https://link.aps.org/doi/10.1103/PhysRevLett.120.173601. (Cited on page 153.)

R. Pires, J. Ulmanis, S. Häfner, M. Repp, A. Arias, E. D. Kuhnle, and M. Weidemüller. Observation of efimov resonances in a mixture with extreme mass imbalance. *Physical Review Letters*, 112:250404, Jun 2014. doi: 10.1103/PhysRevLett.112.250404. URL https://link.aps.org/doi/10.1103/PhysRevLett.112.250404. (Cited on page 3.)

L. Pitaevskii and S. Stringari. *Bose-Einstein condensation and superfluidity*, volume 164. Oxford University Press, Jan 2016. ISBN 9780198758884. doi: 10.1093/acprof:oso/9780198758884.001.0001. URL https://doi.org/10.1093/acprof:oso/9780198758884.001.0001. (Cited on pages 1, 2, 11, 20, 21, 22, 23, 26, 35, 45, 97, 101, 102, 103, and 171.)

L. P. Pitaevskii. Vortex lines in an imperfect bose gas. *Soviet Physics JETP*, 13(2):451–454, 1961. (Cited on pages 2 and 21.)

L. P. Pitaevskii. Dynamics of solitary waves in ultracold gases in terms of observable quantities. *Physics-Uspekhi*, 59(10):1028, oct 2016. doi: 10.3367/UFNe.2016.08.037891. URL https://dx.doi.org/10.3367/UFNe.2016.08.037891. (Cited on page 7.)

E. Poli, T. Bland, C. Politi, L. Klaus, M. A. Norcia, F. Ferlaino, R. N. Bisset, and L. Santos. Maintaining supersolidity in one and two dimensions. *Physical Review A*, 104(6):063307, Dec 2021. doi: 10.1103/PhysRevA.104.063307. URL https://link.aps.org/doi/10.1103/PhysRevA.104.063307. (Cited on page 112.)

C. Politi, A. Trautmann, P. Ilzhöfer, G. Durastante, M. J. Mark, M. Modugno, and F. Ferlaino. Interspecies interactions in an ultracold dipolar mixture. *Physical Review A*, 105(2):023304, Feb 2022. doi: 10.1103/PhysRevA.105.023304. URL https://link.aps.org/doi/10.1103/PhysRevA.105.023304. (Cited on pages 4 and 112.)

S. E. Pollack, D. Dries, M. Junker, Y. P. Chen, T. A. Corcovilos, and R. G. Hulet. Extreme tunability of interactions in a ^{7}Li bose-einstein condensate. *Physical Review Letters*, 102:090402, Mar 2009. doi: 10.1103/PhysRevLett.102.090402. URL https://link.aps.org/doi/10.1103/PhysRevLett.102.090402. (Cited on page 3.)

J. Polo, R. Dubessy, P. Pedri, H. Perrin, and A. Minguzzi. Oscillations and decay of superfluid currents in a one-dimensional bose gas on a ring. *Physical Review Letters*, 123:195301, Nov 2019. doi: 10.1103/PhysRevLett.123.195301. URL https://link.aps.org/doi/10.1103/PhysRevLett.123.195301. (Cited on page 2.)

N. P. Proukakis, N. G. Parker, D. J. Frantzeskakis, and C. S. Adams. Analogies between dark solitons in atomic Bose–Einstein condensates and optical systems. *Journal of Optics B: Quantum and Semiclassical Optics*, 6(5):S380, may 2004. doi: 10.1088/1464-4266/6/5/028. URL https://dx.doi.org/10.1088/1464-4266/6/5/028. (Cited on page 6.)

H. Pu and N. Bigelow. Properties of two-species bose condensates. *Physical Review Letters*, 80(6):1130–1133, Feb 1998. doi: 10.1103/PhysRevLett.80.1130. URL https://link.aps.org/doi/10.1103/PhysRevLett.80.1130. (Cited on pages 7, 27, 98, and 100.)

A. Putra, F. Salces-Cárcoba, Y. Yue, S. Sugawa, and I. B. Spielman. Spatial coherence of spin-orbit-coupled bose gases. *Physical Review Letters*, 124:053605, Feb 2020. doi: 10.1103/PhysRevLett.124.053605. URL https://link.aps.org/doi/10.1103/PhysRevLett.124.053605. (Cited on page 6.)

M. I. Qadir, H. Susanto, and P. C. Matthews. Fluxon analogues and dark solitons in linearly coupled Bose–Einstein condensates. *Journal of Physics B: Atomic, Molecular and Optical Physics*, 45(3):035004, jan 2012. doi: 10.1088/0953-4075/45/3/035004. URL https://dx.doi.org/10.1088/0953-4075/45/3/035004. (Cited on page 171.)

H. Qiu, D. Zhang, and A. Muñoz Mateo. Stripe and junction-vortex phases in linearly coupled Bose-Einstein condensates. *Physical Review A*, 103(2):023316, Feb 2021. doi: 10.1103/PhysRevA.103.023316. URL https://link.aps.org/doi/10.1103/PhysRevA.103.023316. (Cited on page 173.)

C. Qu, L. P. Pitaevskii, and S. Stringari. Magnetic solitons in a binary bose-einstein condensate. *Physical Review Letters*, 116:160402, Apr 2016. doi: 10.1103/PhysRevLett.116.160402. URL https://link.aps.org/doi/10.1103/PhysRevLett.116.160402. (Cited on page 7.)

S. J. Rabello. A gauge theory of one-dimensional anyons. *Physics Letters B*, 363(3):180–183, 1995. ISSN 0370-2693. doi: 10.1016/0370-2693(95)01262-O. URL https://www.sciencedirect.com/science/article/pii/0370269395012620. (Cited on page 73.)

S. J. Rabello. 1d generalized statistics gas: A gauge theory approach. *Physical Review Letters*, 76(21):4007–4009, May 1996. doi: 10.1103/PhysRevLett.76.4007. URL https://link.aps.org/doi/10.1103/PhysRevLett.76.4007. (Cited on page 73.)

R. Radhakrishnan and M. Lakshmanan. Bright and dark soliton solutions to coupled nonlinear schrodinger equations. *Journal of Physics A: Mathematical and General*, 28(9):2683, 1995. doi: 10.1088/0305-4470/28/9/025. URL https://iopscience.iop.org/article/10.1088/0305-4470/28/9/025/pdf. (Cited on page 7.)

S. Raghavan, A. Smerzi, S. Fantoni, and S. R. Shenoy. Coherent oscillations between two weakly coupled bose-einstein condensates: Josephson effects, π oscillations, and macroscopic quantum self-trapping. *Physical Review A*, 59:620–633, Jan 1999. doi: 10.1103/PhysRevA.59.620. URL https://link.aps.org/doi/10.1103/PhysRevA.59.620. (Cited on page 2.)

D. Rakshit, T. Karpiuk, M. Brewczyk, and M. Gajda. Quantum Bose-Fermi droplets. *SciPost Phys.*, 6:079, 2019. doi: 10.21468/SciPostPhys.6.6.079. URL https://scipost.org/10.21468/SciPostPhys.6.6.079. (Cited on page 5.)

A. Recati and S. Stringari. Coherently coupled mixtures of ultracold atomic gases. *Annual Review of Condensed Matter Physics*, 13(1):407–432, 2022. doi: 10.1146/annurev-conmatphys-031820-121316. URL https://doi.org/10.1146/annurev-conmatphys-031820-121316. (Cited on pages 4, 6, 153, and 154.)

A. Recati and S. Stringari. Supersolidity in ultracold dipolar gases. *Nature Reviews Physics*, 5(12):735–743, 2023. doi: 10.1038/s42254-023-00648-2. URL https://www.nature.com/articles/s42254-023-00648-2. (Cited on page 6.)

J. D. Reppy. Superfluid helium in porous media. *Journal of Low Temperature Physics*, 87 (3):205–245, May 1992. doi: 10.1007/BF00114905. URL https://doi.org/10.1007/BF00114905. (Cited on page 113.)

B. Rhyno, N. Lundblad, D. C. Aveline, C. Lannert, and S. Vishveshwara. Thermodynamics in expanding shell-shaped Bose-Einstein condensates. *Physical Review A*, 104(6):063310, Dec 2021. doi: 10.1103/PhysRevA.104.063310. URL https://link.aps.org/doi/10.1103/PhysRevA.104.063310. (Cited on pages 79 and 82.)

F. Riboli and M. Modugno. Topology of the ground state of two interacting Bose-Einstein condensates. *Physical Review A*, 65(6):063614, Jun 2002. doi: 10.1103/PhysRevA.65.063614. URL https://link.aps.org/doi/10.1103/PhysRevA.65.063614. (Cited on page 27.)

A. Richaud, V. Penna, R. Mayol, and M. Guilleumas. Vortices with massive cores in a binary mixture of Bose-Einstein condensates. *Physical Review A*, 101(1):013630, Jan 2020. doi: 10.1103/PhysRevA.101.013630. URL https://link.aps.org/doi/10.1103/PhysRevA.101.013630. (Cited on page 7.)

J. L. Roberts, N. R. Claussen, S. L. Cornish, E. A. Donley, E. A. Cornell, and C. E. Wieman. Controlled collapse of a bose-einstein condensate. *Physical Review Letters*, 86: 4211–4214, May 2001. doi: 10.1103/PhysRevLett.86.4211. URL https://link.aps.org/doi/10.1103/PhysRevLett.86.4211. (Cited on page 6.)

S. M. Roccuzzo and F. Ancilotto. Supersolid behavior of a dipolar Bose-Einstein condensate confined in a tube. *Physical Review A*, 99(4):041601, Apr 2019. doi: 10.1103/PhysRevA.99.041601. URL https://link.aps.org/doi/10.1103/PhysRevA.99.041601. (Cited on page 59.)

S. M. Roccuzzo, A. Gallemí, A. Recati, and S. Stringari. Rotating a supersolid dipolar gas. *Physical Review Letters*, 124(4):045702, Jan 2020. doi: 10.1103/PhysRevLett.124.045702. URL https://link.aps.org/doi/10.1103/PhysRevLett.124.045702. (Cited on page 6.)

S. M. Roccuzzo, A. Recati, and S. Stringari. Moment of inertia and dynamical rotational response of a supersolid dipolar gas. *Physical Review A*, 105(2):023316, Feb 2022. doi: 10.1103/PhysRevA.105.023316. URL https://link.aps.org/doi/10.1103/PhysRevA.105.023316. (Cited on page 6.)

A. Romero-Ros, G. C. Katsimiga, P. G. Kevrekidis, B. Prinari, G. Biondini, and P. Schmelcher. On-demand generation of dark-bright soliton trains in Bose-Einstein condensates. *Physical Review A*, 105(2):023325, Feb 2022. doi: 10.1103/PhysRevA.105.023325. URL https://link.aps.org/doi/10.1103/PhysRevA.105.023325. (Cited on page 7.)

S. Ronen, D. C. E. Bortolotti, and J. L. Bohn. Bogoliubov modes of a dipolar condensate in a cylindrical trap. *Physical Review A*, 74(1):013623, Jul 2006. doi: 10.1103/PhysRevA.74.013623. URL https://link.aps.org/doi/10.1103/PhysRevA.74.013623. (Cited on page 42.)

C. Ryu, M. F. Andersen, P. Cladé, V. Natarajan, K. Helmerson, and W. D. Phillips. Observation of persistent flow of a bose-einstein condensate in a toroidal trap. *Physical Review Letters*, 99:260401, Dec 2007. doi: 10.1103/PhysRevLett.99.260401. URL https://link.aps.org/doi/10.1103/PhysRevLett.99.260401. (Cited on pages 2 and 3.)

M. Saffman, T. G. Walker, and K. Mølmer. Quantum information with rydberg atoms. *Rev. Mod. Phys.*, 82:2313–2363, Aug 2010. doi: 10.1103/RevModPhys.82.2313. URL https://link.aps.org/doi/10.1103/RevModPhys.82.2313. (Cited on page 4.)

H. Saito. Path-integral monte carlo study on a droplet of a dipolar bose–einstein condensate stabilized by quantum fluctuation. *Journal of the Physical Society of Japan*, 85(5):053001, 2016. doi: 10.7566/JPSJ.85.053001. URL https://doi.org/10.7566/JPSJ.85.053001. (Cited on page 5.)

J. Sánchez-Baena, R. Bombín, and J. Boronat. Ring solids and supersolids in spherical shell-shaped dipolar Bose-Einstein condensates. *arXiv preprint arXiv:2312.12164*, 2023a. (Cited on pages 81 and 177.)

J. Sánchez-Baena, C. Politi, F. Maucher, F. Ferlaino, and T. Pohl. Heating a dipolar quantum fluid into a solid. *Nature communications*, 14(1):1868, Apr 2023b. doi: 10.1038/s41467-023-37207-3. URL https://www.nature.com/articles/s41467-023-37207-3. (Cited on page 81.)

L. Santos, G. V. Shlyapnikov, P. Zoller, and M. Lewenstein. Bose-Einstein condensation in trapped dipolar gases. *Physical Review Letters*, 85(9):1791–1794, Aug 2000. doi: 10.1103/PhysRevLett.85.1791. URL https://link.aps.org/doi/10.1103/PhysRevLett.85.1791. (Cited on pages 47 and 49.)

L. Santos, G. V. Shlyapnikov, and M. Lewenstein. Roton-maxon spectrum and stability of trapped dipolar Bose-Einstein condensates. *Physical Review Letters*, 90(25):250403, Jun 2003. doi: 10.1103/PhysRevLett.90.250403. URL https://link.aps.org/doi/10.1103/PhysRevLett.90.250403. (Cited on pages 51 and 52.)

J. Sanz, A. Frölian, C. S. Chisholm, C. R. Cabrera, and L. Tarruell. Interaction control and bright solitons in coherently coupled Bose-Einstein condensates. *Physical Review Letters*, 128(1):013201, Jan 2022. doi: 10.1103/PhysRevLett.128.013201. URL https://link.aps.org/doi/10.1103/PhysRevLett.128.013201. (Cited on page 7.)

F. Schäfer, N. Mizukami, and Y. Takahashi. Feshbach resonances of large-mass-imbalance er-li mixtures. *Physical Review A*, 105:012816, Jan 2022. doi: 10.1103/PhysRevA.105.012816. URL https://link.aps.org/doi/10.1103/PhysRevA.105.012816. (Cited on page 3.)

D. Scheiermann, L. A. P. n. Ardila, T. Bland, R. N. Bisset, and L. Santos. Catalyzation of supersolidity in binary dipolar condensates. *Physical Review A*, 107(2):L021302, Feb 2023. doi: 10.1103/PhysRevA.107.L021302. URL https://link.aps.org/doi/10.1103/PhysRevA.107.L021302. (Cited on page 112.)

M. Schmitt, M. Wenzel, F. Böttcher, I. Ferrier-Barbut, and T. Pfau. Self-bound droplets of a dilute magnetic quantum liquid. *Nature*, 539(7628):259–262, Nov 2016. ISSN 1476-4687. doi: 10.1038/nature20126. URL https://doi.org/10.1038/nature20126. (Cited on pages 5 and 112.)

S. K. Schnelle, E. D. van Ooijen, M. J. Davis, N. R. Heckenberg, and H. Rubinsztein-Dunlop. Versatile two-dimensional potentials for ultra-cold atoms. *Opt. Express*, 16 (3):1405–1412, Feb 2008. doi: 10.1364/OE.16.001405. URL https://opg.optica.org/oe/abstract.cfm?URI=oe-16-3-1405. (Cited on page 3.)

F. Schreck, L. Khaykovich, K. L. Corwin, G. Ferrari, T. Bourdel, J. Cubizolles, and C. Salomon. Quasipure bose-einstein condensate immersed in a fermi sea. *Physical Review Letters*, 87:080403, Aug 2001. doi: 10.1103/PhysRevLett.87.080403. URL https://link.aps.org/doi/10.1103/PhysRevLett.87.080403. (Cited on page 3.)

T. Schulte, L. Santos, A. Sanpera, and M. Lewenstein. Vortex-vortex interactions in toroidally trapped bose-einstein condensates. *Physical Review A*, 66:033602, Sep 2002. doi: 10.1103/PhysRevA.66.033602. URL https://link.aps.org/doi/10.1103/PhysRevA.66.033602. (Cited on page 2.)

T. Schweigler, V. Kasper, S. Erne, I. Mazets, B. Rauer, F. Cataldini, T. Langen, T. Gasenzer, J. Berges, and J. Schmiedmayer. Experimental characterization of a quantum many-body system via higher-order correlations. *Nature*, 545(7654):323–326, May 2017. doi: 10.1038/nature22310. URL https://www.nature.com/articles/nature22310. (Cited on page 153.)

J. Schwinger. The theory of quantized fields. i. *Physical Review*, 82(6):914–927, Jun 1951. doi: 10.1103/PhysRev.82.914. URL https://link.aps.org/doi/10.1103/PhysRev.82.914. (Cited on page 12.)

A. C. Scott, F. Chu, and D. W. McLaughlin. The soliton: a new concept in applied science. *Proceedings of the IEEE*, 61(10):1443–1483, 1973. doi: 10.1109/PROC.1973.9296. URL https://ieeexplore.ieee.org/document/1451226. (Cited on page 6.)

G. Semeghini, G. Ferioli, L. Masi, C. Mazzinghi, L. Wolswijk, F. Minardi, M. Modugno, G. Modugno, M. Inguscio, and M. Fattori. Self-bound quantum droplets of atomic mixtures in free space. *Physical Review Letters*, 120(23):235301, Jun 2018. doi: 10.1103/PhysRevLett.120.235301. URL https://link.aps.org/doi/10.1103/PhysRevLett.120.235301. (Cited on pages 5, 31, and 33.)

S. S. Shamailov and J. Brand. Quasiparticles of widely tuneable inertial mass: The dispersion relation of atomic Josephson vortices and related solitary waves. *SciPost*

Phys., 4(3):18, Mar 2018. doi: 10.21468/SciPostPhys.4.3.018. URL https://scipost.org/10.21468/SciPostPhys.4.3.018. (Cited on pages 6, 97, 171, 172, and 173.)

B. E. Sherlock, M. Gildemeister, E. Owen, E. Nugent, and C. J. Foot. Time-averaged adiabatic ring potential for ultracold atoms. *Physical Review A*, 83:043408, Apr 2011. doi: 10.1103/PhysRevA.83.043408. URL https://link.aps.org/doi/10.1103/PhysRevA.83.043408. (Cited on page 3.)

Y. Shin, G.-B. Jo, M. Saba, T. A. Pasquini, W. Ketterle, and D. E. Pritchard. Optical weak link between two spatially separated bose-einstein condensates. *Physical Review Letters*, 95:170402, Oct 2005. doi: 10.1103/PhysRevLett.95.170402. URL https://link.aps.org/doi/10.1103/PhysRevLett.95.170402. (Cited on page 2.)

S. Sinha and Y. Castin. Dynamic instability of a rotating Bose-Einstein condensate. *Physical Review Letters*, 87(19):190402, Oct 2001. doi: 10.1103/PhysRevLett.87.190402. URL https://link.aps.org/doi/10.1103/PhysRevLett.87.190402. (Cited on page 2.)

D. V. Skryabin. Stability of multi-parameter solitons: asymptotic approach. *Physica D: Nonlinear Phenomena*, 139(1-2):186–193, 2000. doi: 10.1016/S0167-2789(99)00217-1. URL https://www.sciencedirect.com/science/article/abs/pii/S0167278999002171. (Cited on page 7.)

A. Smerzi, S. Fantoni, S. Giovanazzi, and S. R. Shenoy. Quantum coherent atomic tunneling between two trapped bose-einstein condensates. *Physical Review Letters*, 79:4950–4953, Dec 1997. doi: 10.1103/PhysRevLett.79.4950. URL https://link.aps.org/doi/10.1103/PhysRevLett.79.4950. (Cited on page 2.)

J. C. Smith, D. Baillie, and P. B. Blakie. Quantum droplet states of a binary magnetic gas. *Physical Review Letters*, 126(2):025302, Jan 2021. doi: 10.1103/PhysRevLett.126.025302. URL https://link.aps.org/doi/10.1103/PhysRevLett.126.025302. (Cited on pages 4, 112, 113, and 117.)

J. Smyrnakis, M. Magiropoulos, N. K. Efremidis, and G. M. Kavoulakis. Persistent currents in a two-component bose–einstein condensate confined in a ring potential. *Journal of Physics B: Atomic, Molecular and Optical Physics*, 47(21):215302, oct 2014. doi: 10.1088/0953-4075/47/21/215302. URL https://dx.doi.org/10.1088/0953-4075/47/21/215302. (Cited on page 2.)

M. Sohmen, C. Politi, L. Klaus, L. Chomaz, M. J. Mark, M. A. Norcia, and F. Ferlaino. Birth, life, and death of a dipolar supersolid. *Phys. Rev. Lett.*, 126:233401, Jun 2021. doi: 10.1103/PhysRevLett.126.233401. URL https://link.aps.org/doi/10.1103/PhysRevLett.126.233401. (Cited on page 6.)

D. T. Son and M. A. Stephanov. Domain walls of relative phase in two-component Bose-Einstein condensates. *Physical Review A*, 65:063621, Jun 2002. doi: 10.1103/PhysRevA.65.063621. URL https://link.aps.org/doi/10.1103/PhysRevA.65.063621. (Cited on pages 155 and 171.)

I. B. Spielman. Raman processes and effective gauge potentials. *Phys. Rev. A*, 79:063613, Jun 2009. doi: 10.1103/PhysRevA.79.063613. URL https://link.aps.org/doi/10.1103/PhysRevA.79.063613. (Cited on page 4.)

D. M. Stamper-Kurn and M. Ueda. Spinor bose gases: Symmetries, magnetism, and quantum dynamics. *Rev. Mod. Phys.*, 85:1191–1244, Jul 2013. doi: 10.1103/RevModPhys.85.1191. URL https://link.aps.org/doi/10.1103/RevModPhys.85.1191. (Cited on page 3.)

D. M. Stamper-Kurn, M. R. Andrews, A. P. Chikkatur, S. Inouye, H.-J. Miesner, J. Stenger, and W. Ketterle. Optical confinement of a bose-einstein condensate. *Physical Review Letters*, 80:2027–2030, Mar 1998. doi: 10.1103/PhysRevLett.80.2027. URL https://link.aps.org/doi/10.1103/PhysRevLett.80.2027. (Cited on page 3.)

J. Stenger, S. Inouye, D. Stamper-Kurn, H.-J. Miesner, A. Chikkatur, and W. Ketterle. Spin domains in ground-state bose–einstein condensates. *Nature*, 396(6709):345–348, 1998. doi: 10.1038/24567. URL https://www.nature.com/articles/24567. (Cited on page 3.)

K. E. Strecker, G. B. Partridge, A. G. Truscott, and R. G. Hulet. Formation and propagation of matter-wave soliton trains. *Nature*, 417(6885):150–153, 2002. doi: 10.1038/nature747. URL https://www.nature.com/articles/nature747. (Cited on page 6.)

J. Stuhler, A. Griesmaier, T. Koch, M. Fattori, T. Pfau, S. Giovanazzi, P. Pedri, and L. Santos. Observation of dipole-dipole interaction in a degenerate quantum gas. *Physical Review Letters*, 95(15):150406, Oct 2005. doi: 10.1103/PhysRevLett.95.150406. URL https://link.aps.org/doi/10.1103/PhysRevLett.95.150406. (Cited on page 47.)

D. Sukachev, A. Sokolov, K. Chebakov, A. Akimov, S. Kanorsky, N. Kolachevsky, and V. Sorokin. Magneto-optical trap for thulium atoms. *Physical Review A*, 82:011405, Jul 2010. doi: 10.1103/PhysRevA.82.011405. URL https://link.aps.org/doi/10.1103/PhysRevA.82.011405. (Cited on page 4.)

C. Sulem and P.-L. Sulem. *The nonlinear Schrödinger equation: self-focusing and wave collapse*, volume 139. Springer Science & Business Media, 2007. doi: 10.1007/b98958. URL https://doi.org/10.1007/b98958. (Cited on page 7.)

K. Sun, K. Padavić, F. Yang, S. Vishveshwara, and C. Lannert. Static and dynamic properties of shell-shaped condensates. *Physical Review A*, 98(1):013609, Jul 2018. doi: 10.1103/PhysRevA.98.013609. URL https://link.aps.org/doi/10.1103/PhysRevA.98.013609. (Cited on pages 79, 83, and 85.)

Y. Tang, W. Kao, K.-Y. Li, and B. L. Lev. Tuning the dipole-dipole interaction in a quantum gas with a rotating magnetic field. *Physical Review Letters*, 120:230401, Jun 2018. doi: 10.1103/PhysRevLett.120.230401. URL https://link.aps.org/doi/10.1103/PhysRevLett.120.230401. (Cited on page 41.)

L. Tanzi, E. Lucioni, F. Famà, J. Catani, A. Fioretti, C. Gabbanini, R. N. Bisset, L. Santos, and G. Modugno. Observation of a dipolar quantum gas with metastable supersolid properties. *Physical Review Letters*, 122(13):130405, Apr 2019a. doi: 10.1103/PhysRevLett.122.130405. URL https://link.aps.org/doi/10.1103/PhysRevLett.122.130405. (Cited on pages 6, 59, and 112.)

L. Tanzi, S. M. Roccuzzo, E. Lucioni, F. Famà, A. Fioretti, C. Gabbanini, G. Modugno, A. Recati, and S. Stringari. Supersolid symmetry breaking from compressional oscillations in a dipolar quantum gas. *Nature*, 574:382, Sep 2019b. doi: 10.1038/s41586-019-1568-6. URL https://doi.org/10.1038/s41586-019-1568-6. (Cited on page 112.)

L. Tanzi, J. G. Maloberti, G. Biagioni, A. Fioretti, C. Gabbanini, and G. Modugno. Evidence of superfluidity in a dipolar supersolid from nonclassical rotational inertia. *Science*, 371(6534):1162–1165, Feb 2021. doi: 10.1126/science.aba4309. URL https://www.science.org/doi/abs/10.1126/science.aba4309. (Cited on page 6.)

M. N. Tengstrand and S. M. Reimann. Droplet-superfluid compounds in binary bosonic mixtures. *Physical Review A*, 105:033319, Mar 2022. doi: 10.1103/PhysRevA.105.033319. URL https://link.aps.org/doi/10.1103/PhysRevA.105.033319. (Cited on page 5.)

M. N. Tengstrand, D. Boholm, R. Sachdeva, J. Bengtsson, and S. M. Reimann. Persistent currents in toroidal dipolar supersolids. *Phys. Rev. A*, 103:013313, Jan 2021. doi: 10.1103/PhysRevA.103.013313. URL https://link.aps.org/doi/10.1103/PhysRevA.103.013313. (Cited on page 6.)

M. N. Tengstrand, P. Stürmer, J. Ribbing, and S. M. Reimann. Toroidal dipolar supersolid with a rotating weak link. *Phys. Rev. A*, 107:063316, Jun 2023. doi: 10.1103/PhysRevA.107.063316. URL https://link.aps.org/doi/10.1103/PhysRevA.107.063316. (Cited on page 6.)

M. Theis, G. Thalhammer, K. Winkler, M. Hellwig, G. Ruff, R. Grimm, and J. H. Denschlag. Tuning the scattering length with an optically induced feshbach resonance. *Physical Review Letters*, 93:123001, Sep 2004. doi: 10.1103/PhysRevLett.93.123001. URL https://link.aps.org/doi/10.1103/PhysRevLett.93.123001. (Cited on page 3.)

O. Thomas, C. Lippe, T. Eichert, and H. Ott. Experimental realization of a rydberg optical feshbach resonance in a quantum many-body system. *Nature communications*, 9(1):2238, 2018. doi: 10.1038/s41467-018-04684-w. URL https://www.nature.com/articles/s41467-018-04684-w. (Cited on page 3.)

R. C. Thompson. Ion coulomb crystals. *Contemporary Physics*, 56(1):63–79, Jan 2015. doi: 10.1080/00107514.2014.989715. URL https://doi.org/10.1080/00107514.2014.989715. (Cited on page 111.)

C. Ticknor, R. M. Wilson, and J. L. Bohn. Anisotropic superfluidity in a dipolar bose gas. *Physical Review Letters*, 106(6):065301, Feb 2011. doi: 10.1103/PhysRevLett.106.065301. URL https://link.aps.org/doi/10.1103/PhysRevLett.106.065301. (Cited on page 52.)

E. Timmermans. Phase separation of Bose-Einstein condensates. *Physical Review Letters*, 81(26):5718–5721, Dec 1998. doi: 10.1103/PhysRevLett.81.5718. URL https://link.aps.org/doi/10.1103/PhysRevLett.81.5718. (Cited on pages 3, 7, 27, 98, and 100.)

A. Tononi and L. Salasnich. Bose-Einstein condensation on the surface of a sphere. *Physical Review Letters*, 123(16):160403, Oct 2019. doi: 10.1103/PhysRevLett.123.160403. URL https://link.aps.org/doi/10.1103/PhysRevLett.123.160403. (Cited on pages 79 and 80.)

A. Tononi and L. Salasnich. Low-dimensional quantum gases in curved geometries. *Nature Reviews Physics*, 5:398–406, Jul 2023. doi: 10.1038/s42254-023-00591-2. URL https://www.nature.com/articles/s42254-023-00591-2. (Cited on pages 3 and 79.)

A. Tononi, F. Cinti, and L. Salasnich. Quantum bubbles in microgravity. *Physical Review Letters*, 125(1):010402, Jun 2020. doi: 10.1103/PhysRevLett.125.010402. URL https://link.aps.org/doi/10.1103/PhysRevLett.125.010402. (Cited on pages 79 and 80.)

A. Tononi, A. Pelster, and L. Salasnich. Topological superfluid transition in bubble-trapped condensates, Feb 2022. URL https://link.aps.org/doi/10.1103/PhysRevResearch.4.013122. (Cited on page 79.)

A. Trautmann, P. Ilzhöfer, G. Durastante, C. Politi, M. Sohmen, M. J. Mark, and F. Ferlaino. Dipolar quantum mixtures of erbium and dysprosium atoms. *Physical Review Letters*, 121(21):213601, Nov 2018. doi: 10.1103/PhysRevLett.121.213601. URL https://link.aps.org/doi/10.1103/PhysRevLett.121.213601. (Cited on pages 4 and 112.)

M. Trippenbach, K. Góral, K. Rzazewski, B. Malomed, and Y. B. Band. Structure of binary bose-einstein condensates. *Journal of Physics B: Atomic, Molecular and Optical Physics*, 33(19):4017, oct 2000. doi: 10.1088/0953-4075/33/19/314. URL https://dx.doi.org/10.1088/0953-4075/33/19/314. (Cited on page 3.)

T. Tsuzuki. Nonlinear waves in the pitaevskii-gross equation. *Journal of Low Temperature Physics*, 4:441–457, Apr 1971. doi: 10.1007/BF00628744. URL https://doi.org/10.1007/BF00628744. (Cited on pages 35 and 101.)

M. Ueda. *Fundamentals and new frontiers of Bose-Einstein condensation*. World Scientific, Jul 2010. doi: 10.1142/7216. URL https://doi.org/10.1142/7216. (Cited on pages 1 and 11.)

T. van Zoest, N. Gaaloul, Y. Singh, H. Ahlers, W. Herr, S. T. Seidel, W. Ertmer, E. Rasel, M. Eckart, E. Kajari, et al. Bose-Einstein condensation in microgravity. *Science*, 328(5985):1540–1543, Jun 2010. doi: 10.1126/science.1189164. URL https://www.science.org/doi/abs/10.1126/science.1189164. (Cited on page 80.)

F. Wächtler and L. Santos. Ground-state properties and elementary excitations of quantum droplets in dipolar Bose-Einstein condensates. *Physical Review A*, 94(4): 043618, Oct 2016a. doi: 10.1103/PhysRevA.94.043618. URL https://link.aps.org/doi/10.1103/PhysRevA.94.043618. (Cited on pages 5, 56, and 58.)

F. Wächtler and L. Santos. Quantum filaments in dipolar Bose-Einstein condensates. *Physical Review A*, 93(6):061603, Jun 2016b. doi: 10.1103/PhysRevA.93.061603. URL https://link.aps.org/doi/10.1103/PhysRevA.93.061603. (Cited on pages 5 and 56.)

M. I. Weinstein. Nonlinear schrödinger equations and sharp interpolation estimates. *Communications in Mathematical Physics*, 87:567–576, 1983. doi: 10.1007/BF01208265. URL https://link.springer.com/article/10.1007/BF01208265. (Cited on page 6.)

M. Wenzel, F. Böttcher, T. Langen, I. Ferrier-Barbut, and T. Pfau. Striped states in a many-body system of tilted dipoles. *Physical Review A*, 96(5):053630, Nov 2017. doi: 10.1103/PhysRevA.96.053630. URL https://link.aps.org/doi/10.1103/PhysRevA.96.053630. (Cited on pages 6 and 112.)

M. White, H. Gao, M. Pasienski, and B. DeMarco. Bose-Einstein condensates in rf-dressed adiabatic potentials. *Physical Review A*, 74(2):023616, Aug 2006. doi: 10.1103/PhysRevA.74.023616. URL https://link.aps.org/doi/10.1103/PhysRevA.74.023616. (Cited on pages 3 and 79.)

F. Wilczek. Quantum mechanics of fractional-spin particles. *Physical Review Letters*, 49 (14):957–959, Oct 1982. doi: 10.1103/PhysRevLett.49.957. URL https://link.aps.org/doi/10.1103/PhysRevLett.49.957. (Cited on page 12.)

R. M. Wilson, C. Ticknor, J. L. Bohn, and E. Timmermans. Roton immiscibility in a two-component dipolar bose gas. *Physical Review A*, 86(3):033606, Sep 2012. doi: 10.1103/PhysRevA.86.033606. URL https://link.aps.org/doi/10.1103/PhysRevA.86.033606. (Cited on page 122.)

A. Wolf, P. Boegel, M. Meister, A. Balaž, N. Gaaloul, and M. A. Efremov. Shell-shaped Bose-Einstein condensates based on dual-species mixtures. *Physical Review A*, 106(1): 013309, Jul 2022. doi: 10.1103/PhysRevA.106.013309. URL https://link.aps.org/doi/10.1103/PhysRevA.106.013309. (Cited on page 80.)

E. M. Wright, J. Arlt, and K. Dholakia. Toroidal optical dipole traps for atomic bose-einstein condensates using laguerre-gaussian beams. *Physical Review A*, 63:013608, Dec 2000. doi: 10.1103/PhysRevA.63.013608. URL https://link.aps.org/doi/10.1103/PhysRevA.63.013608. (Cited on page 3.)

Z. Wu, E. Zaremba, J. Smyrnakis, M. Magiropoulos, N. K. Efremidis, and G. M. Kavoulakis. Mean-field yrast spectrum and persistent currents in a two-component bose gas with interaction asymmetry. *Physical Review A*, 92:033630, Sep 2015. doi: 10.1103/PhysRevA.92.033630. URL https://link.aps.org/doi/10.1103/PhysRevA.92.033630. (Cited on page 2.)

J. Xu, Q. Jia, H. Qiu, and A. Muñoz Mateo. Gap solitons and nonlinear bloch states in Bose-Einstein condensates with current-dependent interactions. *Physical Review A*, 108(5):053313, Nov 2023. doi: 10.1103/PhysRevA.108.053313. URL https://link.aps.org/doi/10.1103/PhysRevA.108.053313. (Cited on pages 5 and 129.)

D. Yan, F. Tsitoura, P. G. Kevrekidis, and D. J. Frantzeskakis. Dark-bright solitons and their lattices in atomic Bose-Einstein condensates. *Physical Review A*, 91(2):023619, Feb 2015. doi: 10.1103/PhysRevA.91.023619. URL https://link.aps.org/doi/10.1103/PhysRevA.91.023619. (Cited on pages 7, 98, 99, 104, 109, and 110.)

C. N. Yang. Concept of off-diagonal long-range order and the quantum phases of liquid he and of superconductors. *Reviews of Modern Physics*, 34(4):694–704, Oct 1962. doi: 10.1103/RevModPhys.34.694. URL https://link.aps.org/doi/10.1103/RevModPhys.34.694. (Cited on page 14.)

S.-H. Yang, R. Naaman, Y. Paltiel, and S. S. Parkin. Chiral spintronics. *Nature Reviews Physics*, 3(5):328–343, Apr 2021. doi: 10.1038/s42254-021-00302-9. URL https://doi.org/10.1038/s42254-021-00302-9. (Cited on page 5.)

K.-X. Yao, Z. Zhang, and C. Chin. Domain-wall dynamics in Bose–Einstein condensates with synthetic gauge fields. *Nature*, 602(7895):68–72, Feb 2022. doi: 10.1038/s41586-021-04250-3. URL https://www.nature.com/articles/s41586-021-04250-3. (Cited on pages 5 and 129.)

S. Yi and L. You. Trapped atomic condensates with anisotropic interactions. *Physical Review A*, 61(4):041604, Mar 2000. doi: 10.1103/PhysRevA.61.041604. URL https://link.aps.org/doi/10.1103/PhysRevA.61.041604. (Cited on pages 40 and 47.)

S. Yi and L. You. Trapped condensates of atoms with dipole interactions. *Physical Review A*, 63(5):053607, Apr 2001. doi: 10.1103/PhysRevA.63.053607. URL https://link.aps.org/doi/10.1103/PhysRevA.63.053607. (Cited on pages 40 and 47.)

V. Zakharov and S. Manakov. The theory of resonance interaction of wave packets in nonlinear media. *Soviet Physics JETP*, 69(5):1654–1673, 1975. (Cited on page 7.)

V. E. Zakharov and E. Schulman. To the integrability of the system of two coupled nonlinear schrödinger equations. *Physica D: Nonlinear Phenomena*, 4(2):270–274, 1982. doi: 10.1016/0167-2789(82)90068-9. URL https://doi.org/10.1016/0167-2789(82)90068-9. (Cited on page 7.)

A. Zee. *Quantum field theory in a nutshell*, volume 7. Princeton University Press, 2010. (Cited on page 62.)

J.-Y. Zhang, S.-C. Ji, Z. Chen, L. Zhang, Z.-D. Du, B. Yan, G.-S. Pan, B. Zhao, Y.-J. Deng, H. Zhai, S. Chen, and J.-W. Pan. Collective dipole oscillations of a spin-orbit coupled bose-einstein condensate. *Physical Review Letters*, 109:115301, Sep 2012. doi: 10.1103/PhysRevLett.109.115301. URL https://link.aps.org/doi/10.1103/PhysRevLett.109.115301. (Cited on page 5.)

S. C. Zhang, T. H. Hansson, and S. Kivelson. Effective-field-theory model for the fractional quantum hall effect. *Physical Review Letters*, 62(1):82–85, Jan 1989. doi: 10.1103/PhysRevLett.62.82. URL https://link.aps.org/doi/10.1103/PhysRevLett.62.82. (Cited on page 73.)

Y.-C. Zhang, F. Maucher, and T. Pohl. Supersolidity around a critical point in dipolar Bose-Einstein condensates. *Physical Review Letters*, 123(1):015301, Jul 2019. doi: 10.1103/PhysRevLett.123.015301. URL https://link.aps.org/doi/10.1103/PhysRevLett.123.015301. (Cited on page 112.)

Y.-C. Zhang, T. Pohl, and F. Maucher. Phases of supersolids in confined dipolar Bose-Einstein condensates. *Physical Review A*, 104(1):013310, Jul 2021. doi: 10.1103/PhysRevA.104.013310. URL https://link.aps.org/doi/10.1103/PhysRevA.104.013310. (Cited on pages 60 and 112.)

J.-h. Zheng, B. Xiong, G. Juzeliūnas, and D.-W. Wang. Topological condensate in an interaction-induced gauge potential. *Physical Review A*, 92:013604, Jul 2015. doi: 10.1103/PhysRevA.92.013604. URL https://link.aps.org/doi/10.1103/PhysRevA.92.013604. (Cited on page 5.)

L. Zheng, Y.-C. Zhang, and C.-F. Liu. Propagation of dark soliton interacting with domain wall in two immiscible Bose–Einstein condensates. *Chinese Physics B*, 28(11):116701, Oct 2019. doi: 10.1088/1674-1056/ab457e. URL https://dx.doi.org/10.1088/1674-1056/ab457e. (Cited on pages 99, 103, and 104.)

O. Zobay and B. M. Garraway. Two-dimensional atom trapping in field-induced adiabatic potentials. *Physical Review Letters*, 86(7):1195–1198, Feb 2001. doi: 10.1103/PhysRevLett.86.1195. URL https://link.aps.org/doi/10.1103/PhysRevLett.86.1195. (Cited on pages 3, 79, and 82.)

O. Zobay and B. M. Garraway. Atom trapping and two-dimensional Bose-Einstein condensates in field-induced adiabatic potentials. *Physical Review A*, 69(2):023605, Feb 2004. doi: 10.1103/PhysRevA.69.023605. URL https://link.aps.org/doi/10.1103/PhysRevA.69.023605. (Cited on pages 3, 79, and 82.)